NREL National Renewable Energy Laboratory

Innovation for Our Energy Future

Fundamental Materials Research and Advanced Process Development for Thin-Film CIS-Based Photovoltaics

Final Technical Report
2 October 2001 — 30 September 2005

T.J. Anderson, S.S. Li, O.D. Crisalle,
and V. Craciun
University of Florida
Gainesville, Florida

Fundamental Materials Research and Advanced Process Development for Thin-Film CIS-Based Photovoltaics

Final Technical Report
2 October 2001 — 30 September 2005

T.J. Anderson, S.S. Li, O.D. Crisalle, and V. Craciun
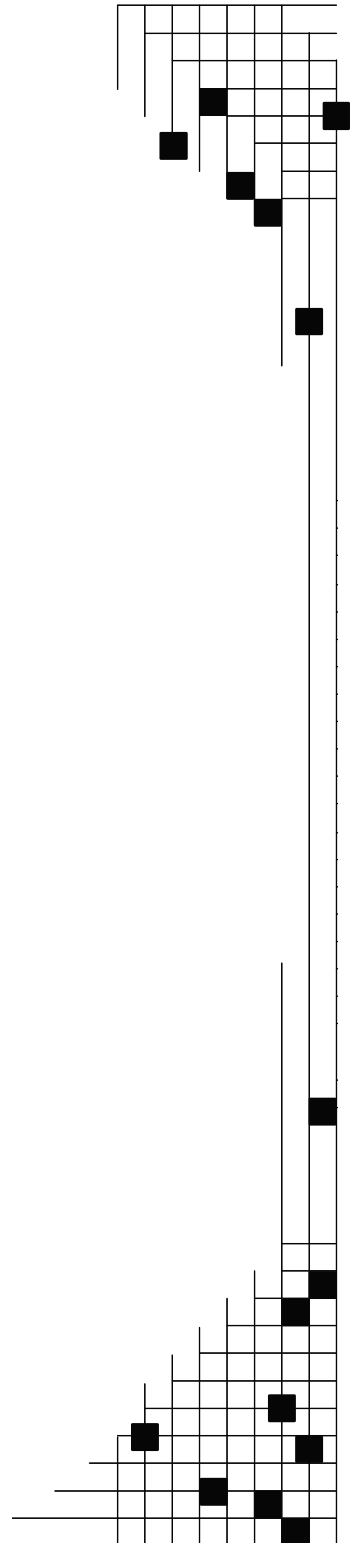*University of Florida*
Gainesville, Florida

NREL Technical Monitor: B. von Roedern
Prepared under Subcontract No. ADJ-2-30630-13

Available electronically at http://www.osti.gov/bridge

Available for a processing fee to U.S. Department of Energy
and its contractors, in paper, from:
     U.S. Department of Energy
     Office of Scientific and Technical Information
     P.O. Box 62
     Oak Ridge, TN 37831-0062
     phone: 865.576.8401
     fax: 865.576.5728
     email: mailto:reports@adonis.osti.gov

Available for sale to the public, in paper, from:
     U.S. Department of Commerce
     National Technical Information Service
     5285 Port Royal Road
     Springfield, VA 22161
     phone: 800.553.6847
     fax: 703.605.6900
     email: orders@ntis.fedworld.gov
     online ordering: http://www.ntis.gov/ordering.htm

TABLE OF CONTENTS

vi

1 Development and Characterization of Buffer Layers for Copper-Indium-Diselenide-Based Solar Cells

1.1 Introduction

In a typical CIGS-based solar cell a very thin CdS buffer layer (< 500Å) is usually deposited between the ZnO window layer and the CIGS absorber layer in order to achieve high conversion efficiency. Among various buffer layer materials such as CdS, (Cd,Zn)S, ZnS, Zn(O,S,OH)$_x$, ZnO, ZnSe, In$_x$(OH,S)$_y$, In$_2$S$_3$, In(OH)$_3$, SnO$_2$, Sn(S,O)$_2$, ZnSe, or ZrO$_2$ deposited by the CBD, ALE, MOCVD, or other deposition processes, the best performance CIGS solar cell with a total-area conversion efficiency of 18.8% [1-1] and other high-efficiency (> 17%) CIGS solar cells [1-2][1-3] were obtained by using the CBD CdS buffer layers. However, the role of CBD CdS buffer layer on the CIGS cell performance is not well understood. In view of the ability of depositing large area and uniform films, the non-vacuum low-temperature CBD process is very advantageous for manufacturing low-cost photovoltaic devices. Although a dry vacuum process has advantages for in-line manufacturing, the CBD process provides a simple, flexible, and cost-effective means for the deposition of buffer layers on the CIS-based solar cells. It has been reported that Cd-partial electrolyte treatment [1-4] modifies the CIGS surface favorably as evidence by the improvement in performance of CIGS solar cells [1-5]. Unfortunately, the basic mechanisms responsible for the cell performance are still not clear.

Using the wider band-gap materials to replace the CdS (E$_g$≈2.4eV) buffer layer could improve the quantum efficiency of the CIGS cell at shorter wavelengths, resulting in an increase of the short-circuit current. The (Cd,Zn)S buffer layer has a band-gap energy greater than 2.4eV, and can provide a better lattice match to the CIGS absorber layer. On the other hand, the toxicity of cadmium (Cd) and the desirability of using a wider band-gap material to achieve a higher spectral response in the blue region have motivated the search for other alternative buffer layer materials. Using ZnS (E$_g$≈3.6eV) and In(OH)$_x$S$_y$ (E$_g$≈2.54eV [1-6]) buffer layers for the CIGS solar cells have achieved high active-area conversion efficiencies of 18.1% [1-7] and 15.7% [1-8], respectively. Thus, both ZnS and In(OH)$_x$S$_y$ thin films are promising candidates for the Cd-free buffer layers among the reported alternative materials

The buffer layer materials of CdS, (Cd,Zn)S, ZnS, or In(OH)$_x$S$_y$ was deposited on the soda-lime glass substrates, Cu(In,Ga)Se$_2$ (CIGS), or Cu(In,Ga)(Se,S)$_2$ (CIGSS) thin films by the chemical-bath-deposition (CBD) process. The impurities in the deposited films and their atomic concentration were characterized by the x-ray photoelectron spectroscopy (XPS) and auger electron spectroscopy (AES) analyses. In addition, the composition of depth profile of the samples was characterized by using the AES. The band-gap energy of the deposited In(OH)$_x$S$_y$ thin films was determined from the optical absorption data. Both the CIGS and CIGSS samples deposited with the CdS, (Cd,Zn)S, ZnS, or In(OH)$_x$S$_y$ buffer layers by the CBD process were fabricated into solar cells. The current-voltage (I-V) characteristics of these cells with the alternative buffer layers were measured, and the results were compared to the cells deposited with CBD CdS buffer layers. The results show a comparable performance among these cells, and further optimization of the deposition conditions should improve the performance of the cells deposited with the alternative buffer layers.

1.2 Processing

1.2.1 Chemical-Bath-Deposition Conditions

In the deposition of thin solid films in a chemical bath by the CBD process the nucleation centers are regularly formed by the absorption of metal hydroxo species on the surface of the substrate. The initial layer of the thin film is formed through the replacement of hydroxo group by the sulphide ions, and subsequently the solid film is grown by the condensation of metal and sulphide ions onto the top of the initial layer.

The aqueous solution consisting of 2.4×10^{-4}M CdCl$_2$, 2.38×10^{-3}M NH$_2$CSNH$_2$, 7.43×10^{-4}M NH$_4$Cl, and 6.61×10^{-4}M NH$_4$OH at a bath temperature in the range of 80 to 85°C was applied for the deposition of CdS films. The CBD In(OH)$_x$S$_y$ films were deposited using a freshly prepared aqueous solution of 0.005M indium chloride and 0.15M thioacetamide at 70°C with deposition times varied between 15 and 25 minutes and with a pH value of 1.8. In order to avoid nucleation centers in the bath for the deposition of In(OH)$_x$S$_y$, the insoluble particles present in the stock solution of thioacetamide were eliminated by filtration. The complexing agent, acetic acid, was added into the bath during the deposition of In(OH)$_x$S$_y$ as a new deposition condition to improve the film quality. The deposition of (Cd,Zn)S buffer layers was carried out with 1.2×10^{-3}M CdCl$_2$, 6.27×10^{-4}M ZnCl$_2$, 1.2×10^{-2}M thiourea, 5.27×10^{-4}M NH$_3$, and 1.39×10^{-3}M NH$_4$Cl, and the bath temperature was maintained at around 85°C. For the CBD ZnS films the deposition bath was prepared with an aqueous solution of 2.5×10^{-2}M ZnSO$_4$, 3.5×10^{-2}M thiourea, 1M NH$_3$, and 3M hydrazine at a bath temperature varied between 70 and 80°C.

Two competitive processes, namely the heterogeneous process of the solid film deposited on the substrate and the homogeneous process of precipitation in the reaction bath, took place simultaneously in the chemical bath during the CBD process. In order to remove the possible precipitation, which may be attached on the surface of the films, the substrates were well rinsed with DI water after the deposition and blown dry with nitrogen stream.

1.2.2 Device Fabrication

The CdS, (Cd,Zn)S, ZnS, or In(OH)$_x$S$_y$ buffer layers were deposited on the CIGS and CIGSS samples provided by the Institute of Energy Conversion (IEC) of the University of Delaware, ISET, and Siemens Solar Industries. The high/low resistivity ZnO bilayer films were then deposited by either the MOCVD or sputtering technique on these samples. The Ni/Al grids as contact pads were finally deposited to obtain the finished cells.

1.3 Characterization of CdS, (Cd,Zn)S, ZnS, and In(OH)$_x$S$_y$ Buffer Layers

1.3.1 Compositional Analysis

The near surface composition of the CdS, (Cd,Zn)S, ZnS, and In(OH)$_x$S$_y$ films deposited on the soda-lime glass substrates and CIGS samples were characterized by the x-ray photoelectron spectroscopy (XPS), and the results are shown in Figure 1-1. The XPS analysis was conducted by using a Physical Electronics 5100 ESCA equipped with a Mg Kα X-ray source and a hemispherical analyzer. Depth profiling was performed with an argon ion source operating at the beam energy of 4 KeV. The charging effects were taken into account by referring the measured spectra to the binding energy peak of C 1s at 285eV. Carbon was initially present for all films deposited by the CBD process described in the previous section but became undetectable during sputter depth profiling, indicating that little carbon was incorporated in the films. Besides carbon, elements of metal (Cd, Zn, or In), sulfur, and oxygen were also identified in the deposited films.
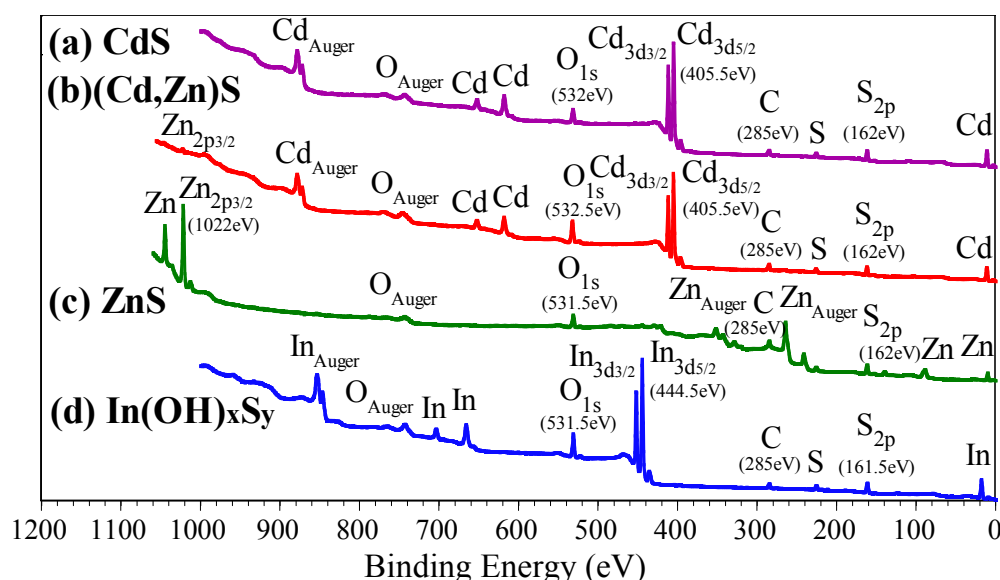
Figure 1-1. XPS spectra of CdS, (Cd,Zn)S, ZnS, or In(OH)$_x$S$_y$ thin films deposited on CIGS thin films by the CBD process.

Before and after sputtering the CBD CdS films the binding energy peaks of Cd 3d$_{5/2}$ and S 2p$_{3/2}$ at about 405.3eV and 161.5eV were obtained, respectively. The result shows that the sulfur peak is in good agreement with the reported data (S-Cd: 161.7eV [1-9]). The binding energies of Cd-S (405.3eV [1-9]), Cd-O (405.2eV [1-9]), and Cd-OH (405.0eV [1-9]) are too close to identify the exact compounds presented in the film from the measured Cd peak at 405.3eV. Two peaks at 529.48eV and 531.09eV obtained from the deconvolution of O 1s binding energy curve demonstrate that the film consists of chemical bonds Cd-O (529.2eV [1-9])

3

and Cd-OH (530.9-532eV [1-9]). The estimated atomic concentration ratios of [Cd]/[S] and [S]/[O] are approximately 1.6 and 5.4, respectively. For the (Cd,Zn)S film the atomic concentration was estimated from the peak area of each element, Cd, Zn, S, and O, in the film. The XPS result indicated that a large amount of oxygen (around 40%) and a small amount of zinc (around 2%) were incorporated in the (Cd,Zn)S film. Because the precipitation of CdS is easier and faster than that of ZnS during the CBD process, the deposited (Cd,Zn)S film only had a very small quantity of zinc even though the concentration of zinc source was an order of magnitude higher than that of cadmium source in the deposition bath.

For the ZnS film, the deconvolution of Zn $2p_{3/2}$ binding-energy spectrum from 1018eV to 1026eV revealed only one peak at 1022.0eV. This is consistent with the energy peaks of possible compounds ZnS and/or ZnO at 1022.0eV and 1021.8eV-1022.5eV [1-9], respectively. No evidence of $ZnSO_4$ was found from the Zn $2p_{3/2}$ peak, where the binding energy peak of $ZnSO_4$ is 1023.1eV. The oxygen 1s photoelectron binding energy spectra were fitted with Gaussian-Lorentzian curves both before and after sputtering the film. The XPS spectra can be represented by two peaks at about 530.6-530.1eV and 531.6eV, which correspond to the chemical bonds of Zn-O (530.4eV [1-9]) and metal-hydroxide compound (530.9-532eV [1-9]), respectively. Thus the results suggest that the CBD ZnS films might be a mixture of ZnS, ZnO, and $Zn(OH)_2$. The estimated atomic concentration ratio of Zn, S, and O was about 5:3:2 after sputtering the film for 4 minutes.

For the $In(OH)_xS_y$ films deposited by CBD with acetic acid in the bath, a binding energy peak of S $2p_{3/2}$ was found at about 161.24eV (see Figure 1-2), which can be assigned to the sulfide compound. In Figure 1-2, a very weak binding energy peak at around 168.96eV suggests that the indium sulfate (169-171eV [1-9]) was also present. After sputtering the film for 4 minutes no peak was found between 167ev and 173eV. We conclude that the sulfate compound only exists at the surface of the film. From Figure 1-3 the montage of binding energy distribution curves between 526eV and 544eV, it is evident that the shape of these curves changes for the oxygen 1s peak during the depth profiling. As shown in the inset of Figure 1-3(a), before sputtering the XPS spectra can be represented by two peaks at 531.4eV and 529.5eV, suggesting that the oxygen is present in the form of In-OH (531.8eV [1-9]) and In-O (529.8eV [1-9]). As exhibited in the inset of Figure 1-3(b), likewise two fitted peaks at 531.5eV and 530.0eV are present in the curve after sputtering the film. This suggests that the film has more indium hydroxide than indium oxide in the near surface region. The estimated atomic concentration ratios of In, O, and S were found to be around 49.9%: 26.5%: 23.6% after sputtering for 4 minutes.
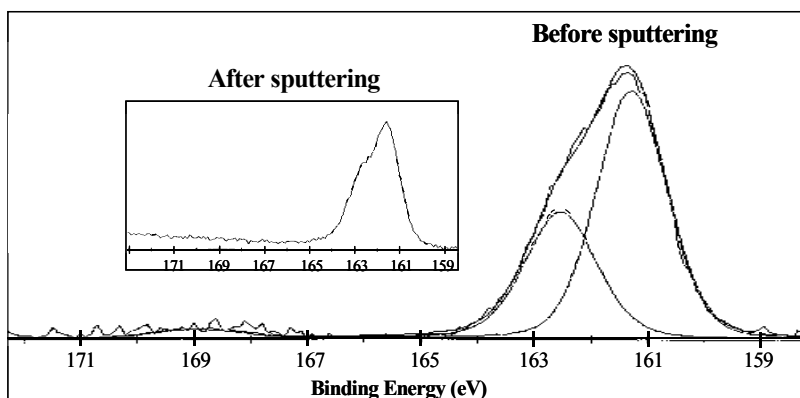
Figure 1-2.   XPS spectra of In(OH)$_x$S$_y$ films.
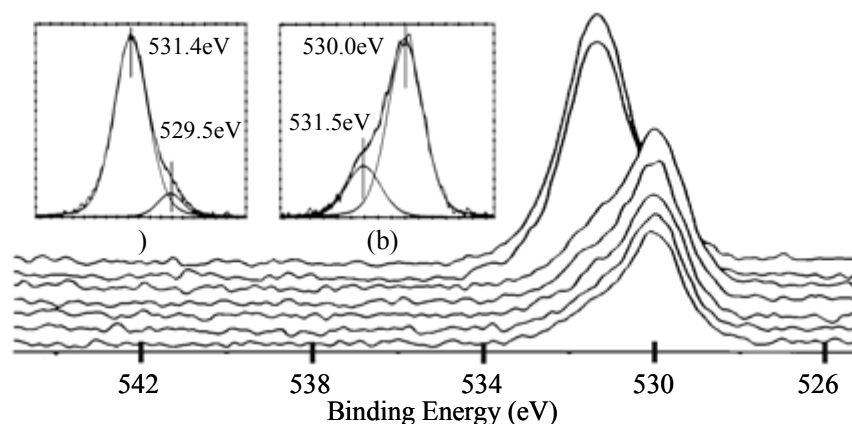
Figure 1-3. Montage of photoelectron binding energy spectra for a depth profile of an In(OH)$_x$S$_y$ film (View with surface curve in the background). The oxygen 1s photolectron binding energy spectra are (a) as-received surface, and (b) after sputtering for 4 minutes.

To determine whether the carbon was only present at the surface or incorporated throughout the film, Auger Electron Spectroscopy (AES) sputter depth profiles were performed. Figure 1-4 shows the differential Auger spectra taken for the initial In(OH)$_x$S$_y$ film and compared to those taken after 3 and 5 minutes of sputtering. The results indicate that the carbon is only at the surface and likely derived from the ambient. The spectra in Figure 1-4 also show that after 5 minutes sputtering time, some regions of the glass were exposed as evidenced by the appearance of Ca and Si signals. An AES depth profile for the CIGS/In(OH)$_x$S$_y$ sample is shown in Figure 1-5. The results indicate that the buffer layer barely covered the CIGS layer. Although intermixing between the In(OH)$_x$S$_y$ and the CIGS layers is suggested from the depth profile, this result is probably attributed to the roughness of CIGS surface.   Interdiffusion between the In(OH)$_x$S$_y$ buffer layer and the CIGS absorber layer is not expected to occur during the low temperature CBD process. However, an observation of intermixing at the interface between CdS

5

and CIGS involving the elements of S, Se, and In was reported recently [1-10]. Furthermore after the completed cell processing a strong intermixing between absorber (CIGS), buffer (CdS), and TCO (ZnO) material in the interface region was found [1-11].
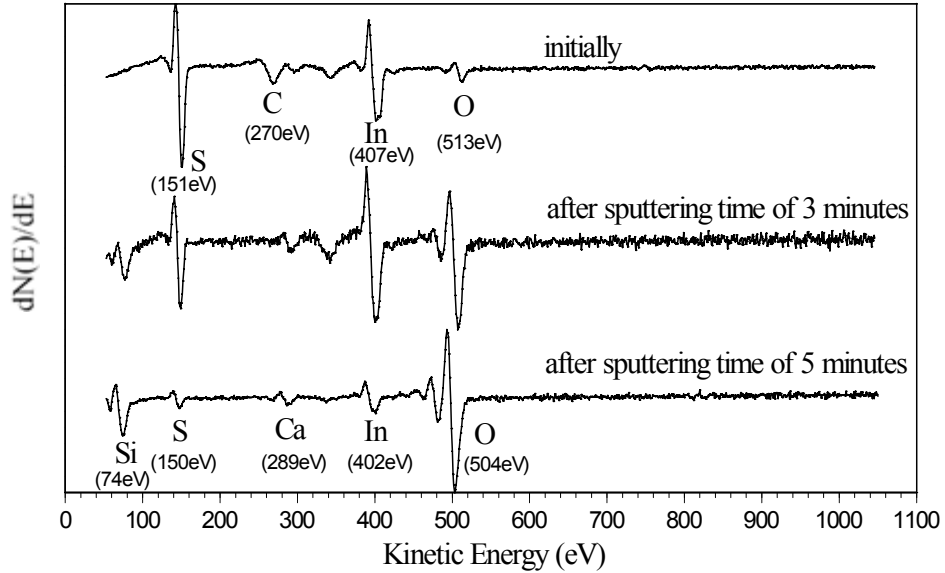
Figure 1-4. Differential Auger spectra of the In(OH)$_x$S$_y$ thin film deposited on the glass substrate.
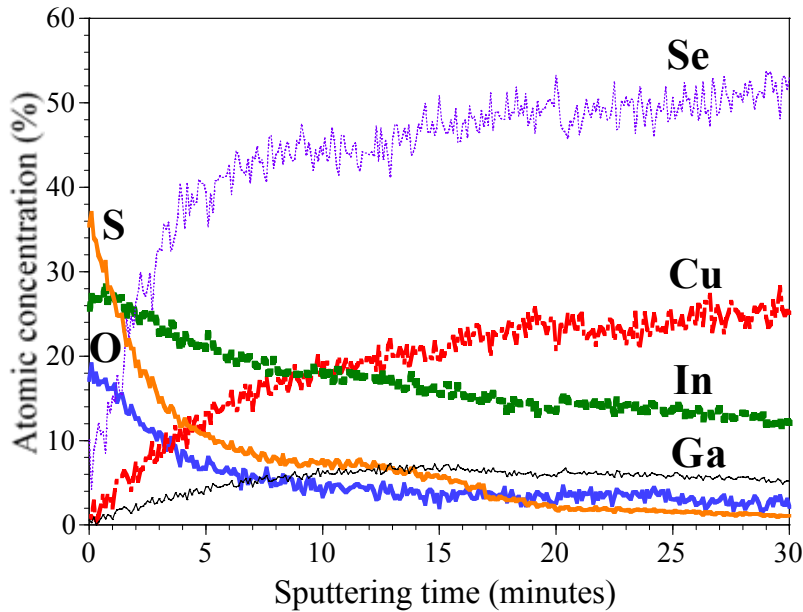
Figure 1-5. The Auger depth profile of the In(OH)$_x$S$_y$ thin film deposited on the CIGS cell by CBD process.

1.3.2 Optical Properties

The spectral dependence of the transmittance for the In(OH)$_x$S$_y$ films grown on the soda-lime glass substrates was measured using a spectrophotometer, and the results are shown in the inset of Figure 1-6. The In(OH)$_x$S$_y$ films with shorter deposition time have a higher transmittance at shorter wavelengths, which will result in an increase of short-circuit current in the CIGS cells. The buffer layers grown with longer deposition time, however, could provide a better shield effect against the sputtering damage during the ZnO deposition step and thereby reduce the interface recombination. Thus, the buffer-layer thickness needs to be optimized for the solar-cell performance. The band-gap energy of In(OH)$_x$S$_y$ was determined from the optical absorption data. To obtain the direct transition, $(\alpha h\nu)^2$ was plotted against $h\nu$ for the In(OH)$_x$S$_y$ films as illustrated in Figure 1-6. A band-gap energy of 2.54eV was obtained from the intercept of this plot. The band-gap energy of In(OH)$_x$S$_y$, which depends on the films stoichiometry, lies between 2eV and 3.7eV, the band-gap energies of In$_2$S$_3$ and In$_2$O$_3$, respectively [1-12].
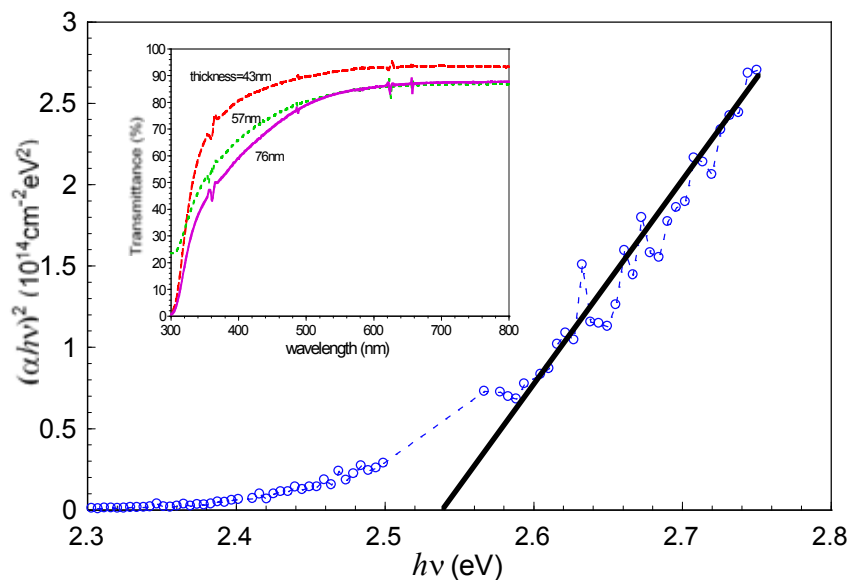
Figure 1-6. $(\alpha h\nu)^2$ versus $h\nu$ plot for the In(OH)$_x$S$_y$ thin film deposited on the glass substrate by the CBD process.

1.4 Current-Voltage Characteristics of CIGS-Based Solar Cells with CdS, (Cd,Zn)S, ZnS, or In(OH)$_x$S$_y$ Buffer Layers

1.4.1 CIGS-Based Cells with CdS or (Cd,Zn)S Buffer Layers

The J-V characteristics of CIGSS solar cells with the CdS or (Cd,Zn)S buffer layers deposited by our baseline CBD process are shown in Figure 1-7, where the CIGSS absorbers are provided by the Siemens Solar Industries. Evidently the CIGSS solar cell with the CdS buffer

layer has the best conversion efficiency. On the contrary the performance of the other cells deposited with the (Cd,Zn)S, ZnS, or In(OH)$_x$S$_y$ buffer layers yields a lower conversion efficiency than that of the CIGSS/CdS cell. From the results of this study further optimization of the alternative buffer layers is needed, which includes the optimization of the deposition conditions to improve the film quality and the investigation of the effects of post-deposition annealing and light soaking on the devices.
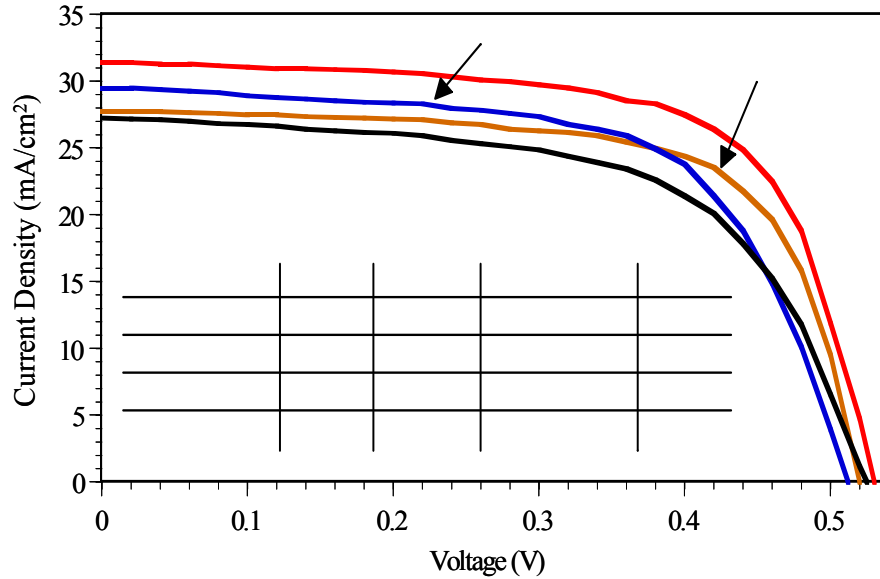
Figure 1-7. The J-V characteristics of the CIGSS cells with CdS, (Cd,Zn)S, ZnS, or In(OH)$_x$S$_y$ buffer layers.

In addition, the CdS buffer layers were also deposited by using the UF baseline CBD process [1-13] with a deposition time of 30 or 40 minutes on the same sets of CIGS samples provided by the IEC. The CIGS/CdS cell with a deposition time of 30 minutes has a better performance with V_{OC} =0.51V, J_{SC} =30.5mA/cm^2, F.F. =63.8%, and conversion efficiency η =9.99%, and the results are listed in Table 1-1. Apparently, the effect of annealing considerably improves the performance of these cells with either the thinner or thicker buffer layers. Also the performance of the CIGS cells can be further enhanced by optimizing the thickness of the CdS buffer layers via the variation of the deposition time.

Table 1-1. The performance of CIGS Cells with CBD CdS buffer layers

	1.1.1 Deposition time	As deposited	Annealing 5 min.
Conversion Efficiency η	40minutes	8.87%	9.91%
	30minutes	8.41%	9.99%
Fill Factor (F.F)	40minutes	61.7%	61.9%
	30minutes	60.8%	63.8%
Open-circuit Voltage V_{OC}	40minutes	0.4745V	0.5017V
	30minutes	0.4697V	0.5136V
Short-circuit Current Density J_{SC}	40minutes	30.31 mA/cm^2	31.88 mA/cm^2
	30minutes	29.47 mA/cm^2	30.51 mA/cm^2

1.4.2   CIGS-Based Cells with ZnS Buffer Layers

Figure 1-8 illustrates the effect of ZnS buffer-layer thickness on the performance of Siemens CIGSS solar cells. By increasing the ZnS buffer-layer thickness the absorption of incident light in the ZnS layer increases, and thus the short- circuit current of the cell decreases. Due to the high resistivity of ZnS buffer layer a thick buffer layer can cause a high series resistance in the solar cell and results in a poor fill factor as shown in Figure 1-8. With a higher band gap of ZnS than that of CdS, the CIGSS/ZnS cell should have a higher short-circuit current than the CIGSS/CdS cell because of the higher quantum efficiency at the shorter wavelength region. However, the highest short-circuit current obtained in this study for the CIGSS/ZnS cell was only 27.74 mA/cm^2 (see Figure 1-7), whereas for the CIGSS/CdS cell a short-circuit current of 31.4 mA/cm^2 was obtained. Thus, the further optimization of ZnS layer thickness and deposition condition is needed in order to achieve the potential of ZnS buffer layers for the CIS-based cells. The performance of the CIGS solar cells fabricated from the same set of ISET CIGS samples with our ZnS or ISET CdS buffer layers is shown in Figure 1-9. The CIGS/ZnS cell has a higher short-circuit current as expected but the cell suffers a comparably low open-circuit voltage.
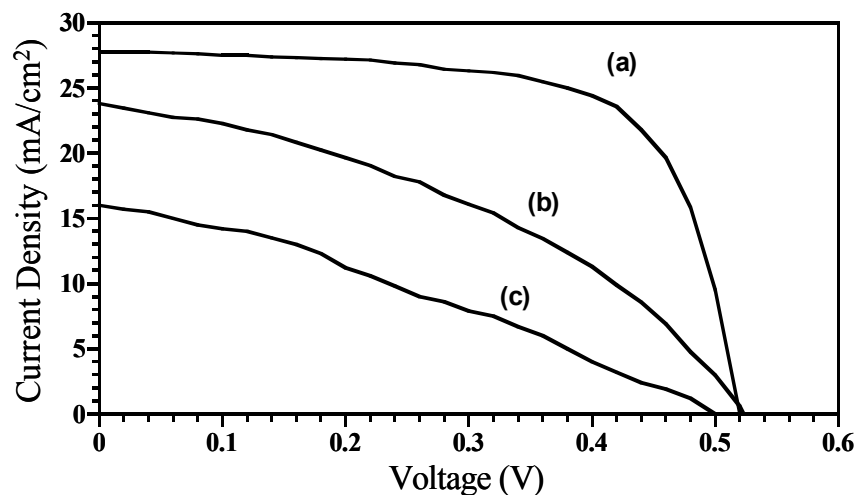
Figure 1-8. The J-V characteristics of CIGSS solar cells using different thickness of CBD ZnS buffer layers deposited for (a) 10min, (b) 20min, and (c) 25min at 70°C.

	Eff.	Voc (V)	Jsc (mA/cm^2)	F.F.
(a) CdS	9.9%	0.435	33.6	68.1%
(b) ZnS	9.3%	0.396	36.6	64.1%
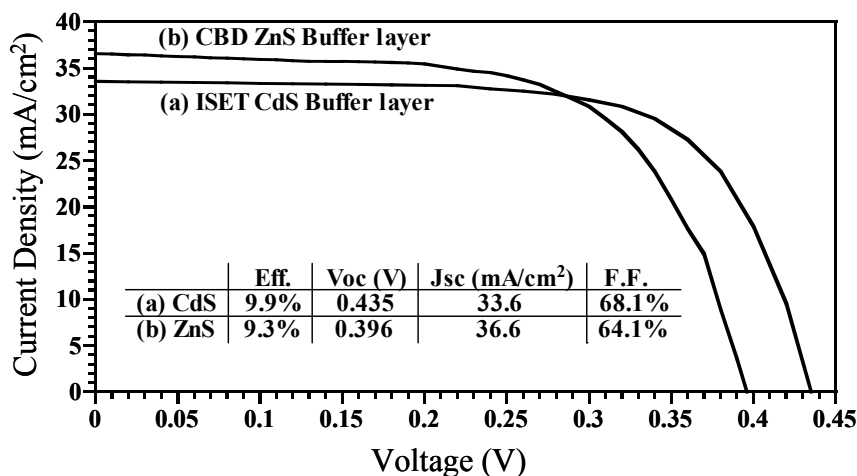
Figure 1-9. The J-V characteristics of CIGS cells with CdS buffer layer deposited at ISET or the ZnS buffer layer deposited at UF.

1.4.3   CIGS-Based Cells with In(OH)$_x$S$_y$ Buffer Layers

In order to obtain an optimum CBD process procedure for the deposition of In(OH)$_x$S$_y$ buffer layers, three different sequences of adding chemicals InCl$_3$ and CH$_3$CSNH$_2$, which might result in the modification of CIGS surface, were applied to the CIGS samples. It was found that the CIGS sample dipped in the DI water for a few seconds prior to the start of the deposition, which might have a precleaning effect on the CIGS surface, showed the best device performance from this experiment. The results are shown in the Table 1-2.

10

Table 1-2. The Performance of the CIGS solar cells with CBD $In(OH)_xS_y$ buffer layers using different procedures of adding chemicals

	1.1.1 Cell- 1	Cell- 2	Cell- 3
Conversion Efficiency η	7.39 %	5.73 %	5.23 %
Fill Factor (F.F)	44.6 %	38.2 %	38.3 %
Open-circuit Voltage V_{OC}	0.57 V	0.52 V	0.51 V
Short-circuit Current Density J_{SC}	29.1 mA/cm^2	28.9 mA/cm^2	27.0 mA/cm^2

Note: For the CBD process: cell- 1 was first immersed in DI water, and then both $InCl_3$ and CH_3CSNH_2 were added into the bath simultaneously; cell- 2 was first immersed in the solution of CH_3CSNH_2, and then $InCl_3$ was added into the bath; cell- 3 was first immersed in the solution of $InCl_3$, and then CH_3CSNH_2 was added into the bath.

Each I-V measurement for the CIGS cells comprised a sweep in the I_{SC} to V_{OC} direction followed immediately by a sweep from V_{OC} to I_{SC} direction. The dark- and photo-I-V curves of the CIGS/$In(OH)_xS_y$ heterojunction cell before and after annealing at $200^{\circ}C$ in the air for 20 minutes are shown in the Figure 1-10. As illustrated a hysteresis loop was observed in the photo-I-V curves of the CIGS/$In(OH)_xS_y$ cells before and after annealing. On the contrary, no evidence of a hysteresis loop in the photo-I-V curves of the CIGS/CdS cells was found in this study.
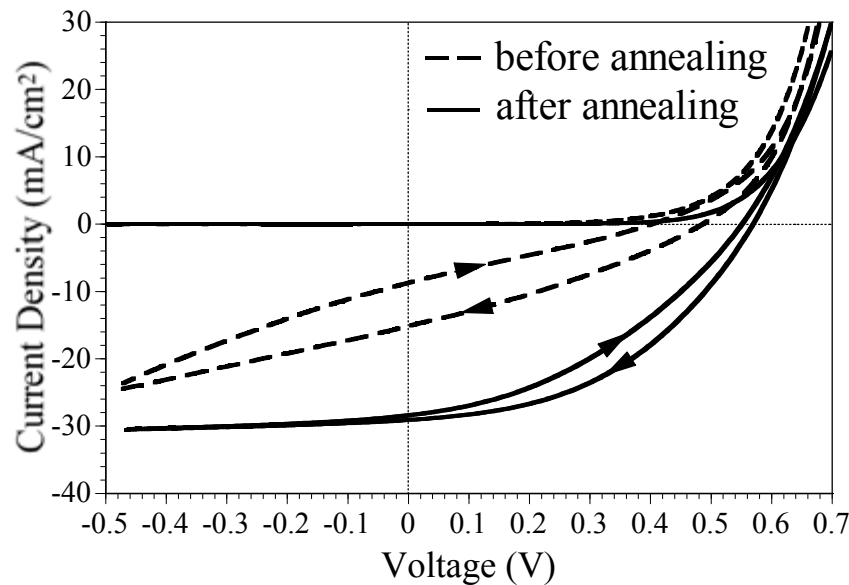
Figure 1-10. The J-V characteristics of the CIGS cell deposited with CBD $In(OH)_xS_y$ buffer layer before and after annealing.

Initially the device without annealing showed the inflected I-V curve. As shown in Figure 1-10 and Figure 1-11, the fill factor (F.F.), J_{SC}, V_{OC}, and hence the conversion efficiency were dramatically improved after annealing time of 20 minutes. The cells, however, showed degradation when the total annealing time was increased to 40 minutes. In order to improve the cell performance, it is necessary to optimize the annealing conditions.
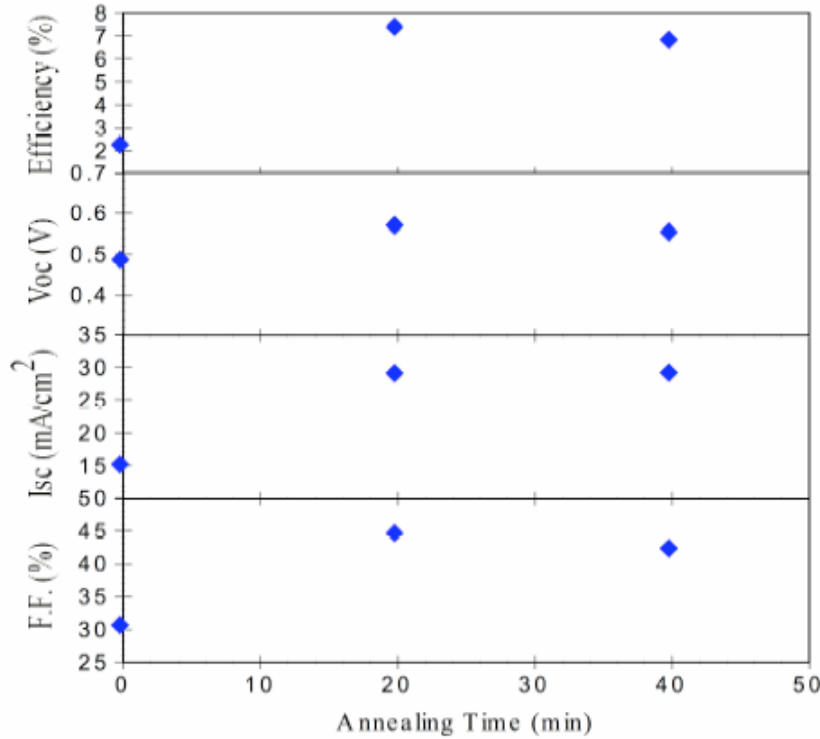
Figure 1-11. The performance of the CIGS solar cells deposited with CBD In(OH)$_x$S$_y$ buffer layers as a function of annealing time.

Comparing the performance of CIGS/CdS cells and CIGS/In(OH)$_x$S$_y$ cells, we have found that the latter has a much higher open-circuit voltage, a comparable short-circuit current density, and a very poor fill factor (V_{OC} =0.57V, J_{SC} =29.1mA/cm^2, F.F. =44.6%, and a low conversion efficiency η =7.39%) as shown in Figure 1-12, while the CIGS/CdS cell yielded a conversion efficiency of 9.99%, V_{OC}=0.51V, J_{SC}=30.5mA/cm^2, and F.F.=63.8%. The possible reason why the CIGS/In(OH)$_x$S$_y$ cell has a higher V_{OC} is that the net acceptor concentration in the CIGS layer is increased and hence the depletion width is reduced. The CBD alternative buffer layer process might influence the charged states at the surface or at the grain boundaries of the CIGS layer and hence modify the electrical properties of the absorber layer as well [1-8]. However, the CIGS/In(OH)$_x$S$_y$ cell has a lower J_{SC} due to the lower quantum efficiency than the CIGS/CdS cell in the long wavelength region [1-8].
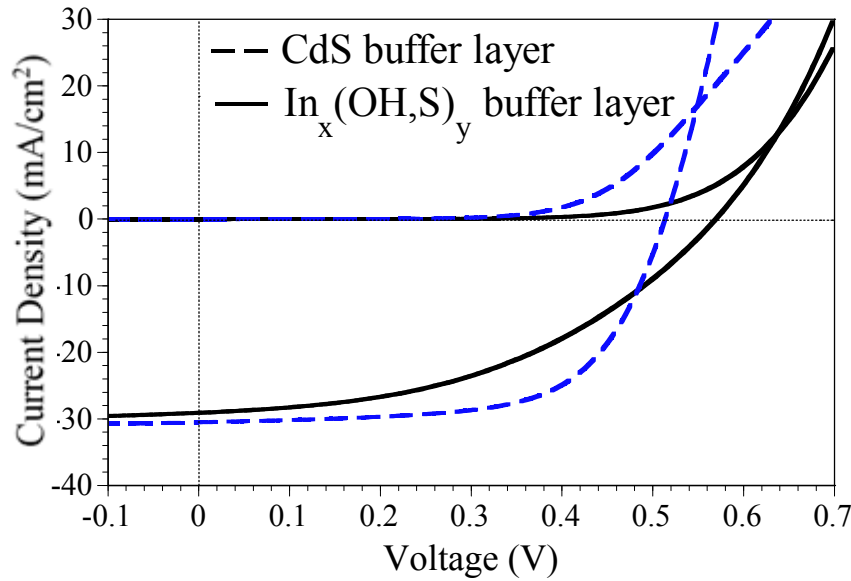
Figure 1-12. J-V characteristics of the CIGS cells with CBD- CdS or CBD-In(OH)$_x$S$_y$ buffer layer (CIGS/CdS solar cell: Eff.=9.99%, V_{OC}=0.51V, J_{SC}=30.5mA/cm^2, F.F.=63.8%; CIGS/In(OH)$_x$S$_y$ solar cell: Eff.=7.39%, V_{OC}=0.57V, J_{SC}=29.1mA/cm^2, F.F.=44.6%).

By adding the complexing agent of acetic acid into the chemical bath, a more adherent, reproducible, homogeneous, and higher quality In(OH)$_x$S$_y$ film [1-14] has been deposited on the glass substrates and Siemens CIGSS samples. The performance of one CIGSS cell deposited with In(OH)$_x$S$_y$ buffer layer using acetic acid and the performance of the CIGSS cells deposited with other buffer layers are shown in Figure 1-7. The result reveals that we can take advantage of the In(OH)$_x$S$_y$ buffer layer deposited by the new deposition method to improve the cell performance.

1.5   Conclusions

A study of the electrical and optical properties of the CBD buffer layers on the soda-lime glass substrates and on the absorber layers was conducted. The XPS results indicated that CdS, (Cd,Zn)S, ZnS, and In(OH)$_x$S$_y$ films deposited by the CBD method were not completely pure. A small amount of carbon was found to incorporate in the first few atomic layers of the films. Also oxygen in the form of metal oxide and/or metal hydroxide was incorporated into the films during the deposition process. A better quality In(OH)$_x$S$_y$ buffer layer has been achieved by adding the acetic acid into the reaction bath. Annealing has been found to be a key factor for improving the conversion efficiency of CIS-based cells deposited with alternative buffer layers. Among the CIS-based solar cells with CdS, (Cd,Zn)S, ZnS, or In(OH)$_x$S$_y$ buffer layers studied in this work, the CIGSS/CdS cell gave the best performance. From the J-V characteristics obtained for the CIS-based solar cells with the alternative buffer layers, the deposition conditions of CBD process are merited to further optimize in order to realize the potential advantages of these buffer layers. Future study of the CIS-based solar cells with alternative buffer layers will focus on optimizing annealing conditions and on investigating the light soaking effects.

1.6 References cited

[1-1]   M. Contreras, B. Egass, K. Ramanathan, J. Hiltner, A. Swartzland, F. Hasoon, and R. Noufi, *Progress in Photovoltaics*, Vol. 7, pp. 311, 1999.

[1-2]   T. Negami, Y. Hashimoto, and S. Nishiwaki, *Solar Energy Materials and Solar Cells*, Vol. 67, pp. 331-335 ,2001.

[1-3]   E. Niemi, J. Hedstrom, T. Martinsson, K. Granath, L. Stolt, J. Skarp, D. Hariskos, M. Ruckh, H.W. Schock, *Conference Record of the 25th IEEE Photovoltaic Specialists Conference*, pp. 801-804, 1996.

[1-4]   J. Kessler, K.O. Velthaus, M. Ruckh, R. Laichinger, H.W. Schock, D. Lincot, R. Ortega and J. Vedel, *6th Photovoltaic Science and Engineering Conference (PVSEC-6) Proceedings*, New Delhi, India, pp. 1005-1010, 1992.

[1-5]   K. Ramanathan, R.N. Bhattacharya, J. Granata, J. Webb, D. Niles, M.A. Contreras, H. Wiesner, F.S. Hasoon, and R. Noufi, *Conference record of the 26th IEEE Photovoltaic Specialists Conference*, p. 319, 1997.

[1-6]   C.H. Huang, Sheng S. Li, W.N. Shafarman, C.-H. Chang, J.W. Johson, L. Reith, S. Kim, B.J. Stanbery, and T.J. Anderson, *Technical Digest of the 11th International Photovoltaic Science and Engineering Conference*, p. 855, 1999.

[1-7]   T. Nakada, and M. Mizutani, *Japanese Journal of Applied Physics*, Part 2, Vol. 41, Issue 2B, pp. L165-L167, 2002.

[1-8]   D. Hariskos, M. Ruckh, U. Rühle, T. Walter, H.W. Schock, J. Hedström, and L. Stolt, *Solar Energy Materials and Solar Cells*, Vol. 41/42, pp. 345-353, 1996.

[1-9]   J.F. Moulder, W.F. Stickle, P.E. Sobol, and K.D. Bomben, *Handbook of X-ray Photoelectron Spectroscopy*, pp. 45, 61, and 213-242, 1995.

[1-10] C. Heske, D. Eich, R. Fink, E. Umbach, T. van Buuren, C. Bostedt, L.J. Terminello, S. Kakar, M.M. Grush, T.A. Callcott, F.J. Himpsel, D.L. Ederer, R.C.C. Perera, W. Riedl, and F. Karg, *Applied Physics Letters*, Vol. 74, pp. 1451-1453, 1999.

[1-11] I. Luck, U. Störkel, W. Bohne, A. Ennaoui, M. Schmidt, H.W. Schock, and D. Bräunig, *Thin Solid Films*, Vol. 387, pp. 100-103, 2001.

[1-12] R. Bayon, C. Guillen, M.A. Martinez, M.T. Gutierrez, and J. Herrero, *J. Electrochem. Soc.*, Vol. 145, pp. 2775-2779, 1998.

[1-13] C. -H. Chang, A. A. Morrone, B. J. Stanbery, C. McCreary, M. Huang, C. H. Huang, S. S. Li, and T. J. Anderson, *AIP Conference Proceedings (NCPV Program Review Meeting)*, No. 462, pp. 114-119, 1998.

[1-14] R. Bayon, C. Maffiotte, and J. Herrero, *Thin Solid Films*, Vol. 353, pp. 100-107, 1999.

2 Growth and Characterization of Chemical-Bath-Deposition of $Zn_xCd_{1-x}S$ Buffer Layers Grown on CIGS Absorbers

2.1 Accomplishments

This report presents a characterization of thin films of $Zn_xCd_{1-x}S$ (denoted as ZnCdS in the suite), prepared by chemical bath deposition (CBD) for deployment as a buffer layer in CIGS thin film solar cells. We determined that ZnCdS materials with specific Zn contents have attractive physical properties for deployment as buffer films in CIGS solar cells. In particular, we deposited buffer layers of various relative stoichiometric compositions of Zn, denoted by the subindex x in the chemical formula $Zn_xCd_{1-x}S$, and investigated their structural, surface, optical, and electrical properties by XRD, SEM, spectrophotometry, and resistivity studies. The degree of crystallinity in the film decreased with increasing relative zinc content x, leading to an amorphous structure at the concentration level x = 0.5. In addition, the resistivity of the ZnCdS films also increased with increasing relative zinc content x. Of particular relevance is also the fact that the energy band gap of ZnCdS is higher than that of CdS, and that the bandgap increases with increasing zinc content x.

We manufactured CIGS solar cells using $Zn_xCd_{1-x}S$ buffer layers with Zn content values x = 0 (CdS), 0.1, 0.2, 0.3, 0.4, and 0.5, and carried out a comprehensive device characterization study in terms of current-density/voltage and quantum efficiency. The results showed that a ZnCdS/CIGS cell using buffer layer with a Zn composition x = 0.2 realized a conversion efficiency that was greater by a factor of 1.30 than the efficiency of a Zn-free reference cell of the form CdS/CIGS. The CIGS absorber films were provided by EPV.

2.2 Introduction

In view of environmental safety, it is highly desirable to replace CdS ($E_g \approx 2.4$ eV) by cadmium (Cd) free and toxic-free alternative buffer layers. In addition, wider band-gap buffer materials are preferred for CIGS cells, since they allow transmission of shorter wavelength photons into CIGS absorber and hence higher short-circuit current density (J_{sc}) could be expected. For this purpose, zinc (Zn)-based compound materials such as ZnO ($E_g \approx 3.3$ eV), $Zn_x(O,S)_y$ ($E_g \approx$ between 3.3 and 3.8 eV), $Zn(O,S,OH)_x$, and ZnS ($E_g \approx 3.8$ eV) deposited by CBD process are proposed as alternative buffer layers for CIGS thin film solar cells.

The addition of Zn to the most widely used CdS buffer layer material decreases the lattice constant with a lattice-match to CIGS and CGS absorbers and produces a more favorable conduction band alignment. Increasing Zn concentration in the $Zn_xCd_{1-x}S$ (CdS: $E_g \approx 2.4$ eV, ZnS: $E_g \approx 3.8$ eV) films increases band-gap energy, which results in an increase in short wavelength photo-response. Therefore, $Zn_xCd_{1-x}S$ could lead to the increase in quantum efficiency (QE) at shorter wavelengths and a favorable conduction band offset at the interface $Zn_xCd_{1-x}S$ buffer and the CIGS or CGS absorber layer. Furthermore, the influence of Zn-composition, x, in the $Zn_xCd_{1-x}S$ films on the properties of interface layers has not yet fully

understood. Therefore, studies of $Zn_xCd_{1-x}S$ buffer layers to replace the CdS buffer layer for the CIGS and CGS solar cells are desirable.

This report presents the development, growth, and characterization of $Zn_xCd_{1-x}S$ (denoted as ZnCdS) films prepared by chemical bath deposition (CBD) for use as buffer layers in CIGS thin film solar cells and the characteristics of I-V and QE of the CIGS solar cells with various Zn compositions in ZnCdS buffer layers. The results are compared to the cells deposited with CBD CdS buffer layer.

2.3 Experimental

2.3.1 Definition of the Relative Zinc Content in the Buffer film and in the CBD Solution

The composition of Zn relative to that of Cd in the chemical-bath-deposition solution is given by the expression

$$x_{bath} = [Zn] / ([Zn] + [Cd])$$

where [Zn] and [Cd] represent the concentrations of Zn and Cd in the liquid solution. On the other hand, the relative composition of Zn in the solid $Zn_xCd_{1-x}S$ buffer film is given by the subindex x, where

x = stoichiometric composition of Zn in a solid $Zn_xCd_{1-x}S$ film

The relationship between x_{bath} and x is still the subject of research; however, for the purposes of reporting results in this document, we make the simplifying assumption that

$$x = x_{bath}$$

Hence, when in this report we refer to a $Zn_xCd_{1-x}S$ film as having a relative fractional zinc composition x = 0.3, this statement should be interpreted to mean that the film in question was grown using a CBD solution with a concentration characterized by $x_{bath} = 0.3$.

2.3.2 Characterizations of $Zn_xCd_{1-x}S$ Thin Films

The chemicals used in this work consist of aqueous solutions of 1.20×10^{-3} M $CdCl_2 \cdot 2(1/2)H_2O$, 1.39×10^{-3} M NH_4Cl, 1.19×10^{-2} M thiourea (H_2NCSNH_2), 6.27×10^{-4} M $ZnCl_2$, and 5.27×10^{-4} M NH_3. By varying the relative ratio of Cd and Zn ions, the $Zn_xCd_{1-x}S$ films with solution composition parameter x_{bath} = 0, 0.3, and 0.5 were deposited on soda-lime-glass (SLG) substrates. The bath temperature of the solution was kept around 85 °C. The deposition time ranged from 20 to 90 minutes according to the mixture ratio in the solution. The value of pH was kept at 7.0 in all sample preparation. SLGs, used as substrates, were cleaned by washing in DI water, detergent, ultrasonic cleaner, and 3 step cascade. The cleaned SLG substrates were submerged into the starting solution vertically for deposition of ZnCdS films.

2.3.2.1 Thickness of ZnCdS Films

The film thickness of ZnCdS buffer layers was measured using a Tencor profiler. The ZnCdS films were deposited on the surface of soda-lime-glass (SLG) substrates, and were covered by #1529 photo resist. The system was then baked for 5 minutes at 110 °C, etched by dipping in diluted 10% HCl solution for 20 seconds, rinsed by D.I. water, and finally cleaned by acetone and isopropyl alcohol.

Figure 2-1 shows the film thickness observed as a function of deposition time for ZnCdS films with relative zinc compositions x = 0, 0.3, and 0.5. It is important to remark that all the films shown in Figure 2-1 were obtained through a single CBD process. For example, for x = 0, three SLG substrates were submerged in the CBD solution at the same time, and the glass substrates were removed from the bath, one at the time, after 20 min., 30 min, and 40 min, respectively.   The results show that the growth rate of ZnCdS films with relative zinc composition x = 0 (CdS) was faster compared to that of ZnCdS films with x = 0.3, and also the growth rate of films with x = 0.3 was faster compared to that of films with x = 0.5 as deposition time grew longer. The deposition rate decreases with increasing relative Zn content in the bath.
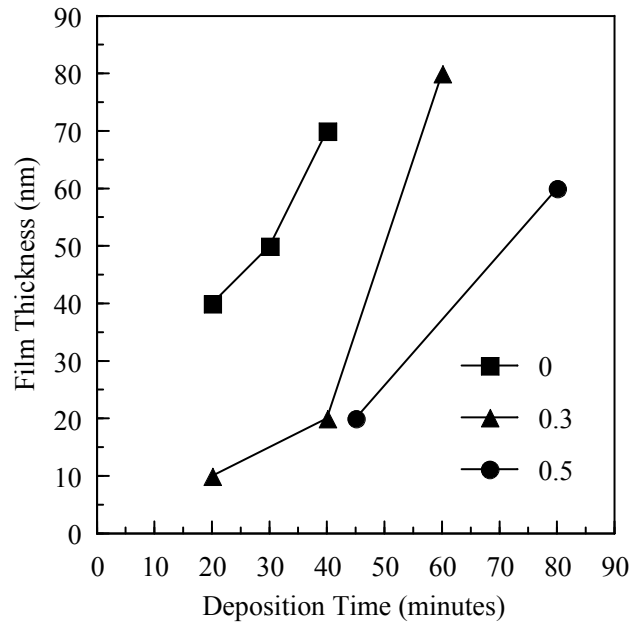
Figure 2-1. Film thickness as a function of deposition time for ZnCdS films with relative zinc compositions x = 0, 0.3, and 0.5.

Figure 2-2 shows the variation of the thickness of the films for different values of relative zinc composition x at a constant deposition time of 50 minutes. The thickness of the films is found to decrease with an increase of Zn content in the bath. Films showed poor adherence, and colors varied from yellow to mostly white with yellow tints, as the composition x increases up to 0.7. Similar observations have been reported in the literature [2-1].
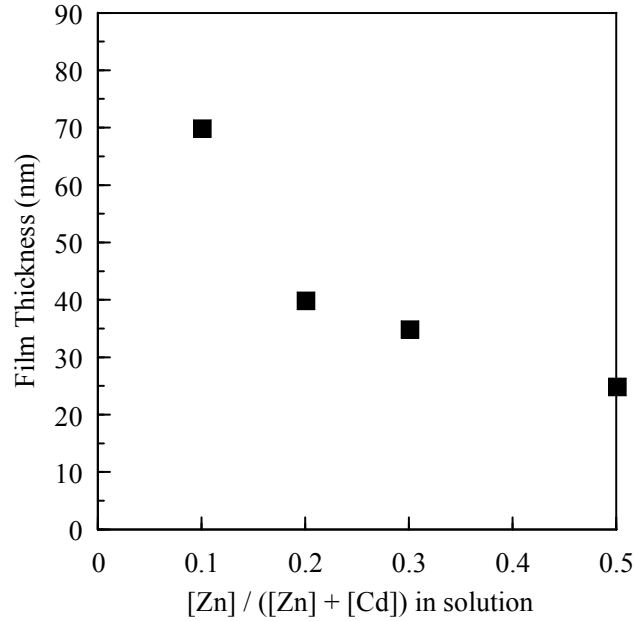
Figure 2-2. Film thickness variation as a function of relative zinc composition x for ZnCdS films with deposition time of 50 minutes.

2.3.2.2   Structural Analysis

A powder X-ray diffractometer with Cu Kα radiation was used to investigate the structural properties of ZnCdS films deposited on soda lime glass (SLG) substrates. The ZnCdS films prepared by a single CBD process did not show any peaks due to the very thin nature of the films. Clear diffraction peaks were obtained using thicker films grown by executing three sequential CBD operations, resulting in an approximate thickness of 200 nm (using a bath with relative zinc composition x = 0), 100 nm (x = 0.3), and 150 nm (x = 0.5). The resulting powder XRD patterns for ZnCdS films with x = 0, 0.3, and 0.5 are shown in Figure 2-3. A comparison of the 2θ peak-positions of the JCPDS XRD spectra data for the film with x = 0 (*i.e.*, a CdS film) suggests that the as-deposited ZnCdS films have hexagonal (wurtzite group) structures with X-ray diffraction peaks corresponding to the (100), (002), (101), (102), (110), (103), (112), and (004) planes. The peaks become weaker for films with at the higher Zn compositions x = 0.3, and no peaks appear for x = 0.5 reflecting the presence of amorphous structures.

It is difficult to analyze X-rays of thin films due to their low diffracted intensities produced by the film compared to those the substrate and background. A approach for analyzing thin films is to use Grazing Incidence-Angle X-ray Diffraction (GIXRD), which intensifies the diffracted signal by increasing the path length of the incident X-ray beam by using a very small angle (ω) between the incident beam and the film surface. To investigate the structural properties of ZnCdS thin layers near the surface or on the surface itself, we used GIXRD with a grazing angle ω = 0.4 °. Thin films with relative zinc compositions x = 0, 0.3, and 0.5 were deposited by a single CBD process on Mo-coated SLG substrates. The approximate thickness of the resulting films was in the range of 50 ~ 60 nm. The GIXRD patterns for ZnCdS films with x = 0, 0.3, and 0.5 are shown in Figure 2-4. It is observed that the 2θ diffraction-angle of the main peaks shifts to a slightly higher angle with increasing relative Zn composition, due to the

elemental substitutions of Zn for Cd. It is also found that the peaks of the ZnCdS thin film with x = 0.5 becomes less pronounced, suggesting a decrease in the crystalline nature of the film at that level of zinc content.
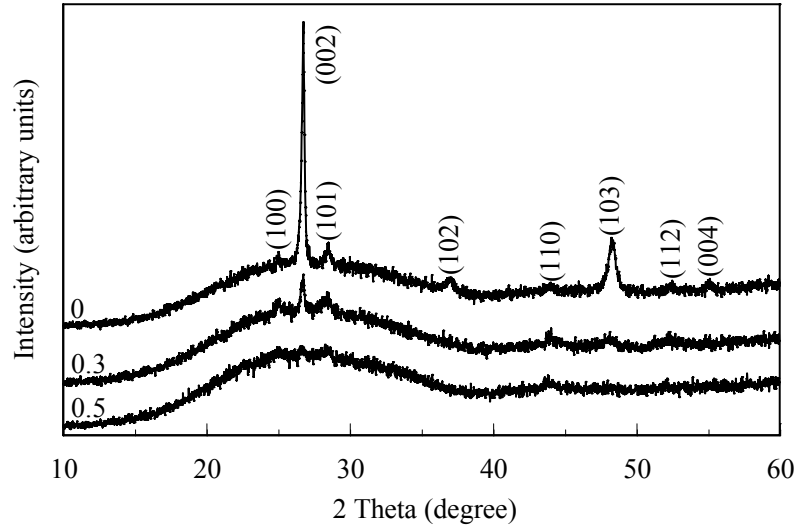
Figure 2-3. Powder XRD patterns of ZnCdS films deposited on the SLG with relative zinc composition x = 0 (film thickness d ≈ 200 nm), x = 0.3 (d ≈ 100 nm), and x = 0.5 (d ≈ 150 nm).
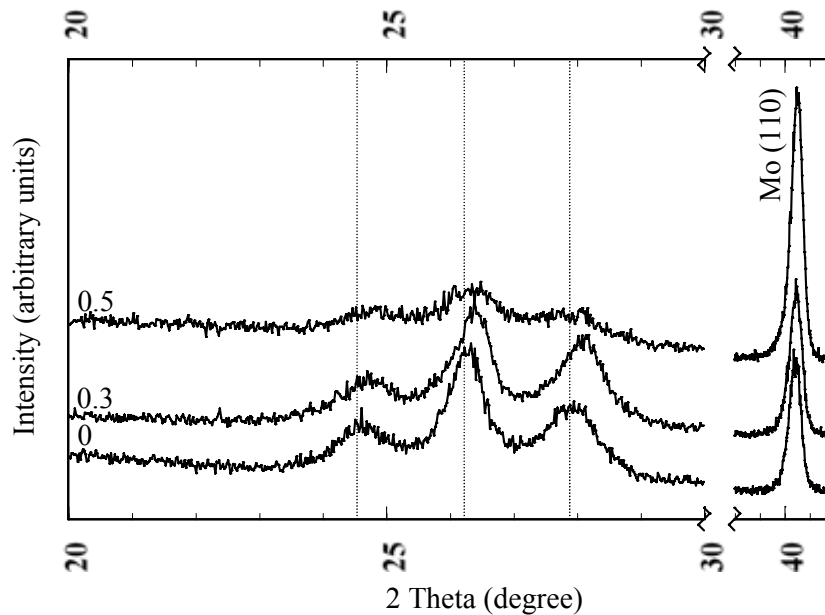
Figure 2-4. Grazing incidence XRD patterns of ZnCdS films, deposited on Mo, with relative zinc compositions x = 0, 0.3, and 0.5.

2.3.2.3 Surface Morphological Analysis

The surface characteristics of ZnCdS films grown on SLG substrates were examined using a field emission scanning electron microscope. The thickness of the ZnCdS films studied lied in the range of 70 to 150 nm. Figures 2-5, 2-6, and 2-7 show SEM micrographs of the ZnCdS films for different values of relative zinc composition x. The film surface shows larger grains as the relative Zn content is increased from x = 0 to x = 0.3. A reduction in crystallinity is observed for the film with x = 0.5. This is also consistent with the evidence found in the powder and grazing incidence XRD patterns, where much sharper peaks are observed for the films with x = 0 and 0.3 compared to the weak peaks observed for the film with x = 0.5.
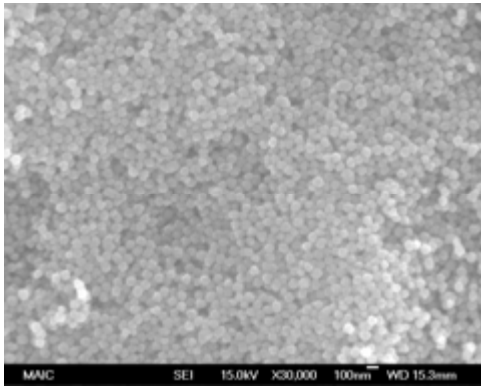
Image 1: Actual magnification: 30,000X
    Accelerating voltage: 15 kV
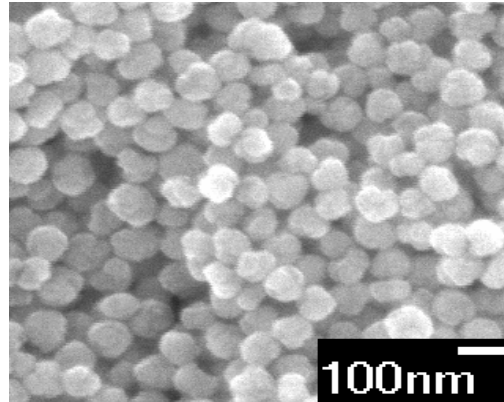
Image 2: Selected region
    Actual magnification: 30,000X

Figure 2-5. SEM micrographs of the surface of a $Zn_xCd_{1-x}S$ thin film with relative zinc composition x = 0 (CdS).
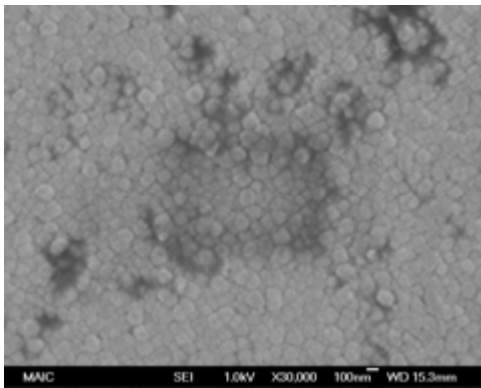
Image 3: Actual magnification: 30,000X
    Accelerating voltage: 1 kV
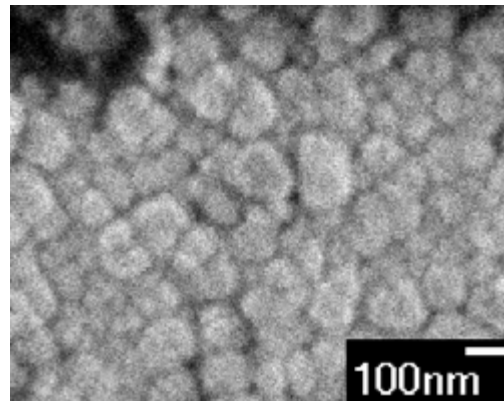
Image 4: Selected region
    Actual magnification: 30,000X

Figure 2-6. SEM micrographs of the surface of a $Zn_xCd_{1-x}S$ thin film with relative zinc composition x = 0.3.
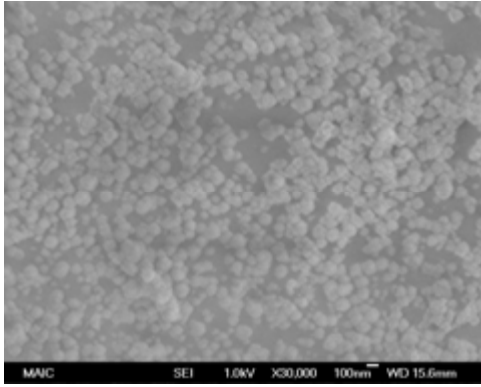
Image 5: Actual magnification: 30,000X   Image 6: Selected region
Accelerating voltage: 1 kV   Actual magnification: 30,000X
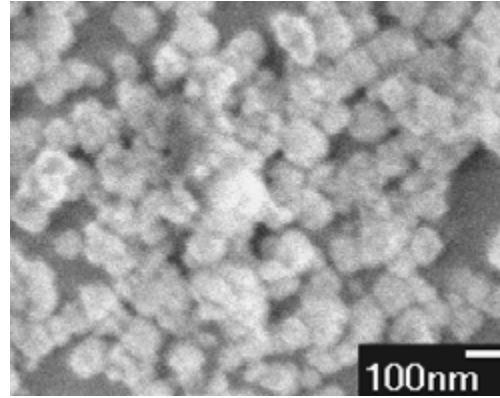
Figure 2-7. SEM micrographs of the surface of a $Zn_xCd_{1-x}S$ thin film with relative zinc composition x = 0.5.

2.3.2.4   Optical Analysis

Optical absorbance and transmittance (T) spectra of ZnCdS films were measured using an HP 8453 UV-Visible spectrophotometer over the wavelength range of 300 to 1100 nm. Figure 2-8 shows the spectral dependence of the transmittance for the ZnCdS films with relative zinc composition x = 0.3 deposited on SLG substrates. For very thin ZnCdS films, better than 80% transmittance was obtained at short and long wavelengths, while the film with a thickness of 80 nm has a 70% transmittance for wavelengths longer than 600 nm. The film with a thickness of 50 nm shows 80% transmittance for wavelengths longer than 600 nm.   These values are comparable to those reported elsewhere [2-2] [2-3].

The thinner films (*i.e.*, those grown with shorter deposition times) have a higher transmittance at shorter wavelengths, which is a desirable feature for enhancing the short-circuit current. On the other hand, thicker films could assist in avoiding damages caused by the subsequent ZnO sputtering deposition process required to build a solar device.   Therefore, optimization of the buffer layer thickness is essential for improving the overall cell performance. Figure 2-9 shows the optical transmittance spectra for ZnCdS films with relative zinc composition x = 0 (*i.e.*, a CdS film) and relative zinc composition x = 0.3. The spectral behavior of these films shows that the absorption edges shift to shorter wavelengths as the relative Zn content increases from x = 0 to 0.3. As indicated in the figure caption, the film thicknesses used in the study were 200 nm (x = 0) and 100 nm (x = 0.3).

The absorption coefficient α (cm^{-1}) for the thin film can be obtained from transmission data in the high absorption region through application of the formula

$$\alpha = (1/d) \times ln(1/T)$$

where d (cm) is the thickness of the film, and T is the transmittance of a single-side deposited ZnCdS film. Once the absorption coefficient is extracted from the transmission data, the values of the optical bang-gap energy (E_g) of ZnCdS films can be estimated using the theoretical

21

relationship

$$\alpha h\nu = \text{constant} \times (h\nu - E_g)^{1/2}$$

where $h\nu$ represents the photon energy. Figure 2-10 shows the resulting plots of the quantity $(\alpha h\nu)^2$ versus photon energies in the range 1.0 - 3.5 eV. Finally, from these plots and the underlying theoretical relationship it is possible to extract the energy band-gap values reported in Table 2-1, which shows that $E_g = 2.40$ eV for $x = 0$ (CdS), $E_g = 2.55$ eV for ZnCdS with $x = 0.3$, and $E_g = 2.70$ eV for ZnCdS with $x = 0.5$. Hence, the net effect of including additional Zn content in the buffer later is to increase the energy bandgap of film.
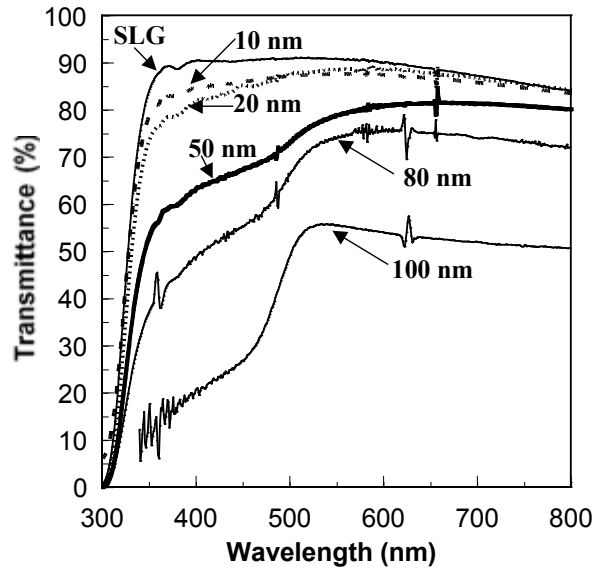
Figure 2-8. Optical transmittance spectra of ZnCdS films with relative zinc composition x = 0.3 for different film thickness.
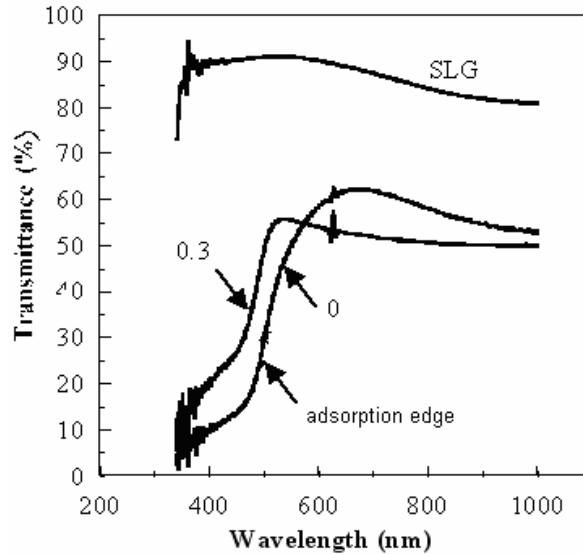
Figure 2-9. Optical transmittance spectra for ZnCdS films with relative zinc compositions x = 0 (thickness d ≈ 200 nm) and x = 0.3 (d ≈ 100 nm).
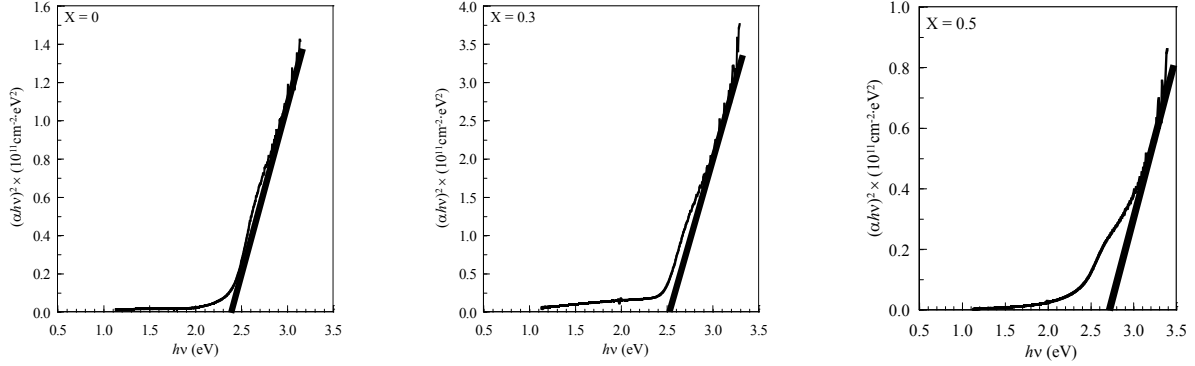
Figure 2-10. Plots of $(\alpha h\nu)^2$ versus $h\nu$ for ZnCdS films with relative zinc compositions x = 0 (thickness d ≈ 200 nm), x = 0.3 (d ≈ 100 nm), and x = 0.5 (d ≈ 150 nm).

Table 2-1. Estimated energy band gaps of ZnCdS films for various relative Zn composition values (x).

x	Film Thickness (nm)	E_g (eV)
0	200	2.40
0.3	100	2.55
0.5	150	2.70

2.3.2.5 Electrical Analysis

The electrical resistivity of the films under study was characterized through I-V measurements using an Al/ZnCdS/ITO "sandwich" structure, and also via MMR Hall effect and Van der Pauw measurements.

The I-V measurements yielded the results reported in Table 2-2, which shows the resistance, resistivity, and conductivity of ZnCdS thin films as a function of the relative composition x. In order to measure the electrical resistivity of CBD-ZnCdS layers, circular aluminum contact dots with a thickness of 100 nm and a diameter of 200 μm were deposited by electron-beam evaporation. Square glass substrates of 1in × 1in in size were coated with 100 nm of indium-tin-oxide (ITO). Prior to the deposition of ZnCdS, the substrates were successively cleaned using acetone, methanol, and isopropyl alcohol. The Al/ZnCdS/ITO sandwich structure produced good Ohmic contacts for the ZnCdS films. The electrical resistance (R), the electrical resistivity (ρ), and electrical conductivity (σ) were estimated using the as-deposited ZnCdS film thickness of 70 ~ 80 nm and a contact area of 3.14×10^{-4} cm^2. The measured values of R, ρ, and σ are summarized in Table 2-2. The measured electrical resistivities of ZnCdS thin films are in the range of 2 ~ 5 × 10^3 Ω·cm, and the resistivity is found to increase with increasing Zn composition.

The electrical resistivity was also measured using a four-probe MMR Hall effect and a Van der Pauw measurement system. The thickness of the films used in this set of measurements lied in the range of 100 to 200 nm. The results indicate that the resistivities of the as-deposited ZnCdS films change from approximately 10^2 to 7×10^3 $\Omega \cdot cm$ as the value of relative zinc composition x increases from 0 to 0.5. Theses results show a trend analogous to the I-V results obtained using the Al/ZnCdS/ITO sandwich structure. It was also observed that the carrier density decreased with increasing Zn content. The carriers found in the films are electrons. Similar trends have also been reported elsewhere [2-4] [2-5].

Table 2-2. Measured values of electrical resistance (R), resistivity (ρ), and conductivity (σ) for as-deposited ZnCdS films on ITO coated glass substrates as a function of the relative Zn compositon x.

x	Film Thickness (cm)	R (Ω)	ρ ($\Omega \cdot cm$)	σ ($\Omega \cdot cm$)$^{-1}$
0	7.0×10^{-6}	53.76	2.41×10^3	4.15×10^{-4}
0.1	7.0×10^{-6}	58.14	2.61×10^3	3.83×10^{-4}
0.3	7.0×10^{-6}	75.19	3.37×10^3	2.97×10^{-4}
0.5	8.0×10^{-6}	117.65	4.62×10^3	2.16×10^{-4}

2.3.3 Photo- J-V and QE of CIGS Solar Cells with ZnCdS Buffer Layers

Buffer layers of ZnCdS with different Zn content were deposited on CIGS samples provided by Energy Photovoltaics Inc. (EPV). The Ga content of the CIGS films was approximately 30 ~ 32%, and due to the copper-rich nature of the surface the films were covered with a thin chalcogenide $Cu_{2-x}Se$ layer. It is well known that copper-rich CIS and CIGS films have high hole densities in the range of $10^{19} \sim 10^{20}$ cm^{-3} because of the coexistence of a the semimetallic $Cu_{2-x}Se$ impurity at the surface. A KCN etching treatment, which consists of dipping the as-deposited CIGS film in a KCN solution for several minutes, has been known to be an effective treatment to remove Cu chalcogenides [2-6] laying on the surface. Prior to depositing the ZnCdS buffer layer, the CIGS films were chemically treated using a 10-wt% KCN aqueous solution at room temperature for four minutes. This is followed by deposition of a ZnCdS buffer layer via CBD and then by a ZnO window layer via sputtering. A high/low resistivity i-ZnO/n$^+$-ZnO bilayer film was then deposited on these samples at EPV. In the next step, Ni/Al grid fingers with dimensions of 50 nm/300 nm serving as front contact pads were finally deposited by electron-beam evaporation to obtain the finished cells. No antireflective (AR) coatings were applied. The measurements taken included the photo- current density-voltage (photo- J-V) relationships under AM 1.5G (100 mW/cm^2) irradiance at a device temperature of $25.0 \pm 1°C$, and as well as spectral response.

In the case where CdS is used as the buffer layer, the results given in Table 2-3 shows that the CdS/CIGS cells fabricated using a KCN etching treatment have improved the open-circuit voltage (V$_{oc}$), short-circuit current density (J$_{sc}$), and fill factor (F.F.), which yield better performance in terms of solar conversion efficiency. The CdS buffer layers were deposited using the University of Florida's baseline CBD. As shown in the table, the CdS/CIGS cell with

ID 21#4, fabricated using a CBD process with a deposition time of 30 minutes and using a KCN etching step, realizes the best performance, with $V_{oc} = 0.482$ V, $J_{sc} = 31.22$ mA/cm^2, F.F. = 65.10 %, and Eff. = 9.8 %.

Figure 2-11 shows spectral response curves for the devices with ID 39#8 and 21#4 of Table 2-3, for the purpose of comparing the effect of the KCN etching step. As can be clearly seen in the figure, the quantum efficiency of the device utilizing a KCN etching treatment is higher than that of the device without the etch treatment.

Table 2-3. Performance of CdS/CIGS cells <u>with and without</u> a KCN etch treatment of the CIGS absorber layers.

Device ID	Device Area (cm^2)	Irradiance (mW/cm^2)	KCN Etch	x	Deposition Time (min)	V_{oc} (V)	J_{sc} (mA/cm^2)	FF (%)	η (%)
39#8	0.429	100	No	0	30	0.420	28.04	51.47	6.06
21#4	0.429	100	Yes	0	30	0.482	31.22	65.10	9.80
22#1	0.429	100	Yes	0	40	0.487	32.82	59.45	9.51
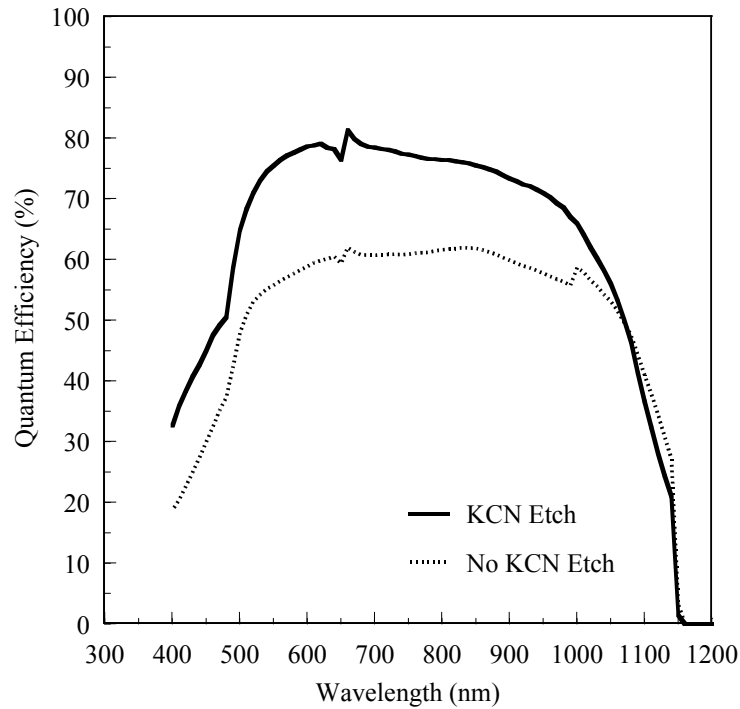
Figure 2-11. Spectral response curves for the CdS/CIGS solar cells shown in Table 2-3 (Device ID: 39#8 and 21#4).

In the case where ZnCdS is used as the buffer layer, Table 2-4 shows that ZnCdS/CIGS cells fabricated using a KCN etching treatment also have improved performance parameters.

The effect of the thickness of the ZnCdS buffer layer on the performance of ZnCdS/CIGS cells can be assessed from Figure 2-12, which shows photo-J-V characteristics of cells with relative zinc composition x = 0.3 and CBD deposition times of 40, 50, and 60 minutes. The deposition times were increased from 40 to 60 minutes. The fill factor was found to increase when the deposition time reached 60 minutes. Table 2-5 shows the performance parameters of these cells. The tested ZnCdS/CIGS cells achieved higher short-circuit currents with respect to those of the CdS/ CIGS films reported in Table 2-3, while at the same time realizing comparable or slightly higher open-circuit voltages.

Table 2-4.   Performance of ZnCdS/CIGS cells <u>with and without</u> a KCN etch treatment of the CIGS absorber layers.

Device ID	Device Area (cm^2)	Irradiance (mW/cm^2)	KCN Etch	x	Deposition Time (min)	V_{oc} (V)	J_{sc} (mA/cm^2)	FF (%)	η (%)
13#B2	0.100	101.5	No	0.3	45	0.502	30.19	50.68	7.56
14#A2	0.090	102.1	Yes	0.3	45	0.518	31.24	63.40	10.05
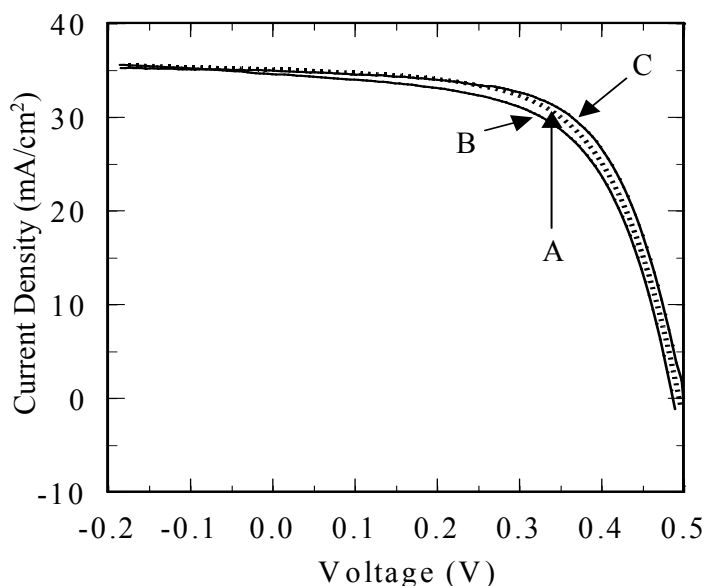
Figure 2-12.   Photo-J-V characteristics of ZnCdS/CIGS cells using different deposition times and relative zinc composition x = 0.3. The CBD-grown ZnCdS buffer layers were fabricated with deposition times of 40 min (A), 50 min (B), and 60 min (C), in an 85 °C bath.

Table 2-5. Performance parameters of ZnCdS/CIGS cells as a function of different deposition times for a relative zinc composition x = 0.3 in the buffer layer.

Device ID	Device Area (cm^2)	Irradiance (mW/cm^2)	KCN Etch	x	Deposition Time (min)	V_{oc} (V)	J_{sc} (mA/cm^2)	FF (%)	η (%)
(A)33#3	0.429	100	Yes	0.3	40	0.493	35.16	60.98	10.57
(B)30#1	0.429	100	Yes	0.3	50	0.487	34.56	60.06	10.11
(C)32#1	0.429	100	Yes	0.3	60	0.501	34.89	66.81	11.67

Given that increasing the relative zinc content x can increase the energy band gap of ZnCdS, the resulting band gap values are higher than that of CdS. In fact, as discussed in Section 1.3.2.4, the ZnCdS film with x = 0.5 had an energy band gap of 2.7 eV, a value that is higher than that of CdS at 2.4 eV. Consequently the ZnCdS/CIGS cells are expected to have a higher short-circuit current than CdS/CIGS cells because of the higher quantum efficiency in the shorter wavelength region. Table 2-6 shows the dependence of the cell performance parameters on the relative zinc composition values x = 0.1, 0.2, 0.3, 0.4, and 0.5. The CIGS layers were etched by KCN before the CBD buffer layer growth.

Relevant subsets of the data of Table 2-6 are plotted in Figure 2-13 as an alternative visualization of the results. Note from Table 6-1 and Figure 2-13 that the ZnCdS/CIGS cell with relative zinc composition x = 0.2 achieved a conversion efficiency of approximately 13% under AM1.5G conditions. Also note that starting with the composition x = 0 (corresponding to a CdS/CIGS cell) the efficiency increases with increasing relative zinc content in the ZnCdS/CIGS cell up to the composition x = 0.2. The data shows then a decrease in efficiency for the compositions x = 0.3 and x = 0.4, and finally a marked decrease in efficiency for the zinc-rich ZnCdS/CIGS cell with x = 0.5. Given the smaller thickness of the buffer film with composition x = 0.2 (*cf.* Table 2-6), it is reasonable to attribute to that fact the relatively sharp change in efficiency between that composition and the efficiency of the cells with x = 0.3 and x = 0.4. It is clear, nevertheless, that a zinc content of x = 0.5 is no longer beneficial for the purpose of efficiency enhancement. Therefore, the efficiency plot given in Figure 2-13 supports the claim that ZnCdS/CIGS cells benefit from the increasing addition of Zn up to a concentration of approximately x = 0.3. A reduction in efficiency is realized at the higher Zn content of x = 0.5.

Figure 2-14 shows the photo-J-V characteristics of ZnCdS/CIGS cells for the cells listed in Table 2-6. As mentioned above, the reason for using ZnCdS buffer layers (which have a wider band-gap energy than CdS) is the potential for increasing the photo-current generation particularly in the spectral region for wavelengths less than 550 nm.

A comparison of the quantum efficiency of selected cells is shown in Figure 2-15, where spectral response curves are given for four ZnCdS/CIGS cells with Zn contents x = 0, 0.1, 0.2, and 0.5. At short wavelengths, all the cells featuring ZnCdS as the buffer have better quantum efficiency than the cell fabricated with a CdS buffer. Furthermore, at those short wavelengths the quantum efficiency of the ZnCdS cells becomes higher as the relative zinc content x increases, as can be expected from the widening of the band gap energy caused by the additional presence of zinc. This results in an increased value of J_{sc}, as shown in Table 2-6. The small

difference in cut-off wavelength can be attributed to the difference in Ga content in the CIGS absorber layers utilized for fabricating the cells. Further studies and optimization of the ZnCdS buffer layer thickness and deposition conditions to improve the film quality are needed for better understanding of this buffer layer and achieving the highest performance possible.

Table 2-6. Performance parameters of ZnCdS/CIGS cells as a function of the relative zinc content x of the buffer layer.

Device ID	Device Area (cm^2)	Irradiance (mW/cm^2)	KCN Etch	X	Thickness (nm)	V_{oc} (V)	J_{sc} (mA/cm^2)	FF (%)	η (%)
(A)21#4	0.429	100	Yes	0	40 ~ 50	0.482	31.22	65.10	9.80
(B)38#8	0.429	100	Yes	0.1	60 ~ 70	0.517	32.85	66.31	11.25
(C)33A#8	0.429	100	Yes	0.2	~ 40	0.526	35.60	69.53	13.02
(D)32#1	0.429	100	Yes	0.3	60 ~ 70	0.501	34.89	66.81	11.67
(E)33B#3	0.429	100	Yes	0.4	60 ~ 70	0.515	34.74	66.85	11.97
(F)31#1	0.429	100	Yes	0.5	60 ~ 70	0.494	35.17	59.68	10.36
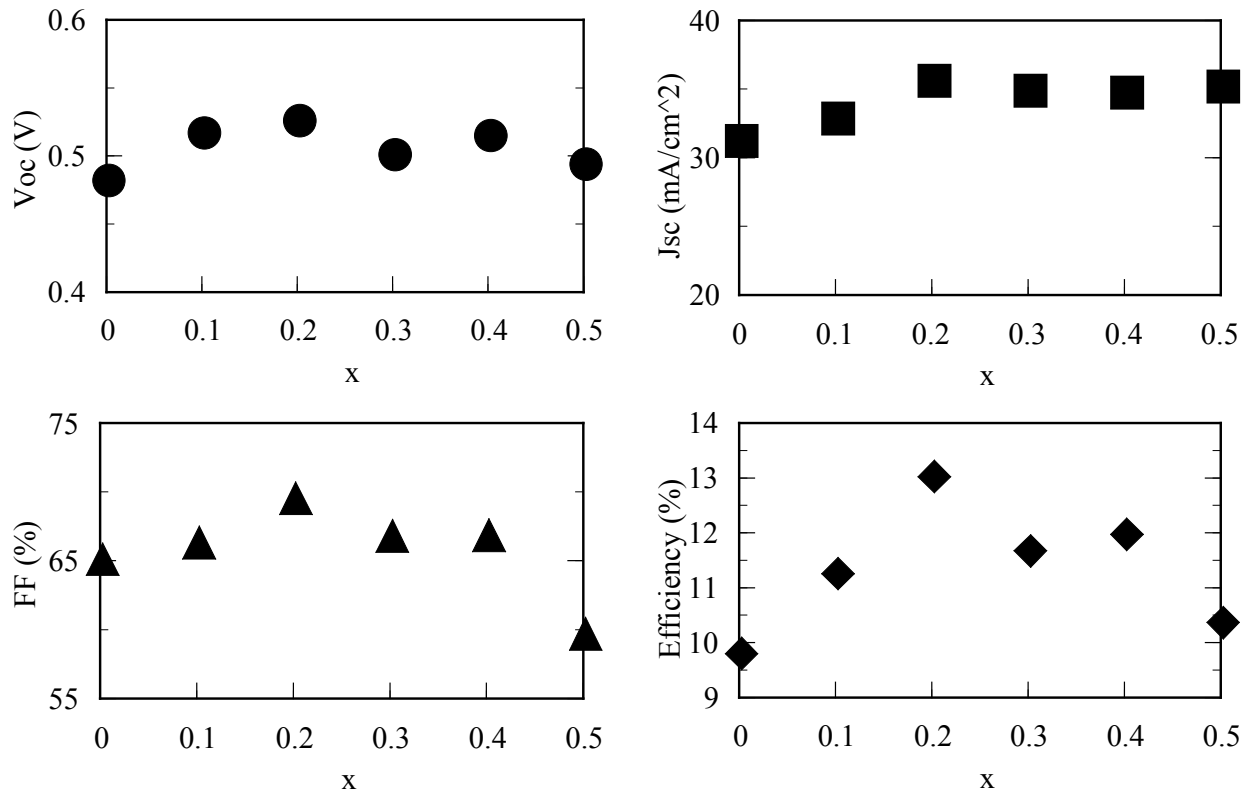
Figure 2-13. Performance parameters of ZnCdS/CIGS cells as a function of the relative zinc content x (graphical representation of the data given in Table 2-6).
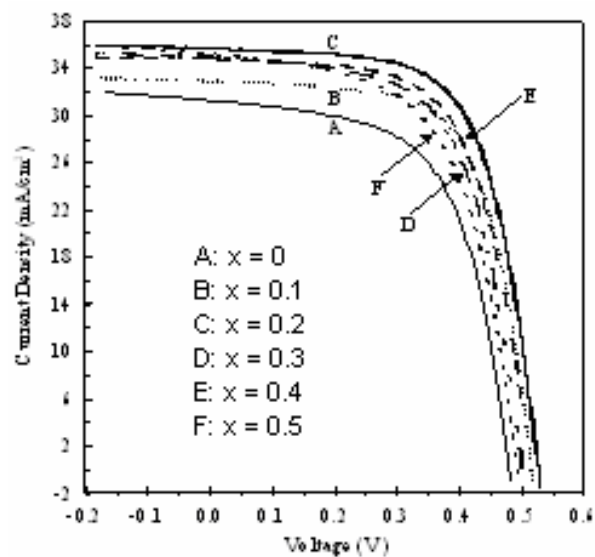
Figure 2-14. Photo-J-V characteristics of ZnCdS/CIGS cells with different relative zinc contents x = 0 (A), x = 0.1 (B), , x = 0.2 (C) , x = 0.3 (D) , x = 0.4 (E), and x = 0.5 (F).
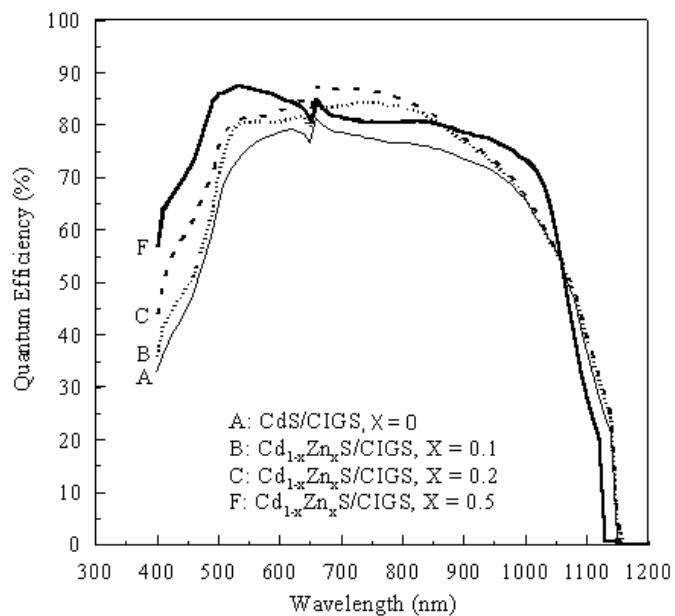
Figure 2-15. Quantum efficiency comparison between a CdS/CIGS solar cell (A), and ZnCdS/CIGS solar cells with relative zinc composition x = 0.1 (B), x = 0.2 (C), and x = 0.5 (F).

2.4   Conclusions

We have demonstrated that ZnCdS materials with specific Zn contents have attractive physical properties for use as buffer layer materials for the CIGS and CGS solar cells. In particular, buffer layers of various relative stoichiometric compositions of Zn, denoted by the subindex x in the chemical formula $Zn_xCd_{1-x}S$, were deposited on the SLG substrates. Their structural, surface morphology, optical, and electrical properties were characterized and analyzed by XRD, SEM, spectrophotometer, and resistivity studies. The experimental studies showed that the film growth rate during the CBD process slows down as the zinc content increases; hence, a longer deposition time is needed for growing a ZnCdS film than for growing a CdS film to a given thickness. The experimental results give an estimate of the expected growth rate as a function of the zinc content in the solution. The degree of crystallinity in the film decreased with increasing relative zinc content x, leading to an amorphous structure at the concentration level x = 0.5. In addition, the resistivity of the ZnCdS films also increased with increasing relative zinc content x. Of particular relevance is also the fact that the energy band gap of ZnCdS is higher than that of CdS, and that the band gap increases with increasing zinc content x. One conclusion is that ZnCdS films with relative zinc composition x = 0.3 showed better than 80% transmittance for wavelengths longer than 600 nm with film thicknesses less than 50 nm. Because of their high transmittance, ZnCdS can be useful as a buffer layer for the CIGS and CGS solar cells. Therefore, it is concluded that from the structural, surface, optical, and electrical analyses, the $Zn_xCd_{1-x}S$ film with relative Zn content x = 0.3 is an excellent candidate as buffer-layer material for the CIGS and CGS solar cells.

To study the effect of $Zn_xCd_{1-x}S$ buffer layers on the performance of CIGS cells, a series of buffer films with relative Zn content of x = 0 (CdS), 0.1, 0.2, 0.3, 0.4, and 0.5 were deposited on the CIGS samples provided by EPV Inc., and a detailed study of the current-density/voltage characteristics and spectral response (QE) was carried out. It was observed that CIGS films treated with KCN etching preceding the buffer CBD step lead to improved cell performance for CIGS cells deposited with either CdS or ZnCdS buffers. Adding Zn in the ZnCdS buffer layer material results in improvement of the performance of ZnCdS/CIGS cells as compared to a Zn-free CdS/CIGS cell. In particular, a ZnCdS/CIGS cell with relative zinc composition x = 0.2 achieved a conversion efficiency of approximately 13 % under AM1.5G conditions, showing improved V_{oc}, J_{sc}, and FF values compared to the CdS/CIGS cell and ZnCdS/CIGS cells with different Zn contents. The 13 % efficiency realized by using x = 0.2 in the ZnCdS/CIGS cell represents a 30% increase in efficiency over the reference CdS/CIGS solar cell used in this study. Furthermore, the quantum efficiency of ZnCdS/CIGS cells becomes higher at shorter wavelengths compared to the CdS/CIGS cell as the relative zinc content x increases, until a maximum relative zinc composition equal to x = 0.5.

2.5   References Cited

[2-1]   J.M. Dona and J. Herrero, "Chemical Bath Codeposited CdS-ZnS Film Characterization," *Thin Solid Films, 268*, pp. 5–12 (1995).

[2-2]   T. Yamaguchi, Y. Yamamoto, T. Tanaka, Y. Demizu, and A. Yoshida, "(Cd,Zn)S thin Films Prepared by Chemical Bath Deposition for Photovoltaic Devices," *Thin Solid Films, 281-282*, pp. 375–378 (2003).

[2-3]   A.M. Salem, "Structure, Refractive-index Dispersion and the Optical Absorption Edge of Chemically Deposited $Zn_xCd_{(1-x)}S$ Thin Films," *Appl. Phys. A* **74**, pp. 205-211 (1996).

[2-4]   K.T. Ramakrishna Reddy and P. Jayarama Reddy, "Studies of $Zn_xCd_{1-x}S$ Films and $Zn_xCd_{1-x}S/CuGaSe_2$ Heterojunction Solar Cells," *J. Phys. D: Appl. Phys*. **25**, pp. 1345–1348 (1992).

[2-5]   N. Romeo, G. Sberveglieri, and L. Tarricone, "Low-resistivity ZnCdS Films for Use as Windows in Heterojunction Solar Cells," *Appl. Phys. Lett*. **32,** No. 12, pp. 807-809 (1978).

[2-6]   Y. Hashimoto, N. Kohara, T. Negami, M. Nishitani, and T. Wada, "Surface Characterization of Chemically Treated $Cu(In, Ga)Se_2$ Thin Films", *Jpn. J. Appl. Phys. Part I, Vol. 35, No. 9A*, pp. 4760-4764 (1996).

3   Effects of Buffer Layer Processing on CIGS Thin Films Characterized by the Dual-Beam Optical Modulation Technique

3.1   Introduction

CuInSe$_2$ (CIS) or CuInGaSe$_2$ (CIGS) thin film solar cells have achieved conversion efficiencies as high as 18.8% AM1.5G [3-1]. However, to accelerate the further optimization of the device performance, a detailed study and a better understanding of the effects of processing on the CIGS/CdS interface and CIGS film transport properties are needed.

Optimization of CuInSe2 (CIS) or Cu(In,Ga)Se2 (CIGS) thin-film solar cell requires the deposition of a thin CdS buffer layer between the CIS absorber layer and the ZnO window layer. A great deal of efforts have been devoted to better understanding the role of CdS buffer layers deposited by different processing techniques on the performance of CIS and CIGS cells. In order to understand why the chemical-bath-deposited (CBD) CdS buffer layer works so well on CIGS solar cells, a study of various CdS buffer layer processes on the excess carrier lifetimes and material characteristics of CIGS solar cells has been carried out. The CBD grown CdS layer is usually thick enough to completely cover the rough surface of CIS or CIGS absorber layers. Thus, a pinhole-free conformal coverage buffer layer is formed. Different buffer layer processes such as MOCVD and sputtering CdS processes are investigated and compared with CBD process. In addition, uncertainties remain as to whether the exchange reactions occurring at the interface of CdS and CIGS region with Cd or S ions which chemically passivate the surface, the effect of water rinsing the surface of CIGS removing the soluble components [3-2], or combinations of these mechanisms affecting the excess carrier lifetimes in the CIGS films. It is shown that Cd binds easily on the surface of CIGS film [3-3]. Thus, CdSe and CdInxSey are suggested to form and are responsible for graded interface structure [3-2]. The chemical modification of the CIGS absorber surface such as Cd- and S-partial electrolyte treatment, DI water rinsing treatment and Ar plasma cleaning treatment prior to CdS deposition are also investigated to study their effects on excess carrier lifetimes. Both the effects of annealing at 200oC after the intermediate treatments and MOCVD deposited CdS on as-deposited as well as after-intermediate-treated samples on excess carrier lifetimes of the CIGS films are discussed.

In this study, the reflection mode DBOM technique is employed to investigate the effects of different CdS buffer layer processings (i.e., CBD, MOCVD, and sputtering) on the properties of CIGS films [3-4]. The results show a significant increase in the DBOM signal ($\Delta I/I$) which is related to the change of the free carrier absorption and of the excess carrier lifetime in the absorber layer, after the buffer layer processing. Mapping of excess carrier lifetimes across the samples can be easily conducted by DBOM technique and it exhibits the substantial inhomogeneity of lifetime even for very high quality CIGS samples from various sources. Thus the capability of DBOM can be applicable to the quality assessment and process optimization for the CIGS films. This novel nondestructive optical technique provides a powerful means for assessing the quality of CIGS films, a vital requirement for the viable CIGS solar-cell manufacturing.

The reflection mode DBOM technique was applied to study the effects of CdS buffer layers deposited by the CBD, MOCVD, and sputtering processes on the excess carrier lifetimes in CIGS films. A detailed comparison of the DBOM data versus different processing, the measurement and mapping of excess carrier lifetimes in the CIGS films by the DBOM technique are presented. Considering the thickness of space charge region between n-type CdS and p-type CIGS as zero, the simplified reflection DBOM theory is employed to obtain the effective excess carrier lifetimes. A summary of the DBOM measurement results for CIGS films grown by National Renewal Energy Laboratory (NREL), Siemens Solar Industries (SSI), and Energy Photovoltaics, Inc. (EPV) using different growth techniques, deposited by different buffer layer processes, and treated by intermediate surface treatments (i.e., as deposited, DI water rinsed, Cd- and S-partial electrolyte treatment, and Ar plasma cleaned) is given in this chapter.

3.2   Simplified Theory for Reflection-Mode DBOM

Since CIGS solar cells use thick Mo as backside ohmic contacts, a reflection mode DBOM technique has been developed for the measurement of excess carrier lifetimes in the CIGS films. The contactless DBOM technique is based on the modulation of the reflected intensity of an infrared (IR) probe beam by a visible pump beam which produces free carrier absorption in the CIGS film. The fractional change in the reflected intensity of the IR probe beam is directly proportional to the effective excess carrier lifetime in the CIGS films. Thus, the DBOM technique can be used to determine the excess carrier lifetimes in the CIGS films. It is also possible to perform depth profiling of the excess carrier lifetimes in the film by changing the wavelength (and hence the absorption depth in the film) of the pump beam.

Figure 3-1 shows the incident and reflected angles of the pump beam and probe beam in the CIGS device structure without p-n junction. The excess electron density, $\Delta n(x)$, generated by the pump beam in the CIGS layer can be obtained by solving the continuity equation for electrons and using the boundary conditions at the top ($x = 0$) and bottom interface ($x = t_b$) of the CIGS film, and the result yields

$$\Delta n(x) = \frac{\alpha \phi_0 (1 - R - T) \cos\theta_3}{D_n (\alpha^2 - \frac{1}{L_n^2})} (C_1 e^{\frac{x - t_b}{L_n}} + C_2 e^{-\frac{x - t_b}{L_n}} - e^{-\alpha x}) \qquad (3\text{-}1)$$

where

$$C_1 = \frac{(\alpha D_n + s_1)(\frac{D_n}{L_n} - s_2) - (\alpha D_n - s_2)(\frac{D_n}{L_n} + s_1)e^{-[t_b(\alpha - 1/L_n)]}}{2[\frac{D_n}{L_n}(s_1 + s_2)\cosh(\frac{t_b}{L_n}) + (s_1 s_2 + \frac{D_n^2}{L_n^2})\sinh(\frac{t_b}{L_n})]} \qquad (3\text{-}2)$$

$$C_2 = \frac{(\alpha D_n + s_1)(\frac{D_n}{L_n} + s_2) - (\alpha D_n - s_2)(\frac{D_n}{L_n} - s_1)e^{-[t_b(\alpha + 1/L_n)]}}{2[\frac{D_n}{L_n}(s_1 + s_2)\cosh(\frac{t_b}{L_n}) + (s_1 s_2 + \frac{D_n^2}{L_n^2})\sinh(\frac{t_b}{L_n})]} \qquad (3\text{-}3)$$

and where θ_3 is the reflection angle of the incident pump beam in the CIGS layer, α, ϕ_0, R, and T are the absorption coefficient, photon flux, total front surface reflectance, and back-interface transmittance at a given pump beam wavelength, while D_n, t_b, τ, s_1, and s_2 are the diffusion coefficient, CIGS film thickness, excess carrier lifetime, front-surface recombination velocity

and back-interface recombination velocity in the CIGS films, respectively.
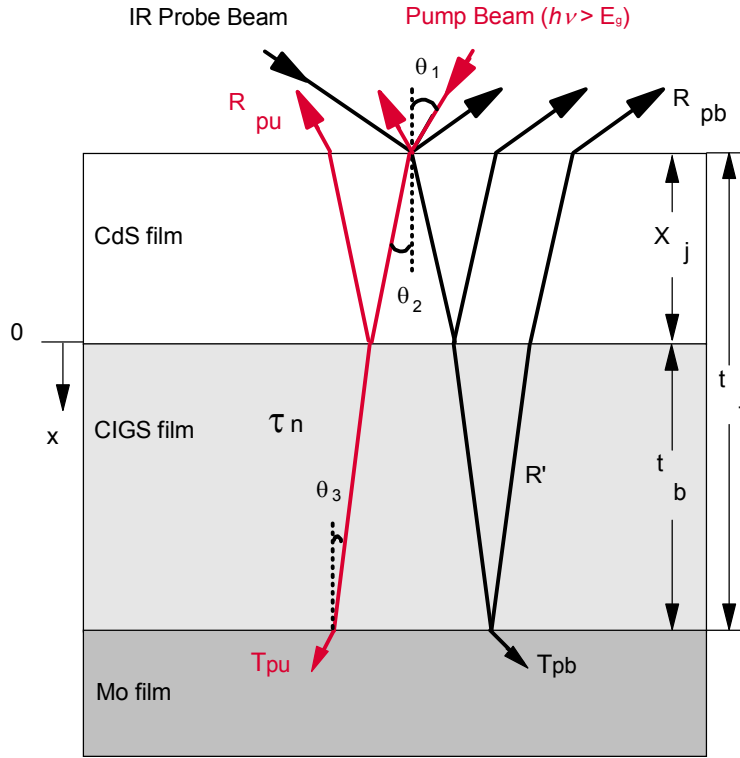
Figure 3-1. Cross sectional view of CIGS cell used in the simplified DBOM theory.

When pump beam is off, the reflected intensity of the probe beam I can be expressed in terms of the transmitted intensity I_0, electron density n_0, hole density p_0, and the optical absorption cross section of electrons and holes, σ_n and σ_p, respectively, as

$$I = I_0 R^{'} \exp[-2 \int_0^{t_b} (\sigma_n n_0 + \sigma_p p_0) dx] \qquad (3\text{-}4)$$

When pump beam is turned on, the excess carriers generated in the CIGS film will modulate the IR reflected beam intensity. Under low injection conditions, the reflected intensity of the probe beam $I^{'}$ can be express as

$$I^{'} = I_0 R^{'} \exp[-2 \Delta N \sigma_{fc} - 2 \int_0^{t_b} (\sigma_n n_0 + \sigma_p p_0) dx] \qquad (3\text{-}5)$$

where

$$\Delta N = \int_0^{t_b} \Delta n(x)dx \tag{3-6}$$

$$= \frac{\alpha\phi_0(1-R-T)\cos\theta_3}{D_n(\alpha^2 - \frac{1}{L_n^2})}[L_n C_1(1-e^{-\frac{t_b}{L_n}}) - L_n C_2(1-e^{\frac{t_b}{L_n}}) + \frac{1}{\alpha}(e^{-\alpha t_b} - 1)]$$

R' is the reflectance at Mo/CIGS interface, $\sigma_{fc} = \sigma_n + \sigma_p$ is the total optical absorption cross-section of electrons and holes.

For $\Delta I \ll I$, the fractional change in the probe beam intensity $\Delta I/I$ (with $\Delta I = I' - I$) can be expressed as

$$\ln(\frac{\Delta I}{I} + 1) \cong \frac{\Delta I}{I} = -2\sigma_{fc}\Delta N \tag{3-7}$$

$$= -2\sigma_{fc}\{\frac{\alpha\phi_0(1-R-T)\cos\theta_3}{D_n(\alpha^2 - \frac{1}{L_n^2})}[L_n C_1(1-e^{-\frac{t_b}{L_n}}) - L_n C_2(1-e^{\frac{t_b}{L_n}}) + \frac{1}{\alpha}(e^{-\alpha t_b} - 1)]\}$$

Since the absorption coefficient ($\alpha \approx 8\times10^4$ cm^{-1}) is very high in the CIGS film for the wavelength of the pump beam (He-Ne laser, $\lambda=632.8$nm), and the bulk trap density in the CIGS film is high [3-2][3-5], the following assumptions prevail for DBOM analysis: (i) $\alpha L_n \gg 1$, (ii) $\alpha D_n \gg s_1, s_2$, (iii) $D_n^2 \gg s_1 s_2 L_n^2$. Based on these assumptions and solving equations (3-1) through (3-7), the fractional change in the probe-beam reflected intensity $\Delta I/I$ can be expressed as

$$\frac{\Delta I}{I} = -2\sigma_{fc}\cos\theta_3\phi_0(1-R-T)\tau_{eff}(1-e^{-\alpha t_b}) \tag{3-8}$$

where

$$\tau_{eff} = \frac{t_b}{s_1 + t_b/\tau} \tag{3-9}$$

is the effective excess carrier lifetime in the CIGS film, which reduces to the bulk film lifetime if the front surface recombination velocity s_1 is much smaller than t_b/τ. Thus, the excess carrier lifetimes in a CIGS film can be obtained by using the values of ΔI and I obtained from the DBOM measurements, and the calculated values of R and T.

The total transmittance and reflectance can be expressed as ($*$ denotes the complex conjugate)

$$T = t \times t^* \tag{3-10}$$

$$R = r \times r^* \tag{3-11}$$

The total transmission and reflection coefficients can be expressed as [3-6][3-7]

$$t = \frac{t_0 t_1 t_2 e^{-i(\delta_1 + \delta_2)/2}}{1 + r_0 r_1 e^{-i\delta_1} + r_1 r_2 e^{-i\delta_2} + r_0 r_2 e^{-i(\delta_1 + \delta_2)/2}} \qquad (3\text{-}12)$$

and

$$r = \frac{r_0 + r_1 e^{-i\delta_1} + r_2 e^{-i(\delta_1 + \delta_2)} + r_0 r_1 r_2 e^{-i\delta_2}}{1 + r_0 r_1 e^{-i\delta_1} + r_1 r_2 e^{-i\delta_2} + r_0 r_2 e^{-i(\delta_1 + \delta_2)}} \qquad (3\text{-}13)$$

where

$$\delta_1 = \frac{4\pi}{\lambda} n_{CdS} t_{CdS} \cos\theta_2 \qquad (3\text{-}14)$$

$$\delta_2 = \frac{4\pi}{\lambda} n_{CIGS} t_b \cos\theta_3 \qquad (3\text{-}15)$$

and where t_0, t_1, and t_2 are the Fresnel transmission coefficients at the air/Cds film, CdS film/CIGS film, and CIGS film/Mo film interfaces, respectively; r_0, r_1, and r_2 are the Fresnel transmission coefficients at the air/Cds film, CdS film/CIGS film, and CIGS film/Mo film interfaces, respectively; δ_1 and δ_2 are the phase changes that result from the double travel of light in the CdS layer and CIGS films; λ is the wavelength of the incident light (laser pump beam); t_{CdS}, t_b, θ_2, and θ_3 are the thickness of CdS layer, thickness of CIGS film, and refraction angles in the CdS layer and CIGS film, respectively; n_{CdS} is the refraction index of the CdS layer; n_{CIGS} is the refractive index of the CIGS film and $n_{CIGS} = N_{CIGS} + ik$, where N_{CIGS} and k (= $\alpha\lambda/4\pi$) are the real and imaginary parts of the refractive index [3-8]; and α is the optical absorption coefficient of CIGS film. The Fresnel transmission and reflection coefficients are given by

$$t_0 = \frac{2\cos\theta_1}{\cos\theta_1 + n_{CdS}\cos\theta_2} \qquad (3\text{-}16)$$

$$t_1 = \frac{2n_{CdS}\cos\theta_2}{n_{CdS}\cos\theta_2 + n_{CIGS}\cos\theta_3} \qquad (3\text{-}17)$$

$$t_2 = \frac{2n_{CIGS}\cos\theta_3}{n_{CIGS}\cos\theta_3 + n_{Mo}\cos\theta_4} \qquad (3\text{-}18)$$

$$r_0 = \frac{\cos\theta_1 - n_{CdS}\cos\theta_2}{\cos\theta_1 + n_{CdS}\cos\theta_2} \qquad (3\text{-}19)$$

$$r_1 = \frac{n_{CdS}\cos\theta_2 - n_{CIGS}\cos\theta_3}{n_{CdS}\cos\theta_2 + n_{CIGS}\cos\theta_3} \qquad (3\text{-}20)$$

$$r_2 = \frac{n_{CIGS} \cos\theta_3 - n_{Mo} \cos\theta_4}{n_{CIGS} \cos\theta_3 + n_{Mo} \cos\theta_4} \qquad (3\text{-}21)$$

where n_{Mo} is the refraction index of the Mo layer, θ_4 is refraction angle in the Mo layer.

Thus the total transmittance T and reflectance R can be obtained by substituting equations (3-12) through (3-21) into equations (3-10) and (3-11). In addition, by measuring the total reflectance, the thickness of CdS layer and CIGS film can be determined by using a contactless dual beam S-polarized reflectance (DBSPR) technique [3-9], which was originally developed to determine the silicon film and buried oxide thickness in SOI materials. Once the total transmittance T and reflectance R are obtained from equations (3-10) and (3-11), the excess carrier lifetimes can be carried out by substituting T and R into equation (3-8).

3.3 Experimental Details

3.3.1 Lifetime Measurement

As shown in Figure 3-2, a long-pass filter with a cutoff wavelength $\lambda_c = 1350$ *nm* ,which is placed between test samples and detector, is used to block the undesired signal, namely the photoluminescence (PL) of CIGS material. A tungsten lamp and a He-Ne CW laser (λ = 632.8nm) are used as probe beam and pump beam, respectively.
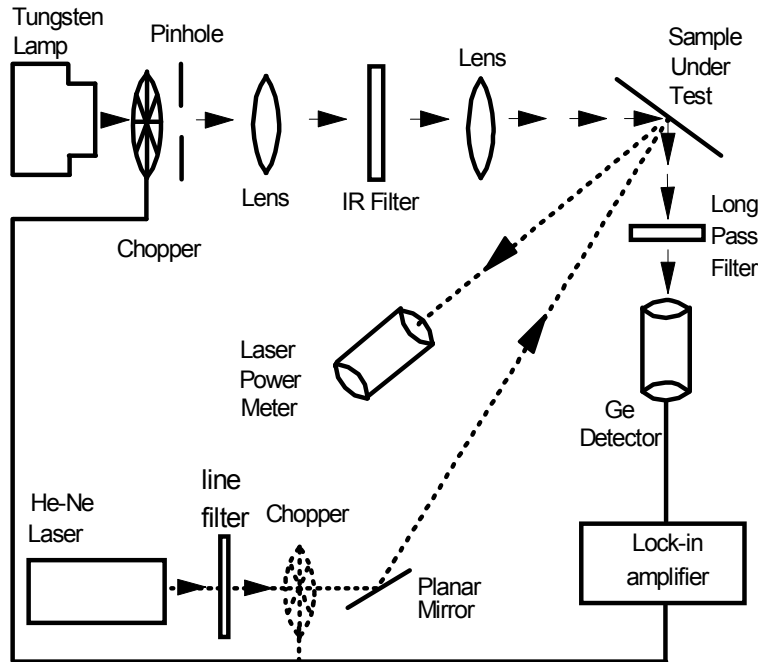
Figure 3-2. Schematic diagram of reflection mode DBOM setup with a long pass filter.

The experimental procedure is composed of two steps. First, the reflected intensity I of an IR probe beam (with $h\nu < E_g$ of CIGS) is measured by chopping the tungsten lamp, and the signal is detected with a lock-in amplifier. Second, the change in the reflected beam intensity ΔI, due to a modulated pump beam ($h\nu \geq E_g$), is measured by using the chopped pump beam, and the resulting IR reflected beam intensity is measured using a lock-in amplifier.

3.3.2 Buffer Layer Processing

Three different CdS processing methods (CBD, MOCVD, and sputtering) were used for the deposition of CdS buffer layers on the Mo-coated CIGS samples, which were supplied by National Renewal Energy Laboratory (NREL), Siemens Solar Industries (SSI), and Energy Photovoltaics Inc. (EPV). Prior to buffer layer processing, intermediate surface treatments (i.e., as deposited, DI water rinsed, Cd- and S-partial electrolyte treatment, and Ar plasma cleaned) were also applied to some of these samples. The DBOM measurements were performed on samples with or without the CdS buffer layers deposited by these processing techniques.

Two sets of CIGS films were grown on soda-lime glass substrates coated with thick Mo films at NREL. For set-one samples, EPMA data taken on these substrates showed Cu 23.72% ($\pm$ 0.123%), In 18.76 ($\pm$ 0.11%), Ga 7.2% ($\pm$ 0.06%), and Se 50.3% ($\pm$ 0.09%). All of these substrates were further divided, and ESCA measurements of the surface and near-surface composition profiles were taken. The ESCA data showed that surfaces of all these films were significantly enriched with indium with respect to their average compositions and the composition in the copper-depleted near-surface region. Figure 3-3 schematically illustrates four processing conditions studied and measurements conducted in each case. The baseline CBD solution consisted of NH_3 (1.44×10^{-4}M), NH_4Cl (7.43×10^{-4}M), $CdCl_2$ (2.4×10^{-4}M), and NH_2CSNH_2 (2.4×10^{-3}M). The cadmium partial electrolyte consisted of a solution with all the same reactant except thiourea, and the sulfur partial electrolyte contained all the baseline reactants in the same concentration except the cadmium salt. The aqueous processing was conducted at a bath temperature of 80-85°C and was continuously stirred. The processing time for the partial electrolyte cases is identical to the baseline CBD process, which produced a uniform, compact, coherent, and colloid-free film with a thickness of about 800Å. MOCVD was performed in a horizontal atmospheric pressure cold wall reactor using dimethyl cadmium and hydrogen sulfide reactants in hydrogen at a substrate temperature of $160\pm10°$C and a VI/II reactant ratio of 100/1 for 2.8 minutes. The MOCVD growths were prenucleated with approximately one minute of exposure to H_2S before the flow of dimethyl cadmium began. The DBOM measurements were conducted on sixteen distinct locations for each substrate at each step in the process per Fig. 3-3.
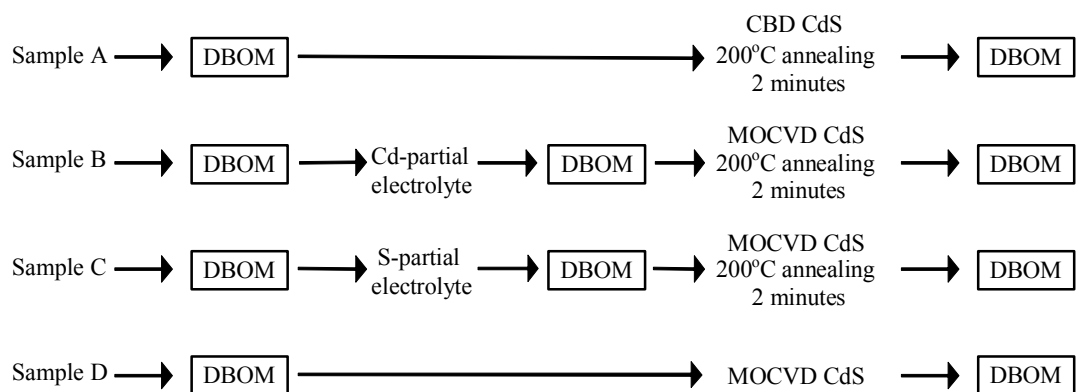
Figure 3-3. Process flow sequence of NREL CIGS samples for the four experimental conditions.

For set-two NREL CIGS samples, the CdS buffer layer was deposited by using the CBD (NREL), sputtering (MRG), and MOCVD (University of Florida) techniques. The processing conditions studied and measurements conducted for these samples are shown in Figure 3-4. These samples measured by DBOM technique were not fabricated into devices but are believed to be comparable to the similar samples with efficiencies of around 14%.
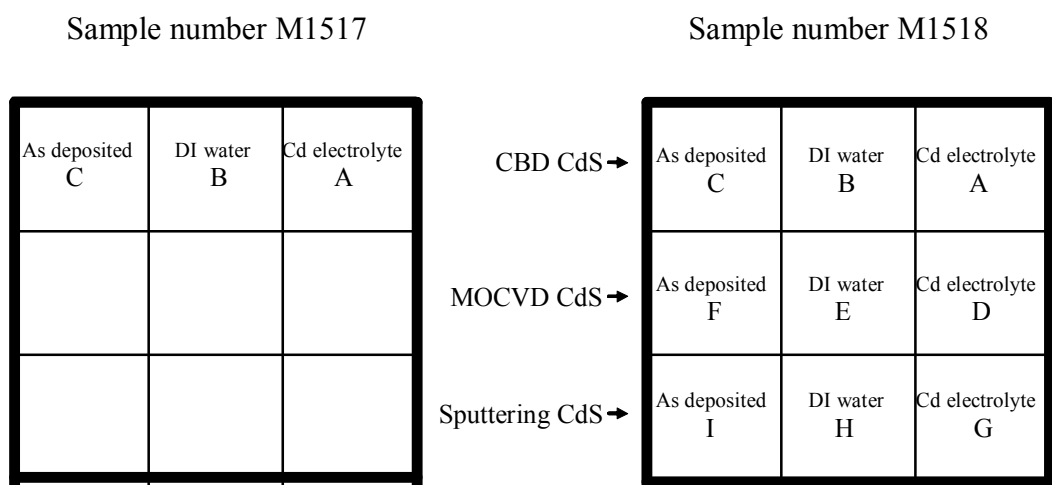
Figure 3-4. The twelve experimental conditions for NREL CIGS samples.

In addition to the samples fabricated by NREL, CIGS films were provided from two different sources (SSI and EPV). The CdS buffer layers for these samples were deposited by using either the CBD (University of Florida) or sputtering (MRG) technique. The CdS deposition (CBD and sputtering) was carried out on the as-deposited CIGS samples and on CIGS samples treated with DI water rinsing and Ar plasma cleaning. These samples measured by DBOM technique were not fabricated into solar cell but are believed to be comparable to similar samples with efficiencies of around 3-5% (best one 9%) fabricated by NREL.

3.4 Results and Discussion

The following results are obtained by using the simplified model (no p-n junction) and the data of ΔI and I measured by the reflection-mode DBOM technique.

3.4.1 Measurements of NREL Samples

The different processing conditions and measurements conducted in each case are illustrated in the Fig. 3-3 for the first set of NREL samples. Fig. 3-5 is a box plot showing a statistically summary of the excess carrier lifetime data taken for each experiment case, initially (as-received), after intermediate surface treatments (Cd- and S-partial electrolyte), and after the completion of processing. Several results are evident. First, the initial lifetimes in the CIGS films, in the range of smaller than 3ns, are typically improved by a factor of two to three in every case except the aqueous sulfur electrolyte exposure. This result is strong negative evidence for attributing the beneficial effects on CIGS device performance of the CBD CdS process to sulfur passivation, an effect well established in the case of III-V compound semiconductors. However, the data does not support the alternative hypothesis that cadmium ion reactions with the surface during the CBD process alone are responsible for the dramatic lifetime improvement shown in the cadmium partial electrolyte case subsequent to the MOCVD growth of CdS, because the lifetimes measured immediately after aqueous processing showed no significant change compared to their initial values. Indeed, considering the substantially poorer initial lifetime in the MOCVD control sample compared to the CBD control and cadmium partial electrolyte samples, it appears that the beneficial effect is provided equally well by the MOCVD growth process alone. Since all the samples were baked in air before final measurement except the MOCVD control sample, the possibility that oxidation or higher temperature interdiffusion effects are required to achieve high lifetimes is not supported by this data. Since the MOCVD control (which was not subjected to any aqueous processing) had a beneficial effect on lifetimes, and the aqueous sulfur electrolyte exposure a neutral effect, water exposure alone cannot be responsible for the observed lifetime increases.
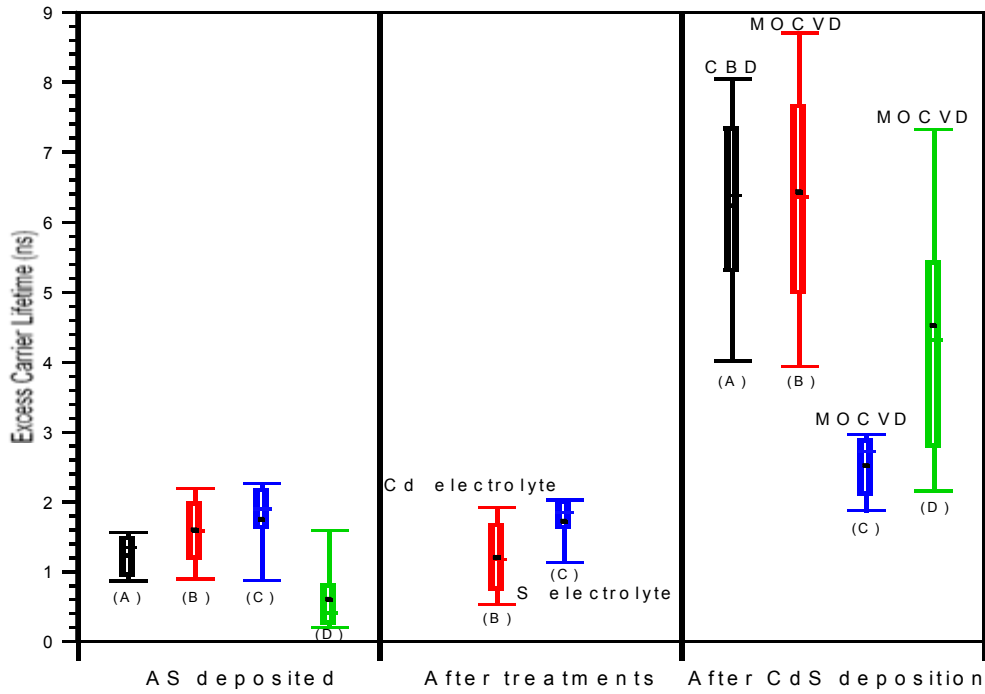
Figure 3-5. A statistical summary of excess carrier lifetimes for the first set NREL CIGS samples.

Figures 3-6, 3-7, 3-8, and 3-9 are the contour-line plots of DBOM data showing the spatial inhomogeneity in excess carrier lifetimes exhibited in these very high quality films initially, after surface treatments, and even for the CIGS samples after the CBD and MOCVD processings. Future studies will use this capability in conjunction with the materials characterization to obtain a correlation with the material parameters and defect structures, which control the recombination processes in these device structures.
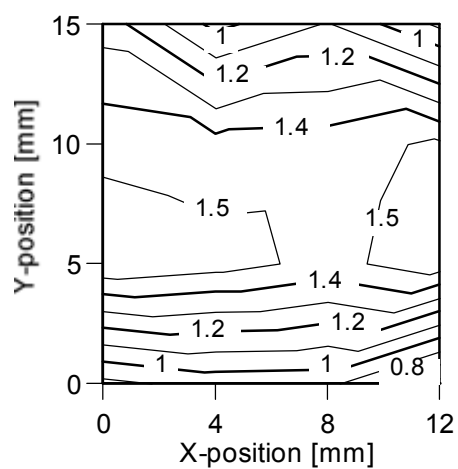
(a) Initially
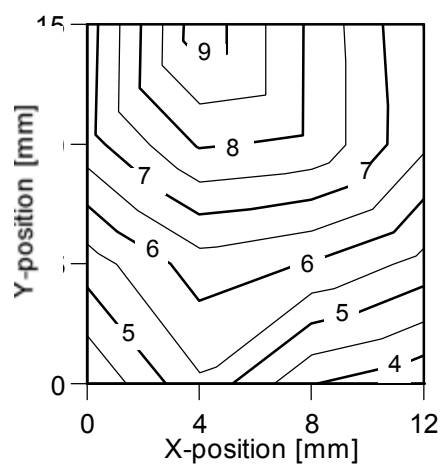
(b) After CBD deposited CdS

Figure 3-6. Contour line plot of excess carrier lifetimes for NREL CIGS sample
(a) initially (as deposited) (b) after CBD deposited CdS.
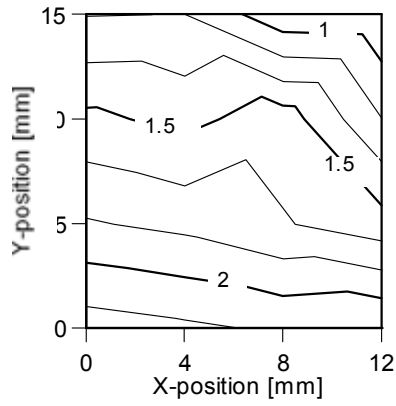
(a) Initially
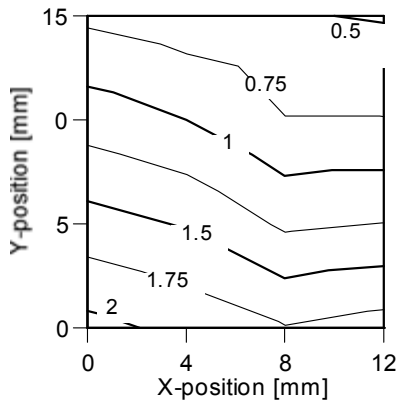
(b) After surface treatment
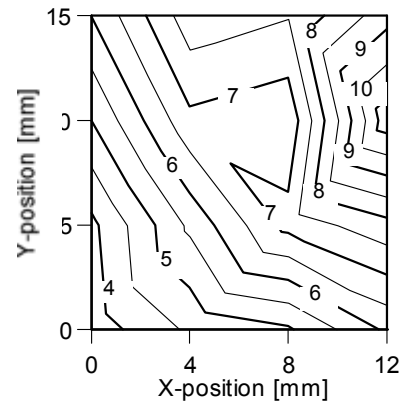
(c) After MOCVD deposited CdS

Figure 3-7. Contour line plots of excess carrier lifetimes for NREL CIGS sample (a) initially (as deposited) (b) after surface treatment (Cd-partial electrolyte) (c) after MOCVD deposited CdS.
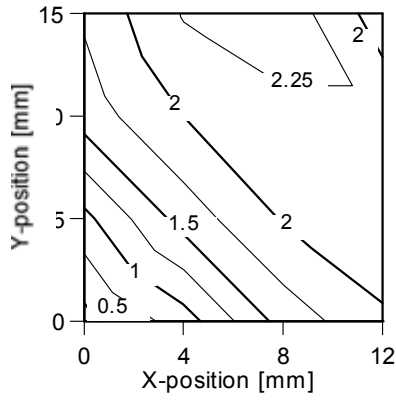
(a) Initially

(b) After surface treatment

(c) After MOCVD deposited CdS

Figure 3-8. Contour line plots of excess carrier lifetimes for NREL CIGS sample (a) initially (as deposited) (b) after surface treatment (S-partial electrolyte) (c) after MOCVD deposited CdS.

(a) Initially   (b) After MOCVD deposited CdS

Figure 3-9. Contour line plot of excess carrier lifetimes for NREL CIGS sample
(a) initially (as deposited) (b) after MOCVD deposited CdS.

It is known that CIGS is the material with photoluminescence (PL). The photoluminescence is the undesired signal for the DBOM measurements. After both the deposition of CdS and annealing process on the sample D, the signal ΔI of DBOM measurement can not be measured correctly. Generally the signal ΔI detected by a lock-in amplifier is in the range of microvolts (μV). Thus, it is possible that the photoluminescence emission from the CIGS sample affects the DBOM measurement. It is shown that the higher temperature of annealing process on CIGS samples results in the higher PL intensity emission from CIGS samples [3-10]. This is the reason why the DBOM measurement can not be performed correctly on the sample D after annealing process. According to the PL spectra of CIGS samples [3-10][3-11], the peak positions of PL intensity are around at wavelength λ = 1280 *nm*. Therefore a long-pass filter with a cutoff wavelength λ_c = 1350 *nm* is used to block the undesired signal, photoluminescence emission from CIGS material, and it is set between test samples and detector as shown in Fig. 3-2. With the long-pass filter, the reflection mode DBOM measurement can be performed on CIGS samples without a hitch.

The results for the second set of NREL CIGS samples were determined by the DBOM technique, and are summarized in Tables 3-1, 3-2, and 3-3, Figures 3-10, 3-11, and 3-12. Table 3-1 and Fig. 3-10 show a statistical summary of the excess carrier lifetimes taken for the experimental cases of as deposited, after DI water rinsed, after Cd partial electrolyte, and after annealing at 200°C for 2 minutes for the samples without CdS. Table 3-2 and Fig. 3-11 summarize the excess carrier lifetimes of the samples without CdS and with CBD, MOCVD, and sputtering deposited CdS and with different surface treatments. For discussing the MOCVD CdS process, Table 3-3 and Fig. 3-12 show the excess carrier lifetimes for each experimental condition: as deposited, after surface treatments, and after MOCVD CdS. And the contour-line plots of excess carrier lifetimes for three CIGS samples as deposited initially, after surface treatments, and MOCVD CdS deposition are shown in Figures 3-13, 3-14, and 3-15. It should be pointed out that there is a considerable variation in the excess carrier lifetimes for the as-

deposited CIGS samples without CdS, as is shown in Table 3-1 and Fig. 3-10, respectively. One of the difficulties in interpreting the DBOM results in these CIGS samples is the fact that we have only the samples with the CBD as well as sputtering CdS deposition and we do not have the DBOM measurements (and hence the excess carrier lifetimes) on these CIGS samples prior the deposition of CdS.

Table 3-1. The excess carrier lifetimes τ_{eff} (ns) of the CIGS samples without CdS.

sample #	As deposited	DI water rinsed	Cd partial electrolyte	Annealing
M1517-A	1.46	---	1.34	1.43
M1517-B	1.90	1.73	---	1.75
M1517-C	0.77	---	---	---

Table 3-2. The average excess carrier lifetimes of NREL samples.

	As deposited		DI water rinsed		Cd partial electrolyte	
	sample #	τ_{eff} (ns)	sample #	τ_{eff} (ns)	sample #	τ_{eff} (ns)
no CdS	M1517C	0.77	M1517B	1.75	M1517A	1.43
CBD CdS	M1518C	3.95	M1518B	2.76	M1518A	3.56
MOCVD CdS	M1518F	17.6	M1518E	1.91	M1518D	4.67
Sputtered CdS	M1518I	12.7	M1518H	7.64	M1518G	5.48

Table 3-3. The excess carrier lifetimes τ_{eff} (ns) of NREL CIGS samples for MOCVD CdS.

sample #	As deposited	DI water rinsed	Cd partial electrolyte	MOVCD CdS
M1518-D	2.29	---	2.08	4.67
M1518-E	1.71	1.70	---	1.91
M1518-F	0.53	---	---	17.6
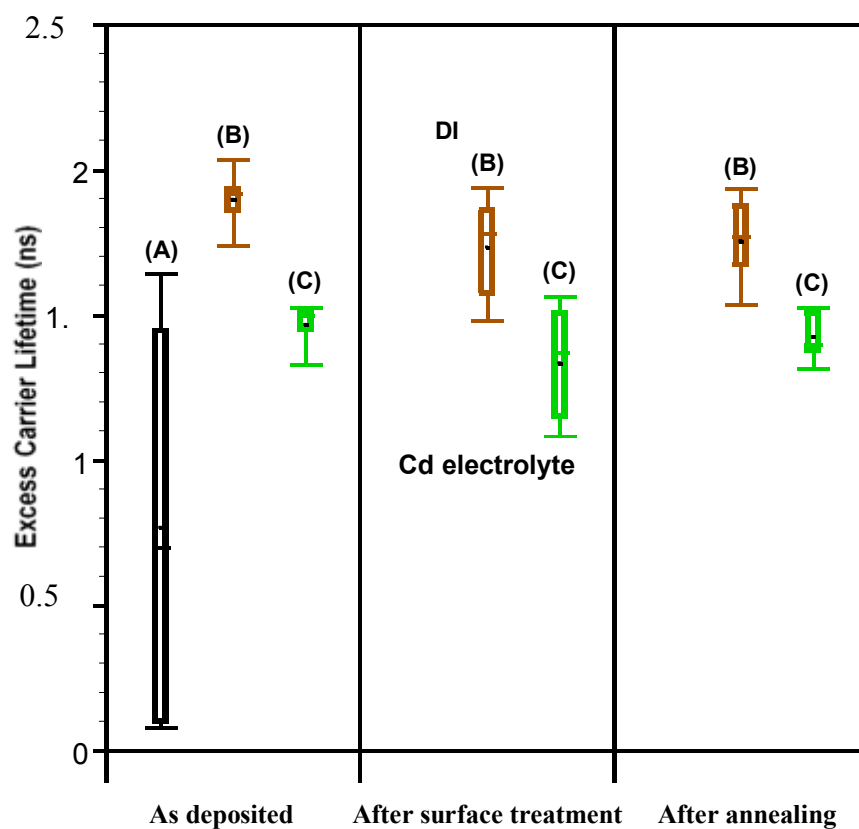
Figure 3-10. A statistical summary of excess carrier lifetimes for the second set NREL CIGS samples (M1517-A,B and C), the experimental conditions: as deposited, after surface treatments and after annealing.

Figure 3-11. A statistical summary of excess carrier lifetime for the second set NREL CIGS samples without CdS and with CBD, MOCVD, and sputtering deposited CdS and with surface treatments.
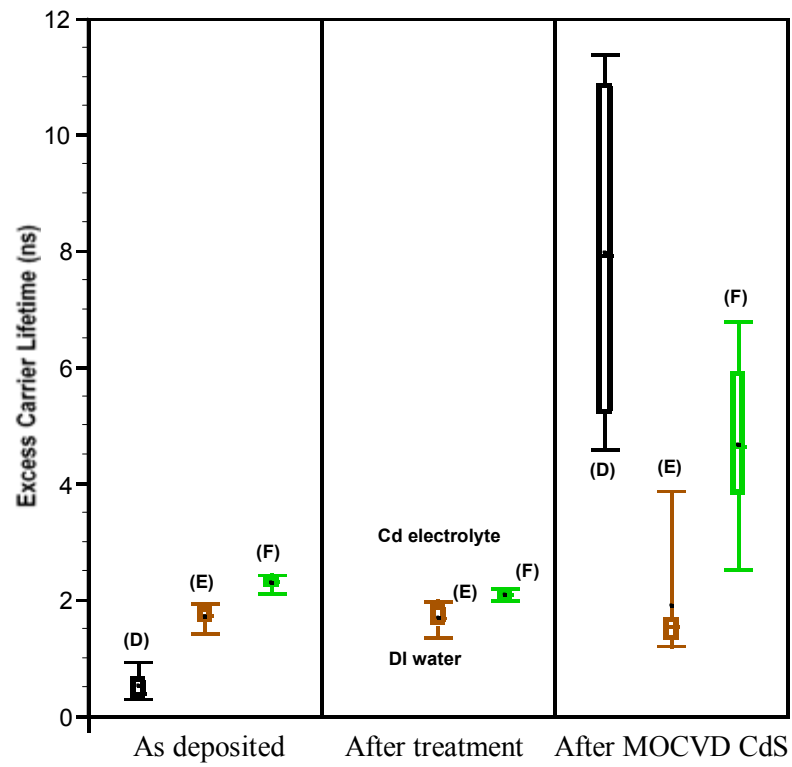
Figure 3-12. A statistical summary of excess carrier lifetimes for MOCVD CdS deposited CIGS samples.
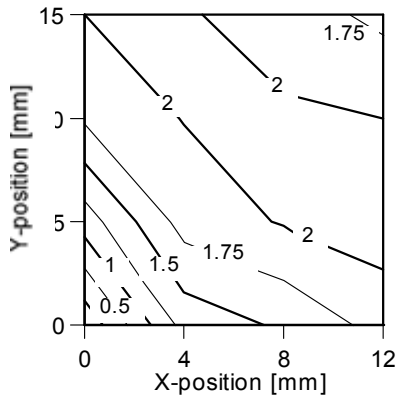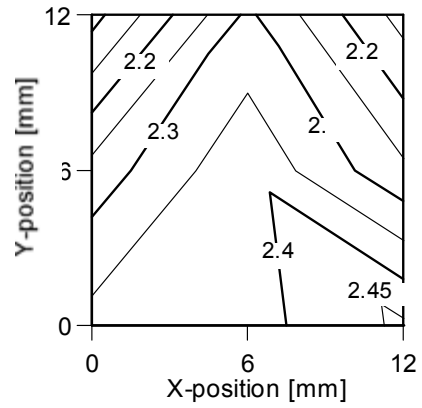
(a) Initially
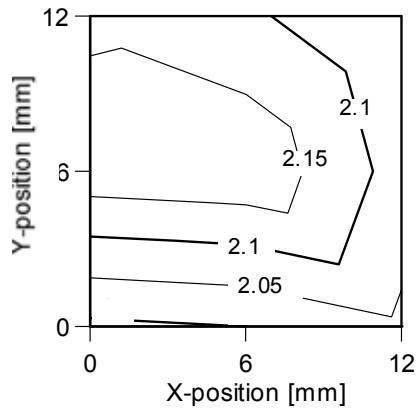
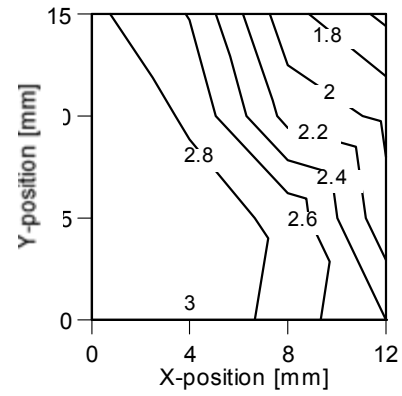(b) After surface treatment
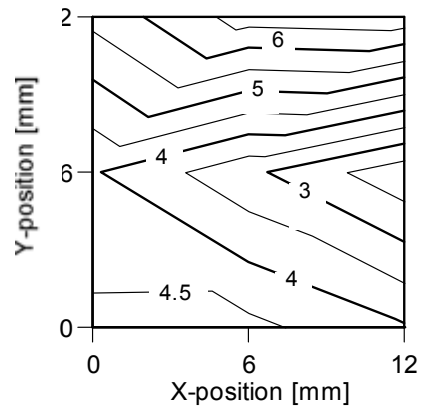
(c) After MOCVD deposited CdS

Figure 3-13. Contour line plots of excess carrier lifetimes for NREL CIGS sample (a) initially (as deposited) (b) after surface treatment (Cd-partial electrolyte) (c) after MOCVD deposited CdS.
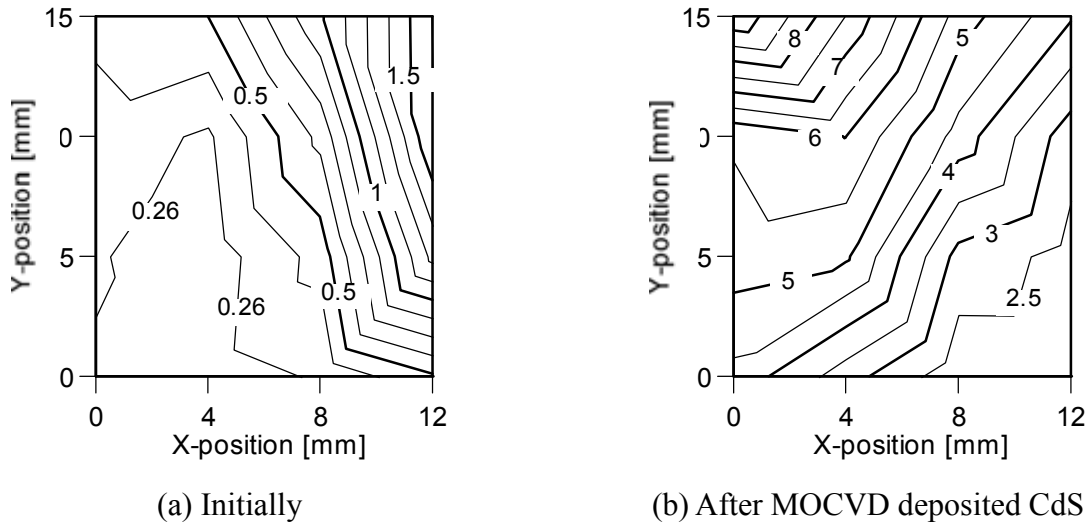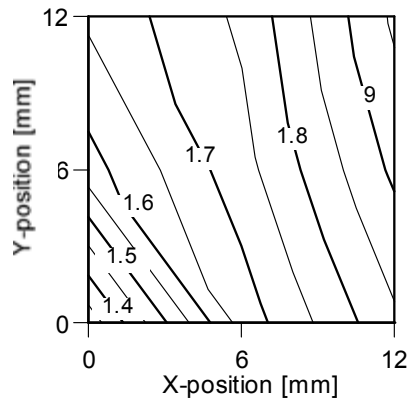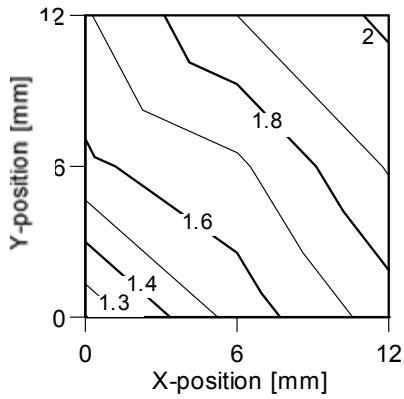
(a) Initially

(b) After surface treatment
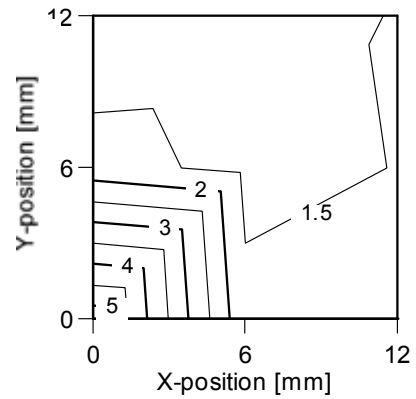
(c) After MOCVD deposited CdS

Figure 3-14. Contour line plots of excess carrier lifetimes for NREL CIGS sample (a) initially (as deposited) (b) after surface treatment (DI water rinsed) (c) after MOCVD deposited CdS.

(a) Initially	(b) After MOCVD deposited CdS
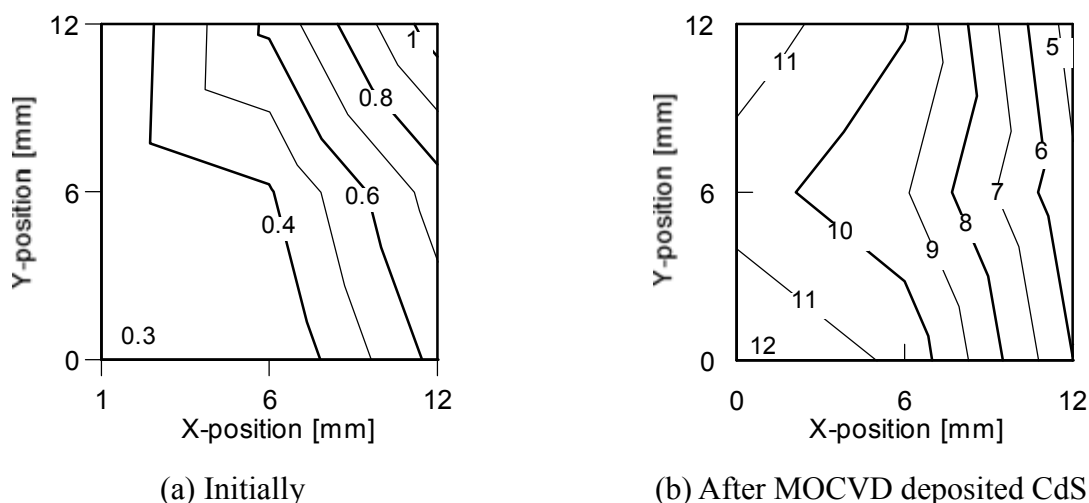
Figure 3-15. Contour line plot of excess carrier lifetimes for NREL CIGS sample (a) initially (as deposited) (b) after MOCVD deposited CdS.

The effect of CdS deposition on the excess carrier lifetimes in CIGS films is obvious. The results reveal that the excess carrier lifetimes are significantly increased with CdS deposition. The CIGS samples with the sputtered CdS show a dramatic increase in excess carrier lifetimes for both the as-deposited and after surface treatments. However, no clear evidence of positive effect of the surface treatments (DI water rinsing and Cd partial electrolyte treatments) and annealing on the excess carrier lifetimes in these CIGS samples is obtained from this study. It is interesting to note that the most dramatic increase in the excess carrier lifetimes was observed in the sputtered CdS deposited samples with no intermediate surface treatments. Also, the direct processing of sputtered CdS on the as-grown CIGS sample yields the longest excess carrier lifetime when compared to the CdS deposited CIGS samples.

3.4.2 Measurements of SSI and EPV Samples

The DBOM results for these samples are shown in Fig. 3-16. No detectable DBOM signal was obtained on all CIGS samples without the CdS buffer layers, as shown in Fig. 3-16. It is obvious that the CdS buffer layers increase $\Delta I/I$ values (and hence excess carrier lifetimes) for both the DI water-treated and as-deposited samples. This is especially true for the sputtering CdS deposited CIGS samples which show a dramatic increase of the DBOM signal for those DI water-treated and as deposited samples, as illustrated in Fig. 3-16. For both the CBD and sputtering CdS deposited samples, the DI water rinsing treatment decreases the excess carrier lifetimes. It is interesting to point out that the Ar plasma cleaning process dramatically increases the DBOM signal for the samples without the CdS buffer layer. The Ar plasma cleaning has the effects of Ar ion bombardment on the surface of the CIGS samples. Thus a smaller depletion width could have been created in the surface junction because of the Ar-plasma cleaning process. After Ar-plasma cleaning process, according to the XPS analysis the data show a clear evidence of chemical change in the samples, especially near the surface. The Cu/In ratio is restored to around unity although the starting surface composition was heavily In-rich. The depletion width

created due to the chemical change near the surface of the CIGS film could be the reason why the similar samples fabricated into devices have an increase in V_{oc} compared to the cells fabricated by using the as-grown and DI water rinsed samples. The created small depletion width and the band bending do have an effect on the results of DBOM measurements, which show an increase in the DBOM signal. However, after the sputtering CdS process on the CIGS samples the DBOM signal decreases.
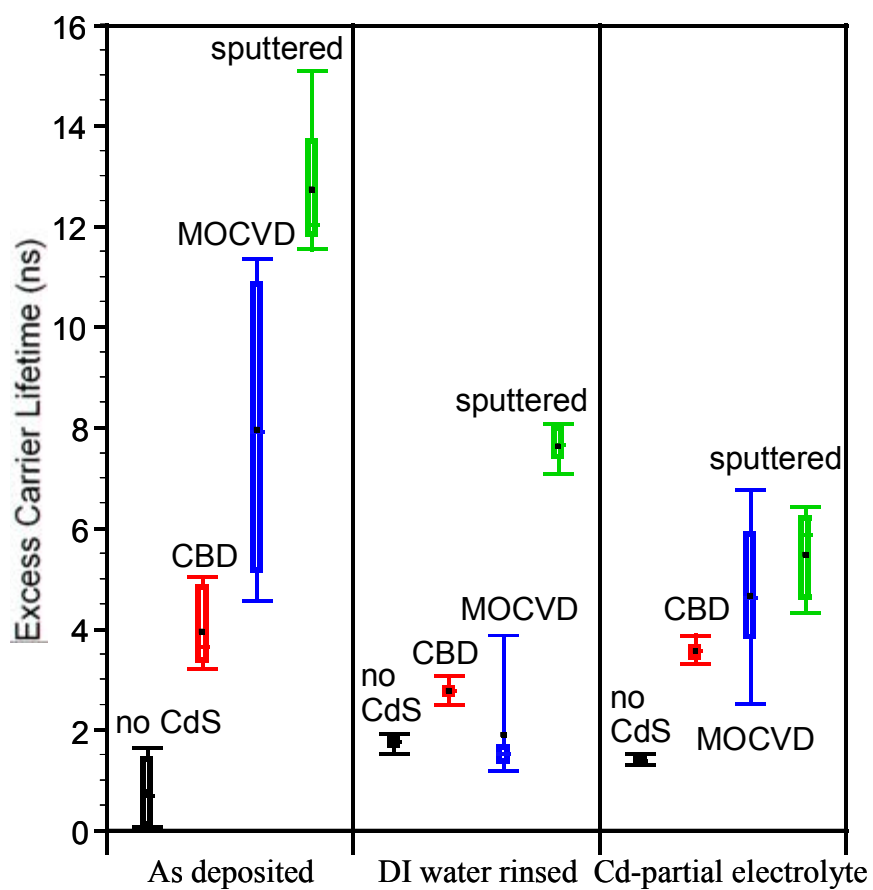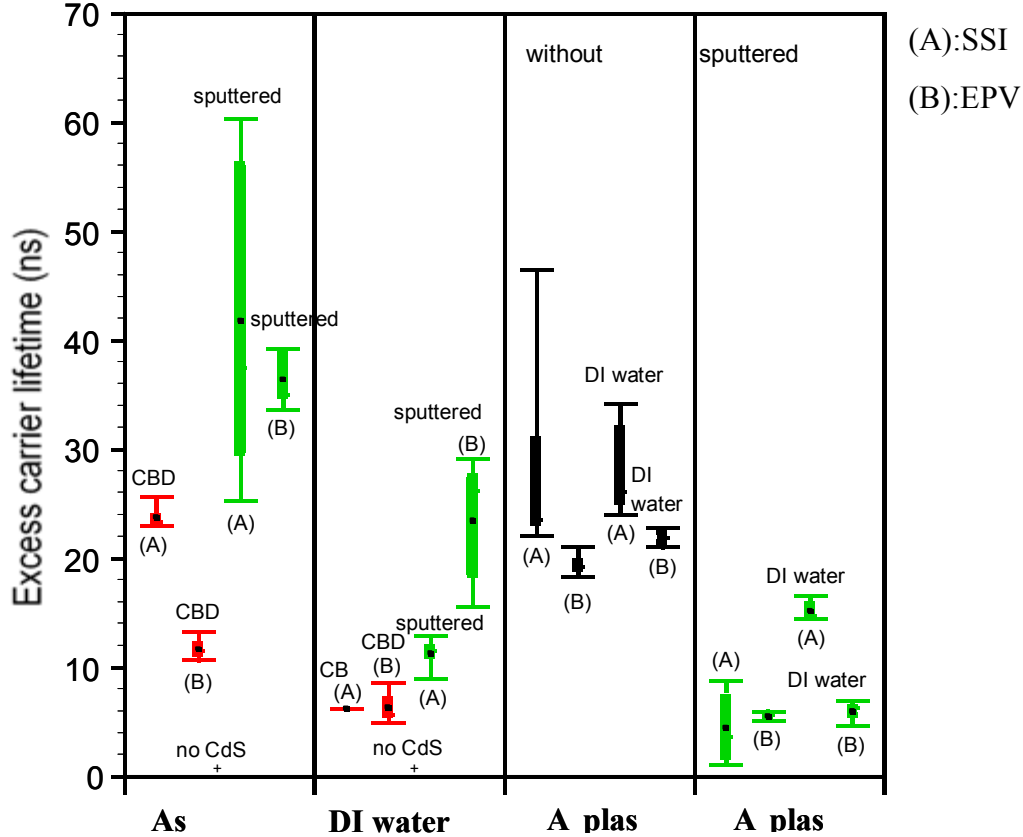

Figure 3-16. A statistical summary of excess carrier lifetimes for SSI and EPV CIGS samples without CdS and with CBD and sputtering deposited CdS, and with surface treatments.

3.5   Conclusions

We have demonstrated a contactless reflection mode DBOM technique developed specifically for determining the excess carrier lifetimes in the CIS and CIGS films. A study of the effects of CBD, MOCVD and sputtering deposited CdS on the excess carrier lifetimes in the CIGS films has been conducted. The results of this DBOM study for the CIGS samples from different laboratories (NREL, EPV, and SSI) are summarized as follows: the CBD, MOCVD and sputtering deposited CdS buffer-layer formation increase the excess carrier lifetimes for all as-deposited, water-rinsed, S- and Cd-partial electrolyte-treated samples. The CdS deposition increases $\Delta I/I$ less for water-rinsed, S- and Cd-partial electrolyte-treated samples than for as-deposited samples. Sputtering CdS deposition decreases the excess carrier lifetimes for the Ar-

plasma cleaned samples. However, prior to the CdS deposition, Ar-plasma cleaning process exclusively increases the excess carrier lifetimes of CIGS films. The intermediate surface treatments (i.e., DI water rinsed, Cd-partial electrolyte treatment, and Ar plasma cleaned) are not a positive effect on excess carrier lifetimes for CdS deposited CIGS samples. Especially, the sputtering of CdS dramatically increases the DBOM signal ∆I/I for as-deposited, water- and Cd-partial electrolyte-treated samples. The relative free carrier absorption change as measured by ∆I/I shows consistent trends for the CIGS films from several laboratories fabricated by the different techniques. The free carrier absorption change measured by the DBOM signal can be directly related to the quality of CIGS films studied in this work.

Further study of the correlation between the excess carrier lifetimes and the performance parameters of CIGS solar cells will be carried out in order to optimize the processing and growth conditions of CIGS films.

3.6 References cited

[3-1] M. Contreras, B. Egass, K. Ramanathan, J. Hiltner, A. Swartzland, F. Hasoon, and R. Noufi, *Progress in Photovoltaics*, Vol. 7, pp. 311, 1999.

[3-2] D. Lincot, R. Ortega-Borges, J. Vedel, M. Ruckh, J. Kessler, K. O. Velthaus, D. Hariskos, and H. W. Schock, *11th E. C. Photovoltaic Solar Energy Conference*, p. 872, 1992.

[3-3] T. M. Friedlmeier, D. Braunger, D. Hariskos, M. Kaiser, H. N. Wanka, and H. W. Schock, *Conference Record of the 25th IEEE PVSC*, p. 845, 1996.

[3-4] Sheng S. Li, B. J. Stanbery, C. H. Huang, C. H. Chang, T. J. Anderson, and Y. S. Chang, *Conference Record of the 25th IEEE Photovoltaic Specialists Conference*, p. 821, 1996.

[3-5] Y.-S. Chang, Sheng S. Li, R. Datta, and L. P. Allen, *Solid-State Electronics*, Vol. 41, p. 1189, 1997.

[3-6] L. Ward, *The Optical Constants of Bulk Materials and Films*, Adam Hilger, England, 1988.

[3-7] M. Levy, E. Scheild, S. Cristoloveanu, and P. Hemment, *Thin Solid Films*, Vol. 148, p. 127, 1987.

[3-8] J. I. Pankove, *Optical Process in Semiconductors*, Dover, New York, 1975.

[3-9] Yun-Shan Chang and Sheng S. Li, *Solid-State Electronics*, 38(2), p. 297, 1995.

[3-10] K. Ramanathan, M. A. Contreras, J. R. Tuttil, J. Keane, J. Webb, S. Asher, D. Niles, R. Dhere, A. L. Tennant, F. S. Hasoon, and R. Noufi, *Conference Record of the 25th IEEE Photovoltaic Specialists Conference*, p. 837, 1996.

[3-11] S. Zott and K. Leo, *Conference Record of the 25th IEEE Photovoltaic Specialists Conference*, p. 817, 1996.

4   Epitaxial Growth of CuInSe₂ at High Temperature

4.1   Introduction

It was possible to grow $CuInSe_2$ (CIS) epitaxially at a relatively low temperature (360 °C) for Cu-rich compositions. The explanation is that the excess Cu-Se phase acts as a surfactant to increase the mobility of surface adatoms and thus allow the adatoms to approach the nucleation sites and to grow epitaxially. It has also been suggested that a Cu-Se liquid phase exists and enhances the epitaxial growth of CIS, although no direct evidence has been reported. For the In-rich composition, the CIS film was not grown epitaxially and it showed only the domains with larger grain size. The polycrystalline growth was attributed to insufficient Cu to form the Cu-Se secondary phase, which increases the surface mobility and thus enhances two-dimensional-layer growth. Therefore, it was postulated that at higher growth temperature, the surface mobility, which increases exponentially with temperature, will be sufficient for epitaxial growth of In-rich films without the help of the Cu-Se phase. For these reasons, the growth of CIS films with both Cu-rich and In-rich compositions was performed at a higher growth temperature (464 vs. 360 °C).

Furthermore, the role of Na on the growth of CIS films is not well understood. From the literature review, it has been suggested that Na affects the growth process to increase the grain size by acting as a surfactant. Therefore, it is hypothesized that Na will also enhance epitaxial growth of CIS film, even without the help of the Cu-Se secondary phase. Four CIS films were grown on (100) GaAs, Cu-rich and In-rich, each with and without Na dosing. The growth mode of the films was studied by several techniques including ICP-OES, SEM, XRD, and TEM.

4.2   Experimental Approach

The three-temperature sequence used for the epitaxial growth of CIS at low growth temperature was tried using higher initial and final temperatures, and resulted in polycrystalline CIS or poor crystalline quality. This is attributed to a lower density of nucleation sites with higher initial temperature to give a longer migration length of adatoms to reach the nucleation site and achieve epitaxial growth.

Four CIS films were grown at the conditions summarized below. A constant growth temperature of 464 °C was used for the growth of CIS films. Because of a limitation in the system design and an increase in the background pressure of the reactor during the growth, this temperature was the maximum achievable one in the system. The background pressure during the deposition process was in the range of $2{\times}10^{-7}$ to $6{\times}10^{-7}$ Torr. The direction of the rotation (counter-clockwise) and the rotating speed (12 rpm) were the same as in low temperature growth experiments. Again, semi-insulating (100) GaAs wafers were used as substrates. The bulk composition of each CIS film was measured by ICP-OES for companion films grown on molybdenum-coated glass substrate by dissolving the film in 15% HNO_3 solution. Two CIS films, one with Cu-rich composition (W558) and the other with In-rich composition (W560) were grown. NaF was used as the Na precursor and delivered to the film from a Knudsen cell. Both Cu-rich (W584) and In-rich (W590) CIS films were dosed with Na with a Na flux impinging on the surface continuously and initiated at the same time as film growth.

4.3 Composition, Phase and Surface Morphology of CIS Films

Table 4-1 summarizes the bulk composition of CIS films. Sample W558 is Cu-rich (Cu/In = 1.10), while sample W560 is slightly In-rich (Cu/In = 0.99).

The level of Na dosing lies between 0.5 and 1 %, as stated in Table 4-1. CIGS absorber layers for high efficiency cells typically show 0.1 at.% of Na inclusion [4-1]. As such a small amount of Na in the films is difficult to detect, secondary ion mass spectroscopy (SIMS) was used to verify the Na level in the film. Depth profiling was also performed to investigate the composition of each element along the depth of CIS film. SIMS analysis was performed using a Perkin-Elmer PHI 6600 SIMS system operating with a 5 keV Cs primary ion beam. The depth profile of the composition of each element is shown in Figure 4-1. In this figure, the depth was calculated from the value of the crater depth after SIMS analysis (1396 nm). The vertical dotted line represents the CIS film/GaAs wafer interface and was estimated by the film thickness of 550 nm as observed in Figure 4-11b by SEM. The element profiles shown in Figure 4-1 indicate considerable diffusion of Cu, In, and Se into the GaAs and the diffusion of Ga from the GaAs into the CIS film. This is, however, believed to be an artifact from uneven sputtering of the rough film surface (AFM image shown in Figure 4-5 with estimated RMS roughness of 3.25 nm). In addition, the raster size was large (400×400 μm). This conclusion is supported from a TEM-EDX scan, which shows that In and Se were not detected in the GaAs substrate (detection limit ~ 0.5%) and Ga is not detected in CIS film though it was not plotted. However, Na was observed to diffuse into the GaAs substrate by TEM-EDX scan. The diffusion of Cu is also supported from the observation of PL peak related to the Cu_{Ga} - Na_i defect states in GaAs.

Table 4-1. Bulk composition of CIS films on Mo-coated glass determined by ICP.

Sample	Cu (at. %)	In (at. %)	Se (at.%) (Δs)	Na (at. %)	Cu/In (Δm)	Growth rate (Å/s)
W558	26.76	24.38	48.87 (-0.022)	-	1.10 (0.098)	0.59
W560	25.30	25.58	49.12 (-0.037)	-	0.99 (-0.011)	0.48
W584	27.06	24.75	47.69 (-0.059)	0.50	1.09 (0.093)	0.52
W590	23.60	26.17	49.24 (-0.036)	0.99	0.90 (-0.098)	0.54
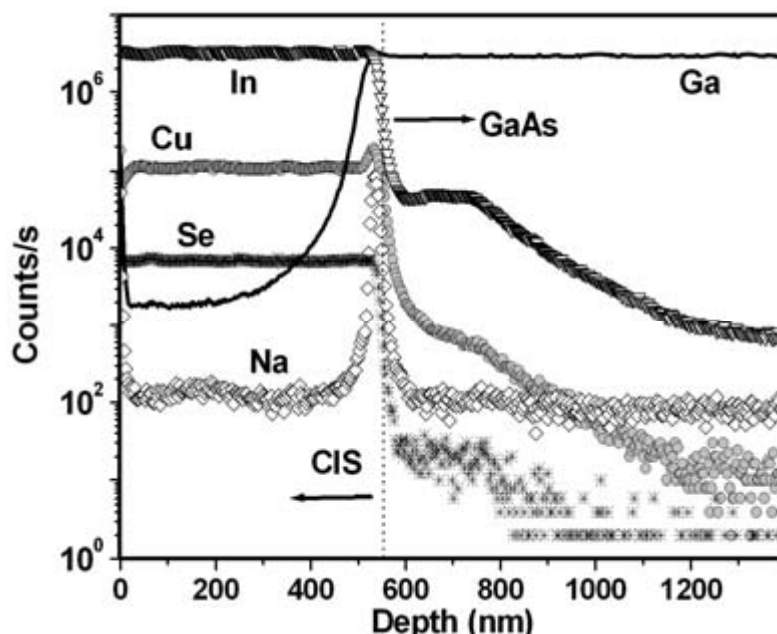
Figure 4-1. Element depth profiles of the In-rich, Na-dosed CIS sample (W590).

To investigate the effect of the Cu/In ratio and inclusion of Na dosing on the crystal quality and growth mode of CIS films at this higher growth temperature, the surface morphologies of the films were investigated by SEM as shown in Figures 4-2 through 4-4. Figure 4-5 is an AFM image as W590 has a very smooth surface that does not show the contrast in a SEM image. The Cu-rich CIS films without (W558, Figure 4-2) and with Na dosing (W584, Figure 4-4) show the island structures embedded in the matrix region similar to the Cu-rich CIS films grown at low temperature. These island structures in Cu-rich CIS films show elongated and faceted structures oriented in [0 1 -1] direction. The density of islands in these two Cu-rich samples is $\sim 5\times10^5$ cm^{-2} for both samples (W558 and W584) and lower than the density of islands in Cu-rich CIS sample (1.1×10^6 cm^{-2}) with Cu/In ratio of 1.09.

(a)   (b)
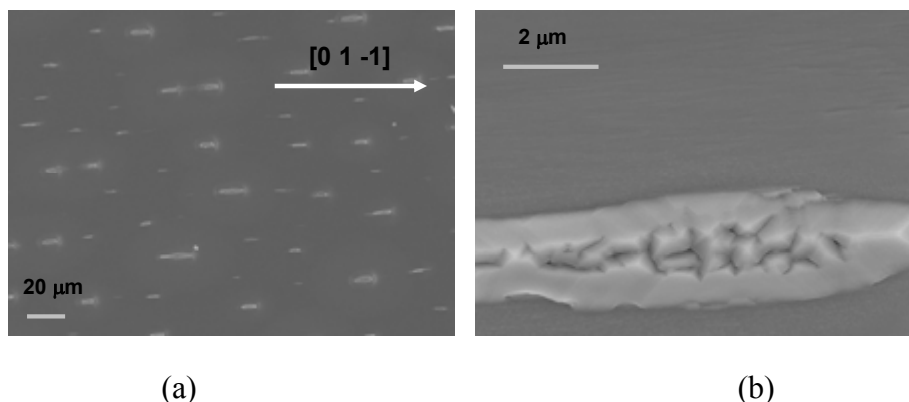
Figure 4-2. SEM image of the surface of the Cu-rich CIS film (W558, Cu/In = 1.10): (a) 500X, (b) island region at 10,000X.

(a)   (b)
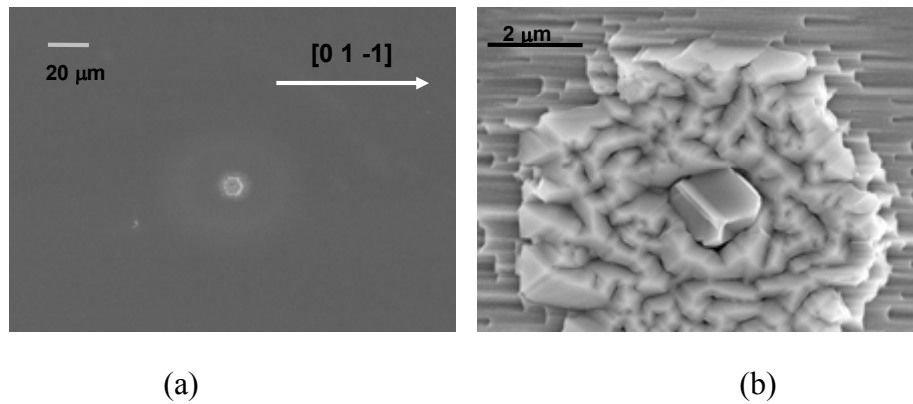
Figure 4-3. SEM image of the surface of the In-rich CIS film (W560, Cu/In = 0.99):
(a) 500X, (b) island region at 10,000X.

There are a few grains boundaries observed in the island regions of the Cu-rich CIS film without Na dosing (W558) while the island regions in the Cu-rich CIS film dosed with Na (W584) do not show faceted grain boundaries.

(a)   (b)
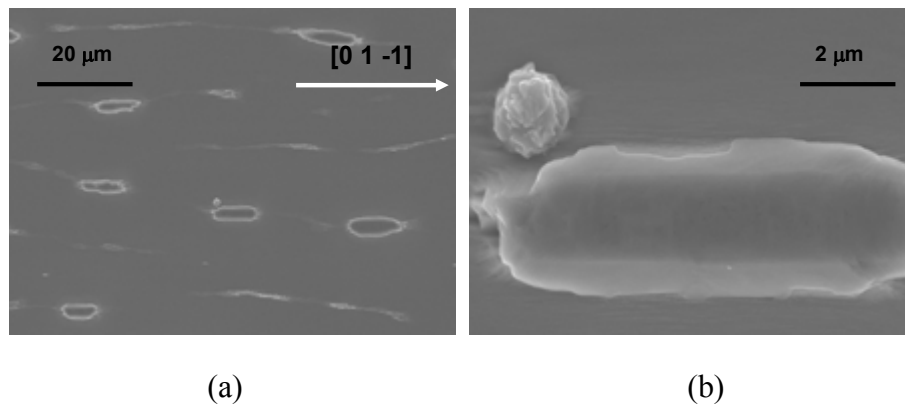
Figure 4-4. SEM image of the surface of the Cu-rich, Na dosed CIS film (W584, Cu/In = 1.10):
(a) 1,000X, (b) island region at 10,000X.

Z = 20 nm/div   **Z = 20 nm/div**

[0 1 -1]   [0 1 -1]

(a)   (b)
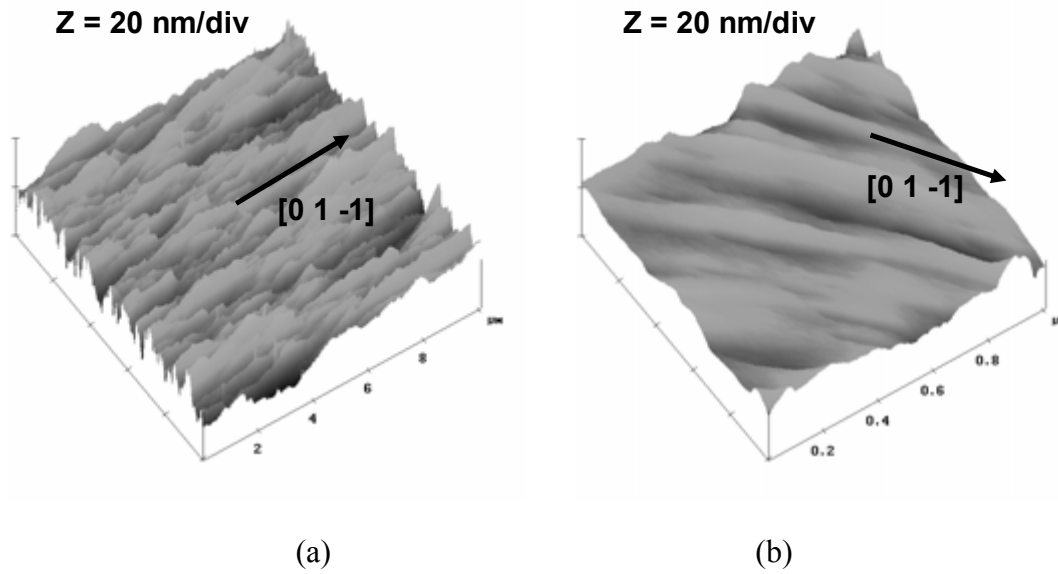
Figure 4-5. AFM image of the surface of the In-rich CIS film with Na dosing (W590, Cu/In = 0.9): (a) 10 μm×10 μm, (b) 1 μm×1 μm.

The matrix regions of both Cu-rich CIS films are textured with the long axis in [0 1 −1] direction of the substrate as was the morphology for the Cu-rich CIS films grown at low temperature. The island dimensions, however, are on the order of 3 μm×20 μm and the distance between islands is on the order of 20 to 30 μm. In contrast, typical dimensions of the island structure for the Cu-rich, epitaxial CIS films grown at lower temperature was 2×8 μm and the interspacing between island structures was on the order of 10 μm. Therefore, it is obvious that higher growth temperature increased the mobility of adatoms, which resulted in a lower density of nucleated islands to produce more elongated island structures. Also, from the similar island density and the dimensions of the island structure for the Cu-rich CIS samples with and without Na (W558 and W584), it appears that the inclusion of Na did not increase the mobility of adatoms in the growth process.

The increased growth temperature also made it possible to grow nearly island-free epitaxial CIS films with an In-rich composition as shown in Figures 4-3 and 4-5 (W560 without Na-dosing and W590 with Na-dosing). From these images and SAD patterns presented in sections 1.5.2 and 1.5.4, it is concluded that the In-rich CIS films (W560 and W590) grew epitaxially. The epitaxial growth of CIS film with an In-rich composition was not observed at lower growth temperature of 360 °C. These In-rich CIS films showed an almost island-free matrix structure. The island structure shown in Figure 4-3 was observed with a density of less than 100 cm^{-2} and almost no island structure was observed in the In-rich CIS film with Na-dosing (W590). Therefore, it is suggested that at high growth temperature, the mobility of adatoms is sufficient to allow layer-by-layer growth without the assistance of a Cu-Se secondary phase. It is noted that the density of islands at a given growth temperature increases as the Cu/In ratio increases. This suggests that the excess Cu-Se is important to the island nucleation and growth process.

The faceted island structure of the Cu-rich CIS films (W558, W584) and the island shown in the slightly In-rich CIS film without Na dosing (W560) are likely a mixture of a Cu-Se secondary phase and CIS as was shown for the Cu-rich CIS films grown at low temperature. Na dosing appears to increase the extent of the segregation of Cu-Se secondary phase in the island region, which will be confirmed by TEM analysis in section 1.5.3.

The matrix regions of both In-rich CIS films (W560, W590) are also textured in [0 1 -1] direction of the substrate. The roughness of this textured structure in In-rich CIS films at high growth temperature, however, is smaller (less than 5 nm) than that (80 nm) in Cu-rich CIS films grown at lower temperature. In the case of Cu-rich CIS films at lower growth temperature, the formation of an undulated textured surface in the matrix region was attributed to the stress relieving process by forming the (1 1 2) CIS planes with the lowest surface energy. For In-rich CIS films (W560, W590) grown at high temperature, however, formation of a very thin buffer layer at the interface between the film and GaAs is suggested. The existence of this buffer layer was proposed from the observation of a small feature in the XRD spectra shown in Figure 4-12 and the TEM-EDX line scan that shows considerable diffusion of Cu atoms into the GaAs substrate (Figure 4-24). The heteroepitaxial stress in the In-rich CIS films (W560, W590) grown at high temperature is apparently relieved by this compliant thin buffer layer, which results in the shallower undulations on the matrix surface.

4.3.1 EPMA Analysis

The compositions of the matrix and the island regions of each film was probed by EPMA to determine if there is a difference between the two regions, as observed in lower temperature growth. The results of the analysis are summarized in Table 4-2.

Table 4-2. EPMA analysis for the matrix and island regions of CIS film.

Sample	Matrix Region				Island Region			
	Cu (at.%)	In (at. %)	Se (at. %)	Cu/In	Cu (at. %)	In (at. %)	Se (at. %)	Cu/Se
W558	26.41	23.67	49.92	1.12	58.31	0.33	41.36	1.41[*]
W560	25.96	23.78	50.26	1.09	59.25	0.68	40.08	1.48[*]
W584	26.09	24.11	49.81	1.08	60.60	0.61	38.79	1.56[*]
W590	26.34	23.48	50.18	1.12	59.25	0.68	40.07	1.48[*]

[*]: Cu/Se ratio after subtracting CuInSe$_2$ composition.

In this analysis, an accelerating voltage of 6 keV was used. Similar to the lower temperature samples, the segregation of Cu-Se into the island region was observed for all CIS films, regardless of their bulk Cu to In metal ratio and Na dosing. It also appears that there was Cu-Se phase segregation near the surface region of the matrix region. EPMA is more surface sensitive (penetration depth of 200 nm at this accelerating voltage), and the Cu to In and Se to In ratios were higher than the bulk average determined by ICP.

To determine whether excess Cu-Se exists as a secondary phase or a solid solution and whether it resides in the matrix or island regions of the CIS films, SEM micrographs were taken after treating each CIS film with a 10% KCN solution to etch any Cu segregates and Cu-Se secondary phases exposed on the film surface. The SEM and AFM micrographs shown in Figures 4-6 to 4-9 are images of the same samples shown in Figures 4-2 to 4-5, but after etching. Note that the images are taken at different magnifications. It is observed that the surface morphology of the matrix region of each sample does not change with etching. The grains in the island regions of the Cu-rich CIS film without Na dosing (W558), however, appear to be covered with a thin layer of a Cu-Se secondary phase. Comparing Figure 4-6b to 4-2b, it is evident that etching resulted in the exposure of grains in the island region.

(a)   (b)
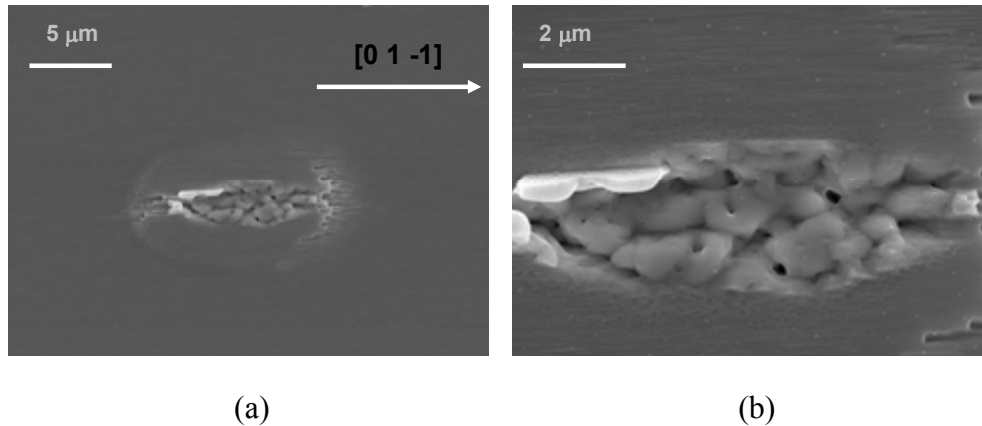
Figure 4-6. SEM image of the surface of the Cu-rich CIS film (W558, Cu/In = 1.10) after etching: (a) 3,000× ,(b) island region at 10,000×.

(a)   (b)
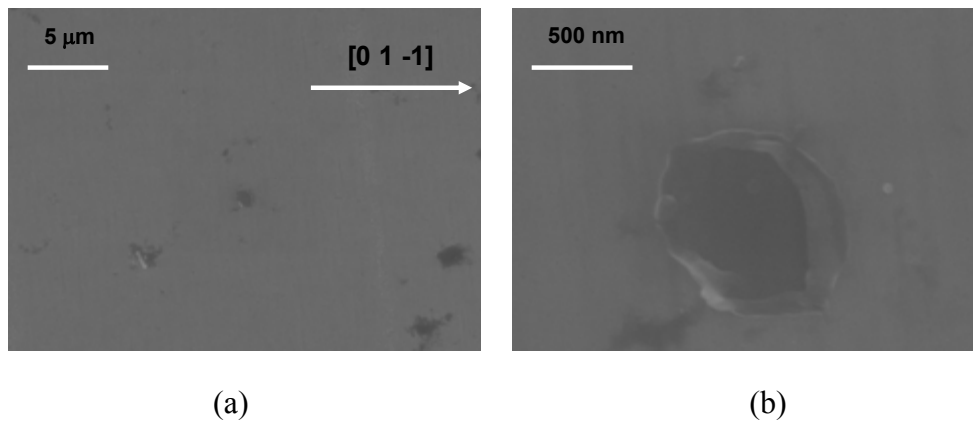
Figure 4-7. SEM image of the surface of the In-rich CIS film (W560, Cu/In = 0.99) after etching: (a) 3,000X, (b) island region at 30,000X.

Interestingly, it is observed that the faceted single grain displayed in Figure 4-4b for the Cu-rich, Na-dosed CIS film (W584), was completely removed by etching (Figure 4-8b). Thus a Cu-Se phase formed a separate grain as the top part of the island structure of the Cu-rich, Na-dosed CIS film (W584).
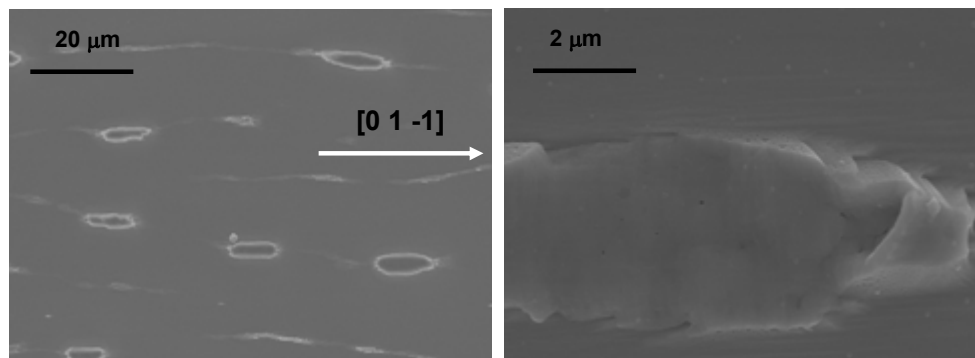
(a)   (b)

Figure 4-8. SEM image of the surface of the Cu-rich CIS film with Na dosing (W584, Cu/In = 1.10) after etching: (a) 1,000X, (b) island region at 10,000X.
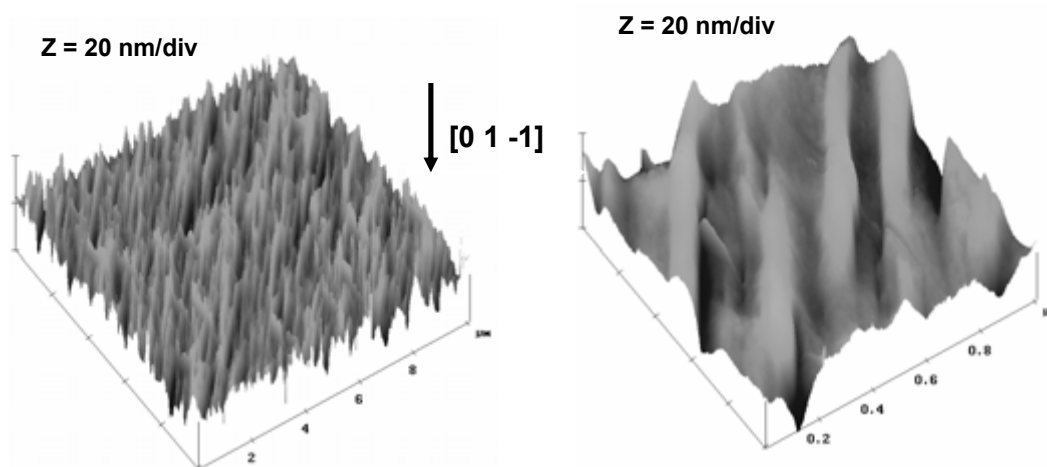
(a)   (b)

Figure 4-9. AFM images of the surface of the In-rich CIS film with Na dosing (W590, Cu/In = 0.9) after KCN etching: (a) 10 μmX10 μm, (b) 1 μmX1 μm.

For the In-rich CIS film without Na dosing (W560), a large crater was exposed after etching at the location of the island structure. Thus the entire island region consists of a Cu-Se secondary phase in this case. The EPMA analysis for the island region of Cu-rich, Na-dosed CIS film (W584) listed in Table 4-2 suggests that the Cu-Se secondary phase is $Cu_{2-x}Se$ with x ~ 0.5, which will be confirmed by TEM analysis (Figure 4-29 in section 1.5.3). The crystal structure, as determined by TEM analysis, of the Cu-Se secondary phase in the island region will also be reported in section 1.5.3.

From the AFM images of In-rich, Na-dosed sample (W590) after etching, it was observed that the RMS surface roughness was increased to 5.83 nm from the RMS value of 3.25 nm before etching. This result indicates that the surface of the In-rich, Na-dosed sample (W590) was covered with a thin layer of the Cu-Se phase.

4.3.2 Cross-sectional SEM Images

To identify the location of the island and the matrix regions and the possible growth mode for each CIS film, cross-sectional SEM micrographs were taken on samples prepared by cleaving the film/GaAs wafers in the [0 1 -1] direction.

The SEM cross sectional images in Figures 4-10 and 4-11 clearly indicate that CIS films grew uniformly regardless of their Cu/In ratio and the addition of Na at this high growth temperature.

(a)   (b)
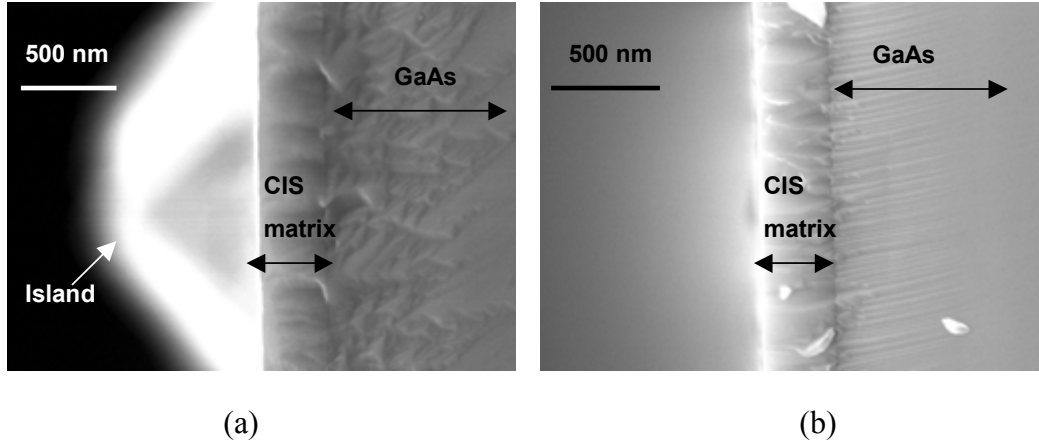
Figure 4-10. SEM cross-sectional images of CIS films without Na-dosing: (a) Cu-rich CIS film (W558, Cu/In = 1.10), (b) In-rich CIS film (W560, Cu/In = 0.99).

(a)   (b)
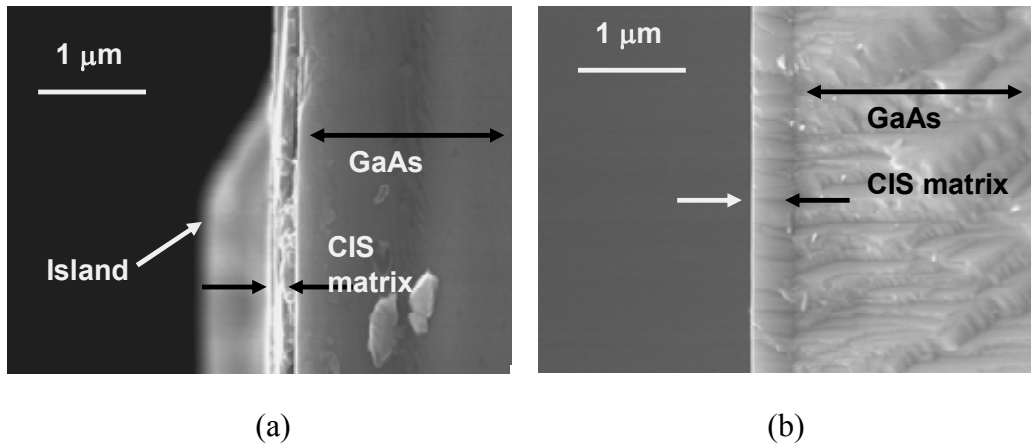
Figure 4-11. SEM cross-sectional images of CIS films with Na-dosing: (a) Cu-rich CIS film (W584, Cu/In = 1.09), (b) In-rich CIS film (W590, Cu/In = 0.90).

CIS films, however, showed different growth modes depending on the Cu/In ratio. Cu-rich CIS films (W558 and W584) were grown epitaxially by the S-K growth mode, while the nearly stoichiometric or In-rich CIS films (W560 and W590) showed layer-by-layer growth mode. From the fact that the layer-by-layer growth mode was observed for both In-rich samples (W560 and W590), the mobility of adatoms was apparently sufficient for layer-by-layer growth at this growth temperature, and did not require the assistance of the excess Cu-Se or Na-dosing.

4.4   XRD Analysis of CIS Films Grown at High Temperature

4.4.1   XRD θ–2θ Scan and ω-rocking Curve Analysis of CIS Films Grown at High Temperature

To determine the film orientation and phase, high resolution XRD θ–2θ scans were taken for each film with the results summarized in Figure 4-12. The XRD spectra for all CIS films showed XRD peaks for only CIS (00n) planes, which is consistent with the epitaxial growth. There was also a small feature at 2θ values slightly greater than that for the GaAs (400) reflection. To estimate the strain in all CIS films, and to help identify the origin of this feature, a XRD space map, which is a series of ω–2θ scans with varying ω values, was performed using the X'Pert system. Unfortunately, it was not possible to separate the feature from the intense (400) reflection. The ratio of the intensity of this feature to that of GaAs was very small (~ 8×10⁻⁴) and the signal from the unknown peak can be overwhelmed by the background intensity. More importantly, for the crystal plane with higher index usually used in XRD space map, the intensity from the feature is very small when there is a strain distribution which is observed from the broad shape of the peak as in this case. It is due to the less coherence of the crystal planes with high index than (00n) planes when there is a strain in the film.
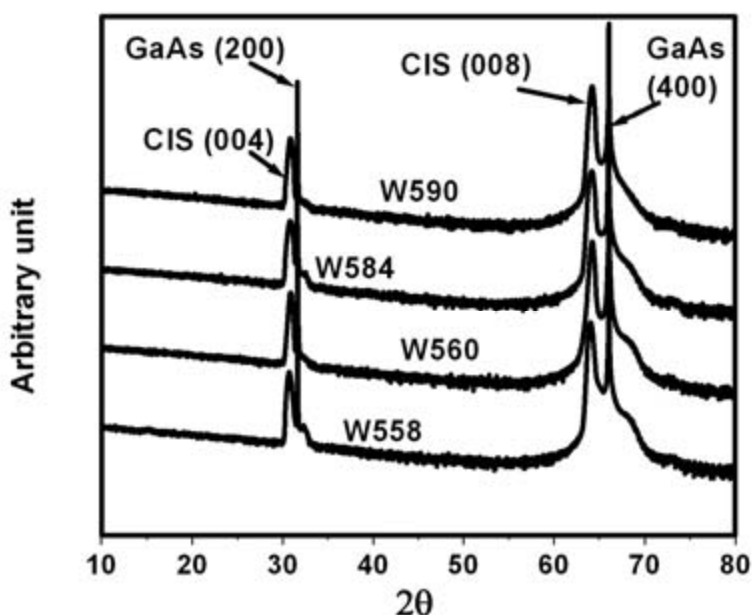
Figure 4-12. XRD θ–2θ scan of each CIS film.

The XRD θ–2θ scan of In-rich CIS film (W560) after etching by KCN solution shows the same feature in the spectrum, which indicates the reflection is not from the Cu-Se secondary phase.
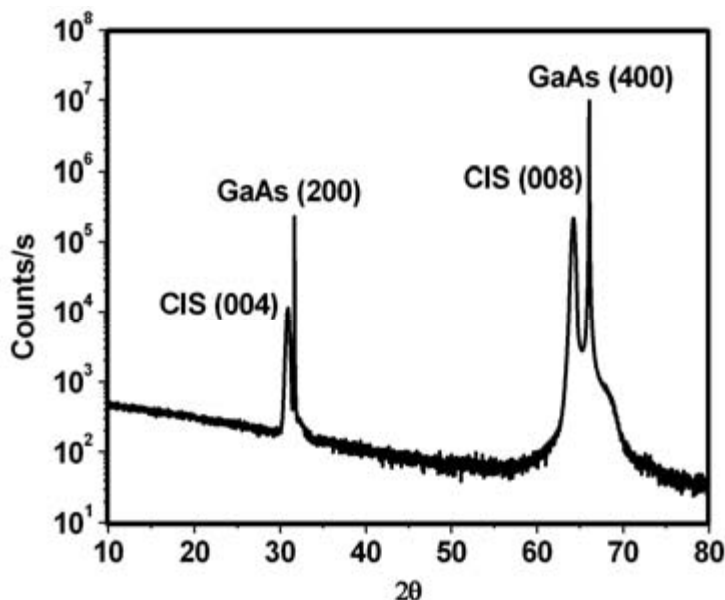
Figure 4-13. XRD θ–2θ scan of the In-rich CIS film without Na-dosing (W560) after KCN etching.

As the bump is located at a higher 2θ value in the [001] direction of the reciprocal space, the phase or region of the film that is responsible for reflection has a smaller c constant than CIS or larger in-plane lattice constant than that of GaAs. Therefore, a possible hypothesis is that a very thin GaAs region is near the interface between the film and the substrate is strained relative to the film. It is also possible that the broad peak is derived from an $In_XGa_{1-X}As$ layer or $CuIn_{1-x}Ga_xSe_2$ layer formed by the inter-diffusion of In or Ga atoms between the film and the substrate. The inter-diffusion of In or Ga will be discussed in section 1.3

To compare the crystal quality of epitaxial CIS films with different Cu/In ratios and Na dosing, ω-rocking curve scans for the (008) plane were recorded for each CIS film. As shown in Figure 4-14, the FWHM values of the rocking curves for the Cu-rich CIS film (W558 or W584) is slightly larger than those for the In-rich CIS films (W560 or W590). This difference in FWHM values is likely attributed to the defects at the boundaries between the matrix and the island regions in Cu-rich CIS films since these samples have a higher density of islands than the In-rich CIS films (W560 and W590), which are nearly island-free. The FWHM value of the substrate (35 arcsec) is considerably smaller than any of the CIS films (in range of 648 to 923 arcsec). Thus the structural quality of the CIS films is considerably less than the GaAs substrate, regardless of the presence of Na or Cu/In ratio. It is concluded that the mobility of the adatoms is sufficient at this high temperature and the Cu-Se secondary phase is not needed for the epitaxial growth. Similarly, the higher FWHM values for CIS films with Na-dosing (W584, W590) than the CIS films without Na-dosing (W558, W560) also indicate that the inclusion of Na did not improve the crystal quality and the surface mobility. The relatively large difference in lattice constants between GaAs and CIS is likely responsible for the presence of a larger defect density and residual strain that dictate the overall structural quality.

4.4.2   Strain Analysis of CIS Films Grown at High Temperature

An analysis to estimate the change of lattice parameters or the strain of each CIS film was performed. A space map analysis was performed on the (228) crystal plane of CIS film and the (224) crystal plane of GaAs for each film. The same X'pert system and procedures described in chapter 2 were was used for the space map analysis. A hybrid 4-bounce monochromator with four Ge (220) single crystals and 1/2 inch slit were used to produce the incident beam, and a triple axis, including two of the Ge (220) single crystals, was used to collect the diffracted beam. The combined resolution for this ω–2θ scan is 0.0001°. The values of the (ω, 2θ) coordinates, were obtained by manually maximizing the intensity of the (228) peak of CIS film and that of the (224) peak of GaAs, respectively.
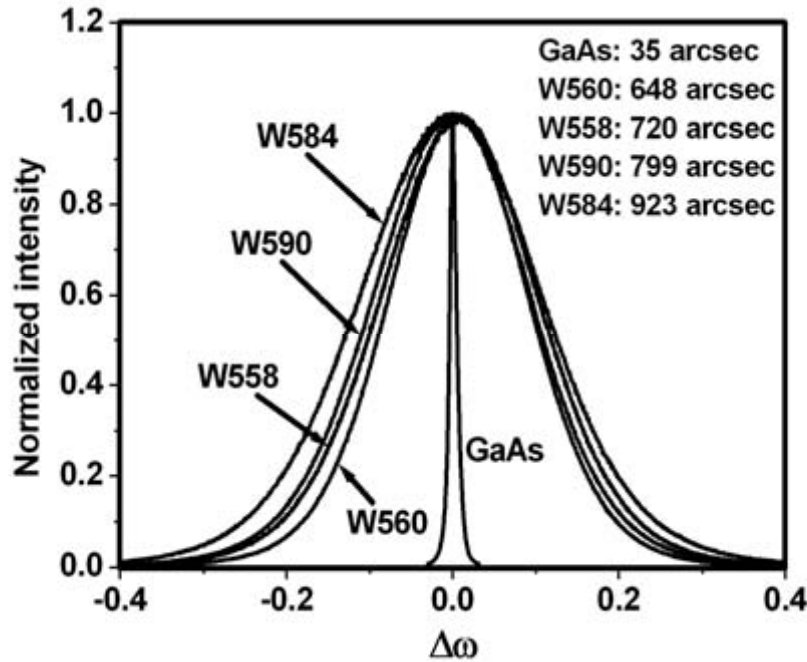
Figure 4-14. ω-rocking curve of the CIS (008) plane for each film and the GaAs (400) plane.

In the XRD space map measurement, only the Cu Kα_1 emission line with a wavelength of 1.54089 Å was used. From this wavelength and the lattice parameter of GaAs (5.654 Å from JCPDS32-0389), the theoretical value for the (ω, 2θ) coordinate set of the GaAs (224) plane is calculated as ω = 6.6146° and 2θ = 83.758°. After considering the offset between the theoretical (6.6146, 83.758) and the measured (6.6466, 83.822) values for the GaAs (224) plane, the values for the CIS (228) crystal plane were calculated and summarized in Table 4-3. Also, from the estimated values presented in Table 4-3, the lattice constants of each film were calculated and listed in Table 4-4. These values were compared to the unstrained lattice parameters of CIS film (a = 5.782 Å, c= 11.619 Å from JCPDS40-1487) to give the lattice constants of each film relative to the GaAs substrate.

Table 4-3. Estimated values of ω, 2θ, φ, and psi for the GaAs (224) and CIS (228) planes.

ID	GaAs				CIS			
	2θ	ω	φ	psi	2θ	ω	φ	psi
W558	83.7580	6.6146	-0.18	0.79	81.1875	5.2932	-0.52	0.78
W560	83.7580	6.6146	-0.22	0.96	81.1947	5.3075	-0.48	0.45
W584	83.7580	6.6146	0.81	0.22	81.1977	5.2990	0.81	0.61
W590	83.7580	6.6146	-0.45	0.27	81.2017	5.2475	-0.45	0.56

Table 4-4. Lattice constants and lattice mismatch relative to GaAs for each CIS film.

ID	k_{008} ($Å^{-1}$)	k_{220} ($Å^{-1}$)	c(Å)	a(Å)	mismatch
W558	0.6893	0.4880	11.606	5.796	2.51%
W560	0.6894	0.4880	11.604	5.796	2.51%
W584	0.6894	0.4881	11.604	5.791	2.42%
W590	0.6889	0.4888	11.613	5.786	2.33%

A plot of the lattice constants of each CIS film in reciprocal space clearly shows that each CIS film grown at this high temperature was nearly fully relaxed (Figure 4-15). In this case, the lattice mismatch between each CIS film and the GaAs substrate might have been accommodated by misfit dislocations in these films, especially near the boundaries of the island structures embedded in the matrix region for the Cu-rich CIS films (W558, W584) and near the interface between the CIS film and GaAs substrate for the In-rich CIS films (W560, W590). As suggested previously in this section, the XRD spectra shown in Figures 4-12 and 4-13 show a small and broad peak positioned at a slightly greater 2θ value than the reference (400) GaAs reflection. It is proposed that a thin buffer layer was formed in the GaAs near the interface between GaAs and CIS film. This buffer layer is thought to be made from the diffusion of Cu, In or Ga atoms to form a graded buffer layer near the interface. This buffer layer is assumed to present an in-plane lattice constant close to that of CIS to permit epitaxial growth of a nearly relaxed film.
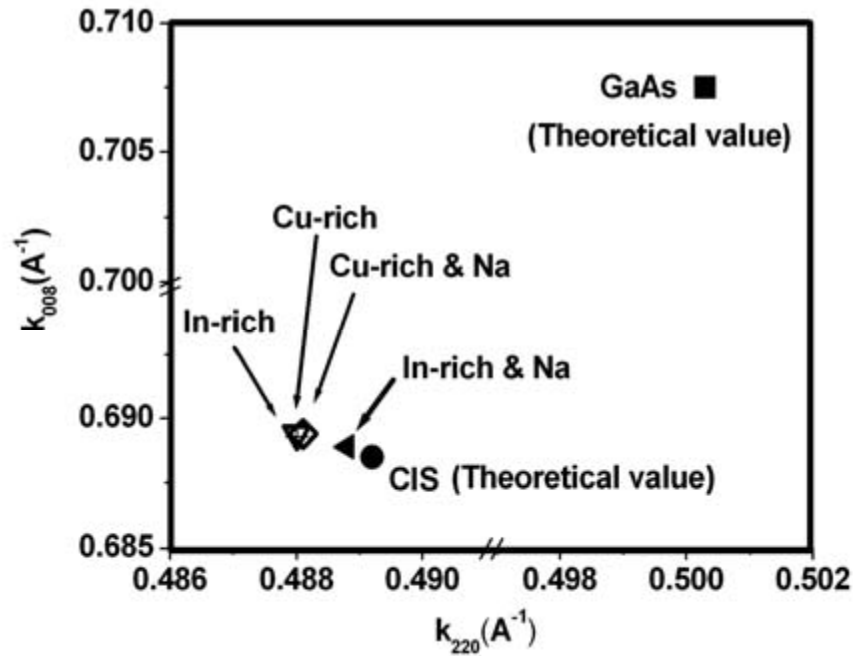
Figure 4-15. Lattice constants of each CIS film in the reciprocal space.

4.5 TEM Analysis of CIS Films Grown at High Temperature

As observed in the SEM micrographs in section 1.3, Cu-rich CIS films (W558, W584) showed the island structures embedded in the smooth matrix region. Also, the top part of the island structure in Cu-rich CIS film with Na-dosing (W584) was suggested as $Cu_{1.5}Se$ from the result by EPMA analysis in section 1.3.1. Therefore, it is necessary to investigate the crystal structure of each CIS film more extensively at high spatial resolution.

For this purpose, TEM analysis was performed in selected areas on each CIS film. Selected area diffraction (SAD) is used to measure the local lattice spacing. For the assignment of each diffraction spot observed using SAD patterns, the distance between the transmitted beam and each diffraction spot is first measured. Then, the inter-planar spacing for each diffraction spot is calculated by the following equation:

$$Rd_{hkl} = \lambda L, \qquad\qquad (4\text{-}1)$$

where R, d_{hkl}, λ, and L are the measured distance between the diffraction spot and the transmitted beam, the inter-planar spacing of the corresponding diffraction spot, wavelength of the electron beam, and the camera length of the microscope (82 cm) used to obtain the diffraction pattern, respectively. The wavelength of the electron beam at the accelerating voltage of 200 kV used in this study is 0.0252 Å. The values of d_{hkl}, is then calculated from Equation 4-1 and the corresponding crystal plane (h k l) is determined by comparing the inter-planar spacing value, d_{hkl} with the theoretical or experimental values.

In TEM analysis, dark field images are often taken to yield an image with better contrast and to better demark the dislocations in the film. Practically, a dark field image is obtained by locating the diffracted beam at the optic axis using a two-beam condition, where diffraction is obscured from only two crystal planes. Therefore, the dark field image under this condition shows the feature in the film that has orientation parallel to the diffracted beam, and those features that have an orientation (h k l) normal to the diffracted beam are not shown in the dark field image. This approach can be used to determine the orientation of a dislocation in the material or to identify an area with a different orientation or crystal structure from other areas.

4.5.1   TEM Analysis of the Cu-rich, Na-free CIS Film (W558)

Though the epitaxial growth of all CIS films were confirmed by XRD analysis as in section 1.4, it is necessary to identify the orientation of the CIS film relative to that of GaAs. SAD patterns of film and substrate for the Cu-rich film without Na addition were taken using selected area aperture with a diameter of 500 nm at [1 -1 0] zone axis as in Figure 4-16.

(a)   (b)
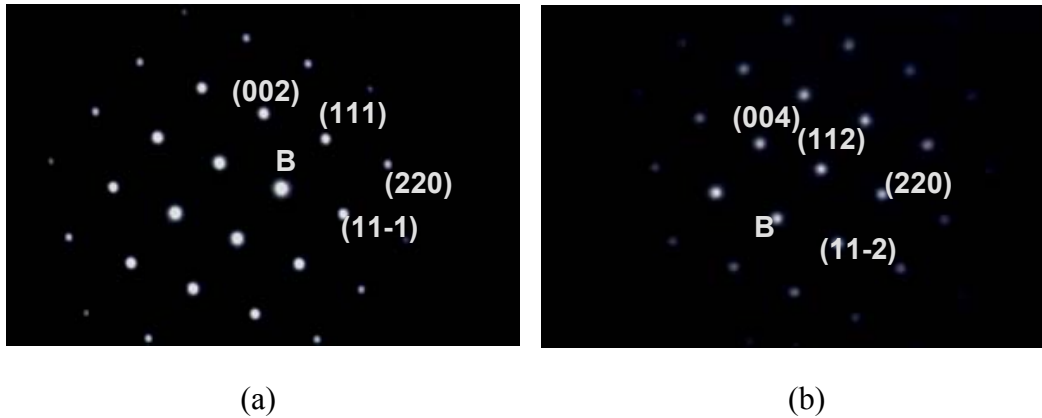
Figure 4-16. SAD pattern of GaAs substrate and CIS region of Cu-rich CIS film without Na (W558) at zone axis [1 -1 0]: (a) GaAs, (b) CIS.

The lattice constants of CIS film were calculated from the pattern shown in Figure 4-16b and a value of 82 cm for the camera length. The value of λL is calculated from the product of the values of the separation distance and the electron beam energy. This is only possible, however, when the sample is positioned exactly at the eucentric position. As in the strain analysis using XRD data, to estimate the offset in the λL value, it is assumed that the in-plane lattice constant of GaAs is the fully relaxed value since it is considerably thick (~ 400 µm) than the overgrown CIS film (~ 0.5 µm). The distance between the transmitted beam (indexed with B in Figure 4-16) and the spot for the (220) plane in the SAD pattern for GaAs area (Figure 4-16a) is 10.7 mm. Therefore, to produce the in-plane lattice constant of GaAs (a = 5.654 Å), the required value of λL is 21.39 mm·Å. For the CIS area, the distance of the (220) spot from the transmitted beam is 10.45 mm, and results in the value of $d_{(220)}$ = 2.047 Å (21.39 mm·Å/10.45 mm) and the in-plane lattice constant, a = $(8)^{1/2}d_{(220)}$ = 5.790 Å. The values for the inter-planar spacing, d_{hkl}, and their crystal plane assignments are summarized in Table 4-5.

Table 4-5. Lattice parameters of GaAs and CIS calculated from SAD pattern at [1 -1 0] zone axis for Cu-rich CIS film without Na (W558).

	Distance to the spot (mm)		Inter-planar spacing, d (Å)		Lattice parameter (Å)	
	(220)	(111) or (112)	$d_{(220)}$	$d_{(111)}$ or $d_{(112)}$	a	c
GaAs	10.70	6.56	1.999	3.261	5.654	5.637
CIS	10.45	6.35	2.047	3.369	5.790	11.86

* Estimated 0.1 mm uncertainty.

The assignments to specific crystal planes are labeled in Figure 4-16. From the lattice constants presented in Table 4-5, this CIS film was grown in a nearly relaxed state. A SAD pattern was also taken at the region near the interface region between CIS and GaAs to check if the Cu-rich CIS film (W558) shows pseudomorphic growth. A selected area (SA) aperture with a diameter of ~ 250 nm was used, where half of the SAD aperture was filled with CIS material and the other half was filled with GaAs material. As the pattern in Figure 4-17 shows, double spots are apparent for each crystal plane, and then the CIS film did not grow pseudomorphically near the interface region.

These results are consistent with the result of the XRD strain analysis presented in the previous section. However, from the observation of the diffused spots in Figure 4-17, it is assumed that the SAD spots in Figure 4-17 might be a mixture of the spots from the bulk region of CIS and GaAs materials and the spots from the buffer layer region since the size of the SAD aperture is too big for a thin buffer layer. Therefore, the growth model is postulated as follows. At the initial stage of the growth, a thin buffer layer with an in-plane lattice close to that of CIS film is formed in the GaAs region near the interface. With the help of this buffer layer and resulting decrease of the heteroepitaxial strain, the CIS film grows epitaxially by 2-D layer growth mode. However, there is also the segregation of Cu-Se phase from the Cu-rich composition at some of the nucleation sites, which results in the faster growth and thicker island region.

The spots labeled as 1 & 1` in Figure 4-17, correspond to the family of (2 2 0) crystal planes, {2 2 0}, and those labeled as 2 & 2`are for the {1 1 1} family.

Dark field image were taken by using (0 0 -4) diffraction vector and the images of the island and matrix regions are presented in Figure 4-18. The images in Figure 4-18 show that the island region consists of an underlying matrix layer and a multiple grain upper region. The image shows the underlying matrix region contains several dislocations originating at the CIS/GaAs interface. The image in Figure 4-18b similarly shows the matrix region contains dislocations.

The dislocations extend from the substrate to both in the island and matrix regions. Therefore, it is proposed that the heteroepitaxial strain due to the lattice mismatch between the CIS film and GaAs was largely relieved by the formation of the misfit dislocations during the initial stage of the growth.
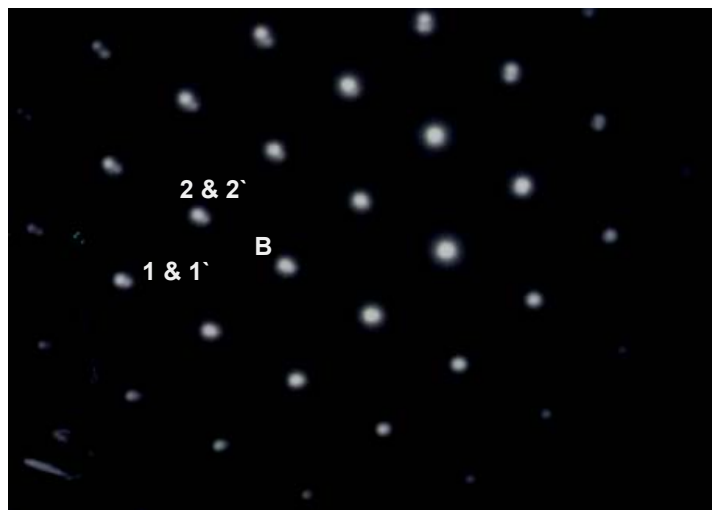
Figure 4-17. SAD pattern at the interface of the Cu-rich CIS film without Na addition (W558) and the GaAs substrate at zone axis [-1 1 0].

(a)　　　　　　　　　　　　　　　　(b)
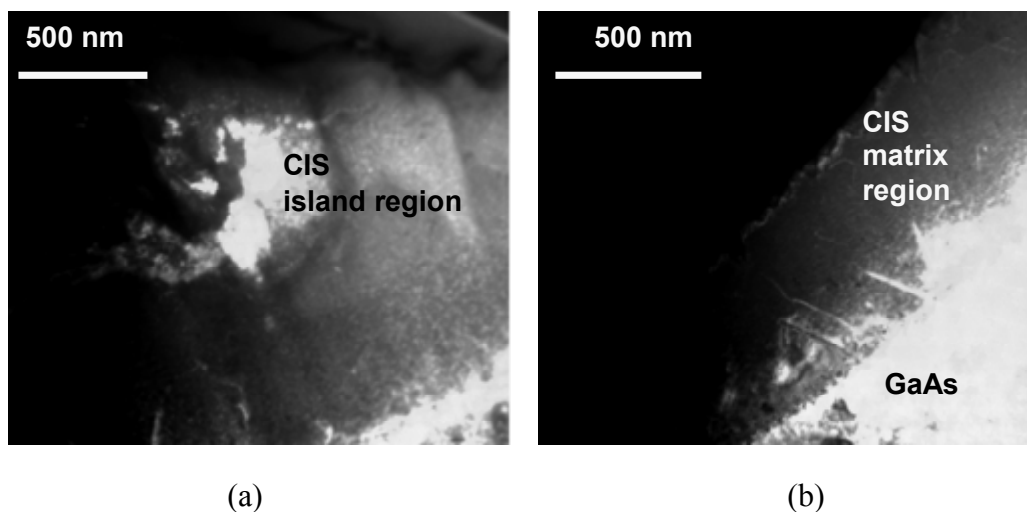
Figure 4-18. Dark field images of the Cu-rich, no Na sample (W558) using g = (0 0 -4) diffraction vector at 50,000X magnification: (a) island region, (b) matrix region.

SAD patterns from a single grain and from multiple grains in the island region were taken (Figure 4-19). These patterns suggest that, as in the case of Cu-rich CIS film grown at lower temperature (See section 2.5 for sample W367), twins are formed, where each grain was grown as a single crystal with a small rotation or mis-orientation relative to each other. The reduction of the heteroepitaxial strain is also attributed to the existence of this twin structure.

(a)   (b)

Figure 4-19. SAD pattern for a single grain and multiple grains in the island region at zone axis [1 -1 0]: (a) Single grain, (b) Multiple grains.

4.5.2 TEM Analysis of In-rich, Na-free CIS Film (W560)

The same TEM analysis was performed on the In-rich, Na-free CIS film (W560), to determine the values of lattice constants and the relative orientation of CIS region with respect to the substrate. Figure 4-20 shows SAD patterns of CIS and GaAs regions of the sample at zone axis [-1 1 0]. As shown in this figure, the SAD patterns for both GaAs and CIS film show the same symmetry and orientation at the zone axis [-1 1 0] but different distances between corresponding different spots.

The same calibration procedure in section 1.3.1 was performed that requires a (GaAs) = 5.654 Å for the 82 cm camera length. It was calibrated for the (2 2 0) spot and the λL value was determined as 20.65 mm·Å. By using this value, the lattice constants of CIS region and GaAs substrate were again calculated and the values are summarized in Table 4-6. In addition, each diffraction spot was assigned to the specific crystal plane as labeled in Figure 4-20.
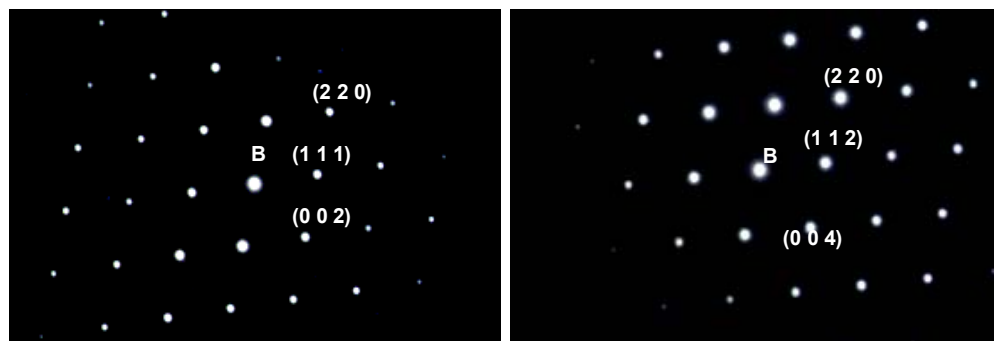
(a)   (b)

Figure 4-20. SAD patterns of the GaAs substrate and CIS region for In-rich, Na-free CIS film (W560) at zone axis [-1 1 0]: (a) GaAs, (b) CIS.

Table 4-6. Lattice parameters of GaAs and CIS region for In-rich CIS film (W560) calculated from SADP at [-1 1 0] zone axis.

	Distance to the spot (mm)		Inter-planar spacing, d (Å)		Lattice parameter (Å)	
	(220)	(002) or (004)	$d_{(220)}$	$d_{(002)}$ or $d_{(004)}$	a	c
GaAs	10.330	7.300	1.999	2.829	5.654	5.658
CIS	10.167	7.250	2.031	2.848	5.745	11.39

* Estimated 0.1 mm uncertainty.

The results shown in Table 4-6 indicate that the in-plane lattice parameter "a" of the In-rich CIS film (W560) is only slightly less than the unstrained material (lattice mismatch = 1.61%). The island-free, In-rich, Na-free CIS film grew heteroepitaxially in a nearly unstrained state with good crystal quality. SAD pattern of the interface region between GaAs and CIS at zone axis [-1 1 0] is shown in Figure 4-21.

Figure 4-21. SADP near the interface between CIS film and GaAs substrate, W560.

The diffraction spots were indexed by comparing with the theoretical values and are labeled in Figure 4-21. The diffraction spots labeled 1, 2 and 3 in the figure are produced from the CIS region and 1`, 2` and 3` are from the GaAs region. Their assignments are summarized in Table 4-7.

Table 4-7. Assignment of diffraction spots for the GaAs and CIS regions near the interface.

	1	2	3
GaAs	{1 1 1} family	{0 0 2} family	{2 2 0} family
CIS	{1 1 2} family	{0 0 4} family	{2 2 0} family

* Estimated 0.1 mm uncertainty.

Values of the lattice parameters were calculated from the measured distance between each spot and the transmitted beam (camera length = 137 cm, λL = 52.77 mm·Å The lattice constants are summarized in Table 4-8. The in-plane lattice constant, "a", of the CIS near the

interface is almost the same as unstrained CIS, which indicates that the film grew in the nearly relaxed state from the interface.

Table 4-8. Lattice parameters of GaAs and CIS near the interface calculated from SAD patterns at [-1 1 0] zone axis.

	Distance to the spot(mm)		Inter-planar spacing, d (Å)		Lattice parameter (Å)	
	(220)	(002) or (004)	$d_{(220)}$	$d_{(002)}$ or $d_{(004)}$	a	c
GaAs	26.4	18.70	1.999	2.822	5.654	5.644
CIS	26.0	18.2	2.030	2.899	5.742	11.60

* Estimated 0.1 mm uncertainty.

Figure 4-22 shows a bright field and a dark field image of W560 using (0 0 -4) diffracted beam. Dislocations are observed in the dark field image of the CIS region, some of which extend to the interface between CIS and GaAs, and release the strain energy that would be produced from the lattice mismatch between CIS and GaAs.

The possible inter-diffusion of Cu, In or Ga was proposed in section 1.4 from the observation of the low intensity, broad peak at slightly higher value of 2θ than the GaAs (400) peak (Figure 4-12). To probe this possibility, TEM-EDX scan was performed across the interface. A bright field image of the scan region and TEM-EDX scan are shown as in Figures 4-23 and 4-24, respectively.

(a)   (b)
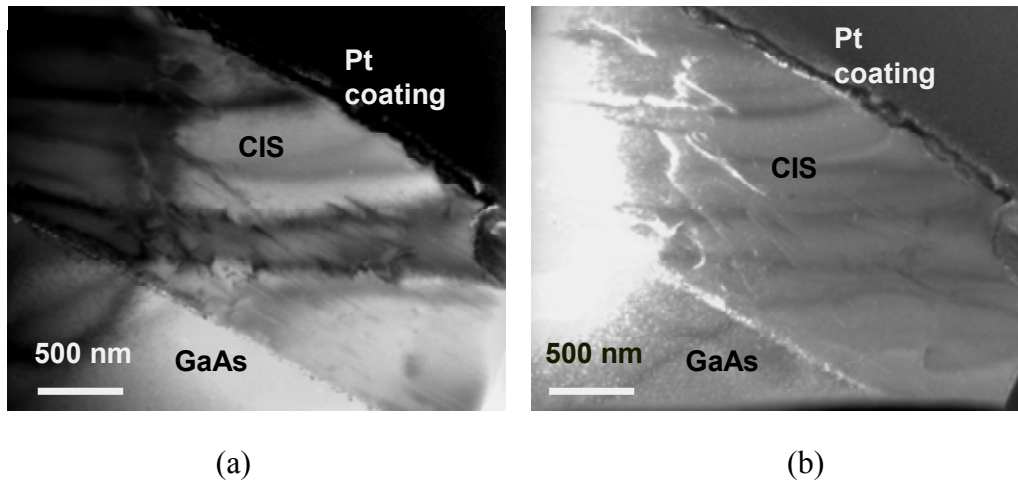
Figure 4-22. Bright field and dark field images of the In-rich, Na-free sample (W560) using g = (0 0 -4): (a) bright field image, (b) dark field image.
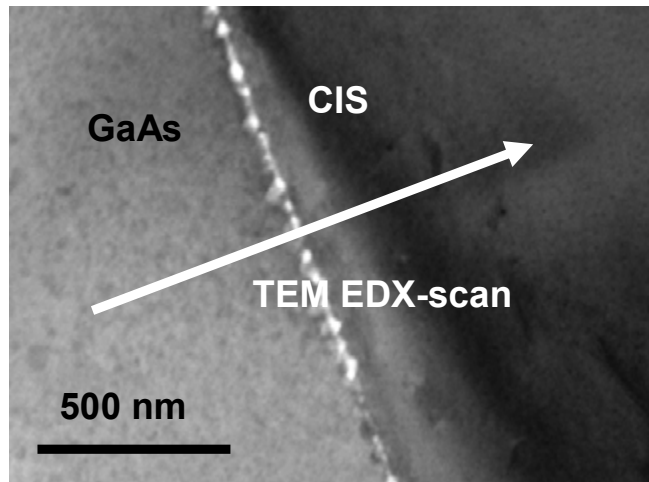
Figure 4-23. Bright field image of the TEM-EDX scan region near the GaAs/CIS interface of In-rich, Na-free sample (W560).

From the EDX scan shown in Figure 4-24, a considerable amount of Cu diffusion from the CIS film into the GaAs was observed. In Figure 4-24, the position of the interface was determined where Se signal sharply decreases to zero. It is known that Cu atom diffuses rapidly in GaAs even at low temperature by an interstitial diffusion process [4-2]. The diffusion coefficient of Cu in GaAs was reported to be as $D = 3 \times 10^{-2}$ cm^{2}s$^{-1} \times \exp(-0.53/kT)$ and 7.641×10^{-6} cm^2/s at 464 °C [4-3]. The solubility was found also to be high (5.66×10^{14}cm^{-3} at 464 °C) [4-3]. Therefore, it is proposed that the bump on the right side of GaAs (400) peak in the XRD spectra is due to Cu diffusion from CIS film to the GaAs during the growth, and the increase of the in-plane lattice constant is attributed to the formation of Cu$_i$ defects in the GaAs substrate. Additionally, the broad feature was not observed in the XRD spectra of CIS films grown at low temperature. However, there was no diffusion of other elements such as Ga or In atoms observed.
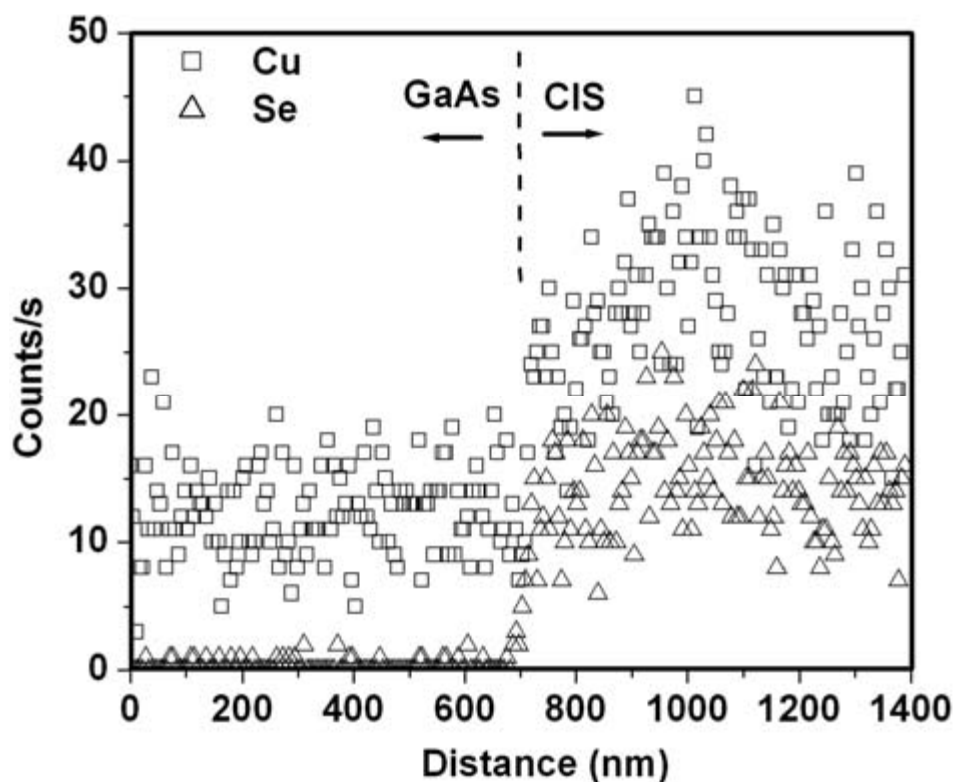
Figure 4-24. TEM-EDX scan of In-rich, Na-free CIS film (W560) near the interface.

4.5.3 TEM analysis of the Cu-rich, Na-dosed CIS film (W584)

It is recalled from the results shown in section 1.2 that the top part of the faceted island structure in the Cu-rich, Na-dosed CIS film (W584) was completely removed after KCN etching (Figure 4-8). The conclusion that the upper layer in the island facets are primarily a Cu-Se secondary phase was further supported by the EPMA results (Table 4-2). The island region of the sample was probed using TEM to independently investigate the upper and lower parts of the island region.

Figure 4-25 shows the bright field images of the island and matrix regions of this CIS film (W584). The EPMA analysis (Table 4-2) suggested that the top part of the island region has composition close to $Cu_{1.5}Se$. Figure 4-26 shows the SAD patterns for both GaAs (a) and the island bottom area (b) that is CIS in the Cu-rich CIS film with Na-dosing (W584).

(a)   (b)
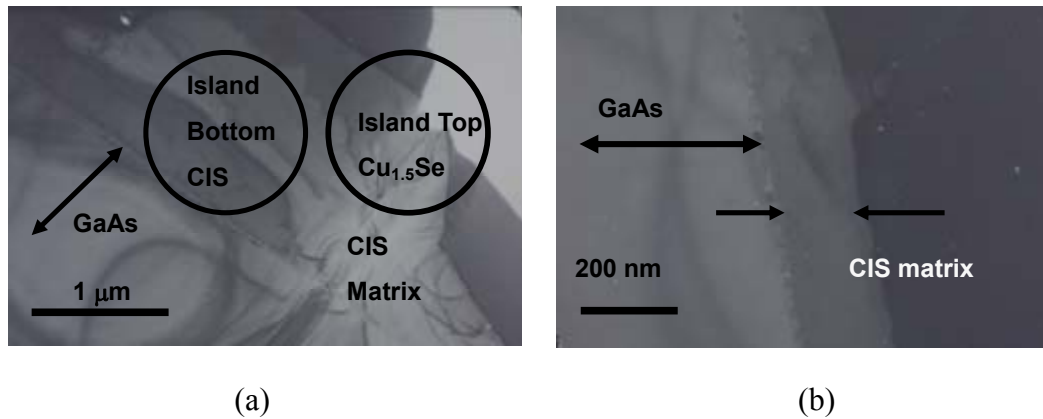
Figure 4-25. Bright field images of the Cu-rich, Na-dosed CIS film (W584): (a) island structure, (b) matrix region.

(a)   (b)
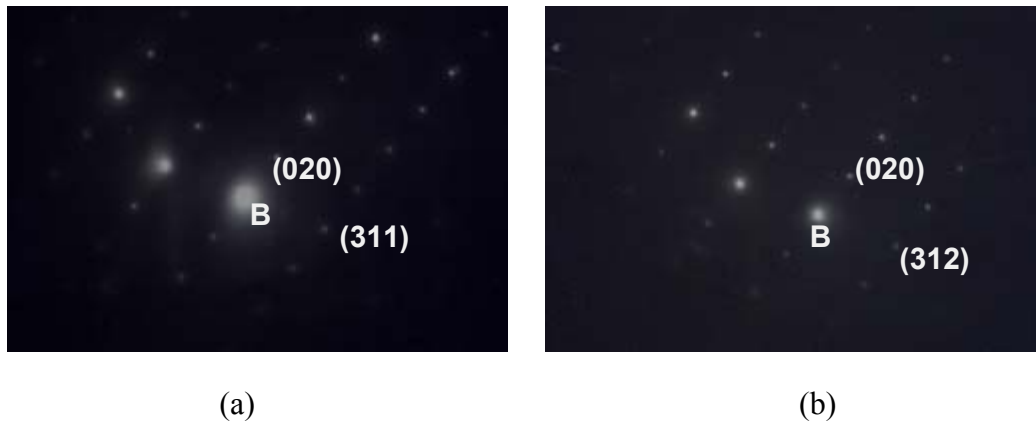
Figure 4-26. SAD pattern of GaAs and matrix regions of the In-rich, Na-dosed sample (W584) at [-1 0 3]: (a) GaAs, (b) matrix region.

As observed in Figure 4-26, the CIS film was again grown epitaxially with the same orientation as the underlying GaAs substrate. The lattice constants of the CIS film were calculated and summarized in Table 4-9. The results indicate that Cu-rich CIS, Na-dosed CIS film (W584) was again grown nearly relaxed epitaxial, regardless of Na-dosing.

Table 4-9. Lattice parameters of GaAs and CIS calculated from SADP at [-1 0 3] zone axis.

	Distance to the spot(mm)		Inter-planar spacing, d (Å)		Lattice parameter (Å)	
	(020)	(311) or (312)	$d_{(020)}$	$d_{(311)}$ or $d_{(312)}$	a	c
GaAs	7.375	12.25	2.827	1.702	5.654	5.556
CIS	7.240	18.20	2.880	1.733	5.760	11.26

* Estimated 0.1 mm uncertainty.

The double spots in the SAD pattern of the interface region are displayed in Figure 4-27., the CIS film appears to have grown in a nearly relaxed state in Figure 4-27. This is the same finding for the film grown without Na-dosing (W558 and W560).
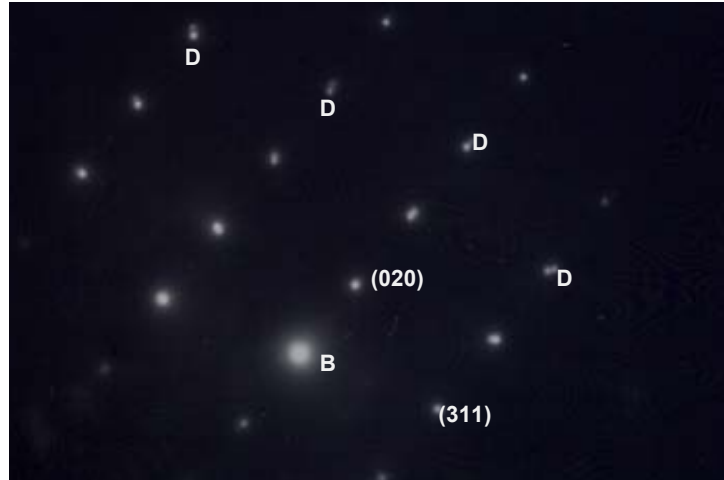
Figure 4-27 .SAD pattern of the interface between GaAs and CIS film at [-1 0 3].

The double spots denoted as D correspond to the spots from both GaAs and CIS film. Figure 4-28 shows the SAD patterns taken for the upper and lower areas in the island region. The lattice constants of each phase, presumably $Cu_{1.5}Se$ for the upper layer and CIS for the lower layer, were calculated from the spot distances measured on patterns shown in Figure 4-28. From the results shown in Table 4-10, the in-plane lattice constant of the $Cu_{1.5}Se$ phase was strained relative to the CIS phase below it.

(a)   (b)

Figure 4-28. SAD pattern of island region of the Cu-rich, Na-dosed sample (W584) at [-1 1 2] zone axis: (a) upper layer of island region ($Cu_{1.5}Se$), (b) lower area of the island region (CIS).

Table 4-10. Lattice parameters of GaAs and CIS calculated from SADP at [-1 0 3] zone axis rL = 20.65.

	Distance to the spot (mm)		Inter-planar spacing, d (Å)		Lattice parameter (Å)	
	(220)	(311) or (312)	$d_{(220)}$	$d_{(311)}$ or $d_{(312)}$	a	c
Upper layer ($Cu_{1.5}Se$)	10.10	6.150	2.045	3.358	5.784	5.882
Island bottom (CIS)	10.10	6.225	2.045	3.317	5.784	11.34

* Estimated 0.1 mm uncertainty.

To verify whether the Cu-Se phase in the top part of the island structure is a $Cu_{1.5}Se$ phase, TEM-EDX line scan was performed along the depth direction of the island structure as in Figure 4-29. As shown in Figure 4-29, it is observed that the Cu/Se ratio of the Cu-Se region in the top part of the island structure where there is no In, is close to 1.5.
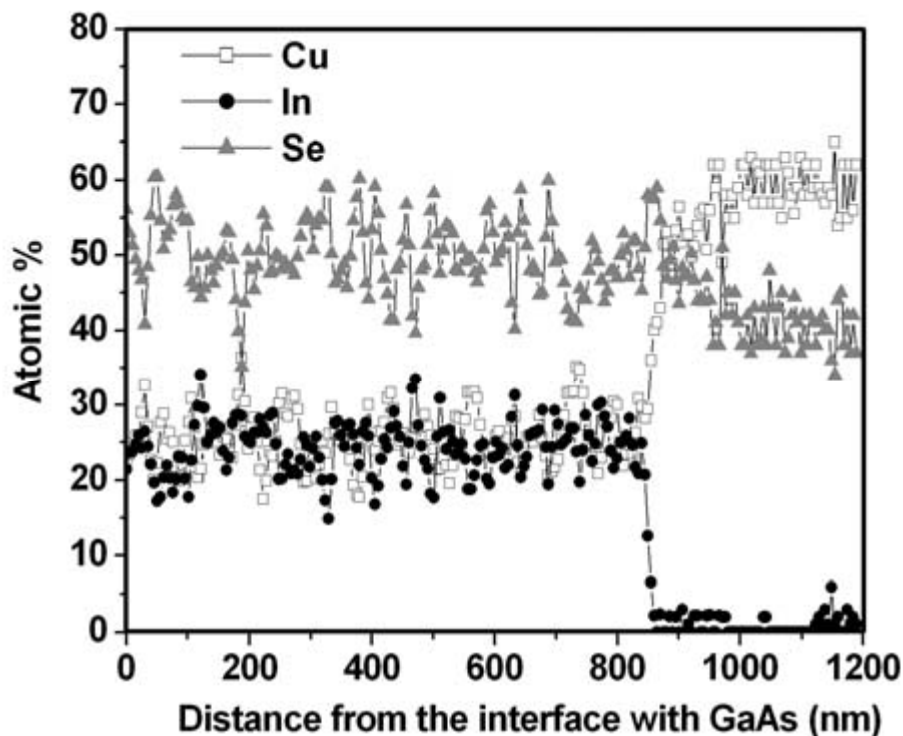
Figure 4-29. TEM-EDX line scans of W584 along the depth of the island structure.

The coexistence of $Cu_{1.5}Se$ phase with CIS in the epitaxial growth of Cu-rich CIS (Cu/In = 1.4 ~ 2.6) was reported before by Fons *et al*. [4-4]. In their work, they reported the existence of the wedge-shaped epitaxial $Cu_{1.5}Se$ phase on the surface of the epitaxial CIS grown on (001) GaAs. They calculated the lattice constant of the $Cu_{1.5}Se$ phase using XRD space map and obtained an in-plane lattice constant of 5.770 Å and an out-of plane lattice constant of 5.722 Å. They also grew epitaxial $Cu_{1.5}Se$ on (001) GaAs substrate without CIS phase and reported the in-plane lattice constant of 5.764 Å as a nearly completely relaxed lattice constant. The in-plane

lattice constant calculated here for the $Cu_{1.5}Se$ phase found in the Cu-rich CIS film with Na-dosing (W584) is, therefore, close to the value reported in their study. Also, as in their study, the in-plane lattice constant of $Cu_{1.5}Se$ was strained to that of CIS.

From the fact that the segregation of the epitaxial $Cu_{1.5}Se$ was not observed in the Cu-rich CIS film without Na-dosing (W558) with the same Cu/In ratio in section 1.5.1, it is proposed that Na dosing resulted in the segregation and the epitaxial growth of the $Cu_{1.5}Se$ phase on top of the epitaxial CIS phase in the island structure by acting as a surfactant during the growth. Also, Na-dosing was known to improve the crystal quality by suppressing the formation of the defect pairs in the film. Therefore, it is postulated that this suppression of defects in CIS film by Na might suppress the existence of Cu-Se nano-crystalline phase in the CIS region and results in the segregation of the Cu-Se phase in the form of $Cu_{1.5}Se$.

4.5.4 TEM Analysis of In-rich, Na-dosed CIS film (W590)

The final sample examined by TEM in the set was grown at the high temperature of 464 °C with In-rich composition and Na-addition. The SEM images and XRD analysis showed this sample grew island-free and nearly relaxed. The dark field images shown in Figure 4-30 were taken using the $g = (0\ 2\ 2)$ diffracted beam.
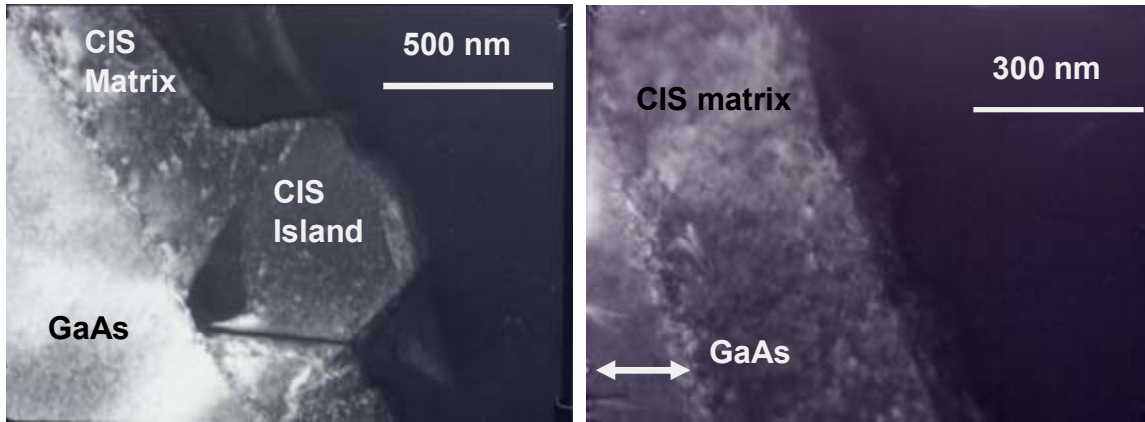
(a) (b)

Figure 4-30. Dark field images of In-rich, Na-dosed CIS film (W590): $g = (0\ 2\ 2)$: (a) Dark field image: Island (50,000X), (b) Dark field image: Matrix (100,000X).

There are a few grain boundaries observed in the island region, which may be the result of the formation of twins. Also, the voids and dislocations are observed at the distinctive interface between the matrix region and the GaAs substrate. The dislocations or grain boundaries from the possible twin structures in the island region are believed to release the heteroepitaxial strain in this film. The SAD patterns (Figure 4-31) were taken for the matrix and substrate region and the spots were assigned to crystal planes as in Figure 4-31.

<center>(a)   (b)</center>
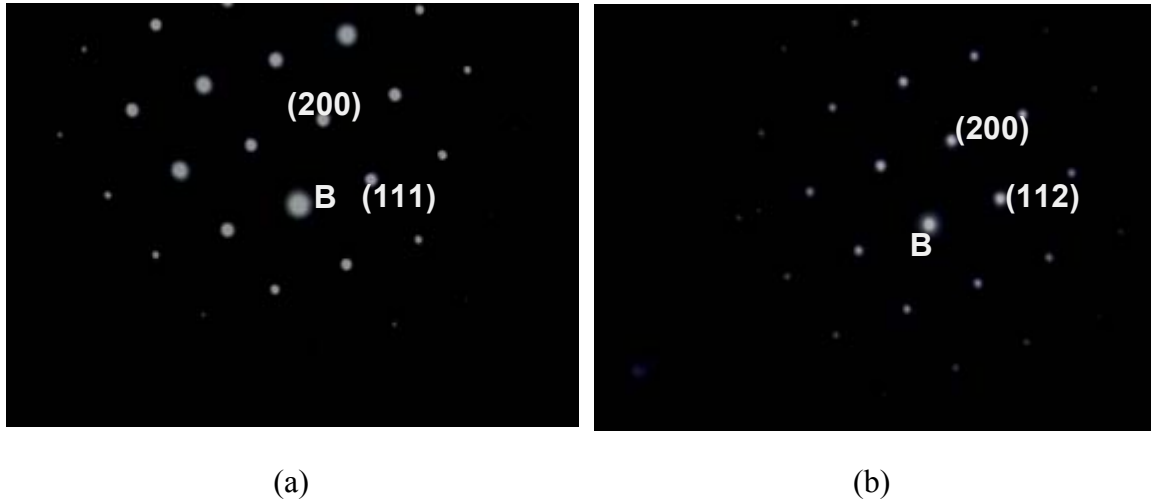
Figure 4-31. SAD pattern of GaAs and matrix regions of In-rich, Na-dosed CIS film (W590) at [0 1 -1] zone axis: (a) GaAs, (b) matrix region (CIS).

Again, the matrix region of the CIS film showed the same orientation as that of GaAs and the epitaxial growth. The lattice parameters of GaAs and the CIS region were also calculated as in Table 4-11.

Table 4-11. Lattice constants of GaAs and CIS calculated from SADP at [0 1 -1] zone.

	Distance to the spot(mm)		Inter-planar spacing, d (Å)		Lattice parameter (Å)	
	(200)	(111) or (112)	$d_{(200)}$	$d_{(111)}$ or $d_{(112)}$	a	c
GaAs	7.48	6.48	2.828	3.264	5.656	5.648
CIS matrix	7.30	6.33	2.897	3.341	5.794	11.54

<div align="right">* Estimated 0.1 mm uncertainty.</div>

The lattice parameter values of the CIS film listed in Table 4-11 show that In-rich, Na-dosed CIS film also grew epitaxially and almost completely relaxed similar to the other CIS films grown at high growth temperature. The double spots in Figure 4-32 indicate that In-rich, Na-dosed CIS film grew epitaxially and with almost no strain.
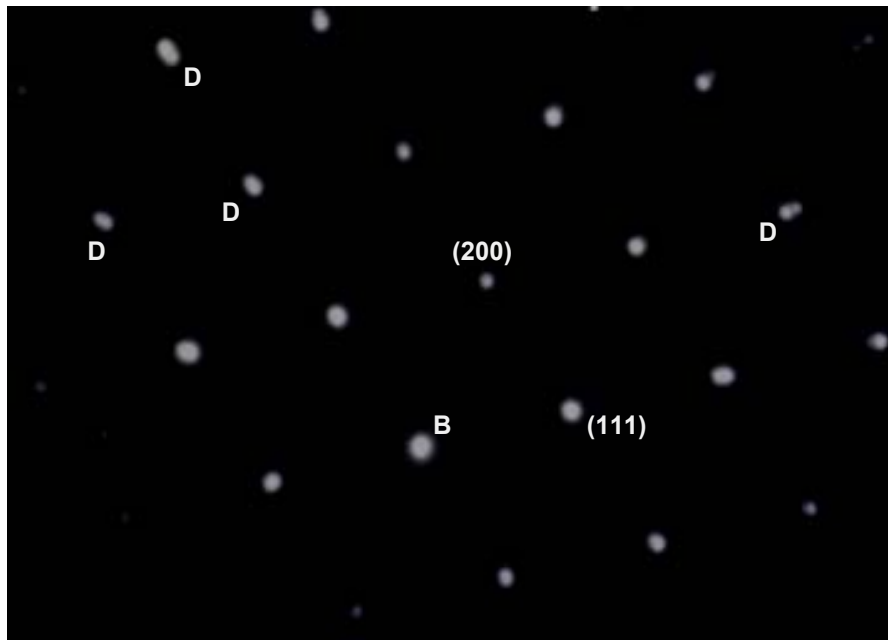
Figure 4-32. SAD pattern of In-rich, Na-dosed CIS film (W590) at the interface between GaAs and CIS film.

Diffraction spots for twins were observed in the SAD pattern of the island structure (Figure 4-33), and it is suggested that the formation of these twins is induced by the heteroepitaxial stress (lattice mismatch = 2.26%). The formation of twins in the island region leads to the epitaxial growth in this film by relieving the heteroepitaxial stress.
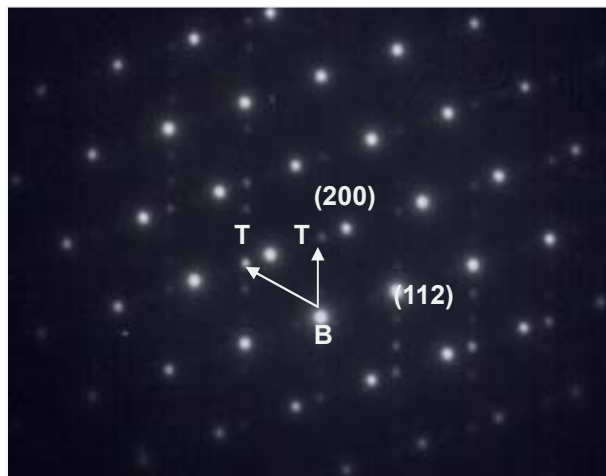
Figure 4-33. SAD pattern of island region above the matrix region of In-rich, Na-dosed CIS film (W590): 'T' means diffraction patterns from twins.

4.6   Conclusions

The Cu-rich CIS films (W558 and W584) showed morphology similar to those of Cu-rich CIS films grown at the low temperature. This morphology consists of a 2-D matrix layer with the nucleation of isolated island regions. The thickness of the matrix under the island region is greater than the island-free area. In contrast, a two-dimensional growth mode resulting a very smooth surface was observed for In-rich CIS films (W560 and W590), regardless of Na dosing. This is also in contrast to the polycrystalline structure observed for the In-rich CIS film grown at low temperature. It is suggested that the surface mobility of adatoms was increased for 2-D epitaxial growth at a high growth temperature. The assistance of Cu-Se secondary phase appears not necessary for the epitaxial growth at this high growth temperature.

The In-rich CIS films (W560, W590) showed very few island structure (100 cm^{-2}), while Cu-rich CIS films (W558, W584) showed highly faceted island structures, which increased their size slightly with Na dosing (from 10 ~ 15 μm to 15 ~ 20 μm). However, the spacing between island structures was nearly the same for Cu-rich CIS films regardless of Na-dosing. XRD θ−2θ scans indicated that all CIS films were grown heteroepitaxially. XRD space maps also indicate that all CIS films grew in a nearly fully relaxed state, which also occurred at the lower growth temperature (Chapter 2).

From the TEM-EDX line scan for the cross-section of In-rich CIS film without Na-dosing (W560), it is observed that there is a considerable Cu-diffusion from the film to the substrate, which is possibly due to the higher growth temperature and possibly attributed to the sequential deposition process of the PMEE reactor allowing longer migration step for the adatoms. It is proposed that this Cu diffusion formed a thin buffer layer with a larger in-plane lattice parameter in the GaAs substrate near the interface region. It is also suggested that the feature of slightly higher value of 2θ than the GaAs (400) peak in the XRD spectra is due to the decrease of c-axis lattice constant (higher 2θ value or lower d_{004}) as well as the increase of in-plane lattice constant in that layer. It is postulated that this buffer layer with increased in-plane lattice constant partly relieved the heteroepitaxial stress between CIS film and the GaAs substrate and enabled CIS films to grow epitaxially without strain along with the strain relieving process by dislocations.

The difference of the growth process between Cu-rich and In-rich CIS films is postulated as follows. As the liquidus of $Cu_{2-x}Se$ was suggested as 525 °C in Fon's *et al.*'s work [4-4], it is possible that the Cu-Se secondary phase in the Cu-rich CIS films at the higher growth temperature of 464 °C exist as a liquid-like state during the growth. As the surface mobility is enough at this temperature without the assistance of the Cu-Se secondary phase, the adatoms form a 2-D layer from the initial stage of the growth with a buffer layer and resulting smaller lattice mismatch at the interface. For In-rich CIS films, part of the heteroepitaxial strain that is not relieved by the formation of the buffer layer is suggested to be relieved by the formation of dislocations at the interface as the film continues to grow with the same growth rate for the entire 2-D layer region. However, for Cu-rich CIS films, the Cu-Se phase is segregated at some of sites where the dislocation is concentrated, and then results in the faster growth rate by even lowering the surface energy with a surfactant effect at the sites, and the formation of the thicker island regions over the sites.

The formation of the epitaxial $Cu_{1.5}Se$ phase at the top part of island structure was observed for the Cu-rich CIS film with Na dosing (W584). It is postulated that the Na results in the segregation of the epitaxial $Cu_{1.5}Se$ phase in the top part of the island region by suppressing the formation of the defects, and the existence of the Cu-Se phase as a nano-crystalline phase in the CIS film. This segregation was not observed for the Cu-rich CIS film without Na-dosing (W558) with the same Cu/In ratio.

The SAD patterns taken at the interface of CIS film and GaAs substrate showed double spots for all CIS films. It confirms that all CIS films grew with relaxed state with in-plane lattice constant close to the original value. Twins were also observed in the island region of the Cu-rich CIS film without Na-dosing (W558) and the island region of the In-rich CIS film with Na-dosing (W590) by TEM-SADP. It is proposed that the heteroepitaxial stress due to the lattice mismatch leads to the formation of those twins in the island region. The composition of the Cu-Se phase observed in the island region of Cu-rich CIS film with Na-dosing (W584) was confirmed as $Cu_{1.5}Se$ by TEM-EDX line scan of the island structure. It is also identified as epitaxial to the CIS film in the island structure. The in-plane lattice constant of this $Cu_{1.5}Se$ phase was calculated from the TEM-SADP analysis and its value, 5.784 Å was close to that of CIS (5.784 Å).

4.7 References cited

[4-1] D.W. Niles, K. Ramanathan, F. Hasoon, R. Noufi, B.J. Tielsch, and J.E. Fulghum, *J. Vac. Sci. Technol. A* **15**, 3044 (1997).

[4-2] F.C. Frank, and D. Turnball, *Phys. Rev.* **104**, 617 (1956).

[4-3] R.N. Hall, and J.H. Racette, *J. Appl. Phys.* **35**, 379 (1964).

[4-4] P. Fons, S. Niki, A. Yamada, and H. Oyanagi, *J. Appl. Phys.* **84**, 6926 (1998).

5 Study of the Defect Structure of CGS by Photoluminescence Spectroscopy

5.1 Introduction

CuGaSe$_2$ has recently received attention as a material for the top cell in a tandem structure solar cell since it has high band gap (1.73 eV at 10 K). Therefore, its defect structure determines the material's electrical properties. From the previous studies, it is known that CGS films are always grown p-type since the compensating donor state, Ga$_{Cu}$, has a much deeper energy level (130 meV) than that of the corresponding donor in CIS (25 meV). The acceptor state, V$_{Cu}$, in CGS has a similar energy level (50 ~ 60 meV) as that of CIS (40 ~ 50 meV). Also, shifting to Ga-rich compositions increases the Cu-deficiency and the resulting increase in the V$_{Cu}$, which is an acceptor. Thus the CGS top cell does not possess a natural buried junction as is thought to exist in CIGS cells. Being able to type convert CGS would be a major contribution. Therefore, it is useful to study its defect structure with varying Cu/Ga ratio and without influence from grain boundaries.

In this study, the defect structure of CGS films was investigated using the same CGS films studied in the previous chapter (Cu-rich and Ga-rich composition). In addition the effect of Na of adding Na during growth was examined to determine its impact on the defect structure of CGS, particularly on the V$_{Cu}$ or Cu$_{Ga}$ defect states. Cu and Ga-rich CGS films with and without Na-dosing were also characterized by photoluminescence (PL). Films were also analyzed by PL after annealing in Se to investigate the effect of Se concentration on the defect structure as well as the transition related to the V$_{Se}$.

5.2 Theoretical Background

Photoluminescence (PL) is a process of photon emission by the transition between two defect states in the forbidden gap or between one of the defect states and band edge (conduction band (CB) or valence band (VB)) after the photon energy is absorbed by the material. When light with photon energy higher than the band gap of the material is absorbed, electron-hole pairs are generated in the material. These electron-hole pairs are usually bound as pairs by electrostatic forces, and are called excitons. When these excitons move freely without being bound to a state in the band gap, they are called free excitons. An exciton does not contribute to the current and it can have a different energy level as it is excited and finally breaks into free electron and free hole. The peaks corresponding to these excitonic transitions are usually observed near the band edge in a PL spectrum, the exact position depending on their excitation states. The binding energy of the exciton can be calculated using the following expression for each excitation energy level n [5-1]

$$E_{ex} = \frac{m_r^* q^4}{2h^2 \varepsilon^2 n^2} \text{ , (n=1, 2, 3...),} \tag{5-1}$$

where m$_r$* is the reduced mass defined as m$_r$* = m$_e$*m$_h$*/(m$_e$* + m$_h$*) with m$_e$* and m$_h$* being the

electron and hole effective masses, respectively. ε is the dielectric constant, h is Planck's constant, and n is an integer and equal to 1 for the exciton ground state. The binding energy of the exciton can be calculated from literature data for m_e^* and m_h^* or alternatively, it can be calculated by using the following equation if the peak energies for the ground state (E_{FX1}) and the first excited state (E_{FX2}) of the free exciton were known.

$$E_{FX} = \frac{4}{3}(E_{FX1} - E_{FX2})$$ (5-2)

Sometimes, a shoulder is observed at the lower energy side of the excitonic emission peak. If the intensity of this shoulder becomes smaller, the shoulder is usually attributed to the bound exciton emission peak, and can be separated from the excitonic emission peak by measuring the PL emission with varying excitation power. In the excitation power dependent PL spectrum, both peaks show a super linear dependence of PL intensity on the excitation power, which is proof of excitonic recombination [5-2]. The emission intensity from excitonic recombination is proportional to the product of the number of electrons in CB and holes in the VB. As the photons generate electron-hole pairs, the emission intensity shows a quadratic dependence on the excitation power in principle. The number of bound excitons in thermal equilibrium with the free ones is also proportional to the square of the number of incident photons, or excitation power. As the free excitons are in thermal equilibrium with bound excitons, the temperature dependence of the integrated excitonic emission intensity from both excitons can be represented as follows,

$$N_{FE} = C_1 e^{-E_{a1}/kT} N_{BE}, \quad N_{FCP} = C_2' e^{-E_{a2}/kT} N_{FE} = C_2 e^{-(E_{a1}+E_{a2})/kT} N_{BE},$$ (5-3)

where $N_{BE}(T)$, $N_{FE}(T)$, and $N_{FCP}(T)$ are the numbers of bound excitons, free-excitons and free carriers, respectively, k is Boltzman constant, E_{a1} is the localization energy of excitons to a bound center and E_{a2} is the dissociation energy of a free exciton to a free electron-hole pair. As the total number of particles is in equilibrium, the total number of bound and free excitons and carriers is proportional to the excitation power, P_{exc}

$$N_{BE} + N_{FE} + N_{FCP} = CP_{exc},$$ (5-4)

where C is a constant. If the emissions from both bound and free excitons are observed, the integrated PL intensity, I(T), can be represented by the following equation:

$$\frac{I(T)}{CP_{exc}} = \frac{r_1 N_{BE} + r_2 N_{FE}}{N_{BE} + N_{FE} + N_{FCP}},$$ (5-5)

where r_1 and r_2 are the ratios of the collected emission through the aperture to the total emission by bound excitons or free excitons, respectively. Finally, the integrated intensity can be represented as:

$$I(T) = C_0 \frac{1 + rC_1 e^{-E_{a1}/kT}}{1 + C_1 e^{-E_{a1}/kT} + C_2 e^{-(E_{a1}+E_{a2})/kT}}$$ (5-6)

with $C_0 = r_1CP_{exc}$, $C_2 = C_1 \times C_2^{'}$, and $r = r_2/r_1$. Therefore, from parameter fitting of the experimental data, the dissociation energy of a free exciton can be obtained and compared to known values. The localization energy of the bound exciton can also be obtained, from which the activation energy of the bound center, E_{BC} can be calculated by using Hayne's rule [5-3], $E_{a2} = CE_{BC}$ with $C \sim 0.1$.

There are usually other peaks present in a PL spectrum, which are often related to the donor-acceptor (D-A) pair transition. They usually exist within 200 meV from the band edge for CIS or CGS. The peak energy of this transition is given by the following expression [5-4].

$$E = E_g - (E_a + E_d) + \frac{e^2}{4\pi\varepsilon_r\varepsilon_0 r} + f(r) \qquad (5\text{-}7)$$

In this equation, E_g is a band gap, E_a is the acceptor state energy level, E_d is the donor state energy level, ε_r is the dielectric constant of the material, ε_0 is the dielectric constant of the vacuum, r is the separation of the donor-acceptor pair involved in the transition. The last term, $f(r)$ is a quantum mechanical correction, which can be neglected if r is large compared to the radii of the acceptor and donor states. If the radii of those states overlap, the position of the emission energy increases by quantum mechanical repulsion, which can be calculated from solution of the stationary Schrödinger equation for those states. The D-A related transition shows a peak shift to higher energy (blue shift) with increasing excitation power as the average distance between the D-A pair decreases with excitation power.

The ionization energies of the states involved in a D-A pair transition can be estimated by the temperature dependent PL measurement [5-2, 5-5] as follows. First, the efficiency of the donor-acceptor recombination for the donor state is represented by

$$\eta_{DA}^{j} = \frac{P_{DA}^{j}}{P_{Dh}^{j} + P_{DA}^{j} + P_{DO}^{j} + P_{TD}^{j}}, \qquad (5\text{-}8)$$

where each term represents recombination with valence band holes with probability of occurrence P_{Dh}^j, the recombination with holes at the acceptor states with probability P_{DA}^j, recombination by other processes with probability P_{DO}^j, and thermal ionization to the conduction band with probability P_{TD}^j, respectively. Also, the efficiency of donor-acceptor recombination for the acceptor state, is given by

$$\eta_{AD}^{j} = \frac{P_{AD}^{j}}{P_{eA}^{j} + P_{AD}^{j} + P_{AO}^{j} + P_{TA}^{j}} \qquad (5\text{-}9)$$

with P_{eA}^j representing the transition probability with electrons at the conduction band, P_{AD}^j the probability of donor-acceptor recombination with electrons at donor state, P_{AO}^j the probability of other processes and P_{TA}^j the probability of thermal ionization to the valence band edge. The overall efficiency of the donor-acceptor recombination is given by the product of equations (5-8) and (5-9),

$$\eta_{DA}^{j}\eta_{AD}^{j} = \frac{P_{DA}^{j}}{P_{Dh}^{j} + P_{DA}^{j} + P_{DO}^{j} + P_{TD}^{j}} \frac{P_{AD}^{j}}{P_{eA}^{j} + P_{AD}^{j} + P_{AO}^{j} + P_{TA}^{j}} \tag{5-10}$$

The integrated intensity of the emission related to the donor-acceptor recombination is given by,

$$I = \eta_{DA}^{j} A \ , \tag{5-11}$$

where A is a constant. As the thermal transition probabilities P_{TA}^{j} and P_{TD}^{j} are given by an exponential function of ionization energy, they can be represented as,

$$P_{TA}^{j} = B_{A} \exp(-E_{A}/kT) \ , \tag{5-12}$$

where E_A and E_D are the ionization energies of the acceptor and donor states, respectively. As only P_{TA}^{j} and P_{TD}^{j} are functions of temperature and all recombination probabilities are independent of temperature, equation (5-11) can be written as follows:

$$I = \frac{C_3}{[1 + C_4 \exp(-E_D/kT)][1 + C_5 \exp(-E_A/kT)]} \ , \tag{5-13}$$

where all recombination probabilities are shown as constants. Therefore, the ionization energies of the donor and acceptor states can be estimated by parameter fitting of the measured integrated emission intensity of the related peak using equation (5-13).

5.3 Experimental Approach

Samples prepared in the MEE reactor were characterized by PL using the facilities at Yungnam University at Kyongsan, Korea. The system is a commercial unit (SPEX750M). The PL measurements were carried out using the 514 nm line of an Ar-ion laser with a beam diameter of ~100 μm and an excitation power of 2 mW. PL spectra were first obtained at 10 K to probe possible excitonic emissions near the band edge as well as any donor-acceptor transitions. The sample temperature was varied from 10 to 300 K and the temperature-dependent PL intensities measured to allow calculation of the activation energies of defect states involved in a particular transition. In addition to characterizing the defect structure of films grown in the MEE reactor, the effect of subsequent annealing in a Se overpressure was performed to better understand the atomic origin of the defect. These PL measurements were performed on samples annealed by placing a solid Se source in the chamber with the as-grown films at 300 °C for 30 min. PL measurements were not performed for CIS films since a photomultiplier tube was the only available detector and thus suitable for the higher band gap energy films.

The CGS samples studied were grown by MEE. The samples were selected to study the effect of Na-dosing on the point defects in CGS. Two CGS films were grown with Cu-rich (Cu/Ga = 1.19, W552) and Ga-rich (Cu/Ga = 0.96, W567) compositions. For the study of the Na effect on the defect structure, Na was incorporated into each film during growth using a Knudsen cell delivering NaF.

5.4   PL Measurements of Epitaxial CGS Films

5.4.1   PL Spectra

PL measurements were performed on the as-grown CGS films and CGS films after Se annealing at 10 K and the resulting spectra are shown in Figures 5-1 through 5-8. All spectra show a distinctive peak near 1.5 eV (between 1.498 and 1.508 eV). This peak is assigned to the transition of excitons bound to copper centers with trigonal symmetry in Cu-doped GaAs by Wang *et al.* [5-6] and they suggested that the $Cu_{Ga} - V_{As}$ defect pair is responsible for this center. Therefore, this observation confirms the diffusion of Cu atoms into the GaAs substrate in all CGS films, and supports the hypothesis proposed in Chapter 4 that a diffusion layer forms within the GaAs substrate.

Figure 5-1. PL spectrum of Cu-rich, Na-free CGS film (W552) at 10 K.

Figure 5-2. PL spectrum of Ga-rich, Na-free CGS film (W567) at 10 K.

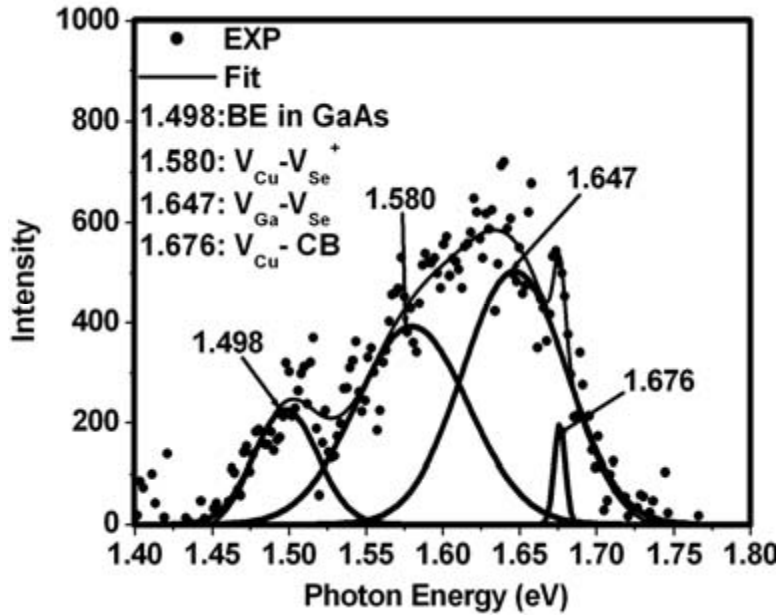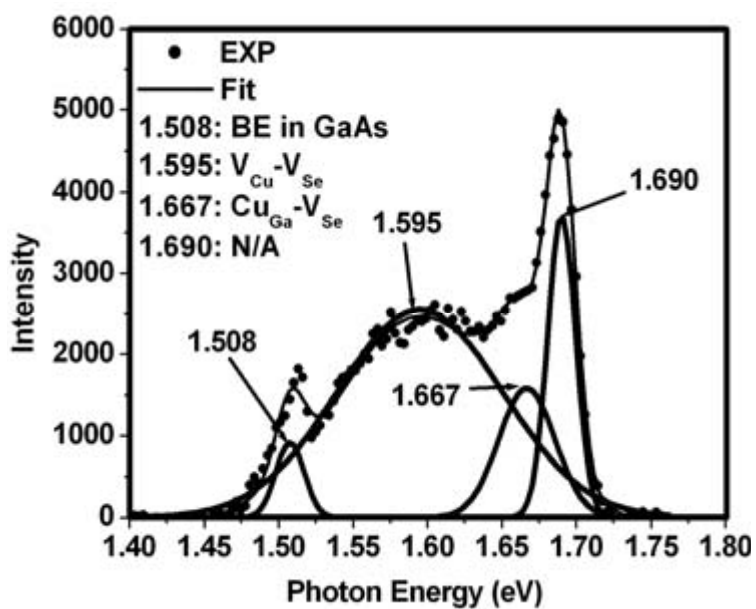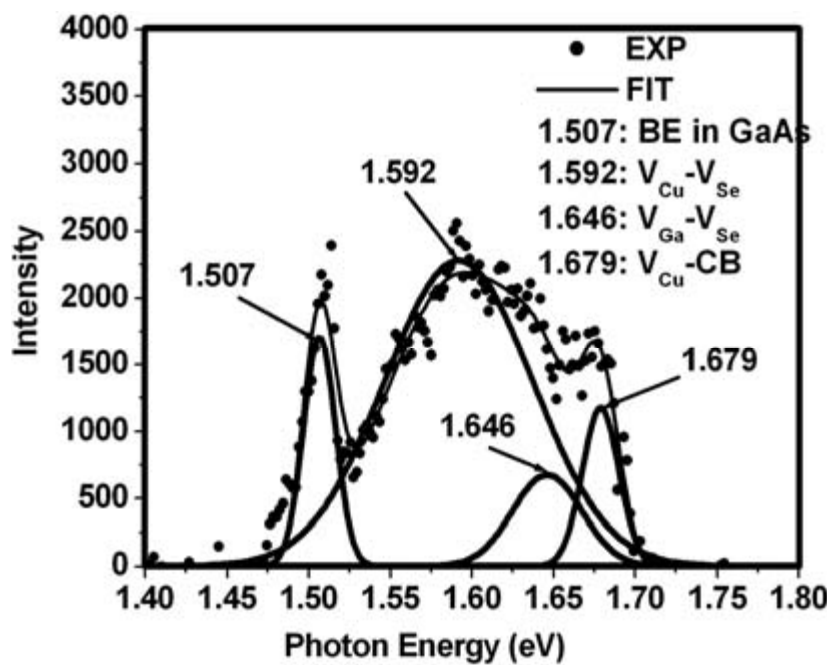Figure 5-3. PL spectrum of Cu-rich, Na-doped CGS film (W583) at 10 K.
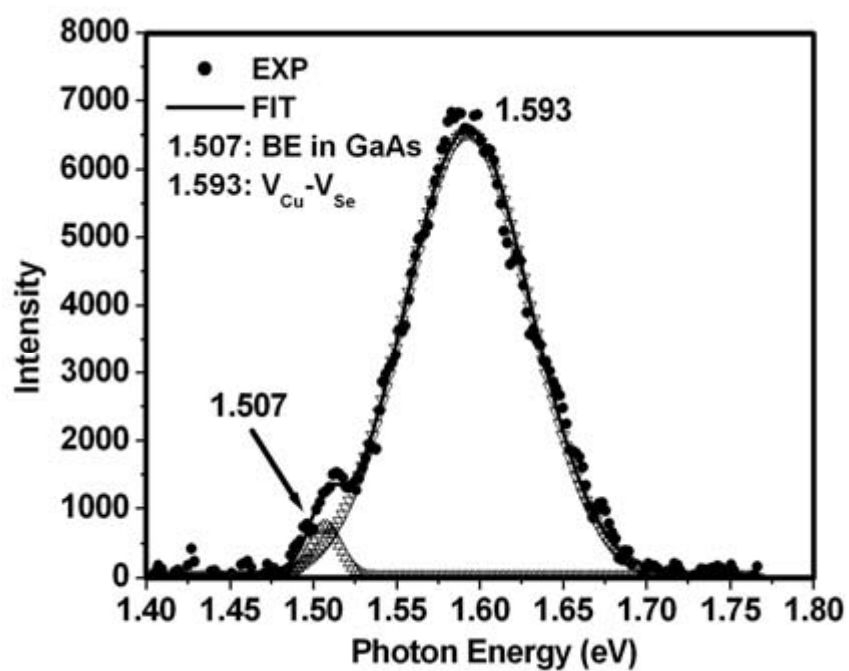
Figure 5-4. PL spectrum of Ga-rich, Na-doped CGS film (W599) at 10 K.
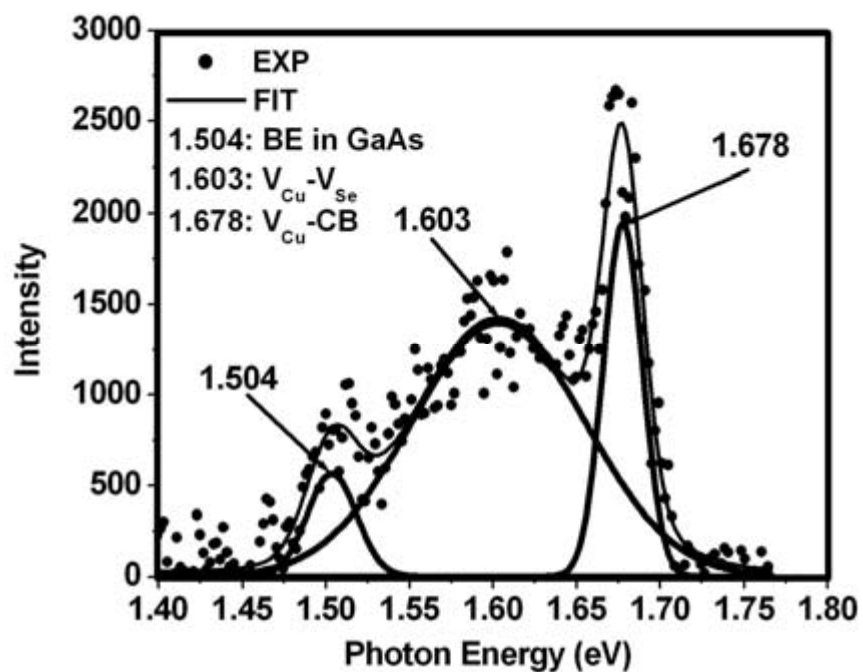
Figure 5-5. PL spectrum at 10 K of Cu-rich, Na-free CGS film (S552) after Se annealing.
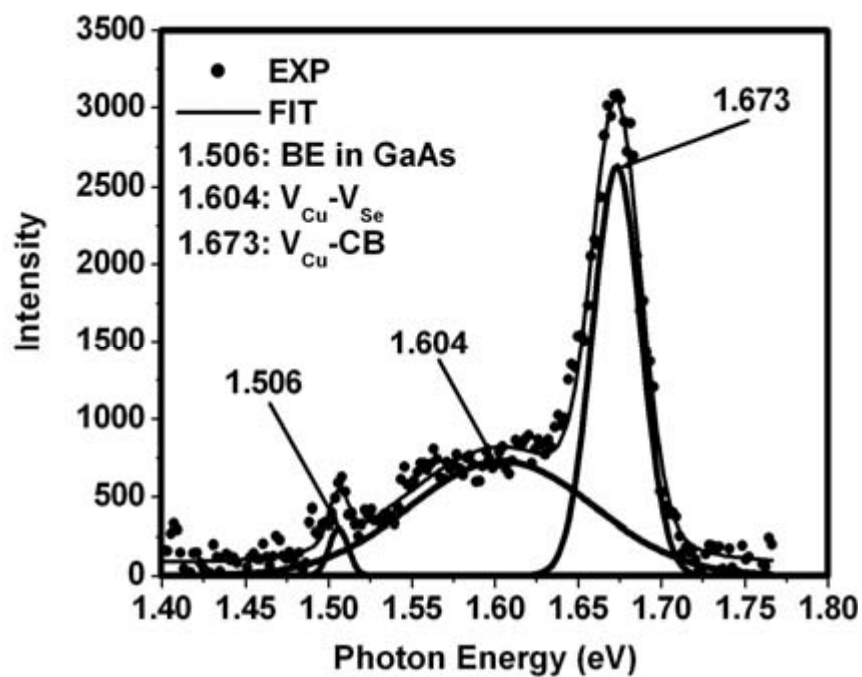
Figure 5-6. PL spectrum at 10 K of Ga-rich, Na-free CGS film (S567) after Se annealing.
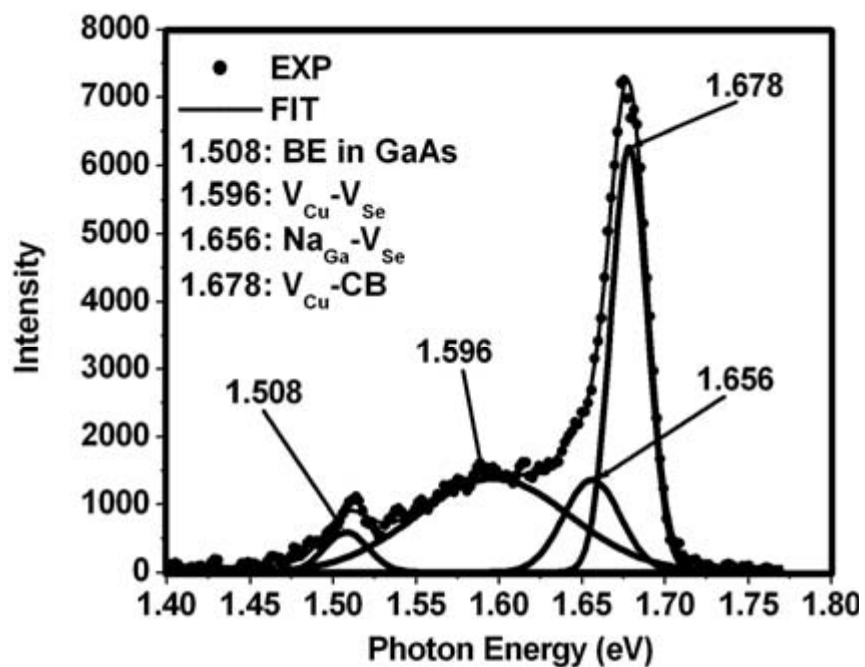
Figure 5-7. PL spectrum at 10 K of Cu-rich, Na-dosed CGS film (S583) after Se annealing.
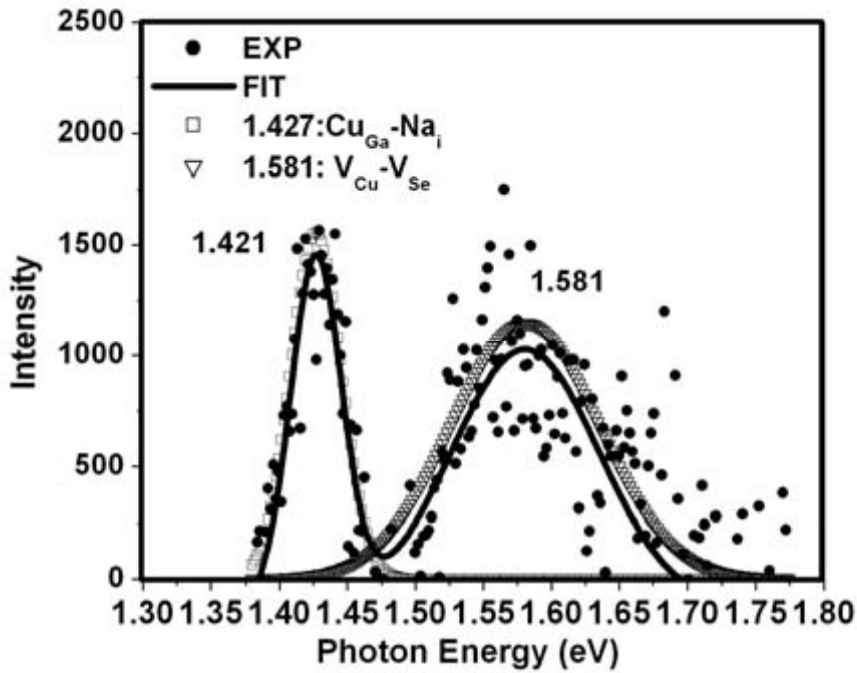
Figure 5-8. PL spectrum at 10 K of Ga-rich, Na-doped CGS (S599) after Se annealing.

The peak position in the range 1.673 and 1.679 eV in each PL spectrum, except in the Ga-rich, Na-free CGS film (W567) spectrum, is assigned to the conduction band to acceptor state transition based on previous studies [5-7, 5-8, 5-9]. From this previous work as well as the peak energy difference (51 ~ 57 meV) from the band edge (1.730 eV at 10 K), the acceptor state involved in this transition is assigned to V_{Cu} acceptor state. It is also observed that the peak at 1.646 or 1.647 eV in the PL spectra of the Cu-rich CGS films (both Na-dosed and Na-free) disappeared after Se annealing (compare Figures 5-1, 5-3, 5-5, and 5-7), which strongly suggests the assignment of this peak to a V_{Se}-related transition.

The peak located at 1.667 eV in the PL spectrum of Ga-rich, Na-free CGS film, W567 (Figure 5-2) also disappeared after Se-annealing. Therefore, it is also assigned to a V_{Se}-related transition. The peak positioned at 1.690 eV in the PL spectrum of the Ga-rich, Na-free CGS film (W567) appears to be related to an excitonic transition. It is not assigned to this specific transition since there is no transition with the corresponding energy difference. For the Ga-rich, Na-dosed CGS film (W599), the PL spectrum (Figure 5-4) included a peak at 1.593 eV, which is assigned to the V_{Cu}-V_{Se} D-A transition as previously suggested in the literature [5-5, 5-8]. The fact that the ratio of this peak to the peak at 1.676 eV assigned to V_{Cu} – CB transition decreases after Se-annealing for all CGS films, is further evidence that this peak involves a V_{Se} – related transition.

The peak for the V_{Cu}-CB transition (at 1.676 eV) that was found in the Ga-rich Na-free CGS film (W567) and the peak at 1.690 eV were not observed in the Ga-rich, Na-dosed CGS film. The disappearances of the V_{Cu}-CB transition in the Ga-rich, Na-dosed CGS film (W599) is likely due to the decrease of V_{Cu} from the formation of Na_{Cu} with Na addition. Also, the disappearance of the exciton related peak at 1.690 eV is likely due to the poorer crystalline

quality of the Ga-rich, Na-dosed CGS film (sample W599 has the highest FWHM in the HRXRD patterns with the lowest Cu/Ga ratio of 0.81) than that of Ga-rich CGS film. Also, a new peak appears at energy of 1.421 eV in the PL spectrum when Na is added to the Ga-rich CGS film (Figure 5-8). Gislason *et al.* proposed that the PL peak at 1.41 eV observed in GaAs doped with Cu and Li atoms is related to the Cu_{Ga}-Li_i-related transition [5-10].

Figure 5-10 is a TEM-EDX line scan of the Cu-rich, Na-dosed CGS film (W583) without Se-annealing for the region shown in the micrograph in Figure 5-9. Considerable diffusion of Na into the GaAs substrate is evident in the profile shown in Figure 5-10. These profiles are consistent with the assignment of observed peak intensities to Na and Cu related defect in GaAs. It is also noted that considerable diffusion of Na and Cu into the substrate occurs when CGS is replaced by CIS for an In-rich composition and of course Na-dosing (Figures 5-11 and 5-12).
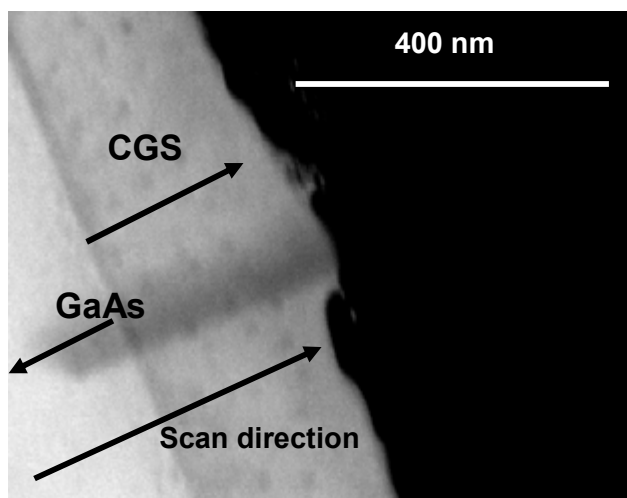
Figure 5-9. TEM-EDX line scan region of the Cu-rich, Na-dosed CGS film (W583).
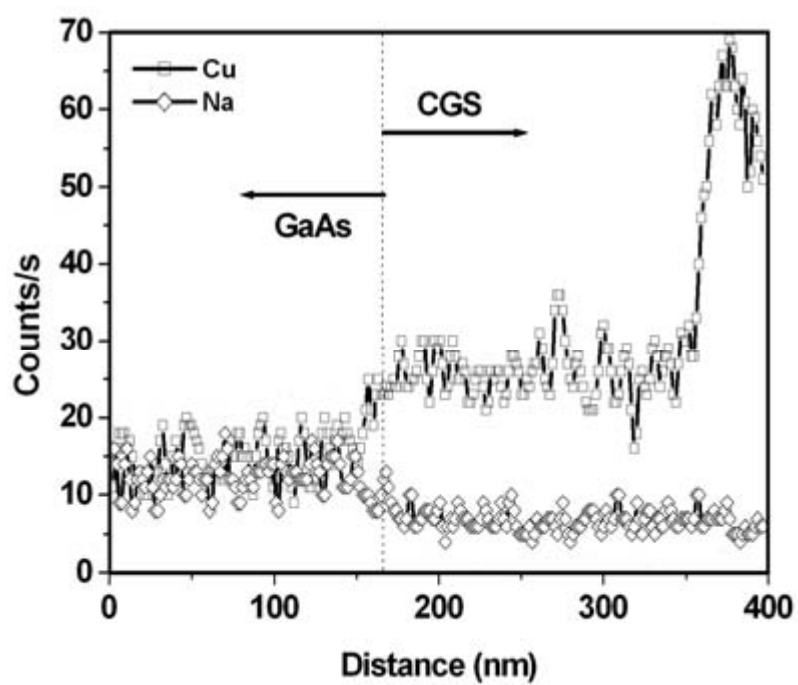
Figure 5-10. TEM-EDX line scan of Cu-rich, Na-doped CGS film (W583) before Se annealing.
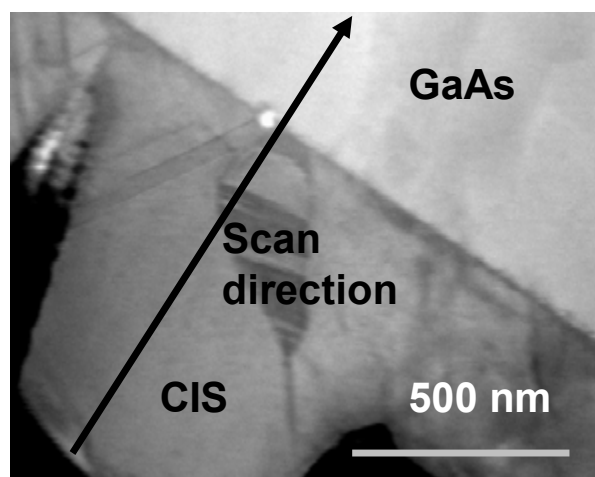
Figure 5-11. TEM-EDX line scan region of In-rich, Na-dosed CIS film (W590).
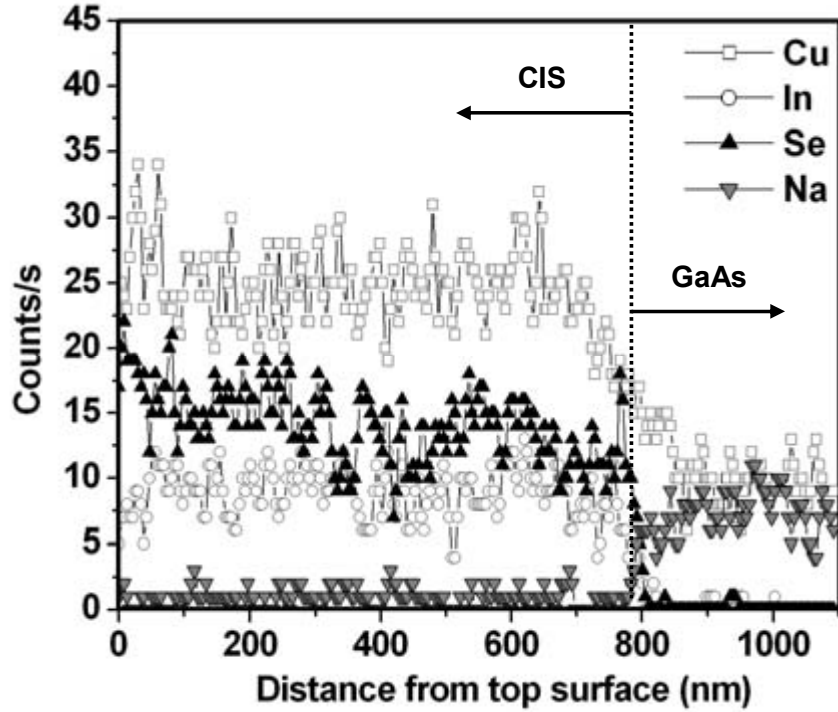
Figure 5-12. TEM-EDX line scan of In-rich, Na dosed CIS film (W590) before Se annealing.

Therefore, it is suggested that this peak at 1.41 eV is related to a Cu_{Ga}-Na_i-related transition in GaAs, which forms upon both Cu and Na diffusion during growth into the GaAs substrate from the film.

There is a new peak observed at 1.656 eV in the PL spectrum of the Cu-rich, Na-dosed CGS film after Se-annealing (S583) as indicated in Figure 5-7. This peak is believed to be related to the transition involving a Na-related defect. Assuming that V_{cu} is present in the material, even for Cu-rich conditions, the search for a transition of a defect state pair with a relatively small formation energy and defect level would include V_{Ga}-V_{Se}: 1.646 eV, V_{Cu}-CB: 1.678 eV, V_{Cu}-V_{Se}: 1.6 eV, Cu(Ga)–V_{Se}: 1.667 eV. Since these defect pairs are accounted for, a Na-related defect is the likely possibility for this peak

5.4.2 Thermal Quenching of PL Peaks

To investigate the PL peaks involving only donor-acceptor transitions, a selected transition was thermally quenched to probe the activation energy of the defect state of the shallower energy level according to the following equation [5-11]:

$$I = \frac{C_1}{(1 + C_2 \exp(-E/k_B T))} \tag{5-15}$$

96
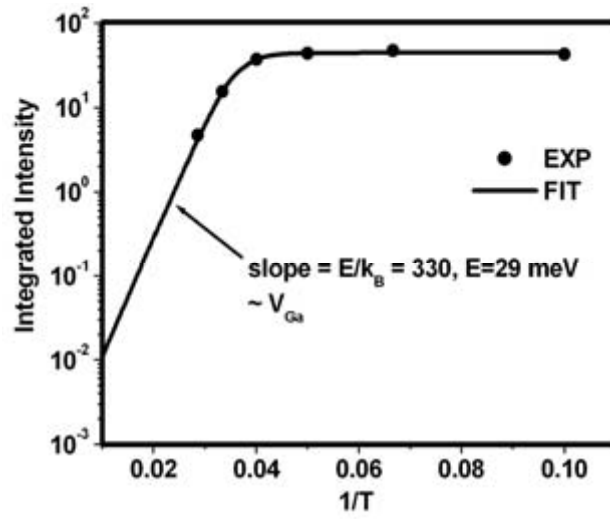
Figure 5-13. Thermal quenching of PL peak at 1.647 eV in the Cu-rich, Na-free CGS film (W552).
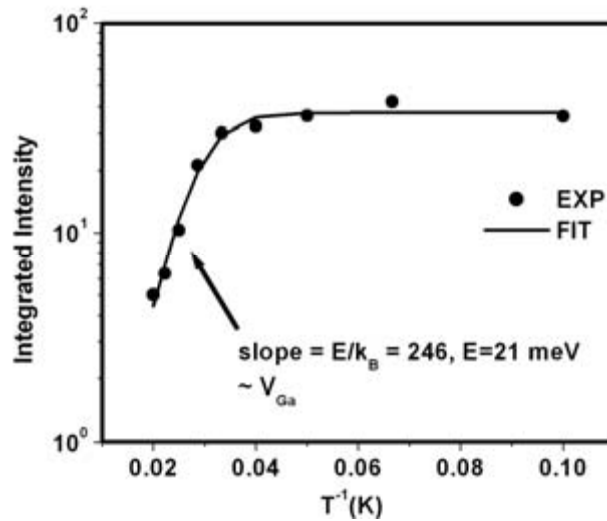
Figure 5-14. Thermal quenching of PL peak at 1.646 eV from Cu-rich, Na-dosed CGS film (W583).
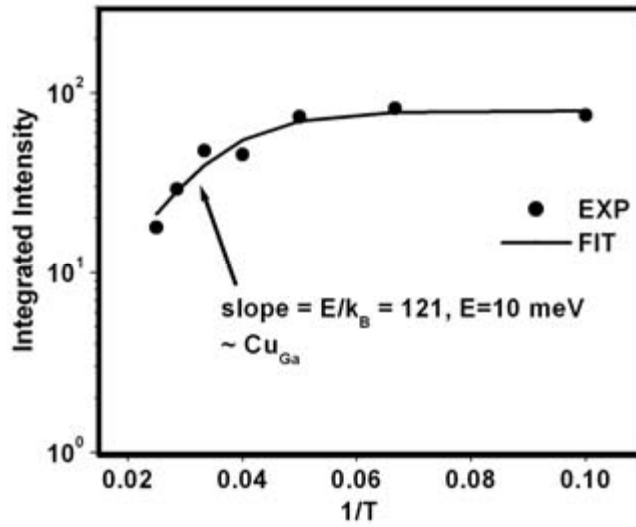
Figure 5-15. Thermal quenching of PL peak at 1.667 eV from Ga-rich, Na-free CGS film (W567).
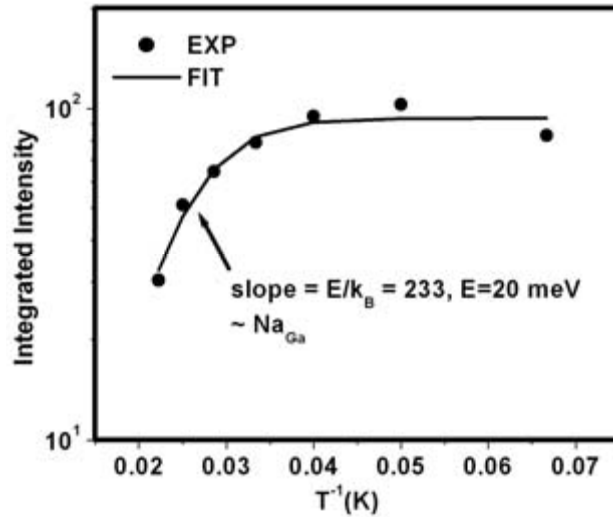
Figure 5-16. Thermal quenching of PL peak at 1.656 eV from Cu-rich, Na-dosed CGS film after Se annealing (S583).

In equation (5-15), I is the integrated intensity, C_1 and C_2 are constants, k_B is the Boltzman constant, and E is the activation energy of the shallower defect state of the two.

The results of the thermal quenching studies are graphically shown in Figures 5-13 to 5-16. Several conclusions can be drawn from these results. First, analysis of the thermal quenching data for the peak at 1.647 eV found in the Cu-rich, Na-free CGS films (W552, W583) shown in Figures 5-13 and 5-14 produces slopes of (29±2.1) and (21±1.4) meV, respectively. These energy levels are likely related to the V_{Ga} defect state, since they are close to the value (20 meV)

reported in a previous study [5-12]. Therefore, the peak at 1.647 eV is assigned to the V_{Ga}-V_{Se} transition. An activation energy of (10±0.34) meV was derived from the thermal quenching data of the PL peak at 1.667 eV (see Figure 5-15). From the fact that this peak disappeared after Se annealing and the value of the activation energy (10 meV) reported for the Cu_{Ga} defect by Bauknecht *et al.* [5-13], this transition is assigned to the Cu_{Ga}-V_{Se} transition.

The spectrum shown in Figure 5-7 reveals a new peak at 1.656 eV for the Cu-rich, Na-dosed CGS film after Se-annealing (S583) The activation energy of this transition was calculated as (20±0.78) meV (Figure 5-14), and it was tentatively assigned to the Na_{Ga} acceptor state. It is also suggested that this peak is related to the Na_{Ga}–V_{Se} transition, and this conclusion is based on the following rationale. First, the activation energies estimated for the V_{Ga} defect from the data shown Figures 5-13 and 5-14, are 29 and 21 meV. In addition, the reported activation energy of the defect level of V_{Se} is 80 meV [5-8]. From these energy levels, the Coulombic term in equation (5-7) for the peak at 1.647 eV is estimated as 18 and 26 meV, respectively. This value shows good agreement with Coulombic energy of 26 meV in the report of Bauknecht *et al.* [5-13] with an estimated typical distance between the two charged defects of 4 nm. Using these values to approximate the Coulombic energy of the defect complex responsible for the peak at 1.656 eV, the donor state involved in this transition is suggested to be a V_{Se} since the activation energy for the donor state is calculated as 72 ~ 80 meV. The peak energies observed for each sample in this study and their assignments are summarized in Tables 5-1 and 5-2.

Table 5-1. Peak energies and their assignments observed in CGS films in this study.

Peak Energy (eV)	Cu-rich	Ga-rich	Cu-rich, Na-dosed	Ga-rich, Na-dosed
1.427				
1.500	$Cu_{Ga} - V_{As}$	$Cu_{Ga} - V_{As}$	$Cu_{Ga} - V_{As}$	$Cu_{Ga} - V_{As}$
1.580	$V_{Cu} - V_{Se}^+$			
1.600		$V_{Cu} - V_{Se}$	$V_{Cu} - V_{Se}$	$V_{Cu} - V_{Se}$
1.647	$V_{Ga} - V_{Se}$		$V_{Ga} - V_{Se}$	
1.656				
1.667		$Cu_{Ga} - V_{Se}$		
1.676	$V_{Cu} - CB$		$V_{Cu} - CB$	

Table 5-2. Peak energies and their assignments observed in CGS films after Se annealing in this study.

Peak Energy (eV)	Cu-rich	Ga-rich	Cu-rich, Na-dosed	Ga-rich, Na-dosed
1.427				$Cu_{Ga} - Na_i$
1.500	$Cu_{Ga} - V_{As}$	$Cu_{Ga} - V_{As}$	$Cu_{Ga} - V_{As}$	
1.580				$V_{Cu} - V_{Se}^+$
1.600	$V_{Cu} - V_{Se}$	$V_{Cu} - V_{Se}$	$V_{Cu} - V_{Se}$	
1.647				
1.656			$Na_{Ga} - V_{Se}$	
1.667				
1.676	$V_{Cu} - CB$	$V_{Cu} - CB$	$V_{Cu} - CB$	

5.5 Conclusions

The point defects of CGS films grown by MEE on GaAs were characterized by low temperature PL spectroscopy. In particular, the effects of the Cu/Ga ratio, Na dosing, and subsequent Se-annealing on the defect states were investigated. Peak assignments to specific defects were suggested by comparing the spectra to previously reported results, observing changes in the spectra as the film composition was changed, and estimating activation energies estimated from the results of thermal quenching experiments. This work supports the findings of previous studies of the defects V_{Cu}, V_{Ga}, Cu_{Ga}, and V_{Se} with corresponding activation energies of $50 \sim 60$, $20 \sim 30$, 10, and $75 \sim 80$ meV. In addition, a new defect state was observed at 20 meV above the valence band edge from the thermal quenching of the peak at 1.656 eV in the Cu-rich, Na-dosed CGS film after Se annealing. For the Ga-rich, Na-dosed CGS film, a new PL peak was observed at 1.427 eV in the PL spectrum after Se annealing and assigned to the transition from the exciton bound to the $Cu_{Ga} - Na_i$ defect pair.

Composition profiles across the CGS/GaAs interface (TEM_EDX) showed substantial diffusion of Cu into the GaAs as well as Na when added to the film. A peak near 1.5 eV was observed in all CGS films. Consistent with previous studies on GaAs, this peak was assigned to the transition from the excitons bound to the $Cu_{Ga} - V_{As}$ defect pair, consistent with diffusion of Cu into the GaAs substrate in all CGS films. The diffusion of Na and Cu into the GaAs substrate was observed by TEM-EDX line scan of In-rich, Na-dosed CIS film (W590). From this observation and the report of the Cu_{Ga}-Li_i-related transition peak in the GaAs doped with Na and Cu, it is proposed that the peak at 1.421 eV observed in the PL spectrum of Ga-rich, Na-dosed CGS film after Se annealing (S599) is related to the Cu_{Ga}-Na_i-related transition.

A peak at 1.67 eV was assigned to the V_{Cu}-CB transition by comparison of the energy difference from the band edge with the values reported in the previous studies. Activation energy in the range 21 to 29 meV was estimated for the peak at 1.647 eV from the thermal quenching experiments, and it was assigned to the activation energy of the V_{Ga} defect, again from comparison with the value in previous studies. From the disappearance of the peak at 1.647 eV after Se-annealing, this peak was assigned to the V_{Ga}-V_{Se} transition.

An activation energy of 10 meV was calculated from the thermal quenching studies as the energy level for a defect state involved in the transition responsible for the 1.667 eV peak in the PL spectrum of Ga-rich, Na-free CGS film. This energy level was assigned to the Cu_{Ga} defect state from the comparison with the results of previous studies and the peak was assigned to the Cu_{Ga}-V_{Se} transition since it also disappeared after Se-annealing.

Another new defect state at 20 meV above the valence band was observed from the thermal quenching of the peak at 1.656 eV in the PL spectrum of the Cu-rich, Na-dosed CGS film after Se-annealing (S583). This energy level was tentatively assigned to the Na_{Ga} acceptor state, and this peak was assigned to the V_{Se}-Na_{Ga} transition from considerations of the activation energy and the energy difference from the band edge including estimation of Coulombic energy.

From the PL measurement results for the Cu-rich CGS films, it is concluded that the V_{Cu} is the dominant defect state, even in the Cu-rich CGS films since it has a low activation energy (50 ~ 60 meV) and the lowest formation energy (0.66 eV, first principles calculation in Table 5-3) of all defect states in CGS. It is also postulated that the disappearance of the peak from the $V_{Ga} - V_{Se}$ transition in the Cu-rich CGS films after Se annealing is a result of a decreased stability of V_{Ga} defect state due to the reduction of V_{Se} concentration for the formation of the stable defect pair.

The Ga_{Cu} defect state was not observed in all CGS films as a result of its deep energy level (130 meV) and high formation energy (3.22 eV, Table 5-4). Therefore, it is expected that Na-dosing may not increase the hole concentration of the CGS films to the extent that it does in CIS films since the concentration of the compensating donor, Ga_{Cu} in CGS films is much lower than that of In_{Cu} in CIS films. This is a result of a large difference in their activation energies (25 meV for CIS and 130 meV for CGS).

Formation of a n-type buried junction near the surface region might be achieved by the formation of a very thin layer of Cu(In,Ga)Se$_2$ with high In/Ga ratio, low Cu/(In+Ga) ratio, and with sufficient Se flux near the surface region should lead to the n-type layer from the formation of In_{Cu} shallow donor states in the layer with less V_{Ga} concentration. Of course, this will lower the band gap energy of this layer and modify the absorption process.

5.6 References cited

[5-1]   J.I. Pankove, *Optical Processes in Semiconductors* (Dover, New York, 1971), p. 12.

[5-2]   A. Yamada, Y. Makita, S. Niki, A. Obara, P. Fons and H. Shibata, *J. Appl. Phys.* **79**, 4318 (1996).

[5-3]   J.R. Haynes, *Phys. Rev. Lett.* **4**, 361 (1960).

[5-4]   H.B. Bebb and E.W. Williams, *Semiconductors and Semimetals in Transport and Optical Phenomena* (Academic Press, New York, 1972) p. 182.

[5-5]   A. Yamada, P. Fons, S. Niki, H. Shibata, A. Obara, Y. Makita and H. Oyanagi, *J. Appl. Phys.* **81**(6), 2794 (1997).

[5-6]   Z.G. Wang, H.P. Gislason and B. Monemar, *J. Appl. Phys.* **58**, 230 (1985).

[5-7]   S. Chichibu, Y. Harada, M. Uchida, T. Wakiyama and S. Matsumoto, S. Shirakata, and S. Isomura, H. Higuchi, *J. Appl. Phys.* **76**, 3009 (1994).

[5-8]   J.H. Schön, F.P. Baumgartner, E. Arushanov, H. Riazi-Nejad, C. Kloc, and E. Bucher, *J. Appl. Phys.* **79**(9), 6961 (1996).

[5-9]   J.H. Schön, and E. Bucher, *Solar Energy Materials & Solar Cells* **57**, 229 (1999).

[5-10] H.P. Gislason, Z.G. Wang, and B. Monemar, *J. Appl. Phys.*, **58** (1), 240 (1985).

[5-11] P.J. Dean, *Phys. Rev.*, **157**, 655 (1967).

[5-12] J.H. Schön, *J. Phys. D* : *Appl. Phys.* **33**, 286 (2000).

[5-13] A. Bauknecht, S. Siebentritt, A. Gerhard, W. Harneit, S. Brehme, J. Albert, S. Rushworth, and M.Ch. Lux-Steiner, *Thin Solid Films* **361-362**, 426 (2000).

6 Investigation of Deep-Level Defects in Cu(In,Ga)Se₂ Solar Cells by Deep-Level Transient Spectroscopy

6.1 Introduction

It is well known that CuInGaSe₂ (CIGS) has a large homogeneity range, and such deviation from stoichiometry in compound semiconductors is often attributed to antisite defects, vacancies, interstitials, and defect clusters in the material. It is important to understand these properties to further improve the cell efficiency and reduce the cost of solar energy. Deep level defects play an important role in determining the recombination and trapping mechanisms (and hence the minority carrier lifetimes) in a semiconductor. Deep level transient spectroscopy (DLTS) is a high frequency transient capacitance technique and is the most sensitive technique for defect detection. Zhang [6-1,6-2] has calculated the transition energy for a large number of defects in CIS. However, there are some discrepancies between his calculation and experimental observations. According to the PL measurement by Schoon [6-3], In_{Cu} should be a shallower donor than Cu_i and has transition energy about 0.2 eV below conduction band. In Zhang's calculation, the anion site defect is neglected. However, many other researches believe that V_{Se} is the shallowest donor level [6-3] with energy level of transition E_c- 0.06 eV and results in a significant lattice relaxation during the ionization process. Knowledge of the defect energies as well as their densities are important inputs to developing meaningful device models. DLTS is a standard diagnostic technique for determining the trap properties such as trap energy level, capture cross section, and trap concentration.

6.2 DLTS Principles and Experimental Procedures

Deep level defects play an important role in determining the recombination and trapping mechanisms (and hence the minority carrier lifetimes) in a semiconductor. The deep level transient spectroscopy (DLTS) is a high frequency transient capacitance technique and is the most sensitive technique for defect detection [6-4]. For a n⁺-p (CdS-CIGS) junction diode, the space charge region extends mainly into the p-region, and the local charges are due to negatively charged ionized acceptors. If a forward bias is applied, the electrons will be injected into region. Once the minority electrons are trapped in a defect level, the net negative charges in the SCR will increase. This in turn will reduce the width of SCR, and causes a positive capacitance change. Thus, the DLTS signal will have a positive peak. If holes are injected into the SCR and captured by the majority carrier traps, the DLTS signal will have a negative sign. Figure 6-1 shows the deep level filling sequence.

A boxcar integrator [6-5] uses a fast sampling technique to obtain an average of the repeated signal transients on some set time which we will call t_1. The double boxcar has the capacity to sample the signal at times, which are termed t_1 and t_2. An analog circuit is used to integrate or average the value of ΔC over the two fixed times which are called windows. Figure 6-2 shows how the rate window works in the analysis of DLTS data. The left side of the figure 6-2 indicates the response of the transient signal, it can be written as

$$\Delta C(t) = \Delta C(0)\exp(-e_n t)$$

(6-1)

If we define time constant $\tau = 1/e_n$, the above equation can be written as

$$\Delta C(t) = \Delta C(0)\exp(-t/\tau)$$

(6-2)

The right side is the resulting DLTS output signal for this fixed rate window. It is

$$\Delta C(t_2) - \Delta C(t_1) = S(\tau) = \Delta C(0)[e^{-t_2/\tau} - e^{-t_1/\tau}]$$

(6-3)

To have the maximum of $S(\tau)$, we need to have $\dfrac{dS(\tau)}{d\tau} = 0$, and this occurs at

$$\tau = \frac{t_1 - t_2}{\ln(t_1/t_2)}$$

(6-4)

Thus, the emission rate corresponding to the maximum of a trap peak observed in a DLTS thermal scan is a precisely defined quantity. If we have a series of temperature measurements using different t_1 and t_2, one can calculate the activation energy using an Arrhenius plot.

DLTS is used to measure the transient capacitance change of a junction device after deep-level traps in the space charge region have been filled with either the majority or minority carrier charges, and the trap density and energy levels of these deep level traps can be extracted from DLTS measurements. By scanning the transient capacitance over a range of temperature, the emission rate as a function of temperature can be obtained. The activation energy for an electron trap and capture cross section can be estimated from an Arrhenius plot:

$$e_n = \frac{1}{\tau} = \sigma_n v_{th} N_c \exp(-\frac{E_a}{kT})$$

(6-5)

where e_n is the electron emission rate, σ_n is the capture cross section, N_c is the electron effective density of states and v_{th} is the electron thermal velocity. The electron trap density, N_T, can be calculated by

$$N_T = \frac{2\Delta C}{C_0} N_a$$

(6-6)

Equation (6-6) is valid for $N_T < N_a$. ΔC is the height of capacitance change due to the emission of charge carriers from the trap level, which is proportional to the probed trap concentration. Carrier concentration, N_a, is determined by the C-V measurements, which give the average carrier concentration in the CIGS absorber layer. C_0 is the zero bias capacitance that is obtained from the C-T data at the corresponding DLTS peak temperature.

6.3 Results and Discussions

DLTS studies were conducted on three types of thin-film photovoltaic cells:

(i)   CIS cells (denoted "UF CIS cells" in the suite for easy reference) developed by the University of Florida using a bilayer precursor process.

(ii)   CIGS cells (denoted "EPV CIGS cells") developed by Energy Photovoltaics Inc. using a physical-vapor deposition process.

(iii)   CIGS cells (denoted "NREL CIS cell") developed by the National Renewable Energy Laboratory using a three-stage precursor process.

Details of the analysis results are discussed in detail below.

6.3.1   UF Samples from Binary Bilayer Rapid Thermal Process

The I-V curve for the UF 5% cell showed a V_{oc}= 0.296 V and fill factor = 49.54%. The J_{sc} for this cell is 34.65 mA/cm^2, which is a very good value for CIS cells. The low fill factor is largely due to the high sheet resistance. This can be improved by adjusting the Cu:In:Se composition ratio, especially Cu to In ratio and and by creating a composition gradient to achieve the bandgap grading with the incorporation of Ga. The V_{oc} is largely affected by the mid gap defects in the space charge region. To detect the defect level in this 5% cell, a Deep Level Transient Spectroscopy (DLTS) measurement was performed on this 5% cell.

Figure 6-3 shows the C-V measurements on the 5% UF cell at different temperatures. The carrier concentration is on order of 10^{15} cm^{-3}. The C-V data was measured on the same cell as that used in the DLTS measurement.

Figure 6-4 shows the measured capacitance versus temperature for the 5% UF cell, which yields the value for C_0 at the corresponding temperature of the DLTS peak. The DLTS spectra measured for this 5% sample with a reverse bias voltage, V_R =-0.5 V, a trap-filling pulse of 0.4 V, and a saturation pulse width of 10 ms are shown in Figure 4-5. The sample is maintained at reverse bias. The 5% sample shows a deep majority carrier trap (negative signal) at a temperature around 290 K. The activation energy calculated from the Arrhenius plot as shown in Figure 6-6 is 0.54 eV above valence band, which may be attributed to the Cu on In interstitial (E_{A6}) according to the diagram. The average carrier concentration at 290 K from the C-V measurements is 2×10^{15} cm^{-3}. Combing the C-T and C-V scans, N_T is determined to be 4.6×10^{12} cm^{-3}.

To detect possible minority traps, the sample was cooled down to 77 K to freeze out all the minority traps. The sample was then heated with a pulse amplitude equal to 0.7 V at the same reverse set-off voltage of -0.5 V and a saturation pulse width of 10 ms to observe the capacitance change due to the minority carrier emission. As expected, a minority carrier trap peak was observed at a lower temperature ~200 K as shown in Figure 6-7. This minority carrier trap is in addition to the majority trap that was observed. The activation energy is 0.52 eV below the conduction band as shown in Figure 6-8. A possible physical origin of this electron trap is

the actually the same as the majority trap, which is Cu on In interstitial [6-1, 2]. The trap density is estimated to be 1.3×10^{12} cm^{-3}.

Optical DLTS was also performed on this 5% sample. In optical DLTS, a laser with wavelength of 532 nm is applied with a reverse bias of 0.5 V. Only minority traps were observed in the optical DLTS spectra as shown in Figure 6-9. The activation energy calculated for E_1 is 0.16 eV shown in Figure 6-10. This trap is attributed to In on Cu site defect In_{Cu}. The activation energy for the E_2 defect at 300 K could not be estimated since the peak shift did not follow the trend; the shorter the rate window, the higher the temperature at which the peak appears. Likely, this is because the capture cross-section is a thermally activated process, and it is related to temperature by [6-4]

$$\sigma = \sigma_0 e^{-\Delta E / kT} \qquad (6-7)$$

6.3.2 EPV CIGS Sample

The EPV samples are produced by the co-deposition in a physical vapor deposition (PVD) system. The DLTS spectra measured from the EPV sample with a reverse bias voltage, $V_R = -0.1$ V, a trap-filling pulse of 0.3 V, and a saturation pulse width of 10 ms is shown in Figure 6-11. The EPV sample showed a deep majority carrier trap (negative signal) at a temperature around 270 K. The DLTS peak shifts to higher temperatures with shorter rate windows. Since the CIGS film is p-type material, the majority carrier trap is referred to as a hole trap, and the minority carrier trap as an electron trap. The activation energy calculated from the Arrhenius plot is 0.94 eV as shown in Figure 6-12, which may be attributed to the Se vacancy V_{Se}. Figure 6-13 shows the C-V data measured on the same EPV cell as that used in the DLTS measurement. The average carrier concentration at 270 K from the C-V measurements is 3×10^{15} cm^{-3}. From the C-T scan (Figure 6-14), C_0 in Eqn. (6-6) was found to be 3.01 pf, and N_T was determined to be 6.5×10^{13} cm^{-3}.

6.3.3 NREL CIGS Sample from Three Stage Process

The absorber from NREL was deposited by three stage process [6-6] in a PVD system. A solar cell 19.2% total area efficiency based on Cu(In,Ga)Se$_2$ thin film material has been produced via their three stage process. In the first stage, the precursor (In,Ga)$_2$Se$_3$ layer is formed by the coevaporation of In, Ga and Se elemental source at substrate temperature about 260°C. In the second stage, the Cu and Se are coevaporated to bring the overall composition to near Cu-rich regime (Cu/(In+Ga) ~ 0.97 – 1.08) at 560°C. Between the second stage and third stage, the substrate is under the Se flux while ramping up the temperature. During the third stage, In, Ga and Se are added with the amount one ninth of the first stage to bring the overall composition back to Cu-poor at the same substrate temperature as the second stage. Then, the film is cooled down to 350 °C by Se flux for 20 min. This process requires very precise control of the source fluxes.

A pulse amplitude equal to 0.4 V was applied to the NREL CIGS sample at a reverse set-off voltage of -0.5 V. A minority carrier trap peak was observed at a lower temperature of around

100 K as shown in Figure 6-15. The activation energy is 0.067 eV below the conduction band as shown in Figure 4-16. A possible physical origin of this electron trap is the Se vacancy (V_{Se}) [6-3]. The trap density is estimated to be 4.2×10^{13} cm^{-3}. The DLTS scan at higher temperature showed another possible positive peak, however, the activation energy for this trap could not be resolved by heating the sample above 300 K.

Therefore, it is noted that the minority traps are likely the dominant traps in the NREL sample. To detect other possible minority traps, a small forward bias (0.1 V) was applied and the sample cooled to 77 K to freeze the minority carriers. The sample was then heated with $V_R = -0.5$ V, trap-filling pulse amplitude of 0.7 V, and a saturation pulse width of 10 ms to observe the capacitance change due to the minority carrier emission. Figure 6-17 shows three minority carrier traps with the addition of a small peak around 250 K, which was not apparent in the DLTS spectra of the 0.4 V pulse amplitude. The Arrhenius plot in Figure 6-18 showed that the activation energy for the trap at 80 K is 0.14 eV. The trap density is estimated to be 2.54×10^{13} cm^{-3}. The electron trap observed at 80 K is possibly related to a vacancy on a Se site, which might be the same trap level as the one observed with the 0.4 V pulse amplitude as shown in Figure 6-15. The activation energy at 335 K could not be estimated since the peak shift does not follow the trend; the shorter the rate window, the higher the temperature at which the peak appears.

6.4 Conclusions

The DLTS and C-V measurements have been performed on UF CIS sample and compared with the DLTS measurements on EPV and NREL CIGS samples. The defect activation energy and density were determined from these measurements. Table 6-1 summarizes the DLTS data on 5% cell by RTP on bilayer precursor. In the UF CIS sample, a middle gap majority trap is detected and three other minority traps are also detected. The middle majority trap seems to be the dominant defect in the cell. This confirms the observation of the low V_{oc} in I-V curve. Therefore, to improve the cell efficiency, the junction quality must be improved by reducing the middle gap defect. Adding Ga or S to create the bandgap gradient and adjusting the Cu:In:Se composition ratio will be the reasonable methods. The EPV sample showed a majority carrier (hole) trap with activation energy and trap density determined. The NREL CIGS sample showed three minority carrier traps. Possible defect origins were suggested from this DLTS study. The results for samples from both locations are listed in Table 6-2. From the analysis in Tables 6-1 and 2, it is concluded that V_{Se} and In_{Cu} are two main donor levels, and V_{Cu} is the shallowest acceptor level, and Cu_{In} is the main middle level recombination center which are consistent with the information from literature [6-1~3, 6-7]. The free energy associated with the formation of some defect structures is so small that little increase in thermodynamic potential results and hence there is insufficient driving force to ensure their elimination under many synthesis conditions. The formation energy of these defects in CIS according to several authors calculations are in the order of $V_{Cu} < In_{Cu} < Cu_{In} \approx In_{Cu} < V_{Se}$ [6-1~2, 6-7]. However, the defect distribution depends significantly on the stoichiometry.

6.5 References cited

[6-1] S. B. Zhang, Su-Huai Wei, and Alex Zunger, *Physical Review B*, Vol. 57, No. 16 pp9642 –9656, 1998.

[6-2] S. B. Zhang, Su-Huai Wei, and Alex Zunger, *Physical Review Letters*, Vol. 78, No. 21 pp4059 – 4062, 1997.

[6-3] J.H. Schon and E. Bucher, *Solar Energy Materials & Solar Cells*, Vol. 57, pp. 229-237, 1999.

[6-4] S.S. Li, *Semiconductor Physical Electronics*, Plenum Press, New York and London, 1993.

[6-5] D.V. Liang, *J. Appl. Phys*, Vol. 45, pp.3014, 1974.

[6-6] B. M. Keyes, P. Dippo, W. Metzger, J. AbuShama, and R. Noufi, *the 29th IEEE Photovoltaic Specialist Conference,* New Orleans, LA, 2002.

[6-7] G. Kühn, W. Möller and W. Engel, *Thermochimica Acta*, Vol. 78, No. 1-3, pp. 129-134, 1984.
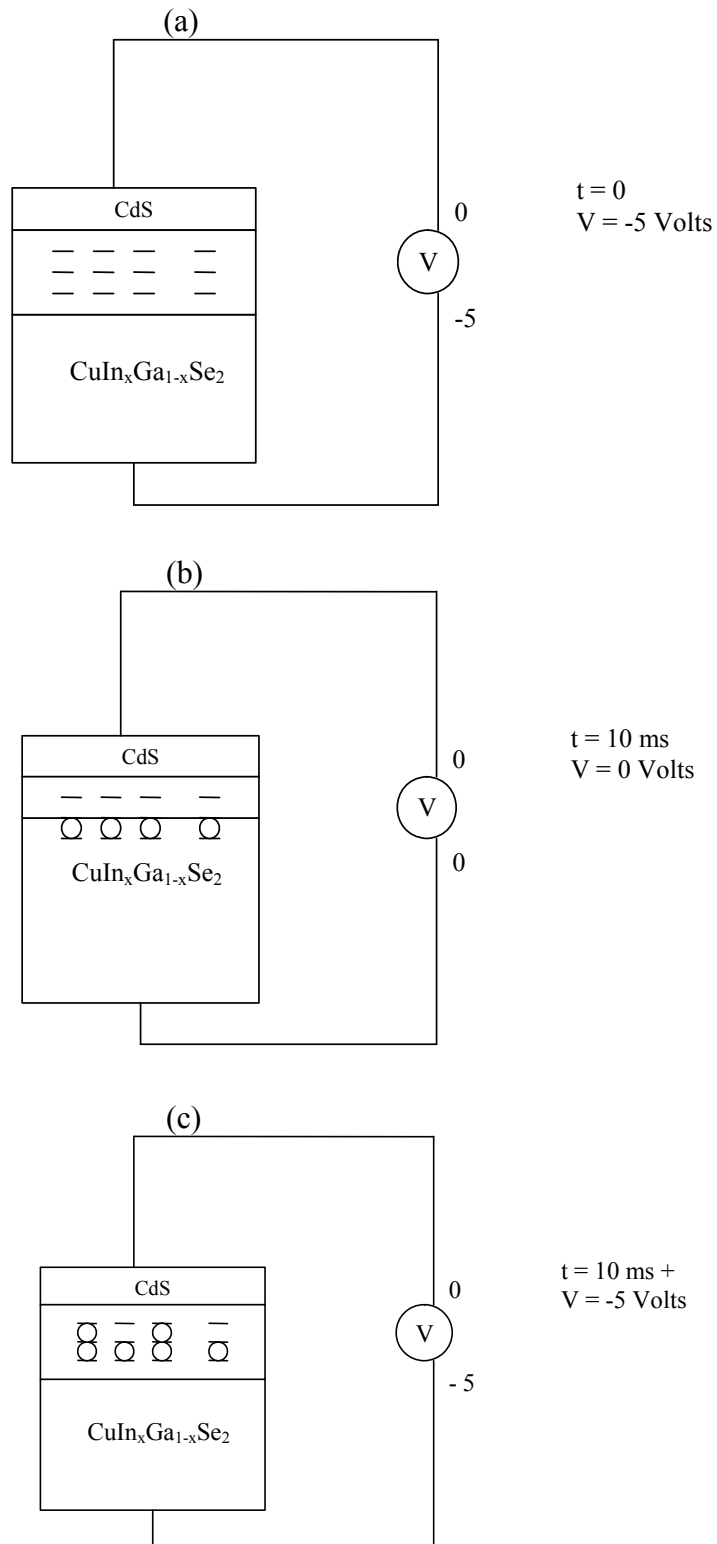
Figure 6-1. DLTS majority trap filling sequence for CdS/CIGS junction (a) under reverse bias without pulse (b) pulse injection (c) after pulse injection.
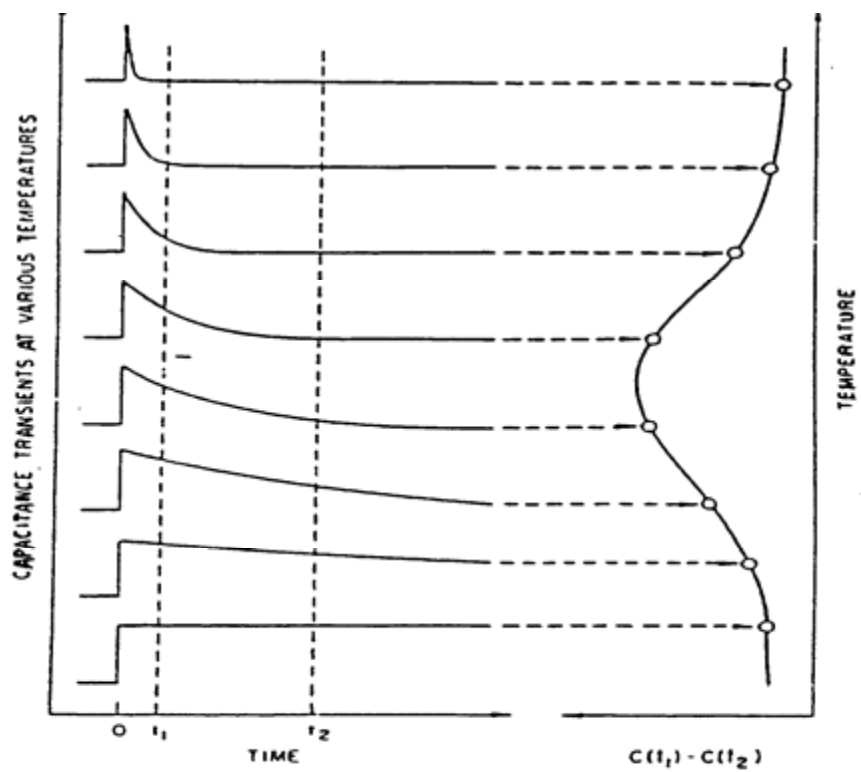
Figure 6-2. Example of how the double boxcar averager is used to define the rate window [6-5].

110
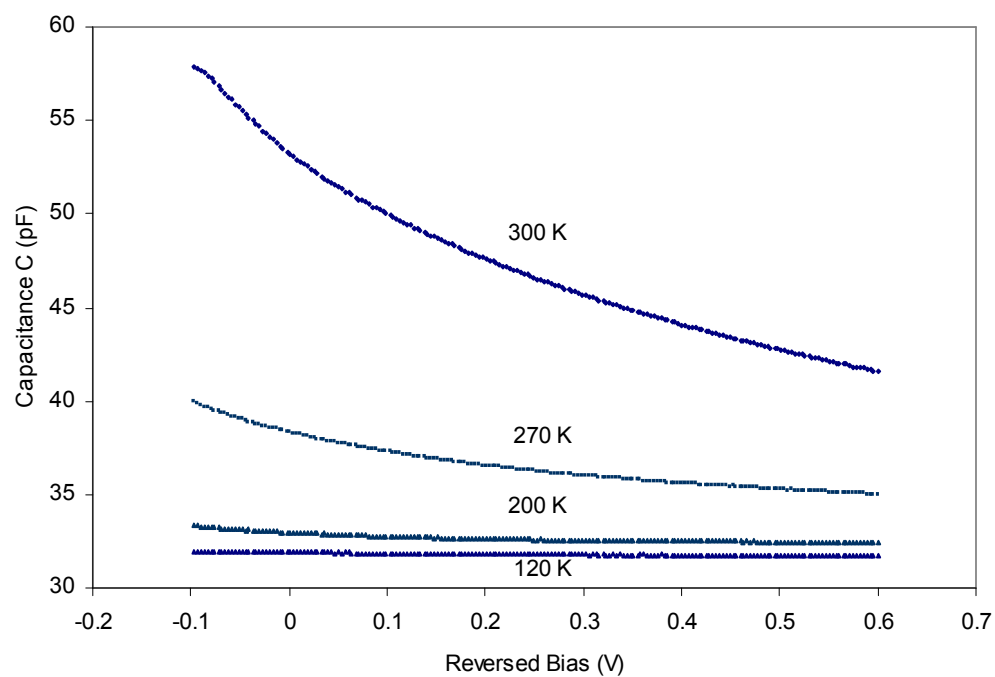
Figure 6-3. Capacitance–Voltage measurement for UF CIS cell.
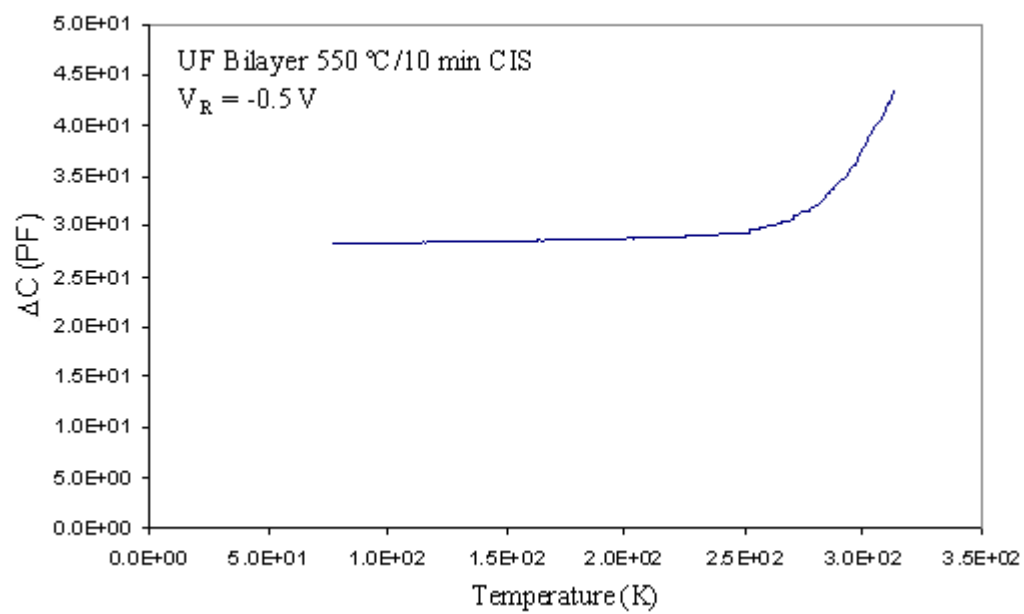
Figure 6-4. Capacitance-temperature measurement of the 5% cell.
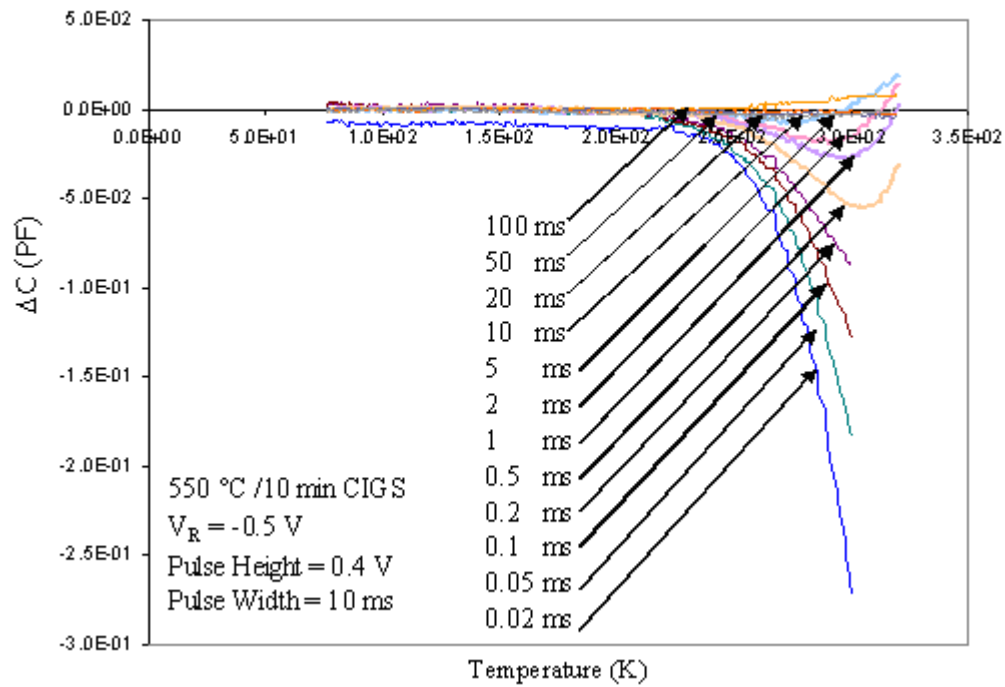
Figure 6-5. . DLTS scan for UF 5% cell at a reverse bias of –0.5 V, a pulse height of 0.4 V, and pulse width of 10 ms.

113
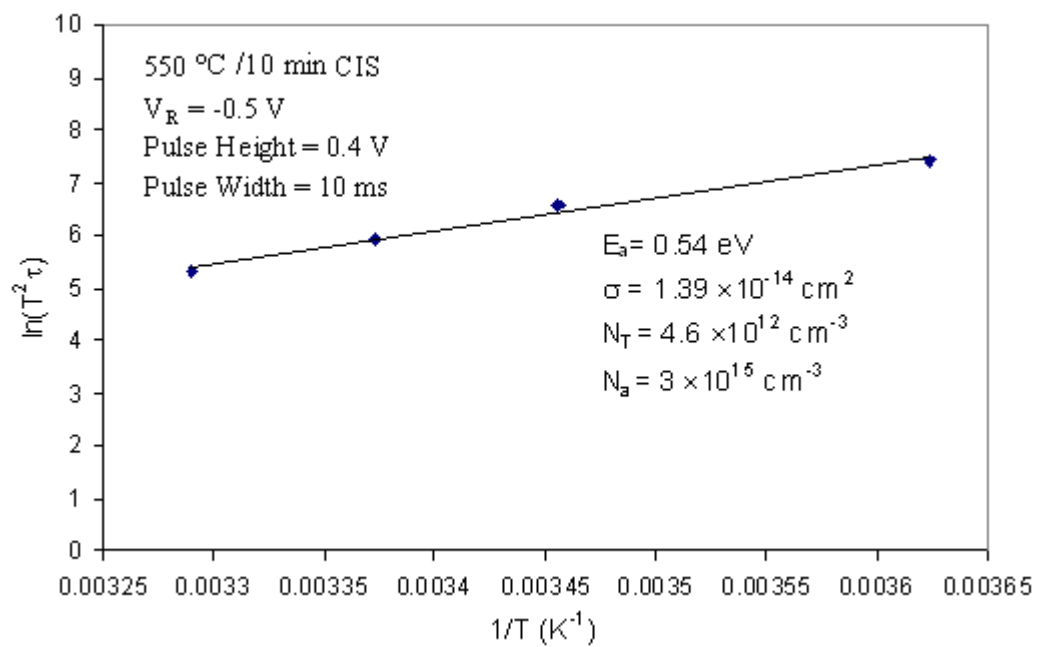
Figure 6-6. The Arrhenius plot of emission rate e_n/T^2 vs. 1/T.
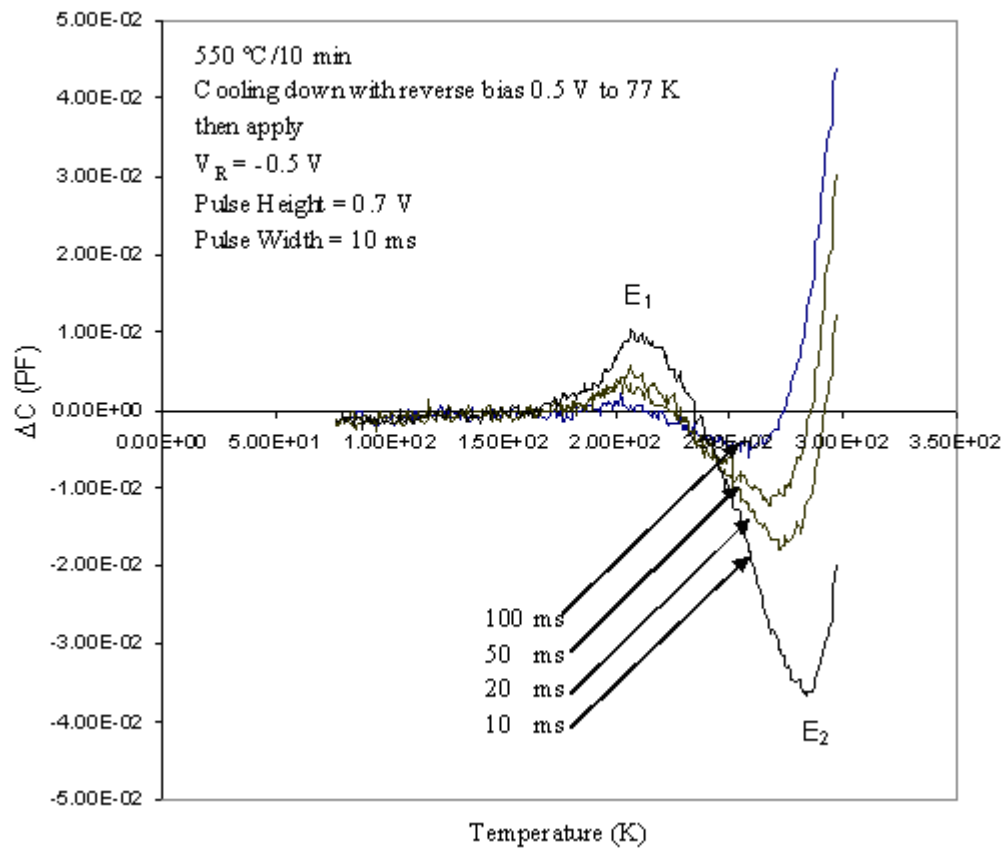
Figure 6-7. DLTS scan for UF 5% cell at a reverse bias of –0.5 V, a pulse height of 0.7 V, and pulse width of 10 ms.
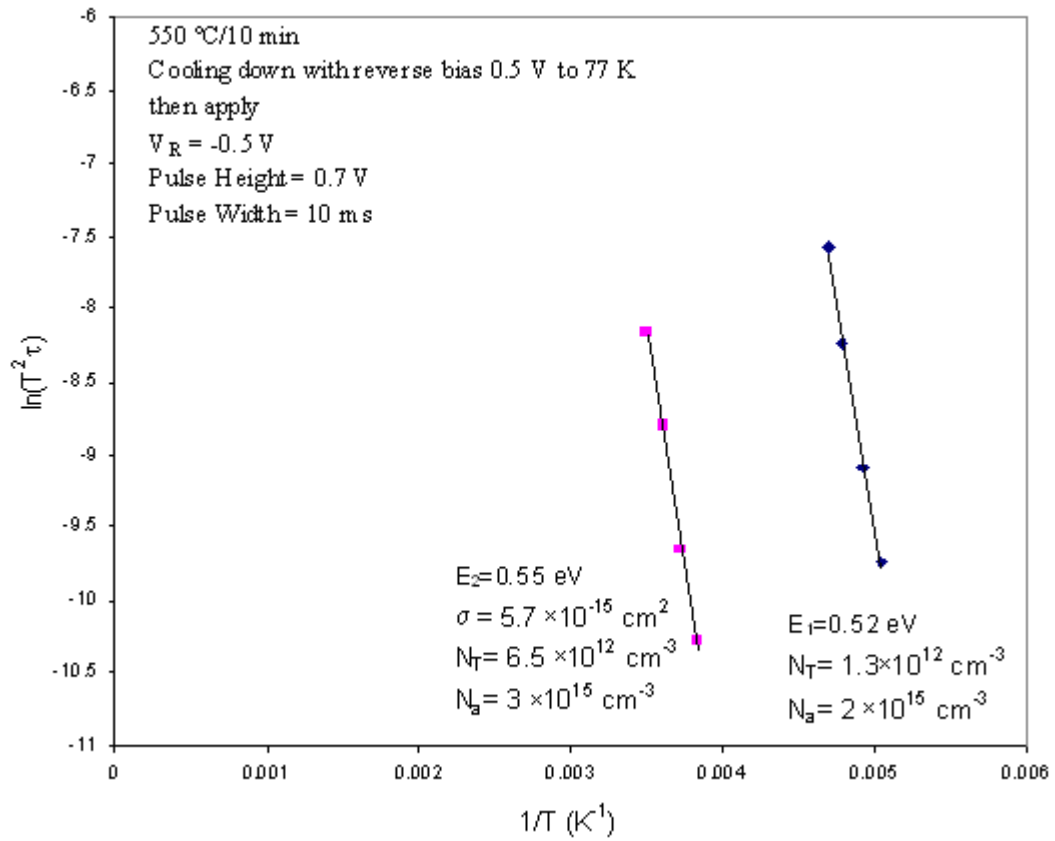
Figure 6-8. The Arrhenius plot of emission rate e_n/T^2 vs. 1/T for DLTS scan at reverse bias 0.5V, pulse height 0.7 V and pulse width 10 ms.
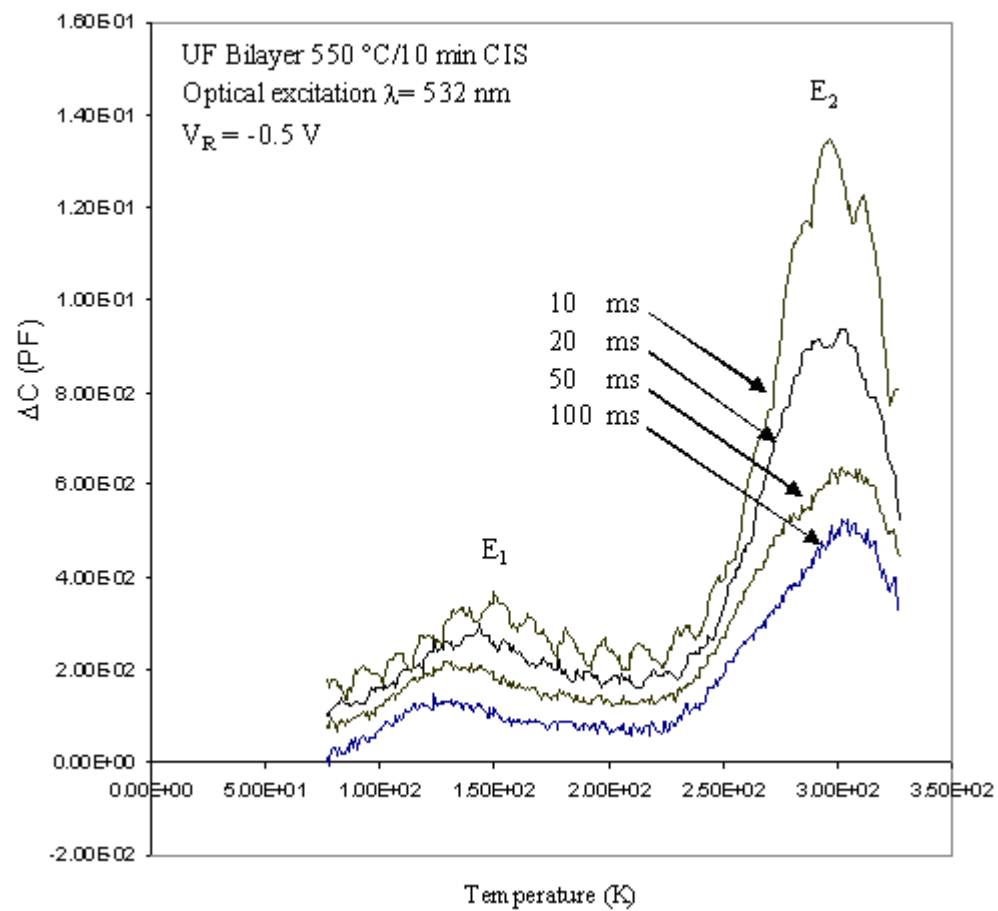
Figure 6-9. Optical DLTS scan for UF 5% cell at a reverse bias of –0.5 V, λ=532 nm, and pulse width of 10 ms.
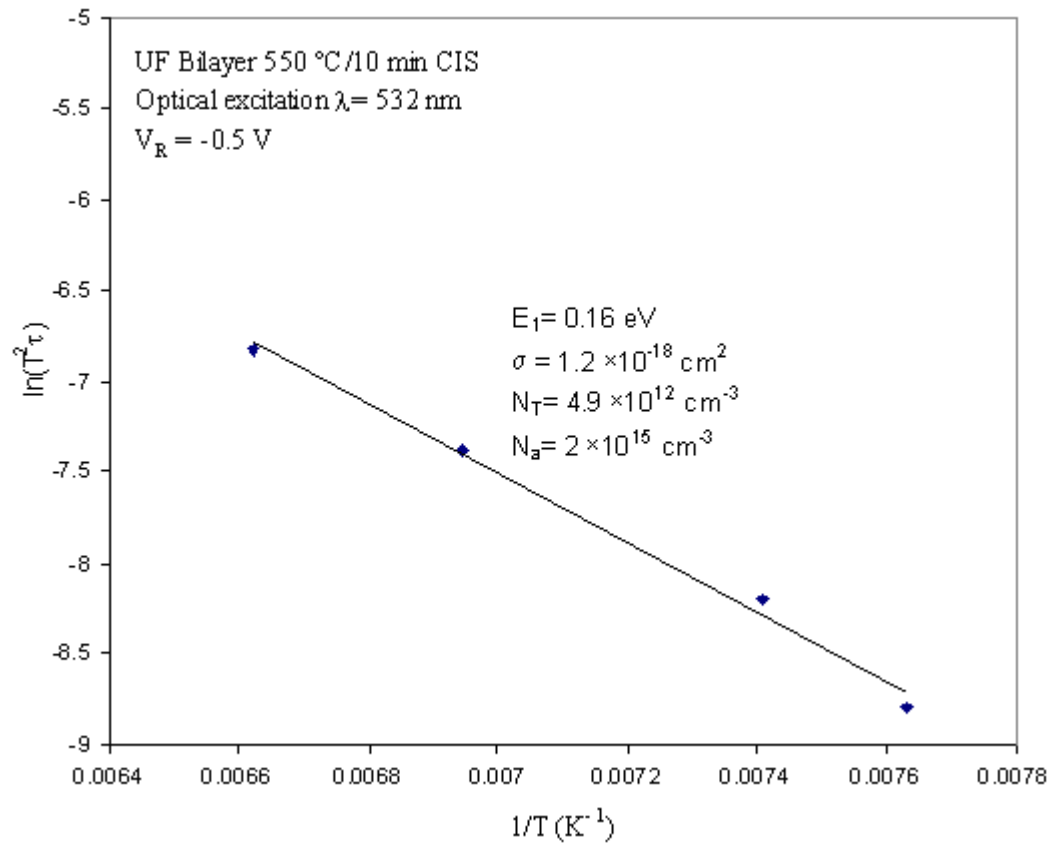
Figure 6-10. The Arrhenius plot of emission rate e_n/T^2 vs. $1/T$ for DLTS scan at reverse bias 0.5 V, pulse height 0.7 V and pulse width 10 ms.
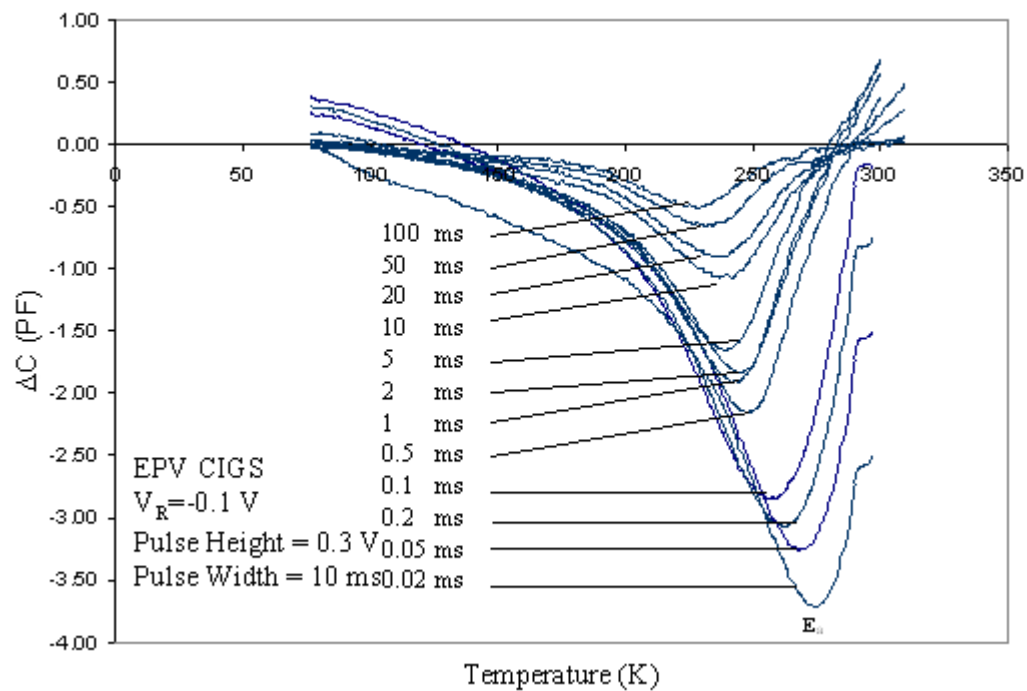
Figure 6-11. DLTS scan for EPV cell at a reverse bias of –0.1 V, a pulse height of 0.3 V, and pulse width of 10 ms.
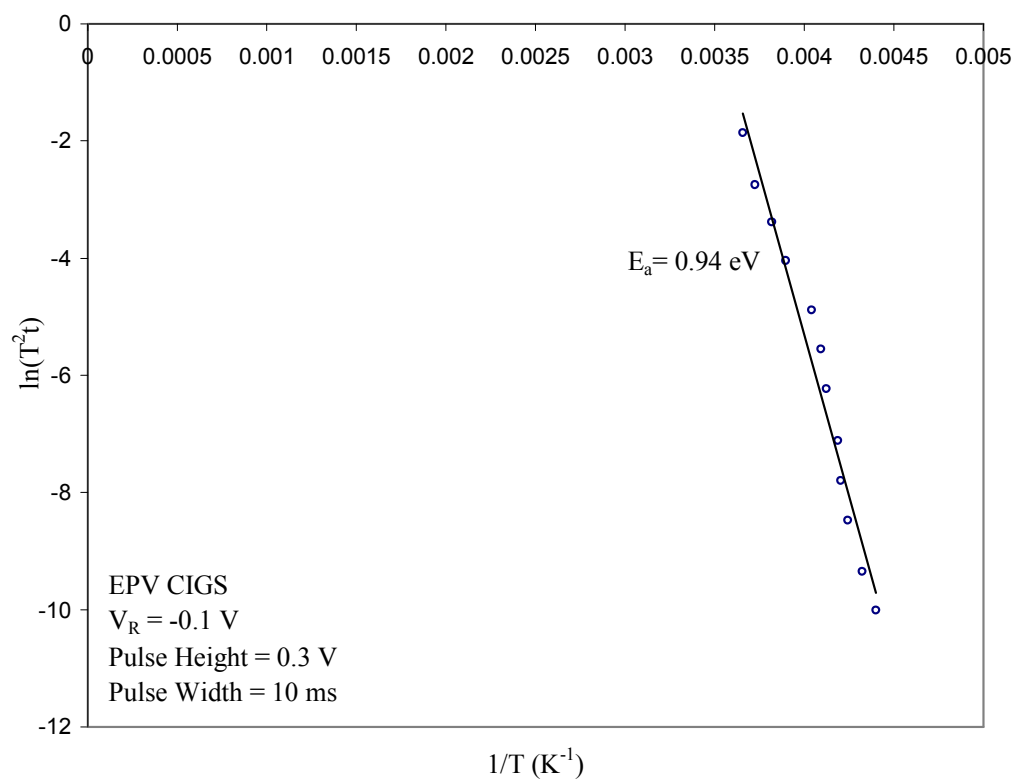
Figure 6-12. The Arrhenius plot of emission rate e_n/T^2 vs. $1/T$.
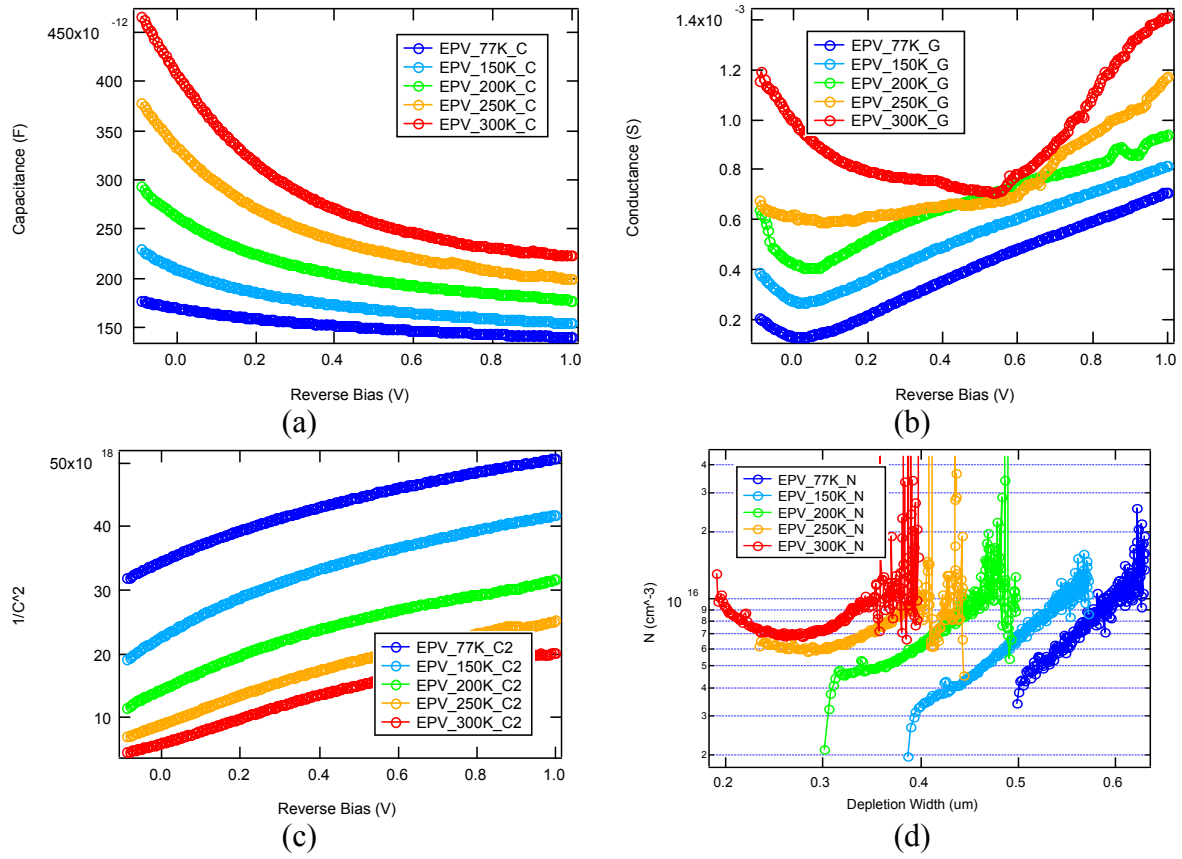
Figure 6-13. C-V data of EPV sample at different temperatures. (a) C-V (b) conductance-voltage (c) $1/C^2$-V (d) carrier concentration-depletion width.
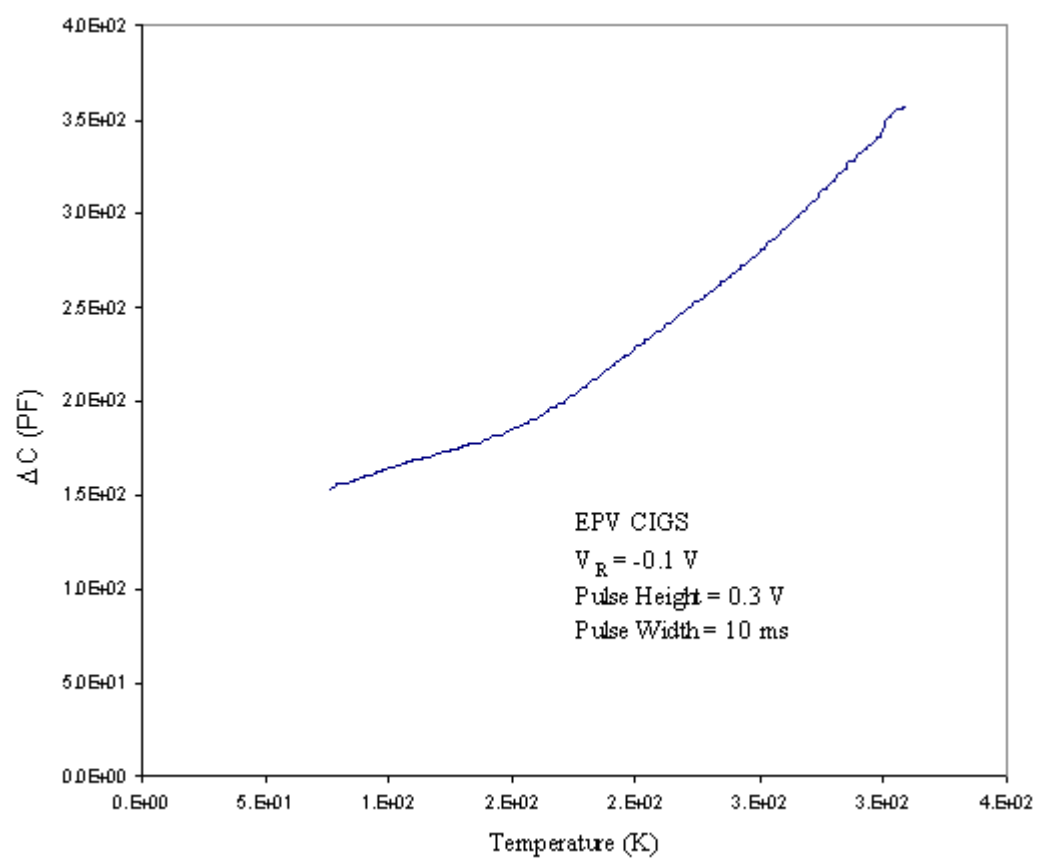
Figure 6-14. The C-T scan for EPV cell at a reversed bias -0.1V.
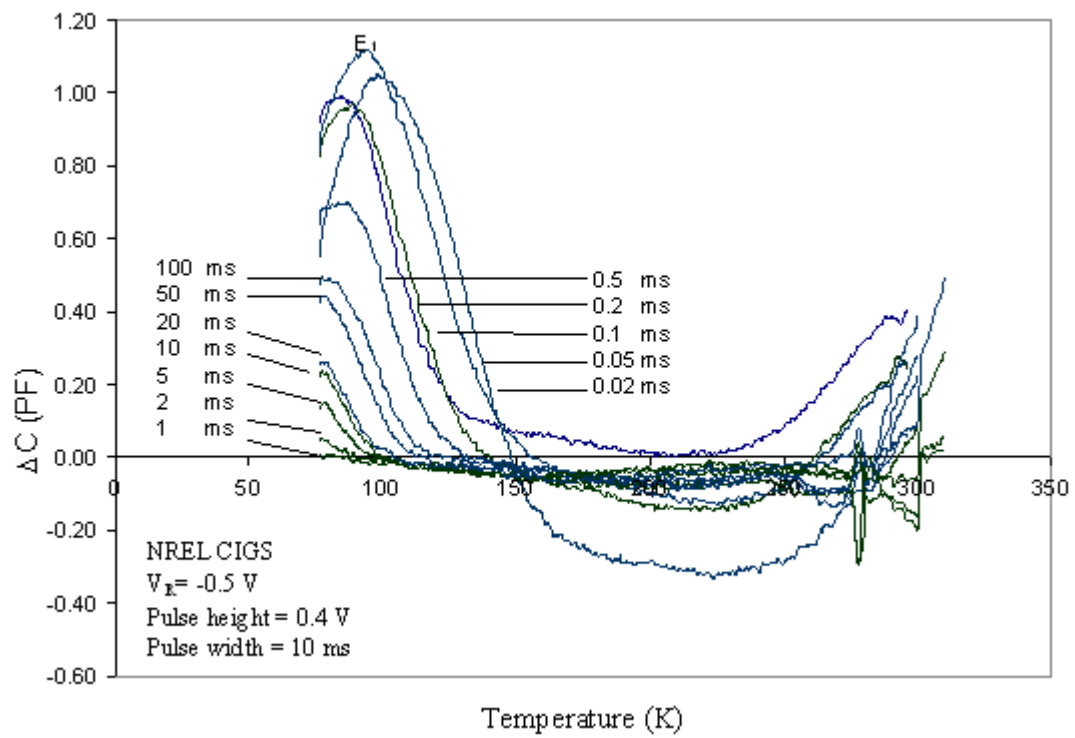
Figure 6-15. DLTS data for NREL sample measured at a reverse bias -0.5 V, pulse amplitude 0.4 V, and pulse width 10 ms.
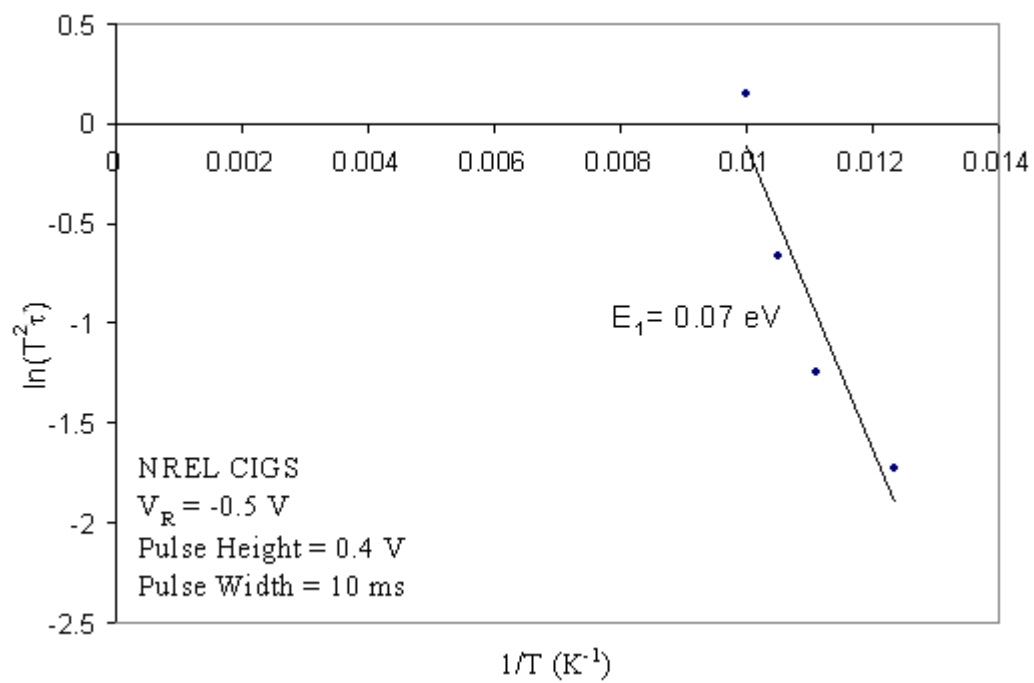
Figure 6-16. Arrhenius plot of the emission rate e_n/T^2 vs. $1/T$.
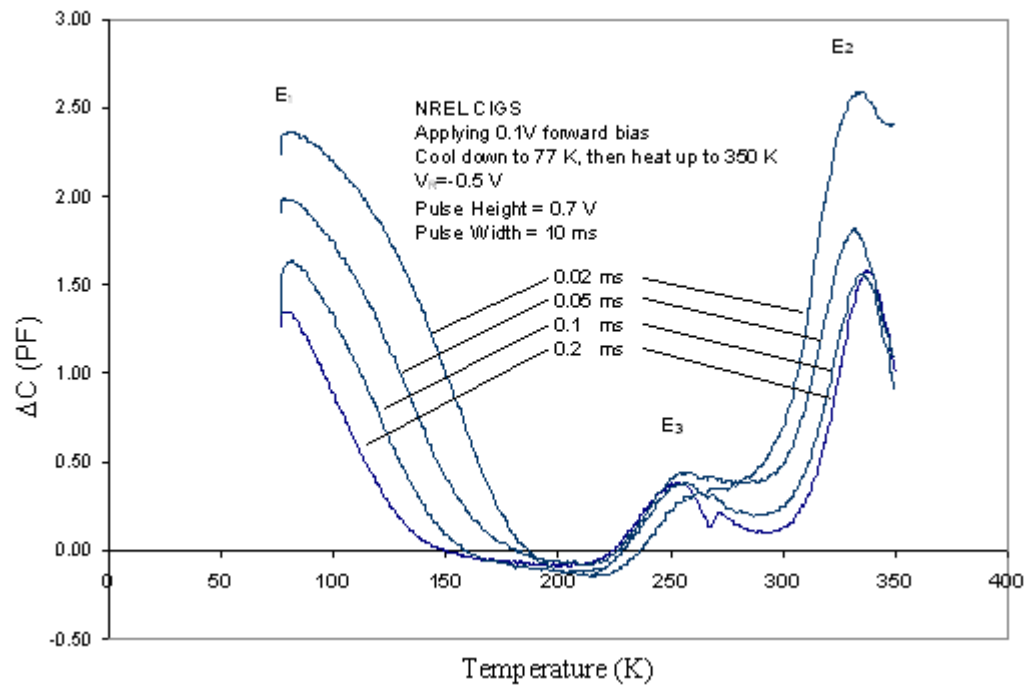
Figure 6-17. DLTS scan for the NREL sample under forward bias (0.1 V) injection, and heat up with reverse bias of -0.5V, pulse height of 0.7V, and pulse width of 10 ms.
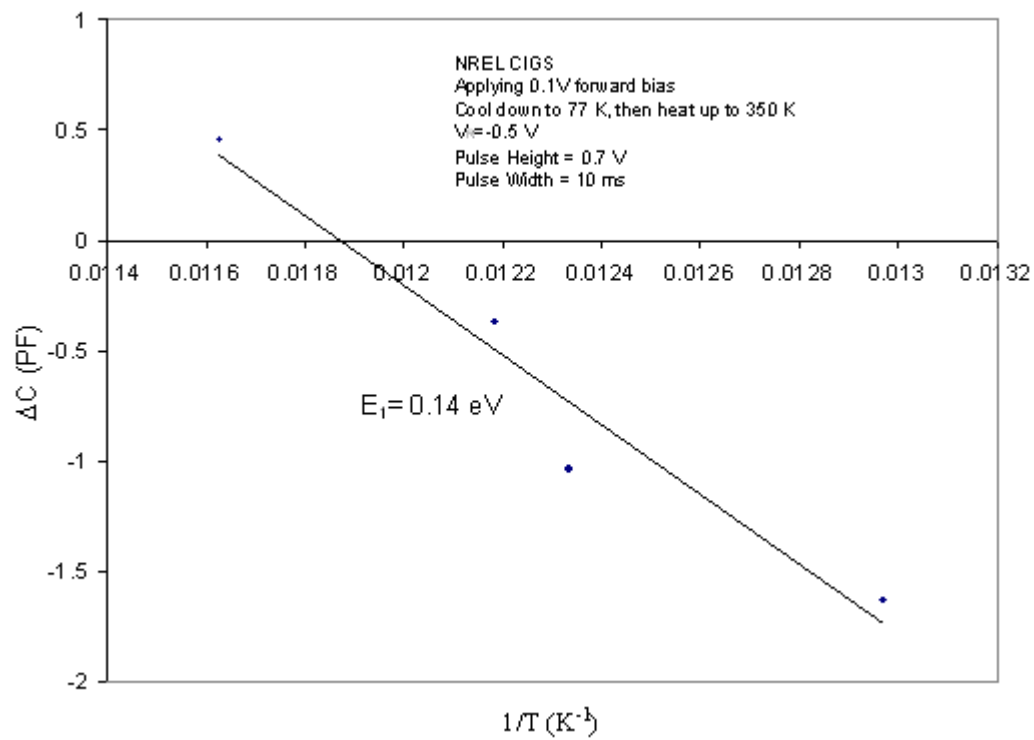
Figure 6-18. Arrhenius plot of emission rate e_n/T^2 vs. $1/T$ for the electron trap E_1.

Table 6-1. Summary of DLTS data on UF CIS sample

	V_R = -0.5 V V_H =0.4 V W= 10 ms	Cool to 77 K with reverse bias - 0.5 V, then apply V_R = -0.5 V V_H = 0.7 V W= 10 ms		Optical DLTS V_R = -0.5 V λ= 532 nm	
Approximate Peak Temperature (K)	290	290	200	150	300
DLTS peak Sign	-	-	+	+	+
Trap Carrier Type	Majority	Majority	Minority	Minority	Minority
Trap Activation Energy E_a (eV)	E_V +0.54	E_V +0.55	E_c -0.52	E_c - 0.16	E_c - 0.5 (?)
Trap Density (cm^{-3})	4.6×10^{12}	6.5×10^{12}	1.3×10^{12}	4.9×10^{12}	3.5×10^{13}
Possible Defect I.D.	Cu_{In}	Cu_{In}	V_{Cu}	In_{Cu}	Cu_{In}
Capture Cross Section σ (cm^2)	1.39×10^{-14}	5.7×10^{-15}		1.2×10^{-18}	

Table 6-2. Summary of DLTS and C-V data for the EPV and NREL samples.

	EPV CIGS	NREL CIGS		
Approximate Peak Temperature	270 K	100K	250 K	335 K
Activation Energy (eV)	E_v+0.94	E_c-0.067		
DLTS peak	-	+	+	+
Trap Carrier Type	Majority	Minority	Minority	Minority
N_a (cm^{-3})	3×10^{15}	2.25×10^{15}		
N_T (cm^{-3})	6.5×10^{13}	4.2×10^{13}		
Possible defect I.D.	V_{Se}	V_{Se}		
Capture Cross Section σ (cm^2)		6×10^{-18}		

7 Thermodynamic Modeling of the Isothermal 500°C Section of the Cu-In-Se System Using a Defect Model

7.1 Introduction

This study aims at establishing a defect model to understand the defect chemistry of the Cu-In-Se system and build a database to calculate the defect and carrier concentrations.

7.2 Experimental Phase Equilibria Data in the Cu-In-Se System

The most complete and recent study on the phase equilibria of Cu-In-Se are conducted by Gödecke *et al.* [7-1] using DTA, XRD, TEM and SEM measurements. The isothermal section at 500 ºC is of major technical importance for the fabrication of thin films for photovoltaic devices because these films are often deposited at temperatures around 500 ºC. A summary of all the phase observed equilibria is listed in Table 7-1. There are sixteen phases participating in the equilibria. Of which, nine are solutions: α-CIS (CuInSe$_2$), β_R-CIS (Cu$_1$In$_3$Se$_5$), γ-CIS(Cu$_1$In$_5$Se$_8$), β_H-CIS(Cu$_2$In$_4$Se$_7$), α_{Cu}, η (Cu$_2$In$_1$), δ (Cu$_7$Se$_3$), β-Cu$_2$Se, and Ionic_liquid. The other phase are the line compounds In$_5$Se$_7$, In$_9$Se$_{11}$, In$_6$Se$_7$, γ- In$_2$Se$_3$, β-In$_2$Se$_3$, InSe and In$_4$Se$_3$. According to their results, in the Se-rich corner and in the In-rich corner, the isothermal section at 500 ºC features small regions of liquid phase (L$_4$ and L$_2$, respectively). The α-CIS phase establishes equilibria with eight solid phases and two liquid phases (L$_4$ and L$_2$). Among the solid phases, α_{Cu}, η (Cu$_2$In$_1$), and δ (Cu$_7$Se$_3$) originate from the In-Cu boundary system, β-Cu$_2$Se from the Cu-Se boundary system and InSe and In$_4$Se$_3$ from In-Se boundary system. The remaining two phases in equilibrium with α-CIS (CuInSe$_2$) are β_R-CIS (Cu$_1$In$_3$Se$_5$) and β_H-CIS(Cu$_2$In$_4$Se$_7$).

7.3 Thermodynamic Modeling of Defect-free Cu-In-Se System at 773 K

To stabilize the phase equilibria in the Cu-In-Se system with many phase interactions, it is important to determine the parameters when the CIS compounds are defect free, and assessment of this complicated Cu-In-Se ternary system begins from this point.

7.3.1 Gibbs Energy Data of Defect-free α-CIS (CuInSe$_2$) β_R-CIS (Cu$_1$In$_3$Se$_5$), γ-CIS(Cu$_1$In$_5$Se$_8$), and β_H-CIS(Cu$_2$In$_4$Se$_7$)

The sublattice model is chosen to describe the α-CIS phases. According to the sublattice model, the defect free Chalcopyrite CuInSe$_2$ (stoichiometry) consists of three sublattices and is presented as

$$(\mathbf{Cu})^{I}_{1}(\mathbf{In})^{II}_{1}(\mathbf{Se})^{III}_{2}$$
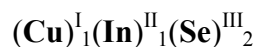
The superscripts, I, II and III identify the sublattices. Analogous to α-CIS, the β_R, γ, β_H-CIS can be expressed by the following sublattices:

$$(\mathbf{Cu})^I_1 (\mathbf{In})^{II}_3 (\mathbf{Se})^{III}_5 \text{ for } \beta_R\text{-CIS}$$

$$(\mathbf{Cu})^I_1 (\mathbf{In})^{II}_5 (\mathbf{Se})^{III}_8 \text{ for } \gamma\text{-CIS}$$

$$(\mathbf{Cu})^I_2 (\mathbf{In})^{II}_4 (\mathbf{Se})^{III}_7 \text{ for } \beta_H\text{-CIS}$$
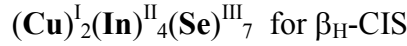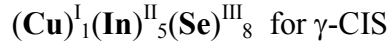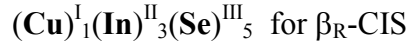
The Gibbs energy evaluation method based on the idea that ordered defect compounds (ODC) are formed by repeating periodically m units of $(2V_{Cu} + In_{Cu})$ for every n unit of α-CIS (CuInSe$_2$) [7-2, 3] are employed to evaluate the Gibbs energy of pure compound α-CIS (CuInSe$_2$) β_R-CIS (Cu$_1$In$_3$Se$_5$), γ-CIS(Cu$_1$In$_5$Se$_8$), and β_H-CIS(Cu$_2$In$_4$Se$_7$). The Gibbs energy data estimated by this method will be used as the compound Gibbs energy for the defect free α, β_R, γ, β_H-CIS so that we can express the Gibbs energy of β_R, γ, β_H-CIS in terms of α-CIS to reduce the number of parameters in the assessment when the defects are incorporated into the sublattices. This is because there is no experimental and calculated data available on the defect energy of β_R, γ, β_H-CIS. This method will provide an approach to express the pure compound and defects of Gibbs energy of β_R, γ, β_H-CIS in terms of the pure compound and defects Gibbs energy of α-CIS. In this method, the Gibbs energy data for β_R-CIS (Cu$_1$In$_3$Se$_5$), γ-CIS(Cu$_1$In$_5$Se$_8$), and β_H-CIS(Cu$_2$In$_4$Se$_7$) are obtained by the following equations:

$$^\circ G(\beta_R\text{-CIS (Cu}_1\text{In}_3\text{Se}_5)) = 2.5 \times {^\circ G}(\alpha\text{-CIS (CuInSe}_2) + V_1 \tag{7-1}$$

$$^\circ G(\gamma\text{-CIS(Cu}_1\text{In}_5\text{Se}_8)) = 4 {^\circ G}(\alpha\text{-CIS (CuInSe}_2)) + V_2 \tag{7-2}$$

$$^\circ G(\beta_H\text{-CIS(Cu}_2\text{In}_4\text{Se}_7)) = 3.5 \times {^\circ G}(\alpha\text{-CIS (CuInSe}_2)) + V_3 \tag{7-3}$$

The parameters V_1, V_2, and V_3 needed to be estimated. The estimation of V_1, V_2, and V_3 follows the following procedure. First, the magnitude of V_1, V_2, and V_3 are given by $0.5 \times \Delta H^0_{f,2V_{Cu}+In_{Cu}}$ or $\Delta H^0_{f,2V_{Cu}+In_{Cu}}$ as an initial parameters since m= 0.5 or 1 for every ODC compound. Then, V_1, V_2, and V_3 are optimized by using the Thermo-Calc Parrot module.

7.3.2 Gibbs Energy of Other Phases

As mentioned previously, seven other line compounds and two small liquid phase region also exist in this isothermal 500 °C diagram, in addition to the four CIS compounds. Among the solid phases, α_{Cu}, η (Cu$_2$In$_1$), and δ (Cu$_7$Se$_3$) originate from the In-Cu boundary system, β-Cu$_2$Se from the Cu-Se boundary system and InSe and In$_4$Se$_3$ from In-Se boundary system.

7.3.2.1 Fcc(Cu) Phase

A regular solution model is used to describe the Gibbs energy of the fcc(Cu) phase.

$$(\mathbf{Cu}, \text{Se, In})$$

Combining the previous Cu-Se and Cu-In binary assessment work [7-4, 5], the ternary interaction parameter $^{CuFcc}L^0_{Cu,In,Se}$ was added. This parameter needs to be optimized.

7.3.2.2   β-Cu₂Se Phase

The β-Cu$_2$Se phase is described by the sublattice model with two Cu sublattices and one Se sublattice represented by the formula:

$$(\mathbf{Cu},In,Va)_1(\mathbf{Se},Va)_1(\mathbf{Cu})_1$$
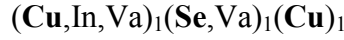
Again a ternary interaction parameter was added to the binary Cu-Se system [7-4] to model the In solubility, $^{\beta-Cu_2Se}L^0_{Cu,In,Va:Se:Cu}$.

7.3.2.3   The η(Cu₂In₁), and δ(Cu₇In₃) Phases

In the binary assessment work [7-5], both phases are described by a two sublattice model. To model the solubility, the two sublattice model was modified so that all the three elements will be involved.

$$(Cu, In, Se)_2(Cu, In, Se)_1 \qquad \text{for} \qquad \eta(Cu_2In_1) \text{ phase}$$

$$(Cu, In, Se)_7(Cu, In, Se)_3 \qquad \text{for} \qquad \delta(Cu_7In_3) \text{ phase}$$

Again a ternary interaction parameter $^{\phi}L^0_{Cu,In,Se:*}$, $^{\phi}L^0_{*:Cu,In,Se}$ was included, where ϕ stands $\eta(Cu_2In_1)$ or $\delta(Cu_7In_3)$ phases.

7.3.2.4   Liquid Phase

The liquid phase is described by an ionic sublattice model with two sublattices, since the ionic two-sublattice model can describe short range ordering and is more straightforward to extend to higher order systems as compared to the chemical theories [7-6]. Based on the previous work on the modeling of the liquid phase in the Cu-Se, In-Se [7-4] and Cu-In [7-5] binary systems, the liquid phase is schematically described in this ternary system as

$$(Cu^{+1},Cu^{+2}, In^{+3})p(Se^{-2},Va^{-1},Se)q$$
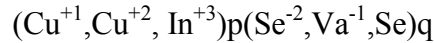
Therefore, three ternary interaction parameters were added to the ionic liquid to describe the Gibbs energy, $^{Ionic\_Liq}L^0_{Cu^{+1},Cu^{+2},In^{+3}:Se^{-2}}$ and $^{Ionic\_Liq}L^1_{Cu^{+1},Cu^{+2},In^{+3}:Se^{-2}}$.

7.3.3   Results and Discussion

The optimized parameters of the stable phases in this Cu-In-Se system with a defect free compound CIS are listed in Table 7-2. The calculated phase diagram over the entire composition range using the optimized parameters is shown in Figure 7-1.

7.4 Defect Model of Off-Stoichiometry α-CuInSe₂

7.4.1 Modeling of Gibbs Energy

7.4.1.1 α-CIS (CuInSe₂)

To model the homogeneity range, the defects have to be incorporated into three sublattices of the stoichiometric chalcopyrite compound α-CIS (CuInSe₂). As reviewed in Chapter 2, four main defects are incorporated into this sublattice model: V_{Cu}, V_{Se}, In_{Cu}, Cu_{In}. Since the model will also incorporate the calculation of free electrons and holes, which is discussed in detail in the next section, it is necessary to consider the donors and acceptors in this phase. In the extrinsic semiconductors, the shallow-level impurities are used mainly for controlling the carrier concentration and the conductivity of the semiconductor, while the deep-level impurities are used to control the recombination and hence the minority carrier lifetime in a semiconductor [7-7]. The Cu vacancy is a shallow level acceptor and the Se vacancy is a shallow-level donor. To simplify the model in this calculation, one acceptor $V_{Cu}{}^{-1}$ and one donor $V_{Se}{}^{+2}$ are considered. Thus, the sublattices for α-CIS phase can be written as

$$(\mathbf{Cu}, In, Va, Va^{-1})^{I}_{1}(\mathbf{In}, Cu)^{II}_{1}(\mathbf{Se}, Va, Va^{+2})^{III}_{2} (\mathbf{Va})^{IV} (\mathbf{Va})^{V}$$
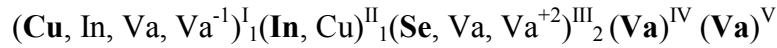
The superscripts, I, II and III identify the sublattices. The major constituents on the normal sublattices are highlighted. The IV and V sublattices are added for incorporation of electrons and holes. For now, just consider the first three sublattices, with the vacancy concentration on sublattices IV and V, $y^{IV}_{Va} = 1$ and $y^{V}_{Va} = 1$.

The Gibbs energy of such a phase α can also be expressed by equation:

$$G^{\alpha} = {}^{ref}G^{\alpha} + {}^{I.D.}G^{\alpha} + {}^{ex}G^{\alpha} \qquad (7\text{-}4)$$

where α stands for non-stoichiometric chalcopyrite α-CuInSe₂ phase. Now, the reference state can be expressed in the form

$$^{ref}G^\alpha = y^I_{Cu}\,y^{II}_{In}\,y^{III}_{Se}\,y^{IV}_{Va}\,y^V_{Va}\,{}^\circ G^\alpha_{Cu\,:\,In\,:\,Se\,:\,Va\,:\,Va} + y^I_{In}\,y^{II}_{In}\,y^{III}_{Se}\,y^{IV}_{Va}\,y^V_{Va}\,{}^\circ G^\alpha_{In\,:\,In\,:\,Se\,:\,Va\,:\,Va}$$

$$+ y^I_{Va}\,y^{II}_{In}\,y^{III}_{Se}\,y^{IV}_{Va}\,y^V_{Va}\,{}^\circ G^\alpha_{Va\,:\,In\,:\,Se\,:\,Va\,:\,Va} + y^I_{Va^{-1}}\,y^{II}_{In}\,y^{III}_{Se}\,y^{IV}_{Va}\,y^V_{Va}\,{}^\circ G^\alpha_{Va^{-1}\,:\,In\,:\,Se\,:\,Va\,:\,Va}$$

$$+ y^I_{Cu}\,y^{II}_{Cu}\,y^{III}_{Se}\,y^{IV}_{Va}\,y^V_{Va}\,{}^\circ G^\alpha_{Cu\,:\,Cu\,:\,Se\,:\,Va\,:\,Va} + y^I_{In}\,y^{II}_{Cu}\,y^{III}_{Se}\,y^{IV}_{Va}\,y^V_{Va}\,{}^\circ G^\alpha_{In\,:\,Cu\,:\,Se\,:\,Va\,:\,Va}$$

$$+ y^I_{Va}\,y^{II}_{Cu}\,y^{III}_{Se}\,y^{IV}_{Va}\,y^V_{Va}\,{}^\circ G^\alpha_{Va\,:\,Cu\,:\,Se\,:\,Va\,:\,Va} + y^I_{Va^{-1}}\,y^{II}_{Cu}\,y^{III}_{Se}\,y^{IV}_{Va}\,y^V_{Va}\,{}^\circ G^\alpha_{Va^{-1}\,:\,Cu\,:\,Se\,:\,Va\,:\,Va}$$

$$+ y^I_{Cu}\,y^{II}_{In}\,y^{III}_{Va}\,y^{IV}_{Va}\,y^V_{Va}\,{}^\circ G^\alpha_{Cu\,:\,In\,:\,Va\,:\,Va\,:\,Va} + y^I_{In}\,y^{II}_{In}\,y^{III}_{Va}\,y^{IV}_{Va}\,y^V_{Va}\,{}^\circ G^\alpha_{In\,:\,In\,:\,Va\,:\,Va\,:\,Va}$$

$$+ y^I_{Va}\,y^{II}_{In}\,y^{III}_{Va}\,y^{IV}_{Va}\,y^V_{Va}\,{}^\circ G^\alpha_{Va\,:\,In\,:\,Va\,:\,Va\,:\,Va} + y^I_{Va^{-1}}\,y^{II}_{In}\,y^{III}_{Va}\,y^{IV}_{Va}\,y^V_{Va}\,{}^\circ G^\alpha_{Va^{-1}\,:\,In\,:\,Va\,:\,Va\,:\,Va}$$

$$+ y^I_{Cu}\,y^{II}_{Cu}\,y^{III}_{Va}\,y^{IV}_{Va}\,y^V_{Va}\,{}^\circ G^\alpha_{Cu\,:\,Cu\,:\,Va\,:\,Va\,:\,Va} + y^I_{In}\,y^{II}_{Cu}\,y^{III}_{Va}\,y^{IV}_{Va}\,y^V_{Va}\,{}^\circ G^\alpha_{In\,:\,Cu\,:\,Va\,:\,Va\,:\,Va}$$

$$+ y^I_{Va}\,y^{II}_{Cu}\,y^{III}_{Va}\,y^{IV}_{Va}\,y^V_{Va}\,{}^\circ G^\alpha_{Va\,:\,Cu\,:\,Va\,:\,Va\,:\,Va} + y^I_{Va^{-1}}\,y^{II}_{Cu}\,y^{III}_{Va}\,y^{IV}_{Va}\,y^V_{Va}\,{}^\circ G^\alpha_{Va^{-1}\,:\,Cu\,:\,Va\,:\,Va\,:\,Va}$$

$$+ y^I_{Cu}\,y^{II}_{In}\,y^{III}_{Va^{+2}}\,y^{IV}_{Va}\,y^V_{Va}\,{}^\circ G^\alpha_{Cu\,:\,In\,:\,Va^{+2}\,:\,Va\,:\,Va} + y^I_{In}\,y^{II}_{In}\,y^{III}_{Va^{+2}}\,y^{IV}_{Va}\,y^V_{Va}\,{}^\circ G^\alpha_{In\,:\,In\,:\,Va^{+2}\,:\,Va\,:\,Va}$$

$$+ y^I_{Va}\,y^{II}_{In}\,y^{III}_{Va^{+2}}\,y^{IV}_{Va}\,y^V_{Va}\,{}^\circ G^\alpha_{Va\,:\,In\,:\,Va^{+2}\,:\,Va\,:\,Va} + y^I_{Va^{-1}}\,y^{II}_{In}\,y^{III}_{Va^{+2}}\,y^{IV}_{Va}\,y^V_{Va}\,{}^\circ G^\alpha_{Va^{-1}\,:\,In\,:\,Va^{+2}\,:\,Va\,:\,Va}$$

$$+ y^I_{Cu}\,y^{II}_{Cu}\,y^{III}_{Va^{+2}}\,y^{IV}_{Va}\,y^V_{Va}\,{}^\circ G^\alpha_{Cu\,:\,Cu\,:\,Va^{+2}\,:\,Va\,:\,Va} + y^I_{In}\,y^{II}_{Cu}\,y^{III}_{Va^{+2}}\,y^{IV}_{Va}\,y^V_{Va}\,{}^\circ G^\alpha_{In\,:\,Cu\,:\,Va^{+2}\,:\,Va\,:\,Va}$$

$$+ y^I_{Va}\,y^{II}_{Cu}\,y^{III}_{Va^{+2}}\,y^{IV}_{Va}\,y^V_{Va}\,{}^\circ G^\alpha_{Va\,:\,Cu\,:\,Va^{+2}\,:\,Va\,:\,Va} + y^I_{Va^{-1}}\,y^{II}_{Cu}\,y^{III}_{Va}\,y^{IV}_{Va}\,y^V_{Va}\,{}^\circ G^\alpha_{Va^{-1}\,:\,Cu\,:\,Va^{+2}\,:\,Va\,:\,Va}$$

(7-5)

Including the ideal entropy of mixing

$$^{ID}G^\alpha = + RT(y^I_{Cu}\ln y^I_{Cu} + y^I_{In}\ln y^I_{In} + y^I_{Va}\ln y^I_{Va} + y^I_{Va^{-1}}\ln y^I_{Va^{-1}})$$

$$+ RT(y^{II}_{Cu}\ln y^{II}_{Cu} + y^{II}_{In}\ln y^{II}_{In})$$

$$+ RT(y^{III}_{Se}\ln y^{III}_{Se} + y^{III}_{Va}\ln y^{III}_{Va} + y^{III}_{Va^{+2}}\ln y^{III}_{Va^{+2}})$$

(7-6)

and finding the excess Gibbs energy of mixing

$$EX_G{}^\alpha = y_{Cu}^I y_{In}^I \left[\begin{array}{l} y_{Cu}^{II} y_{Se}^{III} \left({}^0L_{Cu,In:Cu:Se:Va:Va}^\alpha \right) + y_{In}^{II} y_{Se}^{III} \left({}^0L_{Cu,In:In:Se:Va:Va}^\alpha \right) \\ + y_{Cu}^{II} y_{Va}^{III} \left({}^0L_{Cu,In:Cu:Va:Va:Va}^\alpha \right) + y_{In}^{II} y_{Va}^{III} \left({}^0L_{Cu,In:In:Va:Va:Va}^\alpha \right) \end{array} \right]$$

$$+ y_{Cu}^I y_{Va}^I \left[\begin{array}{l} y_{Cu}^{II} y_{Se}^{III} \left({}^0L_{Cu,Va:Cu:Se:Va:Va}^\alpha \right) + y_{In}^{II} y_{Se}^{III} \left({}^0L_{Cu,Va:In:Se:Va:Va}^\alpha \right) \\ + y_{Cu}^{II} y_{Va}^{III} \left({}^0L_{Cu,Va:Cu:Va:Va:Va}^\alpha \right) + y_{In}^{II} y_{Va}^{III} \left({}^0L_{Cu,Va:In:Va:Va:Va}^\alpha \right) \end{array} \right]$$

$$+ y_{Cu}^I y_{Va^{-1}}^I \left[\begin{array}{l} y_{Cu}^{II} y_{Se}^{III} \left({}^0L_{Cu,Va^{-1}:Cu:Se:Va:Va}^\alpha \right) + y_{In}^{II} y_{Se}^{III} \left({}^0L_{Cu,Va^{-1}:In:Se:Va:Va}^\alpha \right) \\ + y_{Cu}^{II} y_{Va}^{III} \left({}^0L_{Cu,Va^{-1}:Cu:Va:Va:Va}^\alpha \right) + y_{In}^{II} y_{Va}^{III} \left({}^0L_{Cu,Va^{-1}:In:Va:Va:Va}^\alpha \right) \end{array} \right]$$

$$+ y_{Cu}^{II} y_{In}^{II} \left[\begin{array}{l} y_{Cu}^I y_{Se}^{III} \left({}^0L_{Cu:Cu,In:Se:Va:Va}^\alpha \right) + y_{In}^I y_{Se}^{III} \left({}^0L_{In:Cu,In:Se:Va:Va}^\alpha \right) \\ + y_{Cu}^I y_{Va}^{III} \left({}^0L_{Cu:Cu,In:Va:Va:Va}^\alpha \right) + y_{In}^{II} y_{Va}^{III} \left({}^0L_{In:Cu,In:Va:Va:Va}^\alpha \right) \\ + y_{Va}^I y_{Se}^{III} \left({}^0L_{Va:Cu,In:Se:Va:Va}^\alpha \right) + y_{Va}^I y_{Va}^{III} \left({}^0L_{Va:Cu,In:Va:Va:Va}^\alpha \right) \end{array} \right]$$

$$+ y_{Va}^{III} y_{Se}^{III} \left[\begin{array}{l} y_{Cu}^I y_{Cu}^{II} \left({}^0L_{Cu:Cu:Se,Va:Va:Va}^\alpha \right) + y_{In}^I y_{Cu}^{II} \left({}^0L_{In:Cu:Se,Va:Va:Va}^\alpha \right) \\ + y_{Cu}^I y_{In}^{II} \left({}^0L_{Cu:In:Se,Va:Va:Va}^\alpha \right) + y_{In}^I y_{In}^{II} \left({}^0L_{In:In:Se,Va:Va:Va}^\alpha \right) \\ + y_{Va}^I y_{Cu}^{II} \left({}^0L_{Va:Cu:Se,Va}^\alpha \right) + y_{Va}^I y_{In}^{II} \left({}^0L_{Va:In:Se,Va:Va:Va}^\alpha \right) \end{array} \right]$$

$$+ y_{Va^{+2}}^{III} y_{Se}^{III} \left[\begin{array}{l} y_{Cu}^I y_{Cu}^{II} \left({}^0L_{Cu:Cu:Se,Va^{+2}:Va:Va}^\alpha \right) + y_{In}^I y_{Cu}^{II} \left({}^0L_{In:Cu:Se,Va^{+2}:Va:Va}^\alpha \right) \\ + y_{Cu}^I y_{In}^{II} \left({}^0L_{Cu:In:Se,Va:Va:Va}^\alpha \right) + y_{In}^I y_{In}^{II} \left({}^0L_{In:In:Se,Va^{+2}}^\alpha \right) \\ + y_{Va}^I y_{Cu}^{II} \left({}^0L_{Va:Cu:Se,Va^{+2}:Va:Va}^\alpha \right) + y_{Va}^I y_{In}^{II} \left({}^0L_{Va:In:Se,Va^{+2}:Va:Va}^\alpha \right) \end{array} \right]$$

$$(7\text{-}7)$$

where y_i^I, y_i^{II} and y_i^{III} are site fractions on the first three sublattices. °G is the Gibbs energy of a real or fictitious compound. They are called end-members and there are 24 of them as listed in the above equations. The ${}^0L$ parameters are the interaction parameter between the end members.

The Gibbs energy of end-members, which have one defect, $\left({}^\circ G_{Cu:Cu:Se:Va:Va}^\alpha \right.$, ${}^\circ G_{Va:In:Se:Va:Va}^\alpha$, ${}^\circ G_{In:In:Se:Va:Va}^\alpha$, ${}^\circ G_{Cu:In:Va:Va:Va}^\alpha$, ${}^\circ G_{Va^{-1}:In:Se:Va:Va}^\alpha$, ${}^\circ G_{Cu:In:Va^{+2}:Va:Va}^\alpha$, etc) is obtained from defect formation energy and entropy calculation in the literature, which are based on the deviation from that of the same quantity of non-defective CIS.

For the end-members which have two defects, a simple reciprocal relation [7-8] is used to obtain its Gibbs energy.

$${}^\circ G_{Va:Cu:Se:Va:Va}^\alpha = {}^\circ G_{Cu:Cu:Se:Va:Va}^\alpha + {}^\circ G_{Va:In:Se:Va:Va}^\alpha - {}^\circ G_{Cu:In:Se:Va:Va}^\alpha$$

$$^{\circ}G^{\alpha}_{Va^{-1}:Cu:Se:Va:Va} = {}^{\circ}G^{\alpha}_{Cu:Cu:Se:Va:Va} + {}^{\circ}G^{\alpha}_{Va^{-1}:In:Se:Va:Va} - {}^{\circ}G^{\alpha}_{Cu:In:Se:Va:Va}$$

$$^{\circ}G^{\alpha}_{In:Cu:Se:Va:Va} = {}^{\circ}G^{\alpha}_{Cu:Cu:Se:Va:Va} + {}^{\circ}G^{\alpha}_{In:In:Se:Va:Va} - {}^{\circ}G^{\alpha}_{Cu:In:Se:Va:Va}$$

$$^{\circ}G^{\alpha}_{Va:In:Va:Va:Va} = {}^{\circ}G^{\alpha}_{Cu:In:Va:Va:Va} + {}^{\circ}G^{\alpha}_{Va:In:Se:Va:Va} - {}^{\circ}G^{\alpha}_{Cu:In:Se:Va:Va}$$

$$^{\circ}G^{\alpha}_{Va^{-1}:In:Va:Va:Va} = {}^{\circ}G^{\alpha}_{Cu:In:Va:Va:Va} + {}^{\circ}G^{\alpha}_{Va^{-1}:In:Se:Va:Va} - {}^{\circ}G^{\alpha}_{Cu:In:Se:Va:Va}$$

$$^{\circ}G^{\alpha}_{In:In:Va:Va:Va} = {}^{\circ}G^{\alpha}_{Cu:In:Va:Va:Va} + {}^{\circ}G^{\alpha}_{In:In:Se:Va:Va} - {}^{\circ}G^{\alpha}_{Cu:In:Se:Va:Va}$$

$$^{\circ}G^{\alpha}_{Va:In:Va^{+2}:Va:Va} = {}^{\circ}G^{\alpha}_{Cu:In:Va^{+2}:Va:Va} + {}^{\circ}G^{\alpha}_{Va:In:Se:Va:Va} - {}^{\circ}G^{\alpha}_{Cu:In:Se:Va:Va}$$

$$^{\circ}G^{\alpha}_{Va^{-1}:In:Va^{+2}:Va:Va} = {}^{\circ}G^{\alpha}_{Cu:In:Va^{+2}:Va:Va} + {}^{\circ}G^{\alpha}_{Va^{-1}:In:Se:Va:Va} - {}^{\circ}G^{\alpha}_{Cu:In:Se:Va:Va}$$

$$^{\circ}G^{\alpha}_{In:In:Va^{+2}:Va:Va} = {}^{\circ}G^{\alpha}_{Cu:In:Va^{+2}:Va:Va} + {}^{\circ}G^{\alpha}_{In:In:Se:Va:Va} - {}^{\circ}G^{\alpha}_{Cu:In:Se:Va:Va}$$

$$^{\circ}G^{\alpha}_{Cu:Cu:Va:Va:Va} = {}^{\circ}G^{\alpha}_{Cu:Cu:Se:Va:Va} + {}^{\circ}G^{\alpha}_{Cu:In:Va:Va:Va} - {}^{\circ}G^{\alpha}_{Cu:In:Se:Va:Va}$$

$$^{\circ}G^{\alpha}_{Cu:Cu:Va^{+2}:Va:Va} = {}^{\circ}G^{\alpha}_{Cu:Cu:Se:Va:Va} + {}^{\circ}G^{\alpha}_{Cu:In:Va^{+2}:Va:Va} - {}^{\circ}G^{\alpha}_{Cu:In:Se:Va:Va} \qquad (7\text{-}8)$$

The Gibbs energy of end-members, which have three or more than three defects are simply put to an arbitrarily large value [7-8].

The interaction parameter $^{\alpha}L^{0}$ are assumed to follow relationships that reduce the parameters;

$$\,^{\alpha}L^0_{Cu,In:*:*Va:Va} \quad = \quad \,^{\alpha}L^0_{Cu,In:In:Se:Va:Va} = \,^{\alpha}L^0_{Cu,In:Cu:Se:Va:Va} = \,^{\alpha}L^0_{Cu,In:In:Va:Va:Va}$$

$$= \,^{\alpha}L^0_{Cu,In:Cu:Va:Va:Va} = \,^{\alpha}L^0_{Cu,In:In:Va^{+2}:Va:Va} = \,^{\alpha}L^0_{Cu,In:Cu:Va^{+2}:Va:Va}$$

$$\,^{\alpha}L^0_{Cu,Va*:*:Va:Va} \quad = \quad \,^{\alpha}L^0_{Cu,Va:In:Se:Va:Va} = \,^{\alpha}L^0_{Cu,Va:Cu:Se:Va:Va} = \,^{\alpha}L^0_{Cu,Va:In:Va:Va:Va}$$

$$= \,^{\alpha}L^0_{Cu,Va:Cu:Va:Va:Va} = \,^{\alpha}L^0_{Cu,Va:In:Va^{+2}:Va:Va} = \,^{\alpha}L^0_{Cu,Va:Cu:Va^{+2}:Va:Va}$$

$$\,^{\alpha}L^0_{*:Cu,In:*:Va:Va} \quad = \quad \,^{\alpha}L^0_{Cu:Cu,In:Se:Va:Va} = \,^{\alpha}L^0_{In:Cu,In:Se:Va:Va} = \,^{\alpha}L^0_{In:Cu,In:Va:Va:Va}$$

$$= \,^{\alpha}L^0_{Cu:Cu,In:Va:Va:Va} = \,^{\alpha}L^0_{Cu:Cu,In:Va^{+2}:Va:Va} = \,^{\alpha}L^0_{Cu:Cu,In:Va^{+2}:Va:Va} \qquad (7\text{-}9)$$

$$= \,^{\alpha}L^0_{Va:Cu,In:Se:Va:Va} = \,^{\alpha}L^0_{Va:Cu,In:Va:Va:Va} = \,^{\alpha}L^0_{Va:Cu,In:Va^{+2}:Va:Va}$$

$$\,^{\alpha}L^0_{*:*:Se,Va:Va:Va} \quad = \quad \,^{\alpha}L^0_{Cu:Cu:Se,Va:Va:Va} = \,^{\alpha}L^0_{In:Cu:Se,Va:Va:Va} = \,^{\alpha}L^0_{Va:Cu:Se,Va:Va:Va}$$

$$= \,^{\alpha}L^0_{Cu:In:Se,Va:Va:Va} = \,^{\alpha}L^0_{In:In:Se,Va:Va:Va} = \,^{\alpha}L^0_{Va:In:Se,Va:Va:Va}$$

$$\,^{\alpha}L^0_{*:*:Se,Va^{+2}:Va:Va} \quad = \quad \,^{\alpha}L^0_{Cu:Cu:Se,Va^{+2}:Va:Va} = \,^{\alpha}L^0_{In:Cu:Se,Va^{+2}:Va:Va} = \,^{\alpha}L^0_{Va:Cu:Se,Va^{+2}:Va:Va}$$

$$= \,^{\alpha}L^0_{Cu:In:Se,Va^{+2}:Va:Va} = \,^{\alpha}L^0_{In:In:Se,Va^{+2}:Va:Va} = \,^{\alpha}L^0_{Va:In:Se,Va^{+2}:Va:Va}$$

7.4.1.2 *II. β_R-CIS ($Cu_1In_3Se_5$), γ-CIS($Cu_1In_5Se_8$), and β_H -CIS($Cu_2In_4Se_7$)*

Similar to the modeling the non-stoichiometric α-CIS ($CuInSe_2$) phase, a three sublattice model was also used to describe these compounds. Since the electrons and holes are not modeled in these CIS phases, sublattices IV and V are not added.

For β_R -CIS ($Cu_1In_3Se_5$) phase: $(\textbf{Cu}, Va, In)^I_1(\textbf{In}, Cu)^{II}_3(\textbf{Se}, Va)^{III}_5$

For γ - CIS($Cu_1In_5Se_8$) phase: $(\textbf{Cu}, Va, In)^I_1(\textbf{In}, Cu)^{II}_5(\textbf{Se}, Va)^{III}_8$

For β_H-CIS($Cu_2In_4Se_7$) phase : $(\textbf{Cu}, Va, In)^I_2(\textbf{In}, Cu)^{II}_4(\textbf{Se}, Va)^{III}_7$

As mentioned previously, these ODC compounds are formed by repeating periodically m units of $2V^{-1}_{Cu} + In^{+2}_{Cu}$ for every n unit of α-CIS ($CuInSe_2$) [7-9, 10]. The Gibbs energy for these compounds can also be expressed in the similar way as α-CIS ($CuInSe_2$). The value of Gibbs energy of the end-members of one or two defects in these compounds in relation to the Gibbs energy of the end-members of α-CIS ($CuInSe_2$) can be set by the following expression:

$$^{\circ}G^{\beta_R}_{i:j:k:Va:Va} = 2.5\times {^{\circ}G^{\alpha}_{i:j:k:Va:Va}},$$

$$^{\circ}G^{\beta_H}_{i:j:k:Va:Va} = 3.5\times {^{\circ}G^{\alpha}_{i:j:k:Va:Va}},$$

$$^{\circ}G^{\gamma}_{i:j:k:Va:Va} = 4\times {^{\circ}G^{\alpha}_{i:j:k:Va:Va}} \qquad (7\text{-}10)$$

where i, j, and k represent the various sublattice constituents. For example, $^\circ G^{\beta_R}_{Cu\,:\,Cu\,:\,Se\,:\,Va\,:\,Va} =$

$2.5 \times {}^\circ G^{\alpha}_{Cu\,:\,Cu\,:\,Se\,:\,Va\,:\,Va}$.
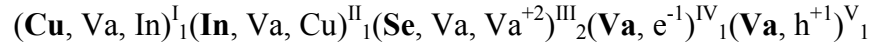
7.4.2 Calculation of the Carrier Concentration in α-CIS (CuInSe$_2$)

The free electrons and holes concentration can be calculated if they are also included in the thermodynamic description. They are supposed to be distributed on different numbers of sites than there are sites in the sublattices [7-11]. As known from the Fermi-Dirac distribution function for electrons in the conduction band and holes in the valence band N_c and N_v stand for the effective density of the conduction and valence band states, respectively. So, let N_c and N_v be the number of sites that electrons and holes can occupy per formula unit.

According to the above description, the α-CIS phase can be described by the following sublattices.

$$(\textbf{Cu}, Va, Va^{-1}, \textbf{In})^I_1(\textbf{In}, Cu)^{II}_1(\textbf{Se}, Va, Va^{+2})^{III}_2(\textbf{Va}, e^{-1})^{IV}_{Nc}(\textbf{Va}, h^{+1})^V_{Nv}$$
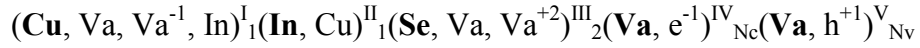
This model can be directly described with the Compound Energy Model (CEM). However, CEM requires N_c and N_v to be constant. Chen *et al.* [7-8] provided an alternative way to solve this problem and transferred the sublattice description to the following:

$$(\textbf{Cu}, Va, In)^I_1(\textbf{In}, Va, Cu)^{II}_1(\textbf{Se}, Va, Va^{+2})^{III}_2(\textbf{Va}, e^{-1})^{IV}_1(\textbf{Va}, h^{+1})^V_1$$

Here is briefly described their transformation methodology by applying it to the α-CIS phase. The effect of adding the IV sublattice for electrons is, instead of having the term, $y^I_* y^{II}_* y^{III}_* G^0_{*:*:*}$, the equation

$$y^I_* y^{II}_* y^{III}_* y^{IV}_{Va} G^0_{*:*:*:Va} + y^I_* y^{II}_* y^{III}_* y^{IV}_{e^{-1}} G^0_{*:*:*:e^{-1}} = y^I_* y^{II}_* y^{III}_* (1 - y^{IV}_{e^{-1}}) G^0_{*:*:*:Va} + y^I_* y^{II}_* y^{III}_* y^{IV}_{e^{-1}} G^0_{*:*:*:e^{-1}}$$

$$= y^I_* y^{II}_* y^{III}_* G^0_{*:*:*:Va} + (G^0_{*:*:*:e^{-1}} - G^0_{*:*:*:Va}) y^I_* y^{II}_* y^{III}_* y^{IV}_{e^{-1}}$$

$$(y^{IV}_{Va} + y^{IV}_{e^{-1}} = 1) \qquad\qquad (7\text{-}11)$$

For simplicity, it is assumed all values $(G^0_{*:*:*:e^{-1}} - G^0_{*:*:*:Va})$ are equal. However, the quantities refer to N_c moles of electron. Denote the electron chemical potential as

$$\Delta G^0_{e^{-1}} - G^{0,ref} = (G^0_{*:*:*:e^{-1}} - G^0_{*:*:*:Va})/N_c \qquad\qquad (7\text{-}12)$$

The $G^{0,ref}$ can be immediately omitted due to the condition of electroneutrality. It will drop out of the final expression for G if the same reference is used for all charged constituents. Substituting equation (7-12) into equation (7-11) yields

$$y_*^I y_*^{II} y_*^{III} y_{Va}^{IV} G^0_{***:Va} + y_*^I y_*^{II} y_*^{III} y_{e^{-1}}^{IV} G^0_{***:e^{-1}}$$

$$= y_*^I y_*^{II} y_*^{III} G^0_{***:Va} + \Delta G^0_{e^{-1}} y_*^I y_*^{II} y_*^{III} (N_c \bullet y_{e^{-1}}^{IV})$$

(7-13)

Since $\sum_I \sum_{II} \sum_{III} y_*^I y_*^{II} y_*^{III} = 1$, all the values of $\Delta G^0_{e^{-1}}$ are equal and similar expressions for the holes exist

$$G^{New} = G^{Old}$$

$$+ \Delta G^0_{e^{-1}}(N_c \bullet y_{e^{-1}}^{IV}) \sum_I \sum_{II} \sum_{III} y_*^I y_*^{II} y_*^{III} + \Delta G^0_{h^{+1}}(N_V \bullet y_{h^{+1}}^{IV}) \sum_I \sum_{II} \sum_{III} y_*^I y_*^{II} y_*^{III} + \Delta G^0_{e^{-1}h^{+1}}(N_c \bullet y_{e^{-1}}^{IV})(N_V \bullet y_{h^{+1}}^{IV})$$

$$+ RTN_c[y_{e^{-1}}^{IV} \ln y_{e^{-1}}^{IV} + (1 - y_{e^{-1}}^{IV})\ln(1 - y_{e^{-1}}^{IV})] + RTN_V[y_{h^{+1}}^{IV} \ln y_{h^{+1}}^{IV} + (1 - y_{h^{+1}}^{IV})\ln(1 - y_{h^{+1}}^{IV})]$$

$$= G^{Old}$$

$$+ [\Delta G^0_{e^{-1}} - \underline{\underline{RT\ln(N_c)}}](N_c \bullet y_{e^{-1}}^{IV}) \sum_I \sum_{II} \sum_{III} y_*^I y_*^{II} y_*^{III} +$$

(7-14)

$$[\Delta G^0_{h^{+1}} - \underline{RT\ln(N_v)}](N_V \bullet y_{h^{+1}}^{IV}) \sum_I \sum_{II} \sum_{III} y_*^I y_*^{II} y_*^{III} + \Delta G^0_{e^{-1}h^{+1}}(N_c \bullet y_{e^{-1}}^{IV})(N_V \bullet y_{h^{+1}}^{IV})$$

$$+ RT\{(N_c \bullet y_{e^{-1}}^{IV})\ln(\underline{\underline{N_c}} \bullet y_{e^{-1}}^{IV}) + [N_c \bullet (1 - y_{e^{-1}}^{IV})]\ln[\underline{\underline{N_c}} \bullet (1 - y_{e^{-1}}^{IV})\} +$$

$$RT\{(N_V \bullet y_{h^{+1}}^{IV})\ln(\underline{N_v} \bullet y_{h^{+1}}^{IV}) + [N_v \bullet (1 - y_{h^{+1}}^{IV})]\ln[\underline{N_v} \bullet (1 - y_{h^{+1}}^{IV})]\}$$

Based on the above formula, the full α-phase CIS is represented as:

$$(\textbf{Cu, Va, In})^I_1(\textbf{In, Va, Cu})^{II}_1(\textbf{Se, Va})^{III}_2(\textbf{Va, e}^{-1})^{IV}_1(\textbf{Va, h}^{+1})^V_1$$

Defining the midgap energy as the energy reference, the following relations exist

$$G^0_{***:Va:Va} = G^0_{***}$$

$$G^0_{***:e^{-1}:Va} = G^0_{***} + \frac{E_g}{2} - RT\ln N_C$$

$$G^0_{***:Va:h^{+1}} = G^0_{***} + \frac{E_g}{2} - RT\ln N_V$$

(7-15)

$$G^0_{***:e^{-1}:h^{+1}} = G^0_{***} + E_g - RT\ln N_C - RT\ln N_V$$

The last relation is not meant to be realistic, but it has a negligible effect because the contributions of both free electrons and holes are small relative to site density. The effective densities N_c and N_v are calculated by the following equations [7-8]:

$$N_c = 2(2\pi m_c^* kT / h^2)^{3/2} \bullet (a^2 c / 8)$$

$$N_v = 2(2\pi m_v^* kT / h^2)^{3/2} \bullet (a^2 c / 8)$$

(7-16)

$(a^2 c / 8)$ is the volume per mole of the formula units and is added to get the densities counted per mole of formula units. m_c^* and m_v^* are the effective masses of electrons at the conduction

band edge and holes at the valence band edge, respectively. *k* is Boltzman's constant, and *h* is Planck's constant. The values of all the parameters are summarized in Table 7-3 [7-12, 13].

7.4.3   Results and Discussion

A reasonable agreement for the α-CIS phase was obtained between the model-calculated values and the phase equilibrium available in the literature as shown in Figure 7-2. The optimized parameters are listed in the Table 7-6. The calculated defect and carrier concentration data is shown in Figure 7-3.

Further work needs to be done to get better agreement of phase equilibrium for all the phases.

7.5   References cited

[7-1]   T. Gödecke, T. Haalboom, and F. Ernst , *Zeitschrift für Metallkunde*, Vol. 91, No. 8 pp.622-662, 2000.

[7-2]   R.D. Wieting, *the 29th IEEE Photovoltaic Specialist Conference*, 2002.

[7-3]   D.X. Liao, A. Rockett, *Applied Physics Letters,* Vol. 82, No. 17, pp. 2829-2831, 2003.

[7-4]   C-H Chang, *Processing and Characterization of Copper Indium Selenide for Photovoltaic Applications*, Ph.D. Dissertation, University of Florida, 2000.

[7-5]   P.R. Subramanian and D.E. Laughlin. *Bulletin of Alloy Phase Diagrams* 10, p. 554, 1989.

[7-6]   W. Zhuang, C-H Chang, J. Sheng, and T.J. Anderson, *CALPHAD*, 2002.

[7-7]   S.S. Li, *Semiconductor Physical Electronics*, Plenum Press, New York and London, 1993.

[7-8]   Q. Chen, M. Hillert, B. Sundman, W.A. Oates, S. G. Fries, and R. Schmid-Fetzer, *Journal of Electronic Materials*, Vol. 27, No. 3   pp.961-971, 1998.

[7-9]   S. B. Zhang, Su-Huai Wei, and Alex Zunger, *Physical Review B*, Vol. 57, No. 16 pp9642 –9656, 1998.

[7-10] S. B. Zhang, Su-Huai Wei, and Alex Zunger, *Physical Review Letters*, Vol. 78, No. 21 pp4059 – 4062, 1997.

[7-11] T. J. Anderson, *CALPHAD*, Vol. 21, No. 2, pp. 266-282, 1997.

[7-12] John B. Mooney and Robert H. Lamoreaux, *Solar Cells*, Vol. 16. pp. 211-220, 1986.

[7-13] O. Madelung, *Numerical Data and Functional Relationships in Science and Technology Semiconductors: Physics of III-V Compounds*, Berlin, New York : Springer-Verlag, 1991.

[7-14] P.R. Subramanian and D.E. Laughlin. *Bulletin of Alloy Phase Diagrams* 10, p. 554, 1989.

[7-15] M. A. Contreras, H. Wiesner, D. Niles, K. Ramanathan, R. Maston, J. Tuttle, J. Keane, and R. Noufi, *the 25th IEEE Photovoltaic Specialist Conference*, Washington, D.C. 1996.

[7-16] A. L. Fahrenbruch, and R. H. Bube, *Fundamentals of Solar Cells,* Academic Press, New York-London, 1983.

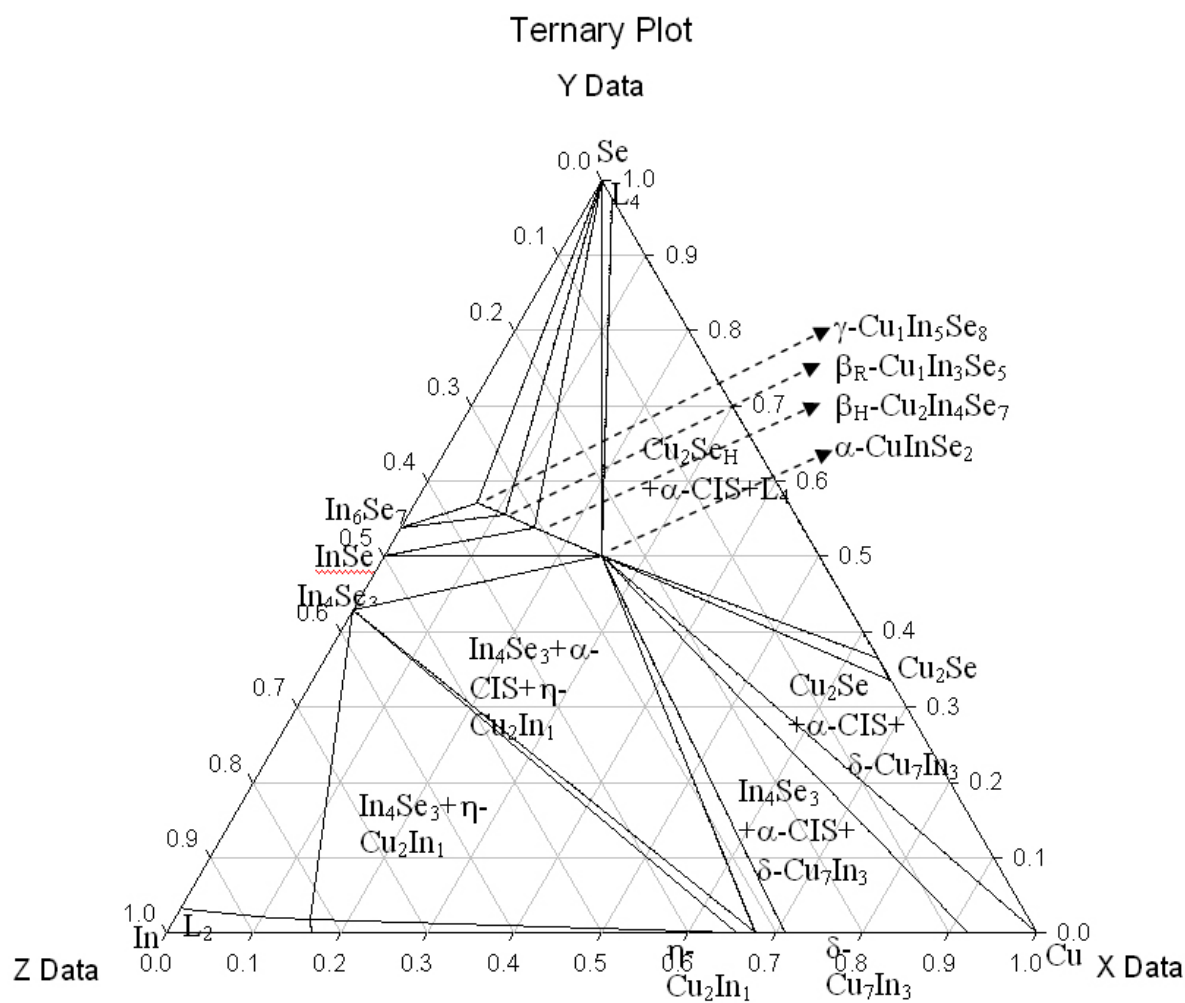[7-17] J.C. Mikkelsen, *Journal of Electronic Materials*, Vol. 10, pp. 541, 1981.

Figure 7-1. Simulation results of defect free Cu-In-Se system.
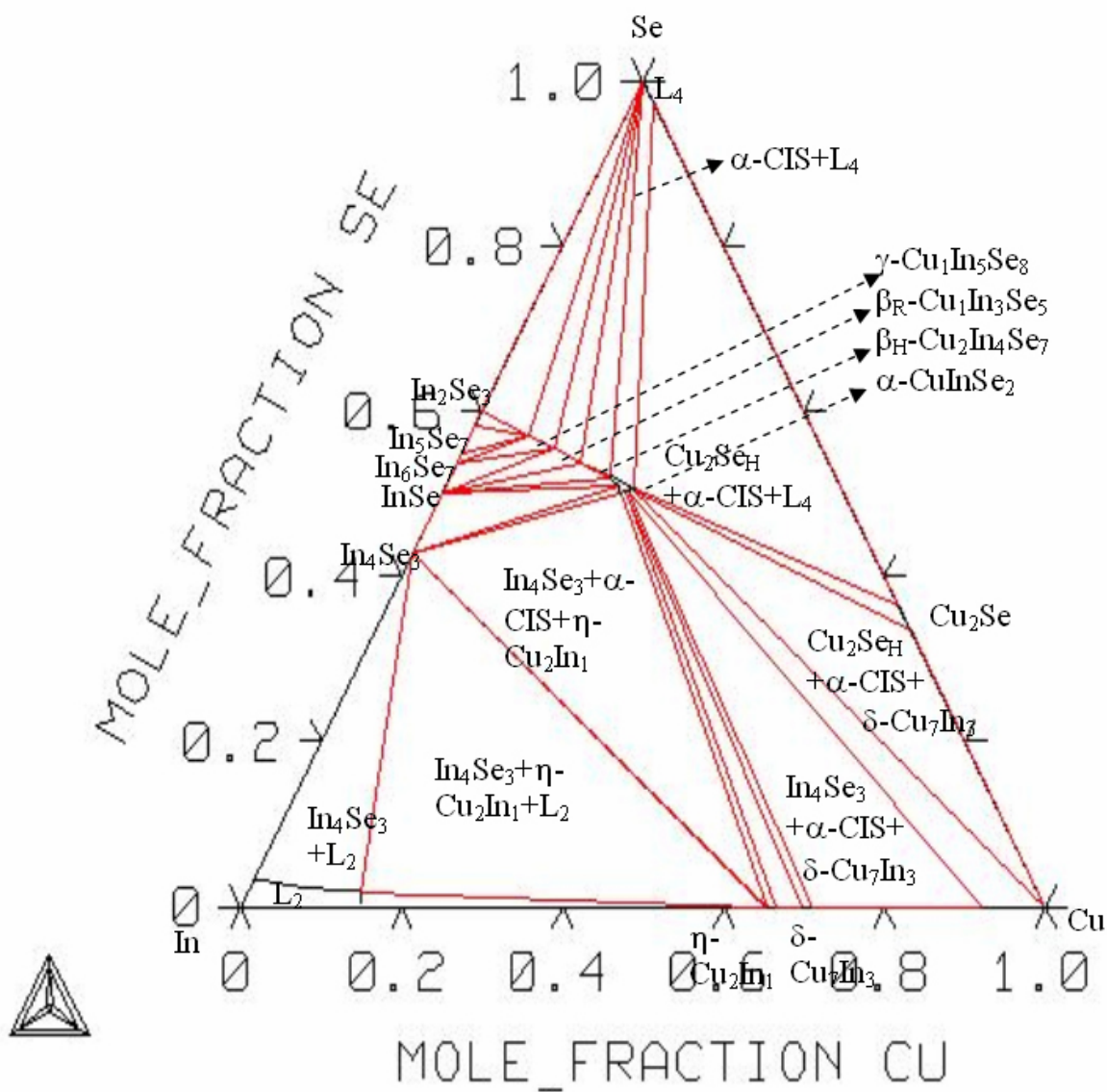
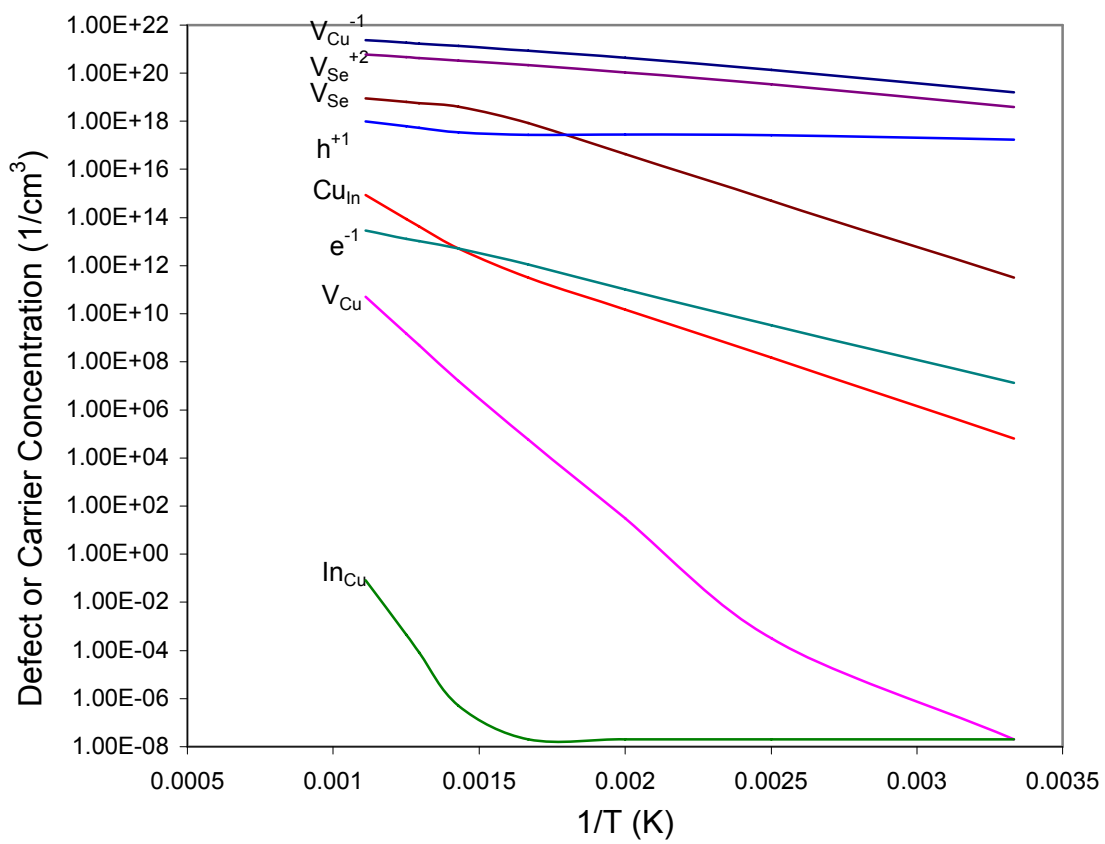Figure 7-2. Predicted phase diagram of the Cu-In-Se system at 773 K that indicates non stoichiometric CuInSe$_2$.

Figure 7-3. Calculated defect and carrier concentration at the α-CIS/β-Cu$_2$Se phase boundary.

Table 7-1. Experimental compositions in the Cu-In-Se system at 773K [7-1].

Phases	Composition, at. % Se	Composition, at. % Cu
α-CIS/β$_R$-CIS/IONIC_LIQ	0.5294/0.553/0.9852	0.1963/0.149/0.00142
IONIC_LIQ/α-CIS	0.5234/0.9904 0.5195/0.9926 0.5141/0.99285	0.2052/0.001896 0.2152/0.001942 0.2250/0.003625
α-CIS /β-Cu$_2$Se /IONIC_LIQ	0.5096/0.3794/0.994	0.2354/0.6157/0.00592
α-CIS /β-Cu$_2$Se /CU_FCC	0.5017/0.33646/0.0054	0.23895/0.6562/0.9061
α-CIS /CU_FCC	0.5003/0/0.00296	0.2371/0.7/0.904
α-CIS /δ (Cu$_7$Se$_3$) /η(Cu$_2$In$_1$)	0.4988/0/0.0064	0.2353/0.7/0.6388
α-CIS / IN$_4$SE$_3$/η(Cu$_2$In$_1$)	0.4983/0.4286/0.001	0.2326/0/0.6225
α-CIS /IN$_1$SE$_1$_A/IN$_4$SE$_3$	0.5012/0.5/0.4286	0.2278/0/0
α-CIS / IN$_1$SE$_1$_A/β$_H$-CIS	0.5052/0.5/0.5141	0.22156/0/0.1388
α-CIS /β$_R$-CIS /β$_H$-CIS	0.5101/0.52795/0.523	0.2123/0.1649/0.161
IONIC_LIQ/γ- In$_2$Se$_3$/γ-CIS	0.961/0.6/0.5942	0/0/0.0332
IONIC_LIQ/γ-CIS /β$_R$-CIS	0.978/0.5932/0.589	0.02/0.0557/0.095
In$_6$Se$_7$/γ-CIS//β$_R$-CIS	0.538/0.5675/0.5537	0/0.0592/0.088
In$_6$Se$_7$/γ-CIS/ In$_9$Se$_{11}$	0.538/0.5720/0.55	0/0.052/0
In$_5$Se$_7$/γ-CIS/ In$_9$Se$_{11}$	0.5933/0.5744/0.55	0/0.0465/0
In$_5$Se$_7$/γ-CIS/β-In$_2$Se$_3$	0.5933/0.5819/0.6	0/0.0368/0

Table 7-2. Summary of the optimized parameters. Note: all the units are in J/mol.

Phases and Functions	Parameters
α-CIS (CuInSe$_2$)	$^\circ G^\alpha_{Cu\,:\,In\,:\,Se\,:\,Va\,:\,Va} = CIS\_A$
β$_R$-CIS (Cu$_1$In$_3$Se$_5$)	$^\circ G^{\beta_R}_{Cu\,:\,In\,:\,Se\,:\,Va\,:\,Va} = 2.5\times CIS\_A + V_1$
β$_H$-CIS (Cu$_2$In$_4$Se$_7$)	$^\circ G^{\beta_H}_{Cu\,:\,In\,:\,Se\,:\,Va\,:\,Va} = 3.5\times CIS\_A + V_2$
γ-CIS (Cu$_1$In$_5$Se$_8$)	$^\circ G^{\gamma}_{Cu\,:\,In\,:\,Se\,:\,Va\,:\,Va} = 4\times CIS\_A + V_3$
η (Cu$_2$In$_1$)	In addition to all the parameters from Cu-In binary system [7-14], the following ternary interaction parameters are added: $^{\eta}L^0_{Cu,In,Se:*} = -1029637$ $^{\eta}L^0_{*:Cu,In,Se} = -1029637$
β-Cu$_2$Se	In addition to all the parameters from Cu-Se binary system [7-4], the following ternary interaction parameter is added: $^{\beta-Cu_2Se}L^0_{Cu,In,Va:Se:Cu} = -20000$
δ (Cu$_7$In$_3$)	In addition to all the parameters from Cu-In binary system [7-14], the following ternary interaction parameters are added $^{\delta}L^0_{Cu,In,Se:*} = -90000$ $^{\delta}L^0_{*:Cu,In,Se} = -90000$
Fcc (Cu)	In addition to all the parameters from Cu-In and Cu-Se binary system[44, 50], the following ternary interaction parameter is added $^{CuFcc}L^0_{Cu,In,Se} = -90000$
Ionic_Liq	In addition to all the parameters from Cu-In In-Se and Cu-Se binary[7-15, 16] system, the following ternary interaction parameters are added: $^{Ionic\_Liq}L^0_{Cu^{+1},Cu^{+2},In^{+3}:Se^{-2}} = -46015$; $^{Ionic\_Liq}L^1_{Cu^{+1},Cu^{+2},In^{+3}:Se^{-2}} = 9015$

Table 7-3. Summary of some of α-CIS property values.

Parameter	Value	Ref
A	5.782 Å	[7-13]
C	2.0097 a = 11.6201 Å	[7-13]
E_g	0.965 -1.086×10^{-4} T^2/(T+97) (eV)	[7-17]
m_c^*	0.091 m$_0$	[7-17]
m_v^*	0.091 m$_0$ (= 9.11×10^{-31} kg)	[7-17]
k	8.617 × 10^{-5} eV/K	[7-17]
h	6.63 × 10^{-34} J · S	[7-17]
$N_c \approx N_v$	6.34 × 10^{-13} T$^{3/2}$	[7-17]

Table 7-4. Summary of the optimized parameters for off-stoichiometry CIS.

Phases and Functions	Parameters
α-CIS (CuInSe$_2$)	$^\circ G^\alpha_{Cu\,:\,In\,:\,Se\,:\,Va\,:\,Va} = \text{CIS\_A}$
	$^\circ G^\alpha_{Va\,:\,In\,:\,Se\,:\,Va\,:\,Va} = \text{VIS\_A}$
	$^\circ G^\alpha_{Va^{-1}\,:\,In\,:\,Se\,:\,Va\,:\,Va} = \text{EIS\_A}$
	$^\circ G^\alpha_{In\,:\,In\,:\,Se\,:\,Va\,:\,Va} = \text{IIS\_A}$
	$^\circ G^\alpha_{Cu\,:\,Cu\,:\,Se\,:\,Va\,:\,Va} = \text{CS\_A}$
	$^\circ G^\alpha_{Cu\,:\,In\,:\,Va\,:\,Va\,:\,Va} = \text{CIV\_A}$
	$^\circ G^\alpha_{Cu\,:\,In\,:\,Va^{+2}\,:\,Va\,:\,Va} = \text{CIH\_A}$
	$^\circ G^\alpha_{Va\,:\,Cu\,:\,Se\,:\,Va\,:\,Va} = \text{CCS\_A+VIS\_A-CIS\_A}$
	$^\circ G^\alpha_{Va^{-1}\,:\,Cu\,:\,Se\,:\,Va\,:\,Va} = \text{CCS\_A+EIS\_A-CIS\_A}$
	$^\circ G^\alpha_{In\,:\,Cu\,:\,Se\,:\,Va\,:\,Va} = \text{CCS\_A+IIS\_A-CIS\_A}$
	$^\circ G^\alpha_{Va\,:\,In\,:\,Va\,:\,Va\,:\,Va} = \text{VIS\_A+CIV\_A-CIS\_A}$
	$^\circ G^\alpha_{Va^{-1}\,:\,In\,:\,Va\,:\,Va\,:\,Va} = \text{EIS\_A+CIV\_A-CIS\_A}$
	$^\circ G^\alpha_{In\,:\,In\,:\,Va\,:\,Va\,:\,Va} = \text{IIS\_A+CIV\_A-CIS\_A}$
	$^\circ G^\alpha_{Va\,:\,In\,:\,Va^{+2}\,:\,Va\,:\,Va} = \text{CIH\_A+VIS\_A-CIS\_A}$
	$^\circ G^\alpha_{Va^{-1}\,:\,In\,:\,Va^{+2}\,:\,Va\,:\,Va} = \text{CIH\_A+EIS\_A-CIS\_A}$
	$^\circ G^\alpha_{In\,:\,In\,:\,Va^{+2}\,:\,Va\,:\,Va} = \text{CIH\_A+IIS\_A-CIS\_A}$
	$^\circ G^\alpha_{Cu\,:\,Cu\,:\,Va\,:\,Va\,:\,Va} = \text{CIV\_A+CCS\_A-CIS\_A}$
	$^\circ G^\alpha_{Cu\,:\,Cu\,:\,Va^{+2}\,:\,Va\,:\,Va} = \text{CCS\_A+CIH\_A-CIS\_A}$
	$^\circ G^\alpha_{Cu\,:\,In\,:\,Se\,:\,Va^{-1}\,:\,Va} = \text{CIS\_A+TEGN}$

147

$$^{\circ}G^{\alpha}_{Va\,:\,In\,:\,Se\,:\,Va^{-1}\,:\,Va} = \text{ VIS\_A+TEGN}$$

$$^{\circ}G^{\alpha}_{Va^{-1}\,:\,In\,:\,Se\,:\,Va^{-1}\,:\,Va} = \text{EIS\_A+TEGN}$$

$$^{\circ}G^{\alpha}_{In\,:\,In\,:\,Se\,:\,Va^{-1}\,:\,Va} = \text{IIS\_A+TEGN}$$

$$^{\circ}G^{\alpha}_{Cu\,:\,Cu\,:\,Se\,:\,Va^{-1}\,:\,Va} = \text{CCS\_A+TEGN}$$

$$^{\circ}G^{\alpha}_{Cu\,:\,In\,:\,Va\,:\,Va^{-1}\,:\,Va} = \text{CIV\_A+TEGN}$$

$$^{\circ}G^{\alpha}_{Cu\,:\,In\,:\,Va^{+2}\,:\,Va^{-1}\,:\,Va} = \text{CIH\_A+TEGN}$$

$$^{\circ}G^{\alpha}_{Cu\,:\,In\,:\,Se\,:\,Va\,:\,Va^{+1}} = \text{CIS\_A+TEGH}$$

$$^{\circ}G^{\alpha}_{Va\,:\,In\,:\,Se\,:\,Va\,:\,Va^{+1}} = \text{ VIS\_A+TEGH}$$

$$^{\circ}G^{\alpha}_{Va^{-1}\,:\,In\,:\,Se\,:\,Va\,:\,Va^{+1}} = \text{EIS\_A+TEGH}$$

$$^{\circ}G^{\alpha}_{In\,:\,In\,:\,Se\,:\,Va\,:\,Va^{+1}} = \text{ IIS\_A+TEGH}$$

$$^{\circ}G^{\alpha}_{Cu\,:\,Cu\,:\,Se\,:\,Va\,:\,Va^{+1}} = \text{CCS\_A+TEGH}$$

$$^{\circ}G^{\alpha}_{Cu\,:\,In\,:\,Va\,:\,Va\,:\,Va^{+1}} = \text{CIV\_A+TEGH}$$

$$^{\circ}G^{\alpha}_{Cu\,:\,In\,:\,Va^{+2}\,:\,Va\,:\,Va^{+1}} = \text{CIH\_A+TEGH}$$

$$^{\circ}G^{\alpha}_{Cu\,:\,In\,:\,Se\,:\,Va^{-1}\,:\,Va^{+1}} = \text{CIS\_A+TEGH+TEGN}$$

$$^{\alpha}L^{0}_{Cu,In:*:*:Va:Va} = \text{LCI}$$

$$^{\alpha}L^{0}_{Cu,Va:*:*:Va:Va} = \text{LCV}$$

$$^{\alpha}L^{0}_{Cu,Va^{-1}:*:*:Va:Va} = \text{LCE}$$

	$^{\alpha}L^{0}_{*:Cu,In:*:Va:Va}$ = LIC $^{\alpha}L^{0}_{*:*:Se,Va:Va:Va}$ = LSV $^{\alpha}L^{0}_{*:*:Se,Va^{+2}:Va:Va}$ = LSH
β_R-CIS (Cu$_1$In$_3$Se$_5$)	$^{\circ}G^{\beta_R}_{Cu\,:\,In\,:\,Se\,:\,Va\,:\,Va}$ = 2.5×CIS_A+44500 $^{\circ}G^{\beta_R}_{Cu\,:\,Cu\,:\,Se\,:\,Va\,:\,Va}$ = 2.5×CCS_A $^{\circ}G^{\beta_R}_{Va\,:\,In\,:\,Se\,:\,Va\,:\,Va}$ = 2.5×VIS_A $^{\circ}G^{\beta_R}_{In\,:\,In\,:\,Se\,:\,Va\,:\,Va}$ = 2.5×IIS_A $^{\circ}G^{\beta_R}_{Cu\,:\,In\,:\,Va\,:\,Va\,:\,Va}$ = 2.5×CIV_A $^{\circ}G^{\beta_R}_{Va^{-1}\,:\,In\,:\,Se\,:\,Va\,:\,Va}$ = 2.5×EIS_A $^{\circ}G^{\beta_R}_{Cu\,:\,In\,:\,Va^{+2}\,:\,Va\,:\,Va}$ = 2.5×CIH_A $^{\circ}G^{\beta_R}_{Va\,:\,Cu\,:\,Se\,:\,Va\,:\,Va}$ = 2.5×CCS_A+2.5×VIS_A-2.5×CIS_A $^{\circ}G^{\beta_R}_{Va^{-1}\,:\,Cu\,:\,Se\,:\,Va\,:\,Va}$ = 2.5×CCS_A+2.5×EIS_A-2.5×CIS_A $^{\circ}G^{\beta_R}_{In\,:\,Cu\,:\,Se\,:\,Va\,:\,Va}$ = 2.5×CCS_A+2.5×IIS_A-2.5×CIS_A $^{\circ}G^{\beta_R}_{Va\,:\,In\,:\,Va\,:\,Va\,:\,Va}$ = 2.5×VIS_A+2.5×CIV_A-2.5×CIS_A $^{\circ}G^{\beta_R}_{Va^{-1}\,:\,In\,:\,Va\,:\,Va\,:\,Va}$ = 2.5×EIS_A+2.5×CIV_A-2.5×CIS_A $^{\circ}G^{\beta_R}_{In\,:\,In\,:\,Va\,:\,Va\,:\,Va}$ = 2.5× IIS_A+2.5×CIV_A-2.5×CIS_A $^{\circ}G^{\beta_R}_{Va\,:\,In\,:\,Va^{+2}\,:\,Va\,:\,Va}$ = 2.5×CIH_A+2.5×VIS_A-2.5×CIS_A $^{\circ}G^{\beta_R}_{Va^{-1}\,:\,In\,:\,Va^{+2}\,:\,Va\,:\,Va}$ = 2.5×CIH_A+2.5×EIS_A-2.5×CIS_A

	$^{\circ}G^{\beta_R}_{In:In:Va^{+2}:Va:Va} = 2.5\times CIH\_A + 2.5\times IIS\_A - 2.5\times CIS\_A$
	$^{\circ}G^{\beta_R}_{Cu:Cu:Va:Va:Va} = 2.5\times CIV\_A + 2.5\times CCS\_A - 2.5\times CIS\_A$
	$^{\circ}G^{\beta_R}_{Cu:Cu:Va^{+2}:Va:Va} = 2.5\times CCS\_A + 2.5\times CIH\_A - 2.5\times CIS\_A$
	$^{\circ}G^{\beta_R}_{Cu:In:Se:Va^{-1}:Va} = 2.5\times CIS\_A + TEGN$
	$^{\circ}G^{\beta_R}_{Va:In:Se:Va^{-1}:Va} = 2.5\times VIS\_A + TEGN$
	$^{\circ}G^{\beta_R}_{Va^{-1}:In:Se:Va^{-1}:Va} = 2.5\times EIS\_A + TEGN$
	$^{\circ}G^{\beta_R}_{In:In:Se:Va^{-1}:Va} = 2.5\times IIS\_A + TEGN$
	$^{\circ}G^{\beta_R}_{Cu:Cu:Se:Va^{-1}:Va} = 2.5\times CCS\_A + TEGN$
	$^{\circ}G^{\beta_R}_{Cu:In:Va:Va^{-1}:Va} = 2.5\times CIV\_A + TEGN$
	$^{\circ}G^{\beta_R}_{Cu:In:Va^{+2}:Va^{-1}:Va} = 2.5\times CIH\_A + TEGN$
	$^{\circ}G^{\beta_R}_{Cu:In:Se:Va:Va^{+1}} = 2.5\times CIS\_A + TEGH$
	$^{\circ}G^{\beta_R}_{Va:In:Se:Va:Va^{+1}} = 2.5\times VIS\_A + TEGH$
	$^{\circ}G^{\beta_R}_{Va^{-1}:In:Se:Va:Va^{+1}} = 2.5\times EIS\_A + TEGH$
	$^{\circ}G^{\beta_R}_{In:In:Se:Va:Va^{+1}} = 2.5\times IIS\_A + TEGH$
	$^{\circ}G^{\beta_R}_{Cu:Cu:Se:Va:Va^{+1}} = 2.5\times CCS\_A + TEGH$
	$^{\circ}G^{\beta_R}_{Cu:In:Va:Va:Va^{+1}} = 2.5\times CIV\_A + TEGH$
	$^{\circ}G^{\beta_R}_{Cu:In:Va^{+2}:Va:Va^{+1}} = 2.5\times CIH\_A + TEGH$
	$^{\circ}G^{\beta_R}_{Cu:In:Se:Va^{-1}:Va^{+1}} = 2.5\times CIS\_A + TEGH + TEGN$
β_H-CIS (Cu$_2$In$_4$Se$_7$)	$^{\circ}G^{\beta_H}_{Cu:In:Se:Va:Va} = 3.5\times CIS\_A + 44500$
	$^{\circ}G^{\beta_H}_{Cu:Cu:Se:Va:Va} = 3.5\times CCS\_A$
	$^{\circ}G^{\beta_H}_{Va:In:Se:Va:Va} = 3.5\times VIS\_A$

150

$$^{\circ}G^{\beta_H}_{In:In:Se:Va:Va} = 3.5\times\text{IIS\_A}$$

$$^{\circ}G^{\beta_H}_{Cu:In:Va:Va:Va} = 3.5\times\text{CIV\_A}$$

$$^{\circ}G^{\beta_H}_{Va^{-1}:In:Se:Va:Va} = 3.5\times\text{EIS\_A}$$

$$^{\circ}G^{\beta_H}_{Cu:In:Va^{+2}:Va:Va} = 3.5\times\text{CIH\_A}$$

$$^{\circ}G^{\beta_H}_{Va:Cu:Se:Va:Va} = 3.5\times\text{CCS\_A}+3.5\times\text{VIS\_A}-3.5\times\text{CIS\_A}$$

$$^{\circ}G^{\beta_H}_{Va^{-1}:Cu:Se:Va:Va} = 3.5\times\text{CCS\_A}+3.5\times\text{EIS\_A}-3.5\times\text{CIS\_A}$$

$$^{\circ}G^{\beta_H}_{In:Cu:Se:Va:Va} = 3.5\times\text{CCS\_A}+3.5\times\text{IIS\_A}-3.5\times\text{CIS\_A}$$

$$^{\circ}G^{\beta_H}_{Va:In:Va:Va:Va} = 3.5\times\text{VIS\_A}+3.5\times\text{CIV\_A}-3.5\times\text{CIS\_A}$$

$$^{\circ}G^{\beta_H}_{Va^{-1}:In:Va:Va:Va} = 3.5\times\text{EIS\_A}+3.5\times\text{CIV\_A}-3.5\times\text{CIS\_A}$$

$$^{\circ}G^{\beta_H}_{In:In:Va:Va:Va} = 3.5\times\text{IIS\_A}+3.5\times\text{CIV\_A}-3.5\times\text{CIS\_A}$$

$$^{\circ}G^{\beta_H}_{Va:In:Va^{+2}:Va:Va} = 3.5\times\text{CIH\_A}+3.5\times\text{VIS\_A}-3.5\times\text{CIS\_A}$$

$$^{\circ}G^{\beta_H}_{Va^{-1}:In:Va^{+2}:Va:Va} = 3.5\times\text{CIH\_A}+3.5\times\text{EIS\_A}-3.5\times\text{CIS\_A}$$

$$^{\circ}G^{\beta_H}_{In:In:Va^{+2}:Va:Va} = 3.5\times\text{CIH\_A}+3.5\times\text{IIS\_A}-3.5\times\text{CIS\_A}$$

$$^{\circ}G^{\beta_H}_{Cu:Cu:Va:Va:Va} = 3.5\times\text{CIV\_A}+3.5\times\text{CCS\_A}-3.5\times\text{CIS\_A}$$

$$^{\circ}G^{\beta_H}_{Cu:Cu:Va^{+2}:Va:Va} = 3.5\times\text{CCS\_A}+3.5\times\text{CIH\_A}-3.5\times\text{CIS\_A}$$

$$^{\circ}G^{\beta_H}_{Cu:In:Se:Va^{-1}:Va} = 3.5\times\text{CIS\_A}+\text{TEGN}$$

$$^{\circ}G^{\beta_H}_{Va:In:Se:Va^{-1}:Va} = 3.5\times\text{VIS\_A}+\text{TEGN}$$

$$^{\circ}G^{\beta_H}_{Va^{-1}:In:Se:Va^{-1}:Va} = 3.5\times\text{EIS\_A}+\text{TEGN}$$

$$^{\circ}G^{\beta_H}_{In:In:Se:Va^{-1}:Va} = 3.5\times\text{IIS\_A}+\text{TEGN}$$

$$^{\circ}G^{\beta_H}_{Cu:Cu:Se:Va^{-1}:Va} = 3.5\times\text{CCS\_A}+\text{TEGN}$$

$$^{\circ}G^{\beta_H}_{Cu:In:Va:Va^{-1}:Va} = 3.5\times\text{CIV\_A}+\text{TEGN}$$

$$^{\circ}G^{\beta_H}_{Cu:In:Va^{+2}:Va^{-1}:Va} = 3.5\times\text{CIH\_A}+\text{TEGN}$$

	$^{\circ}G^{\beta_H}_{Cu:In:Se:Va:Va^{+1}} = 3.5 \times CIS\_A + TEGH$
	$^{\circ}G^{\beta_H}_{Va:In:Se:Va:Va^{+1}} = 3.5 \times VIS\_A + TEGH$
	$^{\circ}G^{\beta_H}_{Va^{-1}:In:Se:Va:Va^{+1}} = 3.5 \times EIS\_A + TEGH$
	$^{\circ}G^{\beta_H}_{In:In:Se:Va:Va^{+1}} = 3.5 \times IIS\_A + TEGH$
	$^{\circ}G^{\beta_H}_{Cu:Cu:Se:Va:Va^{+1}} = 3.5 \times CCS\_A + TEGH$
	$^{\circ}G^{\beta_H}_{Cu:In:Va:Va:Va^{+1}} = 3.5 \times CIV\_A + TEGH$
	$^{\circ}G^{\beta_H}_{Cu:In:Va^{+2}:Va:Va^{+1}} = 3.5 \times CIH\_A + TEGH$
	$^{\circ}G^{\beta_H}_{Cu:In:Se:Va^{-1}:Va^{+1}} = 3.5 \times CIS\_A + TEGH + TEGN$
γ-CIS $(Cu_1In_5Se_8)$	$^{\circ}G^{\gamma}_{Cu:In:Se:Va:Va} = 4 \times CIS\_A + 44500$
	$^{\circ}G^{\gamma}_{Cu:Cu:Se:Va:Va} = 4 \times CCS\_A$
	$^{\circ}G^{\gamma}_{Va:In:Se:Va:Va} = 4 \times VIS\_A$
	$^{\circ}G^{\gamma}_{In:In:Se:Va:Va} = 4 \times IIS\_A$
	$^{\circ}G^{\gamma}_{Cu:In:Va:Va:Va} = 4 \times CIV\_A$
	$^{\circ}G^{\gamma}_{Va^{-1}:In:Se:Va:Va} = 4 \times EIS\_A$
	$^{\circ}G^{\gamma}_{Cu:In:Va^{+2}:Va:Va} = 4 \times CIH\_A$
	$^{\circ}G^{\gamma}_{Va:Cu:Se:Va:Va} = 4 \times CCS\_A + 4 \times VIS\_A - 4 \times CIS\_A$
	$^{\circ}G^{\gamma}_{Va^{-1}:Cu:Se:Va:Va} = 4 \times CCS\_A + 4 \times EIS\_A - 4 \times CIS\_A$
	$^{\circ}G^{\gamma}_{In:Cu:Se:Va:Va} = 4 \times CCS\_A + 4 \times IIS\_A - 4 \times CIS\_A$
	$^{\circ}G^{\gamma}_{Va:In:Va:Va:Va} = 4 \times VIS\_A + 4 \times CIV\_A - 4 \times CIS\_A$
	$^{\circ}G^{\gamma}_{Va^{-1}:In:Va:Va:Va} = 4 \times EIS\_A + 4 \times CIV\_A - 4 \times CIS\_A$
	$^{\circ}G^{\gamma}_{In:In:Va:Va:Va} = 4 \times IIS\_A + 4 \times CIV\_A - 4 \times CIS\_A$

$$^{\circ}G^{\gamma}_{Va\,:\,In\,:\,Va^{+2}\,:\,Va\,:\,Va} = 4\times CIH\_A + 4\times VIS\_A - 4\times CIS\_A$$

$$^{\circ}G^{\gamma}_{Va^{-1}\,:\,In\,:\,Va^{+2}\,:\,Va\,:\,Va} = 4\times CIH\_A + 4\times EIS\_A - 4\times CIS\_A$$

$$^{\circ}G^{\gamma}_{In\,:\,In\,:\,Va^{+2}\,:\,Va\,:\,Va} = 4\times CIH\_A + 4\times IIS\_A - 4\times CIS\_A$$

$$^{\circ}G^{\gamma}_{Cu\,:\,Cu\,:\,Va\,:\,Va\,:\,Va} = 4\times CIV\_A + 4\times CCS\_A - 4\times CIS\_A$$

$$^{\circ}G^{\gamma}_{Cu\,:\,Cu\,:\,Va^{+2}\,:\,Va\,:\,Va} = 4\times CCS\_A + 4\times CIH\_A - 4\times CIS\_A$$

$$^{\circ}G^{\gamma}_{Cu\,:\,In\,:\,Se\,:\,Va^{-1}\,:\,Va} = 4\times CIS\_A + TEGN$$

$$^{\circ}G^{\gamma}_{Va\,:\,In\,:\,Se\,:\,Va^{-1}\,:\,Va} = 4\times VIS\_A + TEGN$$

$$^{\circ}G^{\gamma}_{Va^{-1}\,:\,In\,:\,Se\,:\,Va^{-1}\,:\,Va} = 4\times EIS\_A + TEGN$$

$$^{\circ}G^{\gamma}_{In\,:\,In\,:\,Se\,:\,Va^{-1}\,:\,Va} = 4\times IIS\_A + TEGN$$

$$^{\circ}G^{\gamma}_{Cu\,:\,Cu\,:\,Se\,:\,Va^{-1}\,:\,Va} = 4\times CCS\_A + TEGN$$

$$^{\circ}G^{\gamma}_{Cu\,:\,In\,:\,Va\,:\,Va^{-1}\,:\,Va} = 4\times CIV\_A + TEGN$$

$$^{\circ}G^{\gamma}_{Cu\,:\,In\,:\,Va^{+2}\,:\,Va^{-1}\,:\,Va} = 4\times CIH\_A + TEGN$$

$$^{\circ}G^{\gamma}_{Cu\,:\,In\,:\,Se\,:\,Va\,:\,Va^{+1}} = 4\times CIS\_A + TEGH$$

$$^{\circ}G^{\gamma}_{Va\,:\,In\,:\,Se\,:\,Va\,:\,Va^{+1}} = 4\times VIS\_A + TEGH$$

$$^{\circ}G^{\gamma}_{Va^{-1}\,:\,In\,:\,Se\,:\,Va\,:\,Va^{+1}} = 4\times EIS\_A + TEGH$$

$$^{\circ}G^{\gamma}_{In\,:\,In\,:\,Se\,:\,Va\,:\,Va^{+1}} = 4\times IIS\_A + TEGH$$

$$^{\circ}G^{\gamma}_{Cu\,:\,Cu\,:\,Se\,:\,Va\,:\,Va^{+1}} = 4\times CCS\_A + TEGH$$

$$^{\circ}G^{\gamma}_{Cu\,:\,In\,:\,Va\,:\,Va\,:\,Va^{+1}} = 4\times CIV\_A + TEGH$$

$$^{\circ}G^{\gamma}_{Cu\,:\,In\,:\,Va^{+2}\,:\,Va\,:\,Va^{+1}} = 4\times CIH\_A + TEGH$$

$$^{\circ}G^{\gamma}_{Cu\,:\,In\,:\,Se\,:\,Va^{-1}\,:\,Va^{+1}} = 4\times CIS\_A + TEGH + TEGN$$

Functions	
	CIS_A= GCUFCC+2×GSE_S+GIN_S-226835
	VIS_A= GIN_S+2×GSE_S+20000 (298 ~ 6000 K)
	VIS_B= GIN_S+2×GSE_S-169043
	IIS_A= 2×GIN_S+GSE_S+94873
	CIV_A= GCUFCC+GIN_S+46154.3
	CCS_A= 2×GCUFCC+2×GSE_S-28502
	EIS_A= GIN_S+2×GSE_S-178812
	CIH_A = GCUFCC+GIN_S+43729
	DC_A= 2×GIN_S+2×GSE_S-2×GCUFCC-195049
	LCV = -27468
	LCE = -26218
	LCI = -134189
	LIC = -1039
	LSV = -28861
	LSH= -20000
	TEGN = 46474+233.51T-12.471TLN(T)
	TEGH = 46474+207.55T-12.471TLN(T)
	GCUFCC= -7770.45775+130.485222T-24.11239Tln(T)
	$-.00265684T^2+1.29222833E-07T^3+52477.8T^{-1}$ (298 ~1368 K)
	= -13309.7197+183.649837T-31.38TLN(T) (1358~3200)
	GIN_S= -6978.89011+92.3381153T-21.8386Tln(T)
	$-.00572566T^2-2.12032167E-06T^3-22906T^{-1}$ (298~430 K)
	$= -7032.8091+124.475108T-27.4562Tln(T)+5.4607E-04T^2$
	$-8.36698333E-08T^3-211707.5T^{-1}$ (430~3800 K)

	GSE_S = $-6657.653+92.539695T-19.14T\ln(T)$ $\quad-.012295T^2+2.6766666E\text{-}06T^3$ (298~ 494 K) $\quad=\qquad\qquad-6657.653+92.539695T-19.14T\ln(T)-$ $.012295T^2+2.6766666E\text{-}06T^3$ (494~760K) $\quad=\ -9059.16586+150.334216T-28.552T\ln(T)$ (760~1500 K) Note : All the units are in J/mol

8 Formation of α-CuInSe₂ by Rapid Thermal Processing of a Stacked Binary Compound Bilayer

8.1 Introduction

Common methods of CIS absorber formation (e.g., physical vapor deposition (PVD) and selenization) require high-temperature growth conditions. The PVD needs precise control of the flux of each element. The temperature for the process is over 550 °C for the formation of CIS such as that used in the NREL three stage process. The selenization involves a number of reactions and the complex interdiffusion of intermediate phases affecting the controllability of the film quality. Care must be taken to prevent the formation of high melting temperature phases, such as $Cu_{2-x}Se$ and In_2Se_3, which will hinder the formation of CIS. Researchers use H_2Se instead of selenium for selenization to solve the selenium dewetting problem and to avoid the formation of high melting temperature secondary phase. However, H_2Se is highly toxic, and the selenization rate is slow. Thus the purpose of this work is to demonstrate a low temperature route for the formation of CIS by rapid thermal processing (RTP) of binary bilayer precursors.

8.2 Background

The ultimate goals of the research and development efforts are to create low cost, reproducible process with good process control. To accomplish these goals, fundamentally sound decisions must be made regarding the basic process and equipment to be employed, and then the entire process must be understood and characterized in terms of device behavior as a function of processing conditions. Among all the techniques, RTP is promising. Rapid implies high throughput as well as potentially lower thermal budget and safer process. The rapid heating feature can also give better control of the process kinetics. Most of all, a steeper temperature profile lowers substrate temperature. Lower thermal budget also give larger flexibility on the substrate selection.

The Cu-In-Se phase diagram suggests that alternative precursor structures can be used for the selenization method for the CIS absorber formation. A scheme of the proposed precursor structure is shown in Figure 8-1. It consists of a slightly Se-rich In-Se or Cu-Se binary layer deposited at a low temperature on a Mo-glass substrate, followed by the deposition of a Se-rich Cu-Se or InSe binary layer, respectively. The stacked metal-Se bilayer precursor structure (Cu-Se/In-Se/Mo/glass) was rapidly deposited at 200˚C in a custom designed Migration Enhanced Epitaxy (MEE) system [8-1] that accommodated 8 2" by 2" substrates, and subsequently annealed using RTP.

This structure was suggested by an examination of the Cu-In-Se phase diagram for conditions that show α-CuInSe₂ in equilibrium with a liquid phase at low temperature. Precursor layer compositions were then selected on the likelihood of forming the liquid phase while avoiding high melting temperature compounds. The α-CuInSe₂ phase is seen to lie on the tie line connecting the In_2Se_3 and Cu_2Se phases, and it shows a solid solution range of several atomic

percent [8-2]. A low-temperature single phase Se-rich liquid solution is located near the Se corner of the phase diagram. The triangle connecting the α-CuInSe$_2$ phase boundary to the Se corner represents the α-CuInSe$_2$ plus Se-rich liquid two-phase region and is the target for the overall film composition. Phase diagram calculations suggest that the Se-rich liquid phase can exist at a temperature as low as 211 °C [8-3]. They also suggest that the synthesized CIS will be Se-rich and excess Se can easily volatilize during annealing. Starting from binary metal-Se layers in contact promises to avoid certain reactions that yield high melting temperature compounds and to increase grain size through liquid phase assisted growth. The rapid thermal processing mitigates undesirable solid to solid transformations predicted at low temperatures.

Why do we choose Cu:Se and In:Se layers with composition of ~ 1:1? The compounds CuSe and InSe have much lower melting temperature than Cu$_2$Se and In$_2$Se$_3$ [8-3], and the liquid phase can be easily achieved by rapid thermal processing because the rapid heating can allow us to avoid the solid and solid transformation. So, the slightly Se-rich CuSe and InSe composition are the best pair for the formation of α-CIS. With the precursor structure of CuSe/InSe/Mo/Glass, the top CuSe can prevent the In and Se loss from the bottom InSe. The vice versa structure (InSe on top of CuSe) will provide more efficient use of liquid phase which is formed by CuSe phase and thus achieve large grain growth.

8.3   Experimental apparatus

The system used for absorber layer growth on binary compound-based precursor is a 4100 HEATPULSE Rapid Thermal Processing system supplied by AG Associates [8-3]. The RTP system is located in a clean room at the Surge Area at the University of Florida. The system is a single-wafer, cassette-to-cassette rapid thermal processor, capable of processing in inert or corrosive ambient. Currently, only N$_2$ is being used in the system. The HEATPULSE 4100 system components include: Heating Chamber, Quartz Isolation Tube, System Controller, Robot, Gas Control Electronics, ULPA Filtration System, Cooling Water Manifold, and Temperature Measurement Instruments. The oven isolates the wafer to be processed on a quartz wafer tray inside a quartz tube located inside the actual heating chamber. The quartz isolation tube has a small opening in the rear for the introduction of gas used in wafer processing. This is the purge inlet fitting. Gas is exhausted through a hole in the door flange. The 208V, 1200W tungsten halogen lamps are arranged in a bank of 10 above and 11 below the isolation tube. The lamps are connected at each end to the triac plate mounted directly above the oven. The tungsten halogen lamps are controlled by triacs. The triacs are protected by an over-temperature sensor.

The RTP system is controlled by software that is menu-driven. The computing and user-interface functions of the RTP system consist of a computer and a touch screen. The wafer-handling system is comprised of the robot, robot controller, and connections for communications signals and vacuum. The robot provides automated loading and unloading of samples. Software modifications had been made to slow the speed of the robot movements.

The gas box is mounted on the left side of the system, and it can be connected to the house exhaust system by the exhaust hood mounted on the top of the gas cabinet. The ULPA filter unit is located above the wafer handling area, and it provides a local clean environment for loading and unloading samples. The entire unit can be removed if filter replacement or other servicing is required. The cooling system contains oven chamber cooling, pyrometer cooling,

tube cooling, and electronic assembly cooling. The heating chamber cooling system is connected to house chilled water at 65°F. The pyrometer cooling is provided by the internal closed loop chiller at about 15°C. The wafer temperature is monitored by either an optical pyrometer or a type K thermocouple. The pyrometer or thermocouple sensing offers precise closed-loop temperature control. Currently, the wafer temperature is monitored by an optical pyrometer. The front view of the HEATPULSE 4100 RTP system is shown in Figure 8-2.

The HEATPULSE 4100 RTP system offers a great deal of flexibility in designing time/temperature profiles. Variable ramp rate, time, and temperature for each step in a cycle, and multi-step cycles that incorporate more than one steady state period can be programmed in the RTP system. The ramp rate can be as high as 250°C/sec. The programmable range for the steady state process time is 1~600 sec.

The short processing time and high ramp rate characteristics of this RTP can dramatically reduce volatilization losses during the reaction and provides liquid-phase assisted growth of the absorber layer. By carefully designing and choosing binary pairs for the precursor, the RTP can also help to avoid the high melting temperature phase formation. To understand the processing parameter effects on the reaction and crystallization kinetics, various temperature profiles were used by varying for example the temperature ramp rate, maximum temperature and soak time, and etc. Therefore, our objective is to utilize the processing advantages of RTP for the manufacture of CIS and CIGS solar cells while tailoring the precursor structure using the research PMEE reactor.

8.4 Film Characterization

The instruments used to study the film properties include XRD and SEM for structural characterization; EDS, AES, EPMA and ICP for composition analysis; I-V and QE for device performance measurements; and Deep Level Transient Spectroscopy for trap level and trap density study.

8.4.1 Crystal Structure Determination by X-ray Diffraction (XRD)

The XRD is the most widely used technique for individual crystalline phase identification and its relative amount determination. An atomic plane (hkl) is spaced d_{hkl} apart in distance from one another. (hkl) are the Miller indices for an atomic plane. The XRD instrument used in this study is Philipe 3720. It uses X-ray wavelength of 1.54 Å Cu Kα source. When X-rays are scattered by the atomic plane in a crystal and the diffraction angle $2\theta_{hkl}$ satisfies the Bragg's law $\lambda=2d_{hkl}\sin\theta_{hkl}$, a diffraction peak can be observed. θ_{hkl} is the angle between the atomic planes and the incident (or diffracted) X-ray beam. The measured d-spacing in the diffraction pattern is compared with known standards in the JCPDS powder diffraction file to identify the present phases. If there are several phases in the films, the proportion of each phase can be determined from integrated intensities in the diffraction pattern.

8.4.2 Topographical Information - Scanning Electron Microscopy (SEM)

The SEM is a commonly used instrument for image analysis. A source electron beam is

focused into a fine probe and rastered over the surface of the sample. With appropriate detectors, secondary electron and backscattered images can be obtained to provide the surface topographical information.

8.4.3 Local Composition Analysis - Energy Dispersive Spectroscopy (EDS)

When an ionized atom returns to its ground sate, it can release a characteristic X-ray. The concentrations of all the elements in the sample can be given by the analysis of the histogram of counts versus X-ray energy. EDS is always attached to electron column instruments like the SEM.

8.4.4 Composition Depth Profile - Auger Electron Spectroscope (AES)

The electron bombardment on the surface will produce an inner shell vacancy for the atom. Once the inner shell vacancy is created in an atom, the atom may then return toward its ground state via emission of a characteristic X-ray or through a radiationless Auger transition. The number of Auger electrons from a particular element emitted from a volume of material is proportional to the number of atoms of the element in the volume. Therefore, the relative ratio of elemental concentration can be determined from the energy distribution output of the detector. The Auger spectroscope is combined with ion-beam sputtering to remove materials from the surface and to continue to monitor the composition and the chemistry of the remaining surface. By this means, the depth concentration profile is obtained.

8.4.5 Local Composition Analysis - Electron Probe X-ray Microanalysis (EPMA)

The physical basis of the EPMA is essentially the same as that of the EDS analysis. The only difference is the detector. The EDS uses the photoelectric absorption of the X-ray in a semiconductor crystal (silicon or germanium), with proportional conversion of the X-ray energy into charge through inelastic scattering of the photoelectron. The quantity of the charge is measured by a sophisticated electronic circuit linked with a computer-based multichannel analyzer to collect data. The EMPA detector is a focusing device and is based on the phenomenon of Bragg diffraction of X rays incident on a crystal. It has different crystals to detect a wide energy range. Therefore, The EPMA has higher peak-to-background ratio than EDS and can detect lower concentrations.

8.4.6 Overall Composition Analysis - Inductively Coupled Plasma (ICP)

In ICP, ions are generated in an inductively coupled plasma and subsequently analyzed in a mass spectrometer. The CIS film is dissolved by nitric acid prior to the analysis and is introduced to the plasma as a liquid.

8.4.7 I-V Measurements

A solar cell mainly consists of a diode, whose forward bias dark current-voltage relationship (i.e., I-V curve under no light illumination) can be expressed as

$$I = I_0 \left\{ \exp\left[q(V - IR_s) / AkT \right] - 1 \right\} \tag{8-1}$$

where I_0 is the reverse saturation current and is proportional to absorber bandgap by $\exp(-E_g / nkT)$, R_s is the sheet resistance, n is any integral number larger than 1 and A is the diode factor.

Under illumination,

$$I = I_0 \left\{ \exp\left[q(V - IR_s) / AkT \right] - 1 \right\} - I_L \tag{8-2}$$

where I_L is the light generated current. The optimal bandgap for the output of maximum efficiency is 1.4~1.5 eV. Increasing bandgap E_g will decrease I_0 and in turn increase the voltage obtainable from the cell. However, increasing E_g will also decrease the I_L because less solar spectrum is absorbed.

There are several important parameters other than light-generated current involved in a solar cell. Short-circuit current (I_{SC}) is the output current of the solar cell when the external circuit is shorted, i.e., zero load resistance. Open-circuit voltage (V_{OC}) is the output voltage of the solar cell when the external circuit is open, i.e., infinite load resistance. The V_{oc} is also referred to as photovoltaic voltage. I_m and V_m are the current and voltage for maximum power. The solar efficiency of the cell is defined as follows:

$$\eta = I_m V_m / P_{incident} \tag{8-3}$$

$I_m V_m$ is related to V_{oc} and I_{sc} by the fill factor ff:

$$ff = I_m V_m / I_{sc} V_{oc} \tag{8-4}$$

8.5   Experimental Results and Discussions

8.5.1   Susceptor Design

The design of the susceptor went through three stages due to problems encountered at each stage as shown in Figure 8-3. Susceptor I (Figure 8-3 (a)) is designed to solve the cracking problem when using a silicon wafer as the susceptor as evidenced by the optical microscopy of CIS absorber plan view shown in Figure 8-4. Unfortunately, In and Se losses occurred while using susceptor I according to Auger (Figure 8-7) and XRD (Figure 8-5) analysis. Thus, Suceptor II (Figure 8-3 (b)) was designed to solve this problem. However, non-uniform heating occurred with the increased sample size. Therefore, Susceptor III (Figure 8-3 (c)) has been designed to successfully solve this problem.

8.5.1.1   Susceptor I

The SLG sample with sample size 0.5" by 0.5" was initially placed on the top of a piece of graphite wafer. After processing films with this design, the bottom of the sodium-lime glass was observed to have exceeded the glass transition temperature. The test samples were all cracked and adhered to the silicon wafer. Optical micrographs of the samples were taken before and after the RTP and are shown in Figures 8-4. Therefore, a 4-inch diameter graphite plate as shown in Figure 8-4 was substituted for the silicon wafer to increase the heat conductivity of the sample tray. Several RTP experiments were conducted using graphite wafer. The plane view optical micrograph shown in Figure 8-4 (c) shows that the cracking and sticking are avoided by using the graphite tray.

Three samples with precursor structure CuSe/InSe/Mo/sodium-lime glass were processed. Samples were placed on a 0.5 mm thick piece of 4-inch diameter graphite with a N_2 purge flow originating from the back of the oven. The RTP annealing recipes for the 3 samples are summarized in Table 8-1.

Table 8-1. RTP conditions for processing CuSe/InSe/Mo/SLG sample

Sample	Soak time	Temperature	Ramp rate
1-1	70 s	550 °C	20 °C/s
1-2	70 s	750 °C	20 °C/s
1-3	140 s	550 °C	20 °C/s

The processed films were characterized by the XRD, Auger, and optical microscopy. From the XRD data shown in Figure 8-5, it can be seen that after RTP, the α-CuSe phase disappeared and the α-CuInSe$_2$ and Cu$_{2-x}$Se phases formed. The relative intensity of the peak around $2\theta = 26.560$ decreased when the soak time increased from 70 s (sample 1-1) to 140 s (sample1-3). This is attributed to the longer soak time increasing the In and Se losses and thus increasing the extent of formation of the Cu$_{2-x}$Se phase. It is likely that the In$_2$Se species is responsible since it has a high vapor pressure. There is little difference in the XRD spectra when the temperature is increased from 550 °C (sample 1-1) to 750 °C (sample 1-2) for the same soak time.

From the Auger data shown in Figure 8-7, In and Se loss is observed after RTP and as the temperature increases from 550 ºC to 750 ºC, there are more loss of these two elements.

From the plane-view optical micrographs, as illustrated in Figures 8-6 (a)-(c), it can be seen that when the set temperature is at 750 °C (sample 1-2), the surface morphology of the processed film is much rougher than the one processed at 550 °C.

The above preliminary experimental results indicated that a high RTP temperature should be avoided and the loss of In and Se needs to be reduced. Therefore, a new sample holder was designed using a piece of flat quartz as a cover. This design is termed susceptor II.

8.5.1.2   Susceptor II and Influence of RTP Parameters Effect Study

A set of RTP experiments was performed on precursor samples (0.5" by 0.5") with CuSe/InSe/Mo/Glass structure to determine the effects of the RTP processing variables (temperature, soak time, delay times, sample size, and preheat intensity) on the composition change and phase transition of the film using susceptor design II as shown in Figure 8-3 (b).   In this design, a quartz lid is used to cover the sample to minimize volatilization losses.   A typical RTP cycle is shown in Figure 8-8.

Preheat Intensity Effect

Two kinds of preheat intensity were employed, 0% and 25%, for the same process condition 600 ˚C, 60 s, 60 ˚C/s Delay I 60 s, and Delay II time 200 s. The XRD and ICP results are shown in Figure 8-9. There is no significant change in film properties when increasing the preheat intensity to 25% except a slight increase in peak intensity at 26.5°. This increase is due to the increase extent of formation of $Cu_{2-x}Se$ because even though $Cu_{2-x}Se$ peak overlaps with the CIS peak, $Cu_{2-x}Se$ usually has another peak at the shoulder of 112 peak position and the FWHM value for $Cu_{2-x}Se$ is less than that of CIS due to its higher crystallinity. The maximum preheat intensity for this RTP is 30%. Therefore, lower preheat intensity is preferred.

Steady State Temperature

For both soak times (Figure 8-10 and 11), when increasing the temperature there is more Se loss. The FWHM of the decreases of the 112 peak due to increase formation of $Cu_{2-x}Se$. Therefore, a lower soak temperature is preferred.

Ramp Rate

When decreasing the ramp rate (Figure 8-12), the XRD pattern shows similar peak position, peak intensity and FWHM at 26.5°. There is a large decrease in Cu/In ratio when increasing the ramp rate while the Se composition remains the same. This means that a higher ramp rate will favor the formation of CIS and thus have more indium in the film. Therefore, a higher ramp rate is preferred.

Soak Time

At both a high temperature (Figure 8-13) and a low temperature (Figure 8-14), when decreasing the soak time, the FWHM decreases by 30%. This means that less CIS phase is formed in the film processed at a shorter soak time. There is no significant difference in composition when varying the soak time. Therefore, a longer soak time is preferred at both a high and a low temperature to form the CIS phase.

In conclusion, the film cracking and elemental loss issues were largely resolved by using a graphite sample tray and quartz cover even though slight loss of In and Se is still observed. From the XRD patterns measured for the films before and after the RTP, it can be seen that both the α-CuInSe$_2$ and $Cu_{2-x}Se$ phases are synthesized by the RTP from the binary bilayer precursors and the α-CuInSe$_2$ phase exhibited a chalcopyrite structure as indicated by the presence of the

101, 103, 211 and 105 reflections [8-4, 5]. The α-CuSe phase, which is the dominant phase in the precursor film, disappeared and reacted to form CuInSe$_2$ or Cu$_{2-x}$Se phases upon RTP. The narrow peaks indicate large crystal sizes. This suggests that the Cu-rich secondary phase is the competing phase in the binary bilayer process. However, it modifies the film morphology and results in large grain growth. From the XRD and ICP results, a higher ramp rate and a longer soak time have a significant positive influence on the α-CIS phase formation. A higher temperature will produce more loss in Se. Therefore, the starting RTP conditions for the following experiments on the precursor structure CuSe/InSe/Mo/Glass are: higher ramp rate, longer soak time, 0% preheat intensity, and lower steady temperature (around 500 °C).

8.5.1.3   Susceptor III

The RTP experiments were performed on new precursor series (growth run 230) with the structure CuSe/InSe/Mo/glass. For this sample set, the sample size was increased to 1" by 1" to allow cells to be fabricated. Experiments performed in the sample susceptor II (Figure 8-3 (b)) produced large lateral temperature gradients during RTP because of the relatively small size of the quartz cover. XRD spectra of the three different locations (see Figure 8-15) were taken, and the phase constitution of the three regions is shown in Figure 3-16. It can be seen that the Cu-Se secondary phase peak (2θ=21.3°) decreases in the center region as compared to the edge, consistent with a higher center temperature. The reaction in the center is thus more complete than at the edge. To improve heating uniformity, a new sample holder was designed (Figure 3-3 (c)). In this design, a recess is milled in a piece of graphite stock that holds the sample. A second recess is milled at a larger diameter to accommodate a flat quartz cover. This design used for the RTP experiments was made to minimize Se loss and to achieve a uniform temperature.

8.5.2   Phase Transition Study on CuSe/InSe/Mo/Glass Precursors

A phase transition study was conducted on the precursor structure CuSe/InSe/Mo/Glass using susceptor III to find a suitable reaction pathway for the formation of α-CIS.

Experimental

The stacked metal-Se bilayer precursor structure (Cu-Se/In-Se/Mo/glass) was rapidly deposited at 200˚C in a custom-designed Migration Enhanced Epitaxy (MEE) system [8-1] that accommodated 8 2" by 2" substrates. A single precursor film was then annealed in a series of 4 steps in the RTP system. Each anneal step exposed the sample to a different ambient by coating the glass cover with either InSe or Se. The RTP experiments were performed on 1" by 1" samples from the same growth run.

The whole investigation consists of five steps as follows:

Step I. Anneal using a clear quart cover

Initial experiments were conducted using a simple quartz cover with the gas ambient established by volatilization of the sample. The RTP conditions of a set-point temperature 480 °C, soak time 60 s, and ramp rate 60 °C/s were first tested. The XRD results, however, indicated

163

incomplete formation of α-CuInSe$_2$, with intermediate phases (predominantly InSe, In$_6$Se$_7$, Cu$_{2-x}$Se and CuSe$_2$) remaining (see Fig. 8-17). Suspecting reaction limited processing, the set point temperature was raised to 600°C and the soak time increased to 120 s. The XRD results shown in Fig. 3-18, however, do not show a significant change in the annealed film constitution. The overall composition of the annealed sample (temperature 480°C, soak time 60 s, and ramp rate 60 °C/s) was determined by the ICP analysis to be Cu 29.4%, In 23.6%, and Se 47.0 %. This composition is located in the three-phase region (liquid + Cu$_{2-x}$Se + α-CuInSe$_2$) according to the isothermal section of the phase diagram [8-2]. These results suggest that Se volatilization occurred during processing. To maintain the Se concentration during annealing, Se was added to the system by depositing a thin layer of either InSe or Se on the bottom of the quartz cover.

Step II. Anneal using a quartz cover with an InSe film

To modify the gas ambient, an1 μm film of InSe was deposited onto the quartz cover. The sample annealed in step I at RTP conditions 480 °C, 60 °C /s, and 60 s was again processed under the same conditions but with the InSe coated cover in place. As shown in the XRD pattern in Fig. 8-19, Cu$_{2-x}$Se was still present.

Step III. Anneal using a quartz cover with a Se film

To increase the Se overpressure, a thin layer of elemental Se was next deposited on the cover and the same sample was once more processed under identical RTP conditions (480 °C, 60 °C /s, 60 s). The XRD analysis showed an increase in the peak intensity at 2θ of 26.5˚ attributed to α-CuInSe$_2$, suggesting that InSe reacts with Cu$_{2-x}$Se in the presence of Se (see Fig. 8-20). In addition small amounts of Se-rich CuSe$_2$ and In$_6$Se$_7$ were also apparent.

Step IV. Anneal with a clear quartz cover

To reduce or eliminate the Se-rich CuSe$_2$ and In$_6$Se$_7$ phases, the same film was again annealed at the same conditions, but with no deposit on the underside of the cover plate. The results shown in Fig. 8-21 indicate that the final film is a single-phase α-CuInSe$_2$.

Discussions and Conclusions

XRD analysis of the precursor film (see Fig. 8-22) reveals only α-CuSe in the starting Cu-Se layer and no apparent crystalline phase in the In-Se layer. After the step I annealing, crystallization of InSe is evident, while secondary Cu$_{2-x}$Se is formed, presumably in the top layer as a result of Se loss. The compound α-CuSe will decompose to Cu$_{2-x}$Se with loss of Se at 377 ˚C [8-5] according to:

$$\alpha - CuSe(s) \rightarrow \tfrac{1}{2}\beta - Cu_{2-x}Se(s) + \tfrac{1}{4}Se_2 \qquad (8\text{-}5)$$
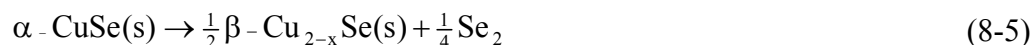
The constitution did not change significantly when the same sample was again annealed using an InSe coated slide. Apparently, there was insufficient mass transfer between layers to allow measurable reaction according to:

$$\beta - Cu_{2-x}Se(s) + InSe(s) \rightarrow \alpha - CuInSe_2(s) \tag{8-6}$$

Although no significant reaction of β-Cu$_{2-x}$Se(s) with InSe(s) occurred in steps I to III, the formation of α-CuInSe$_2$ proceeded rapidly in step IV. When a Se ambient is present during anneal, the following overall reaction occurs:

$$\beta - Cu_{2-x}Se(s) + 2InSe(s) + \tfrac{1}{2}Se_2(g) \rightarrow 2\alpha - CuInSe_2(s) \tag{8-7}$$
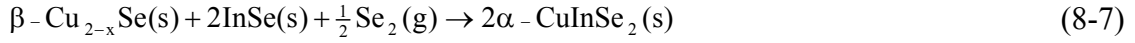
This reaction occurs rapidly with an activation energy of 25 kJ/mol as determined by a study of the selenization of Cu-In bilayers [8-6]. The apparent role of Se is to retain the CuSe phase by the reaction:

$$\beta - Cu_{2-x}Se(s) + Se_2(g) \rightarrow CuSe(s) \tag{8-8}$$
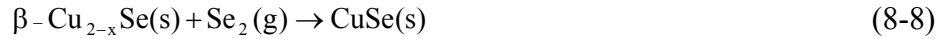
The SEM micrographs (see Fig. 8-23) support the above observations and the proposed reaction mechanism. The micrograph of the precursor structure (see Fig. 8-25(a)) clearly delineates the Cu-Se/In-Se/Mo layered structure. After the first anneal (step I), the three-layers are still evident, but the microstructure has changed (see Fig. 8-25(b)). According to the EDS analysis, the layer next to Mo layer is InSe, and the surface layer is β-Cu$_{2-x}$Se while α-CuInSe$_2$ is formed between these two layers. Fig. 8-25(c) shows the final film structure after step IV. As desired, a single-phase α-CuInSe$_2$ is now present with a grain size on the order of a few microns.

Based on the above experimental observation, we conclude that Se control is an essential requirement for the RTP process of binary bilayer precursor, and a higher substrate temperature will be suggested to support the formation of a Se-rich liquid Cu$_x$Se phase in Cu-Se film to assist the growth.

$$\beta - Cu_{2-x}Se(s) \xrightarrow{Se} CuSe(s) \xrightarrow{High\ T} Cu_xSe(Liquid) \tag{8-9}$$
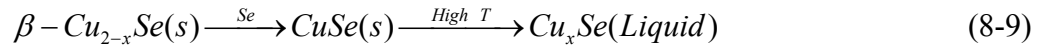
The liquid Cu$_x$Se can help the diffusion of In atom and thus the following reaction will happen:

$$Cu_xSe(Liquid) + InSe \rightarrow \alpha\text{-}CuInSe_2 \tag{8-10}$$

8.5.3   RTP Experiments on CuSe/InSe/Mo/Glass Precursors in PVD system

As discussed in the previous section, a Se ambient is needed for the formation of CIS, and a higher temperature is suggested to help the diffusion of In assisted by the formation of liquid Cu$_x$Se phase. Therefore, the following three runs were performed under Se over pressure of 5 Å/s control by RTP on CuSe/InSe/Mo/Glass binary bilayers in the PVD system at NREL:

Run 1. 500 °C, 2.5 minutes

Run 2. 550 °C, 4.5 minutes

Run 3. 550 °C, 10 minutes

A safety limit on the PVD system restricted the ramp rate to 3 °C/s for all three experiments. This ramp rate is about 10 times faster than the regular ramp rate used in the normal PVD process. As discussed in the background section, a faster ramp rate enhances the reaction of these two layers by forming a liquid phase and results in a lower substrate temperature and shorter processing time. A conventional RTA system can have a ramp rate up to 120 ºC/s. Therefore, a conventional RTA system should allow the formation of CIS at lower process temperature and shorter processing time compared to the PVD system.

As seen from the XRD pattern in Figure 8-22, only the CuSe phase is present in the precursor (before RTP). The bottom InSe phase does not show any peaks because it is in the amorphous state. The SEM cross section of the precursor (Figure 8-24b) shows the separate InSe and CuSe layer of thickness about 1 μm each. The plane view of the precursor (Figure 8-24a) shows the hexagonal CuSe grains. The shoulder near (112) peak in the XRD pattern (Figure 8-25) of the film after Run 1 indicates the formation of the high temperature $Cu_{2-x}Se$ phase. The bright dots in the plane view micrograph indicated by an arrow in the Figure 8-26a points out the $Cu_{2-x}Se$ phase. The cross-sectional micrograph (Figure 8-26b) shows the small grain site in the bottom portion of the layer because of incomplete nucleation of CIS. It is believed that these small grains are not well nucleated CIS grains and that the bottom InSe is completely consumed as evidenced by absence of InSe secondary phase by XRD (usually InSe will crystallize upon heating). This also suggests that In diffusion in CuSe is slower than Cu diffusion into InSe. This is because the In atom is larger than the Cu atom, and InSe is amorphous which makes the Cu diffusion much easier.

EPMA is a useful technique to determine the existence of any Cu rich secondary phases because it probes the upper layer composition, and Cu-rich secondary phases tend to segregate near the surface [8-6]. The EPMA composition for this film after Run 1 is Cu: 27.9 at.%, In 24.1 at.%, Se 48.0 at.% yielding a Cu/In ratio of 1.16. This result is consistent with the existence of a Cu-rich secondary phase. Therefore, the temperature was increased to 550 °C and the soak time increased to 4.5 min in Run 2 to enhance In diffusion and thus formation of CIS in the top CuSe layer. The XRD pattern (Figure 8-27) shows the single CIS phase and the disappearance of $Cu_{2-x}Se$ on the surface as suggested by the SEM plane view micrograph (disappearance of small surface grains in Figure 8-28(a)). The grain size in the bottom layer enlarged (Figure 8-28(b)). The composition as determined by EPMA for film after run 2 is Cu 23.5 at.%, In 26.5 at.% and Se 50.0 at.% with Cu/In ratio of 0.887 and this ratio lies in single phase CIS region. This suggests that the top layer is also fully converted to the CIS phase. To promote CIS grain growth in the bottom layer, a longer soak time, 10 min was tried (Run 3). From the SEM picture cross-section micrograph shown in Figure 8-29(b), a relatively homogenous grain size is evidence throughout the film, and the plane view SEM micrograph shows highly textured CIS grains as in Figure 8-29(a) and this is the highly oriented CIS 112 peak.

I-V Measurements

The next step was to fabricate cells from the absorbers synthesized in Runs 1-3. The I-V measurement for the first device is shown in Figure 8-30 (without Se overpressure after Run 1). The device is shorted apparently due to the presence of the conducting $Cu_{2-x}Se$ phase. For Run 2 with XRD and SEM suggesting single phase CIS with two different grain size layers, the efficiency is 2.78 %. Further increase of grain size (Run 3) produced an increased efficiency of

5.08 %. The J_{sc} for this 5 % cell is 34.65 mA/cm^2, which is a good value for CIS. Fill factor and V_{oc}, however, are very low. A high sheet resistance contributes to the low fill factor. This can be improved by adjusting the Cu:In:Se composition ratio and thus the doping level, especially Cu to In ratio and by creating a composition gradient to achieve the bandgap grading with the incorporation of Ga. The V_{oc} is largely affected by the mid gap defects in the space charge region. To detect the defect level in this 5 % cell, a Deep Level Transient Spectroscopy (DLTS) measurements were performed on this 5 % cell.

8.5.4   RTP Experiments on InSe/CuSe/Mo/Glass Precursors

A preliminary study of samples with the In-Se binary layer on the top of the Cu-Se layer (precursor structure InSe/CuSe/Mo/glass) was undertaken. Samples with this structure, when processed at 450 to 600 °C, showed a rough surface morphology after the RTP as shown in Figure 8-31 (a). This is believed to be a result of poor adhesion of the bottom layer to Mo layer. Therefore, a seed thin layer of InSe was first deposited on the Mo/Glass substrate to give structure InSe (1 μm)/CuSe (1 μm)/InSe(500 Å)/Mo/Glass. This structure greatly improves the surface morphology as seen in the optical micrograph as shown in Figure 8-31(b). The structure and process conditions however need to be optimized to make device quality films.

8.6 Conclusions

An alternative low temperature route to CuInSe$_2$ formation was demonstrated using RTP on the stacked precursor structure Cu-Se/In-Se/Mo/glass. The influence of various ambient compositions on phase transformations after RTP was determined. A short time annealing of 60 s at 480 ˚C in a Se ambient generated by volatilization of a thin Se layer on the sample cover, followed by a second anneal using a clear cover, was able to produce single-phase α-CuInSe$_2$ with relatively large grain size. The high melting temperature secondary phase Cu$_{2-x}$Se(s) does not react with InSe without Se overpressure. Based on these results, a 5.08% device with V_{oc}= 0.296 V, J_{sc} = 34.65 mA/cm^2 and fill factor = 49.54% was fabricated using the absorber that is obtained by RTP on the CuSe/InSe/Mo/Glass precursor under Se control in a PVD system. It is worth noting that this 5.08% cell was achieved without full optimization of the process. Therefore, the RTP on binary bilayer process is promising.

8.7 References cited

[8-1]   B.J. Stanbery, C.-H. Chang, S. Kim, S. Kincal, G. Lippold, S.P. Ahrenkiel, L. L. Kerr, T.J. Anderson, M.M. Al-Jassim, *Self Organized Processes in Semiconductor Alloys*, MRS Symposium Proceedings, Vol. 583, 195-200, 2000.

[8-2]   T. Gödecke, T. Haalboom, and F. Ernst , *Zeitschrift für Metallkunde*, Vol. 91, No. 8 pp.622-662, 2000.

[8-3]   C-H Chang, *Processing and Characterization of Copper Indium Selenide for Photovoltaic Applications*, Ph.D. Dissertation, University of Florida, 2000.

[8-4] R. Friedfeld, R.P. Raffaelle, and J.G. Mantovani, *Solar Energy Materials and Solar Cells*, Vol. 58, pp. 375-385, 1999.

[8-5] I. Forbes, F.O. Adurodija and M.J. Carter, *Proceedings of the 6th International PVSEC, New Delhi*, pp.1965-1968, 1996.

[8-6] N. Orbey, H. Hichri, R.W. Birkmire and TWF Russell, *25th IEEE Photovoltaic Specialist Conference*, May 13-17, Washington, D.C. pp. 981-982, 1996

CuSe (at 50-55% Se)
InSe (at 50-55% Se)

or

InSe (at 50-55% Se)
CuSe (at 50-55% Se)

RTP $\longrightarrow$

α-CuInSe$_2$
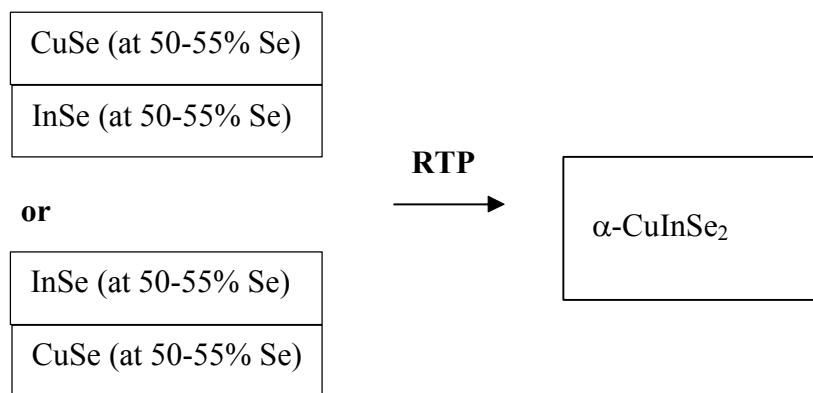
Figure 8-1. Novel precursor structure consisting of stacked metal-Se layers.

(a)

(b)
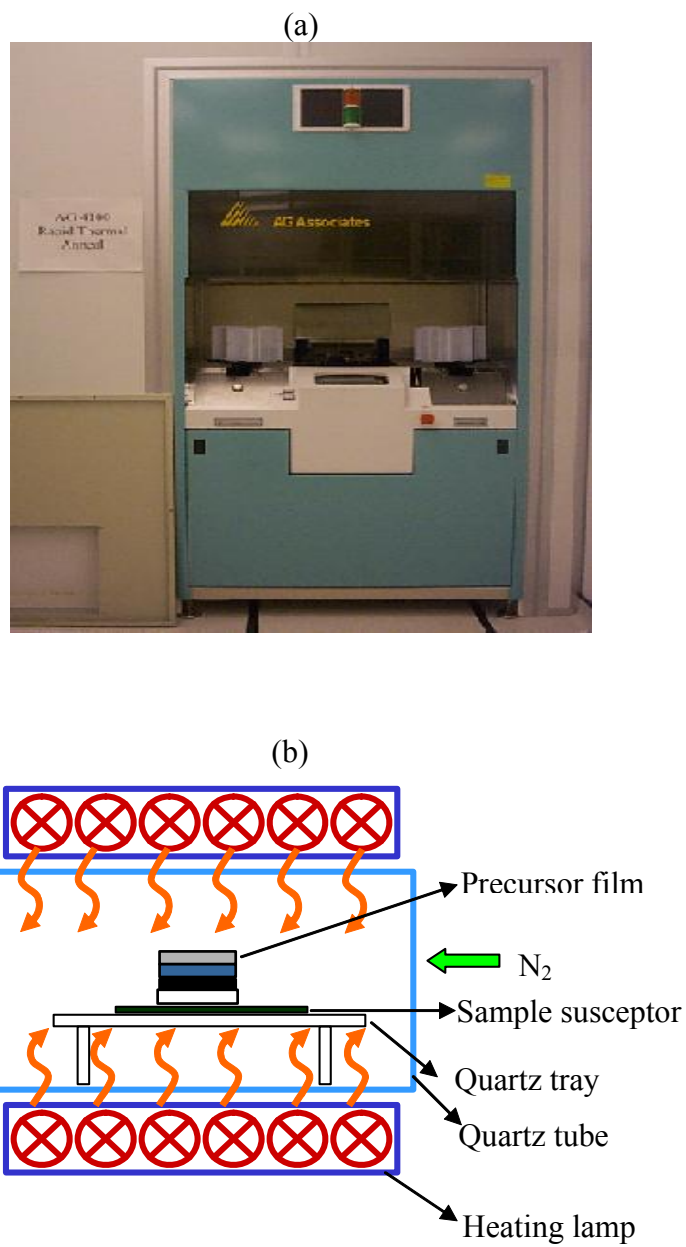
Figure 8-2. AG Associates Heatpulse 4100 RTP system (a) front view, (b) schematic of the oven.
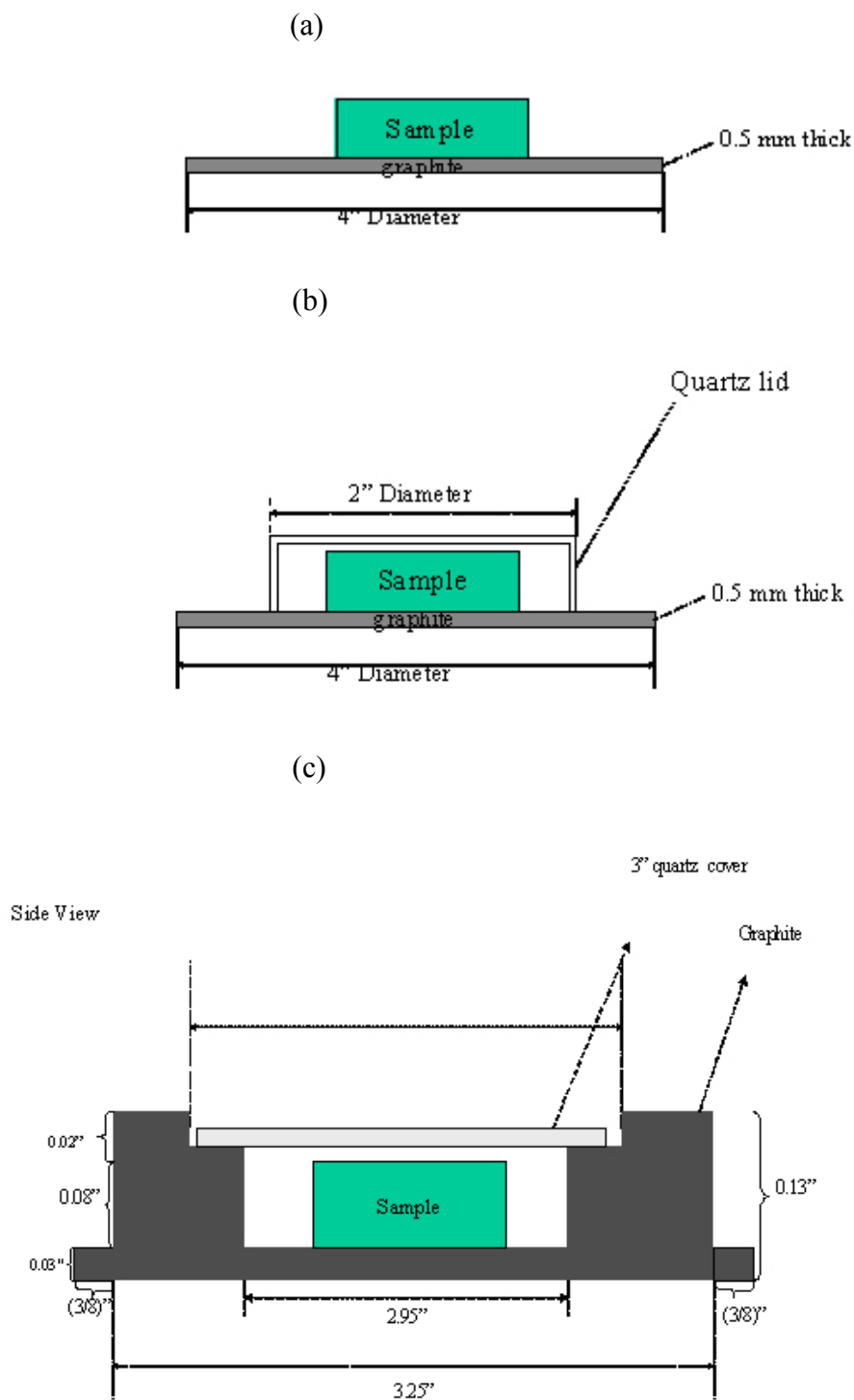
Figure 8-3. Susceptors design schematic (a) I, (b)II, and (c) III.

(a) Trial sample before RTP.   (b) Trial sample after RTP by   (c) Trial sample after RTP by
                               using silicon wafer as the   using graphite wafer as the
                               susceptor.   susceptor.

Figure 8-4. Comparison of film optical micrograph when using Si or graphite as
the susceptor at magnification 10x..
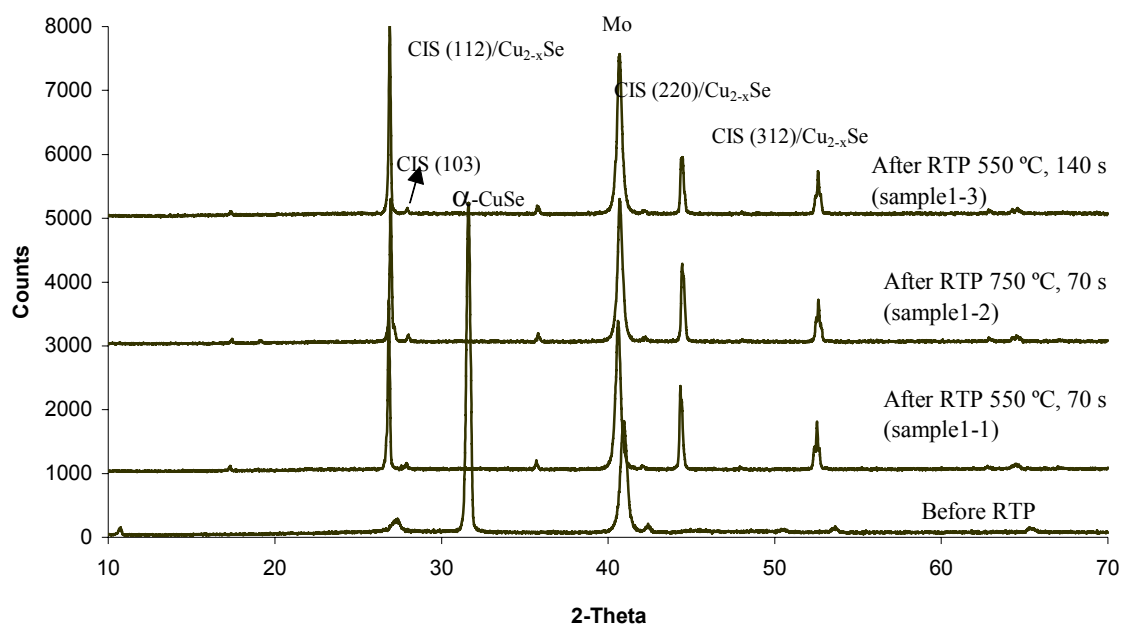
Figure 8-5. XRD pattern comparison for the films at different RTP conditions
(Susceptor I)..
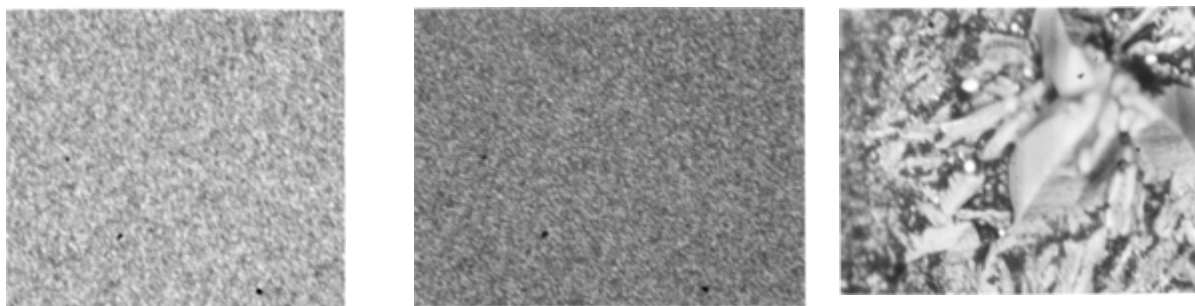
(a) Plane-view optical micrograph of sample 1-0 before RTP

(b) Plane-view optical micrograph picture of sample 1-1

(c) Plane-view optical micrograph picture of sample 1-2

Figure 8-6. Optical micrographs of 1-0, 1-1 and 1-3 samples at magnification 10x..
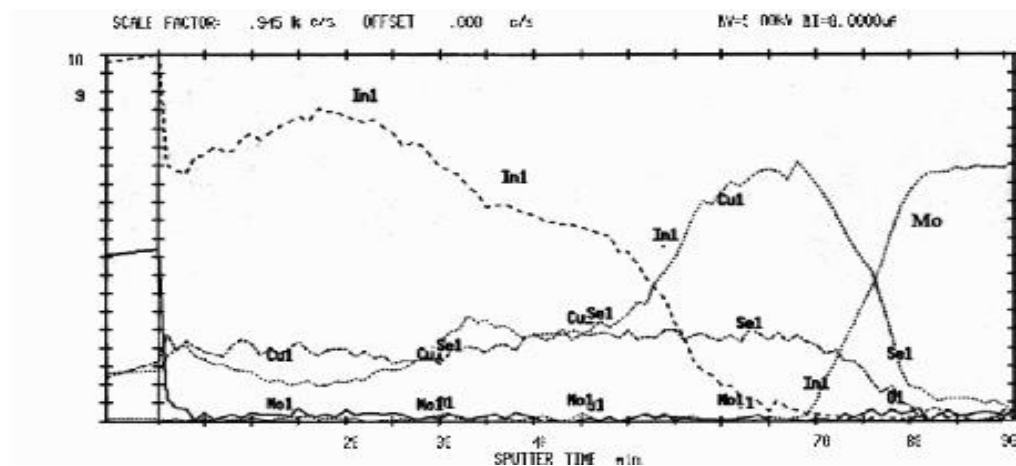
Figure 8-7 (a). Auger depth profile of sample 1-0 before RTP [8-3].
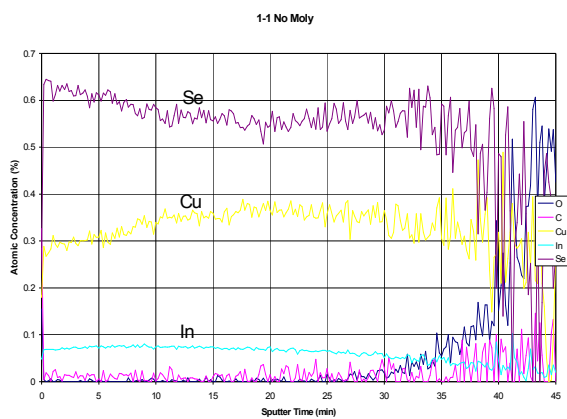
Figure 8-7 (b). Auger depth profile of sample 1-1.
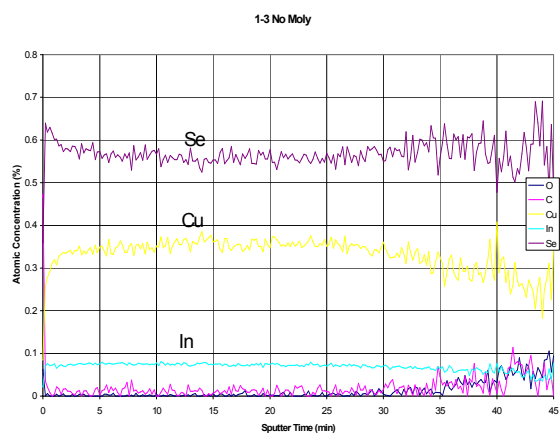
Figure 8-7 (c). Auger depth profile of sample 1-3.

173
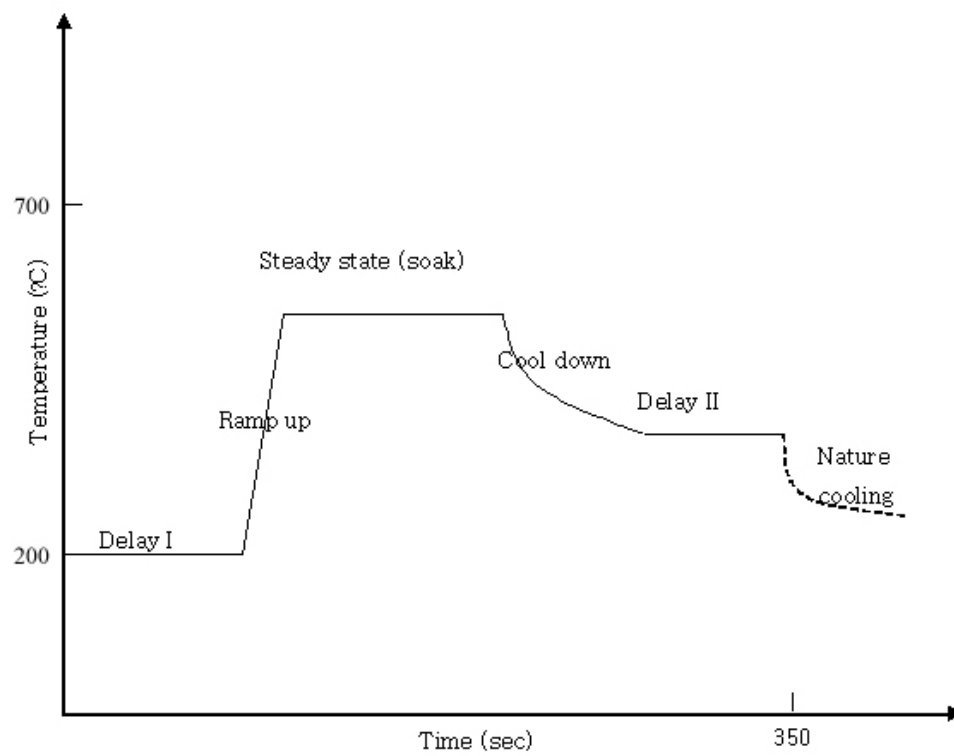
Figure 8-8. Typical Cycle time for Rapid Thermal Processing.
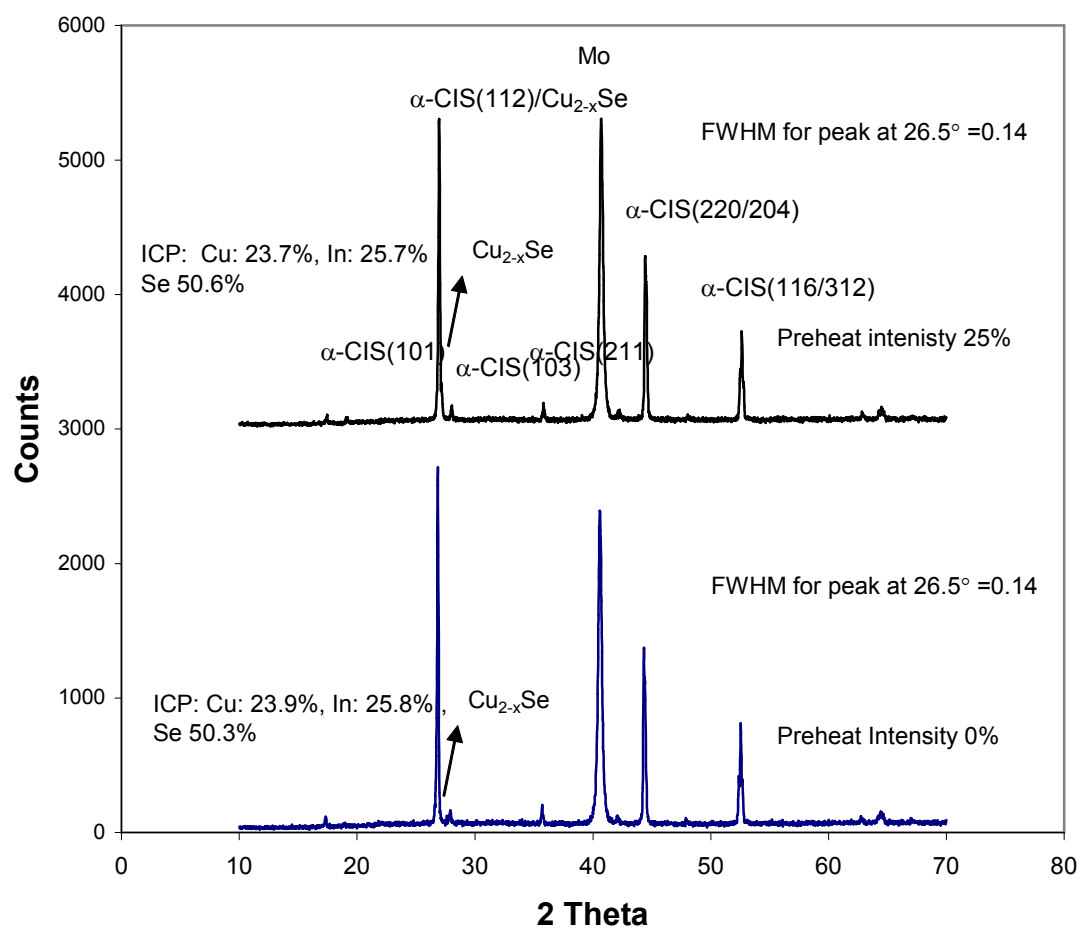
Figure 8-9. The influence of preheat intensity on the phase formation (XRD pattern) and film composition (ICP).
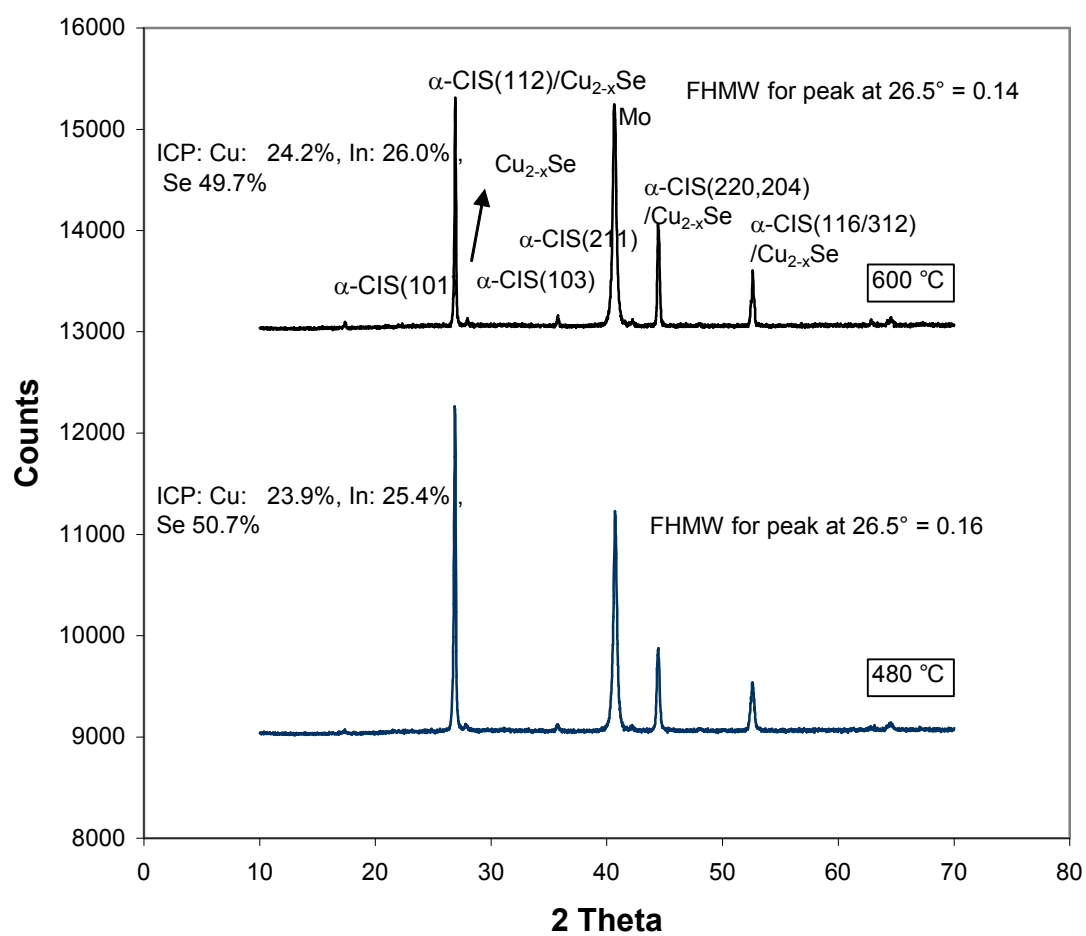
Figure 8-10. The effect of soak temperature at shorter soak time (XRD pattern and film composition by ICP).
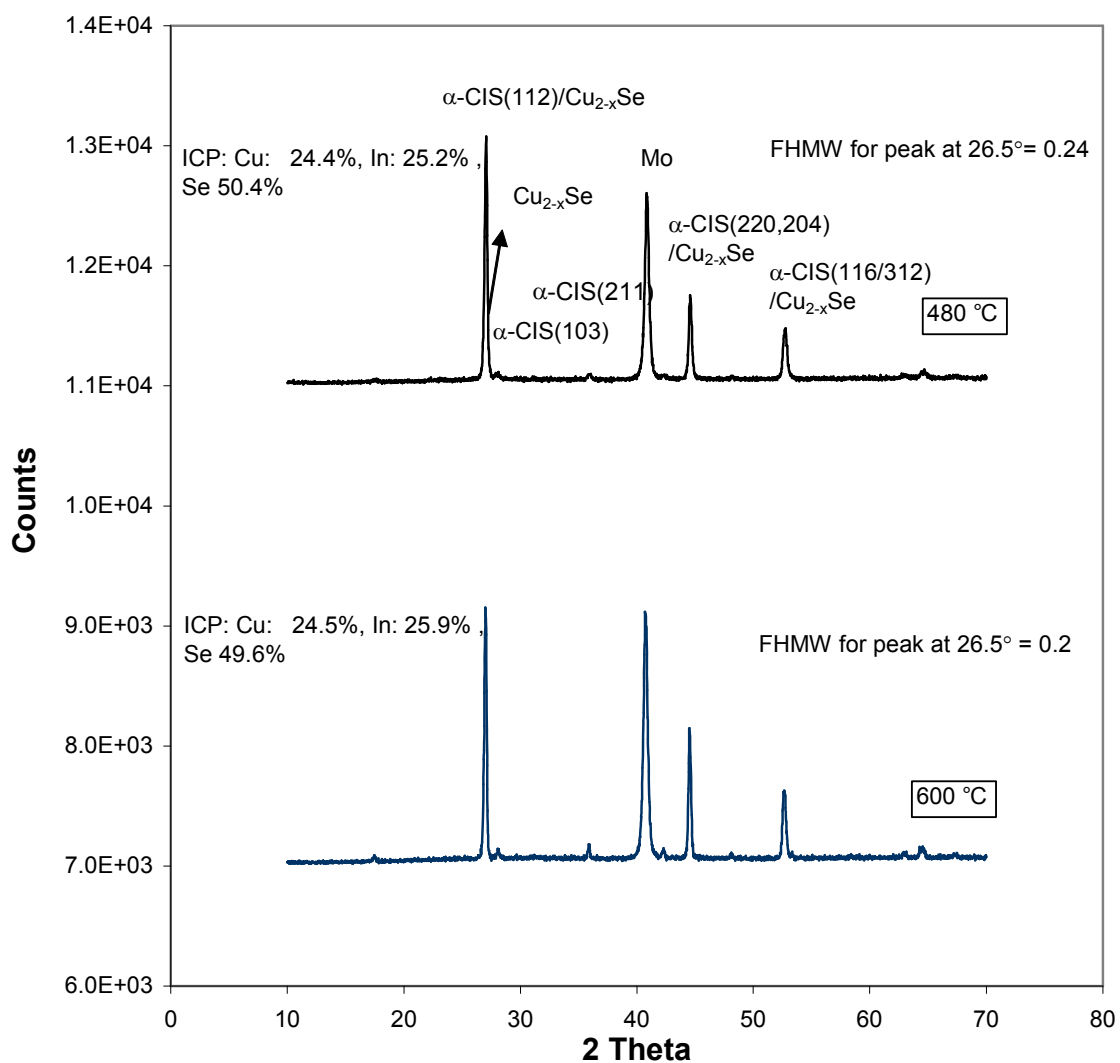
Figure 8-11. The effect of soak temperature at longer soak time (XRD pattern and film composition by ICP).
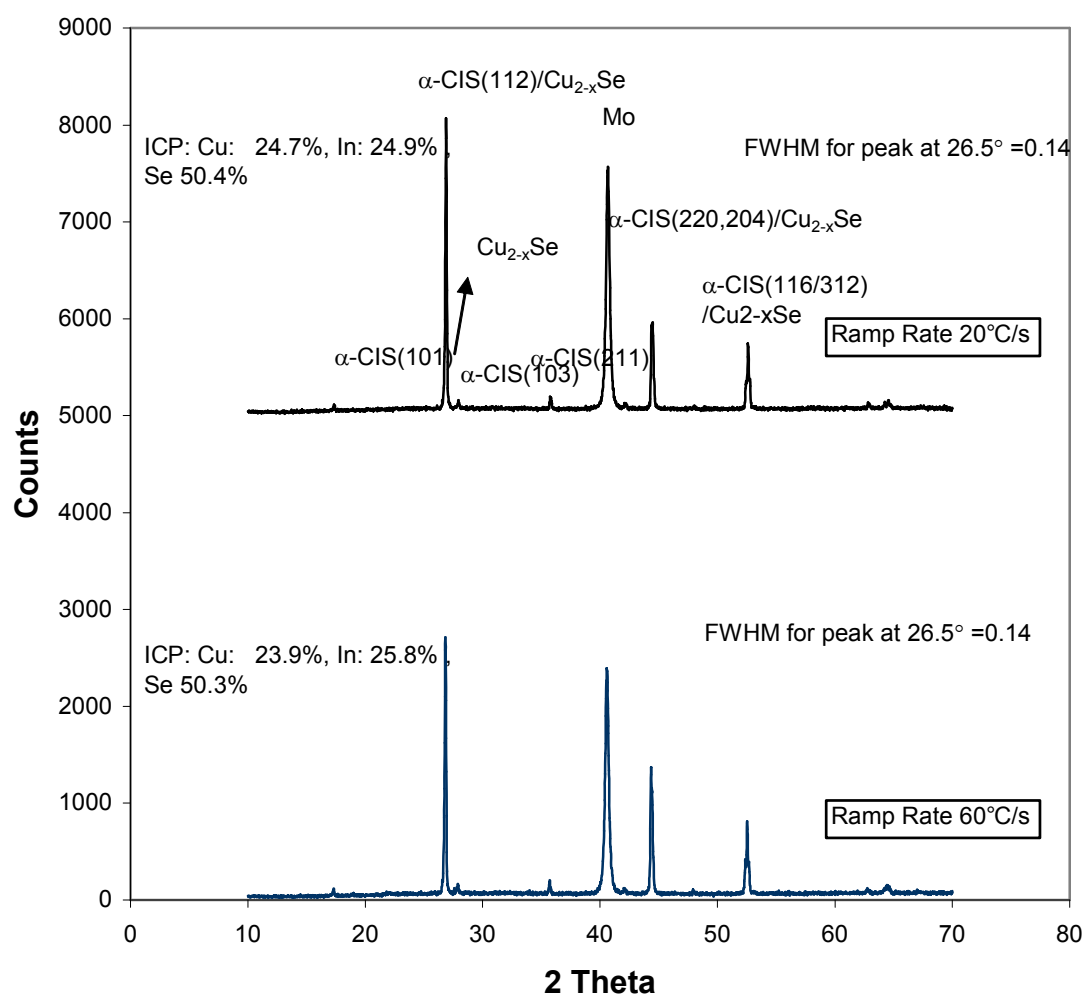
Figure 8-12. The effect of ramp rate (XRD pattern and film composition by ICP).
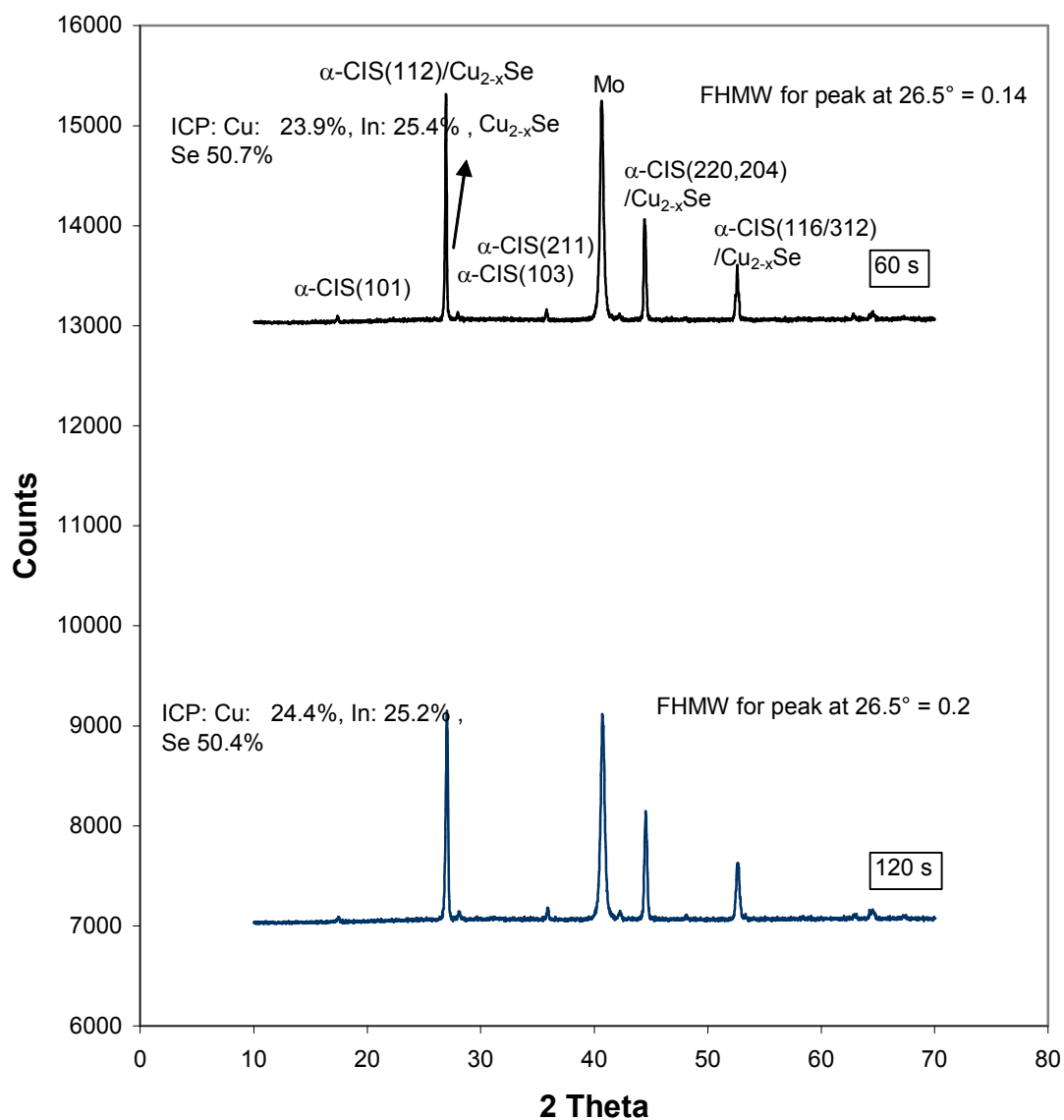
Figure 8-13. The influence of soak time at higher steady state temperature on phase formation (XRD pattern) and film composition (ICP).
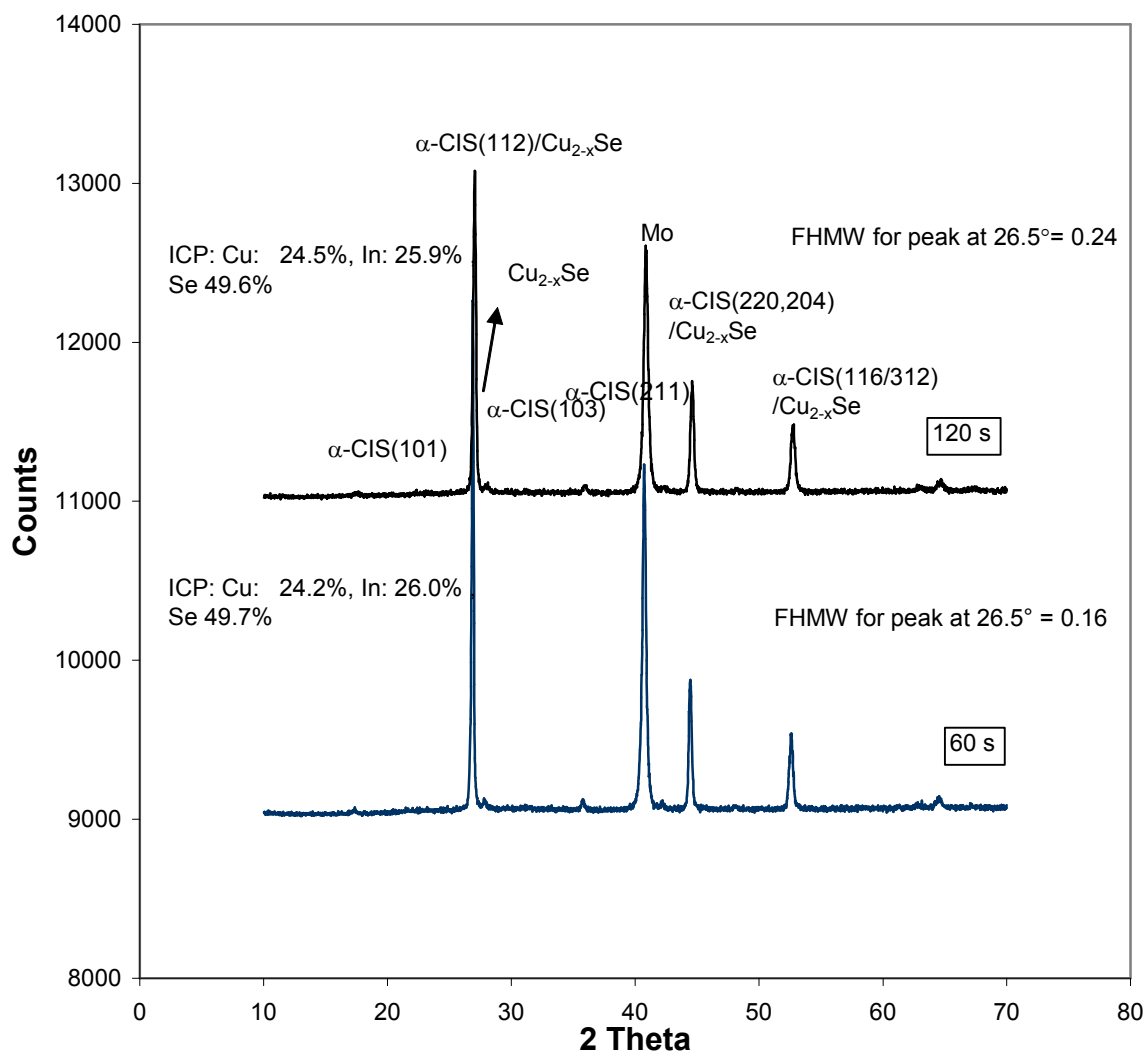
Figure 8-14. The influence of soak time at lower steady state temperature on phase formation (XRD pattern) and film composition (ICP).
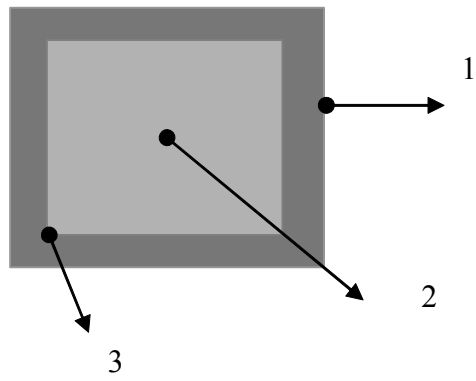
Figure 8-15. Non-uniformly heated surface.
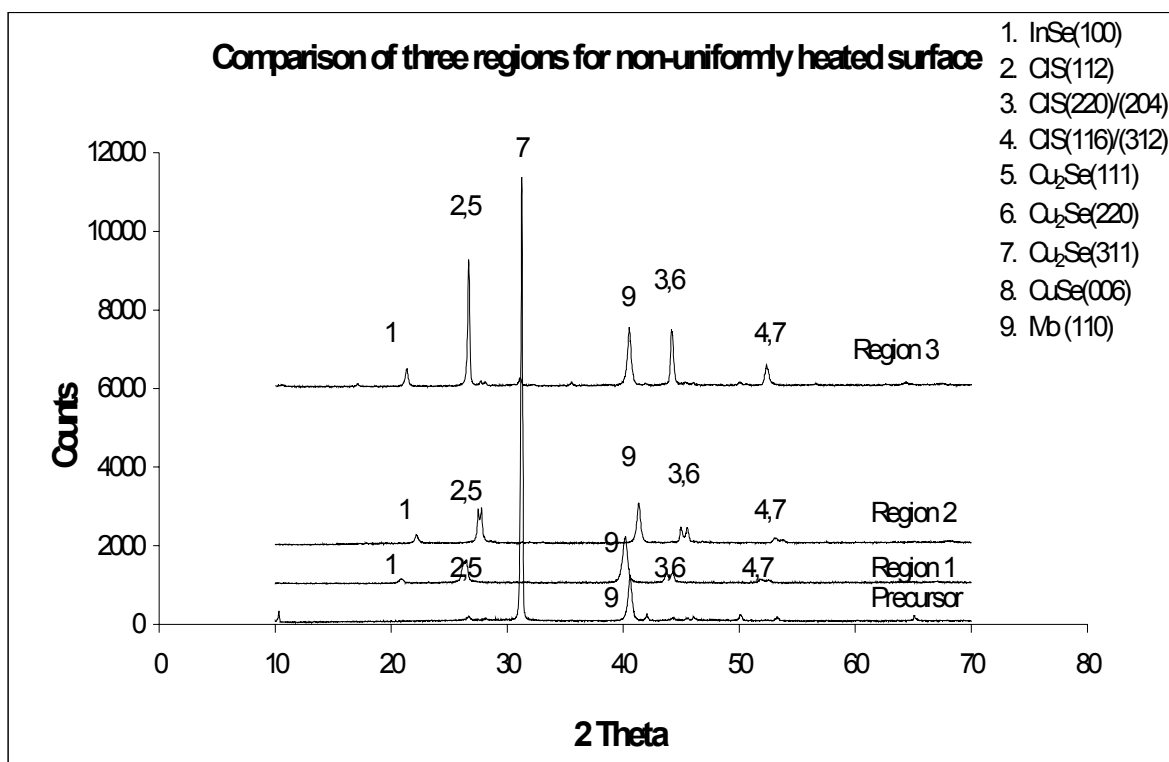
Figure 8-16. XRD pattern of different regions of non-uniform heated surface.
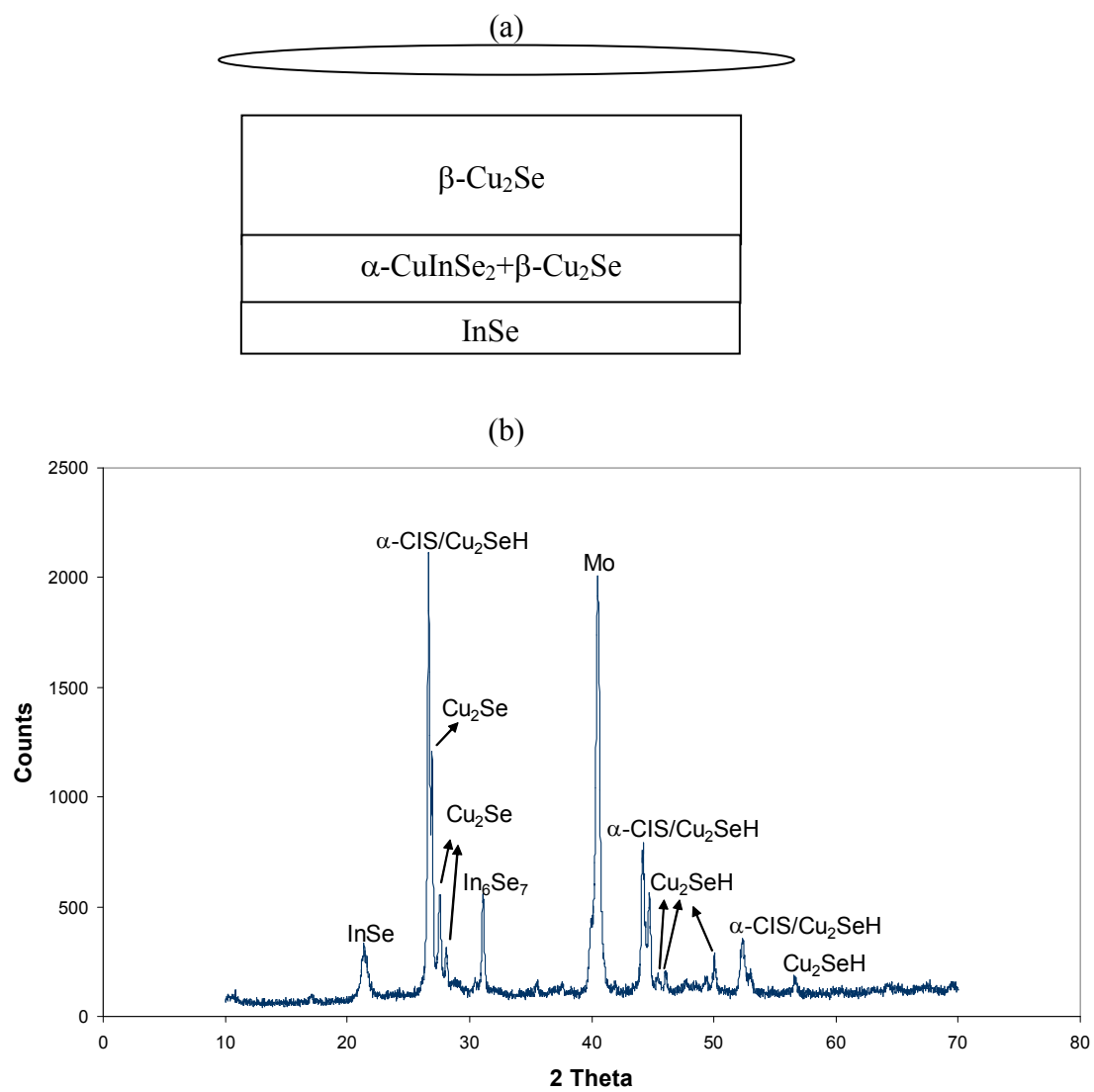
Figure 8-17. Film after step **I:** 480 ˚C, 60 s, 60 ˚C/s (a) structure (b) XRD
pattern.
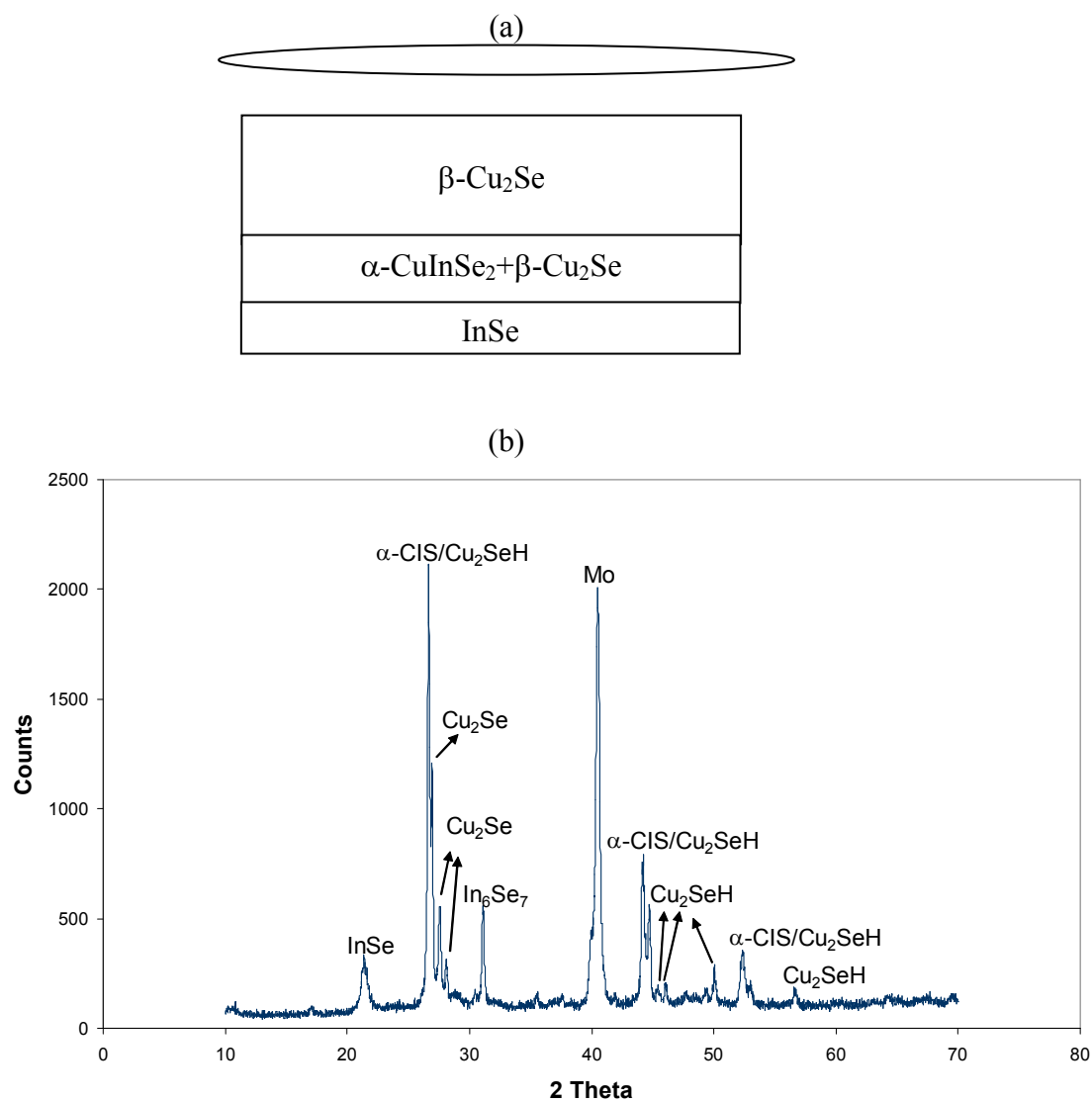
Figure 8-18. Film using higher temperature for step **I:** 550 ˚C, 120 s, 60 ˚C/s
(a) structure (b) XRD pattern.
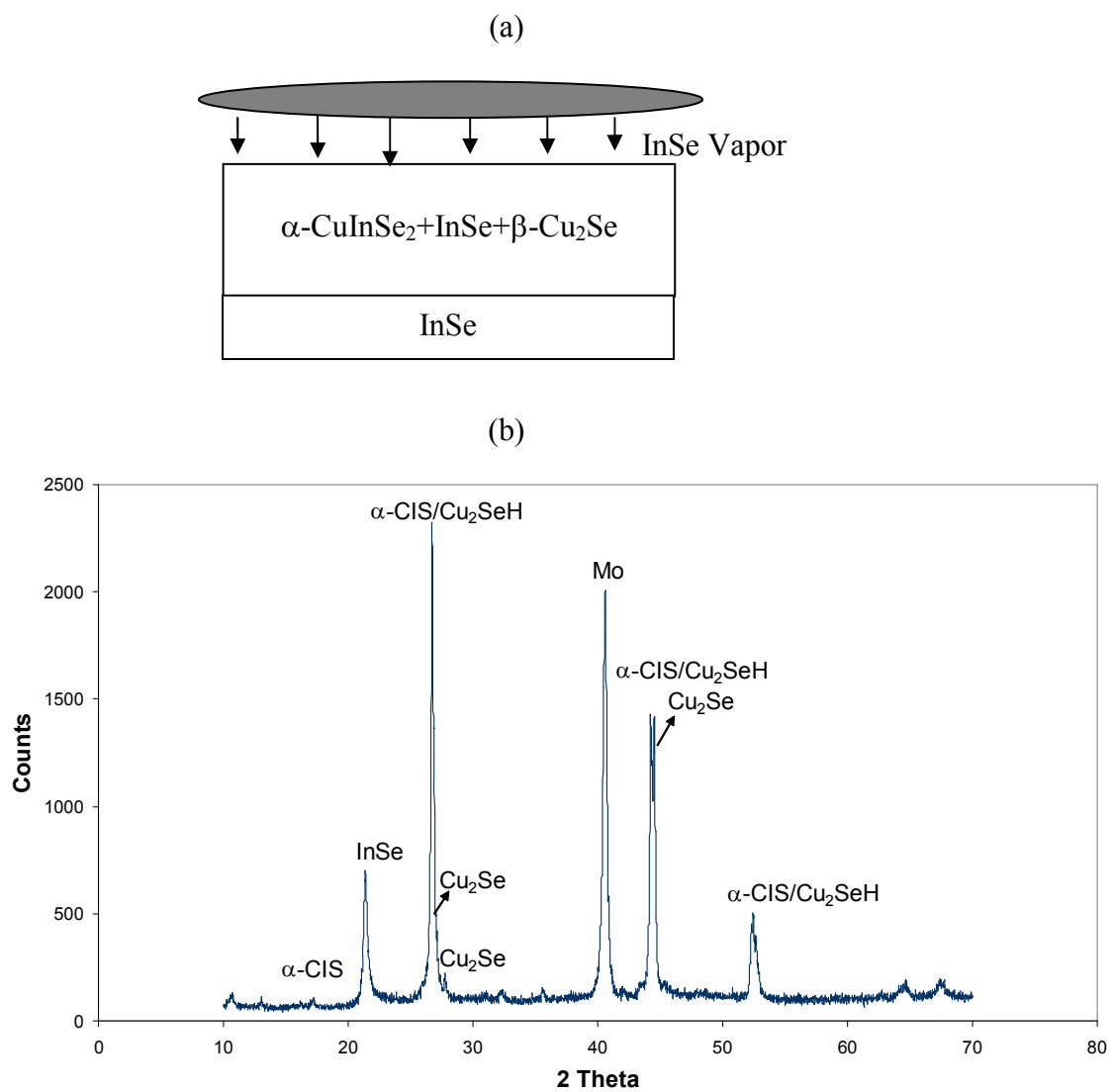
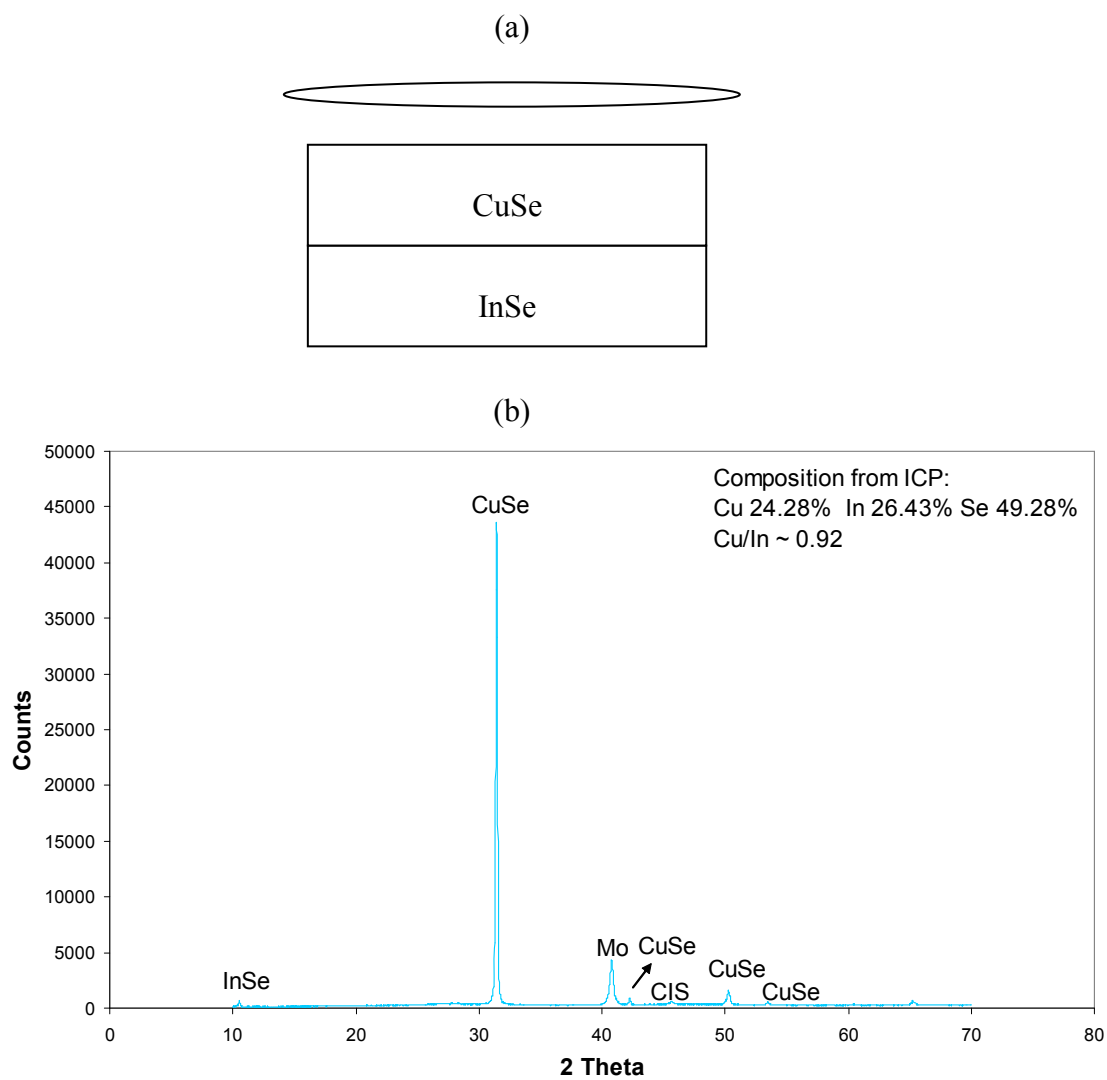Figure 8-19. Film after step **II:** 480 ˚C 60 s, 60 ˚C/s with InSe lid (a) structure (b) XRD pattern.
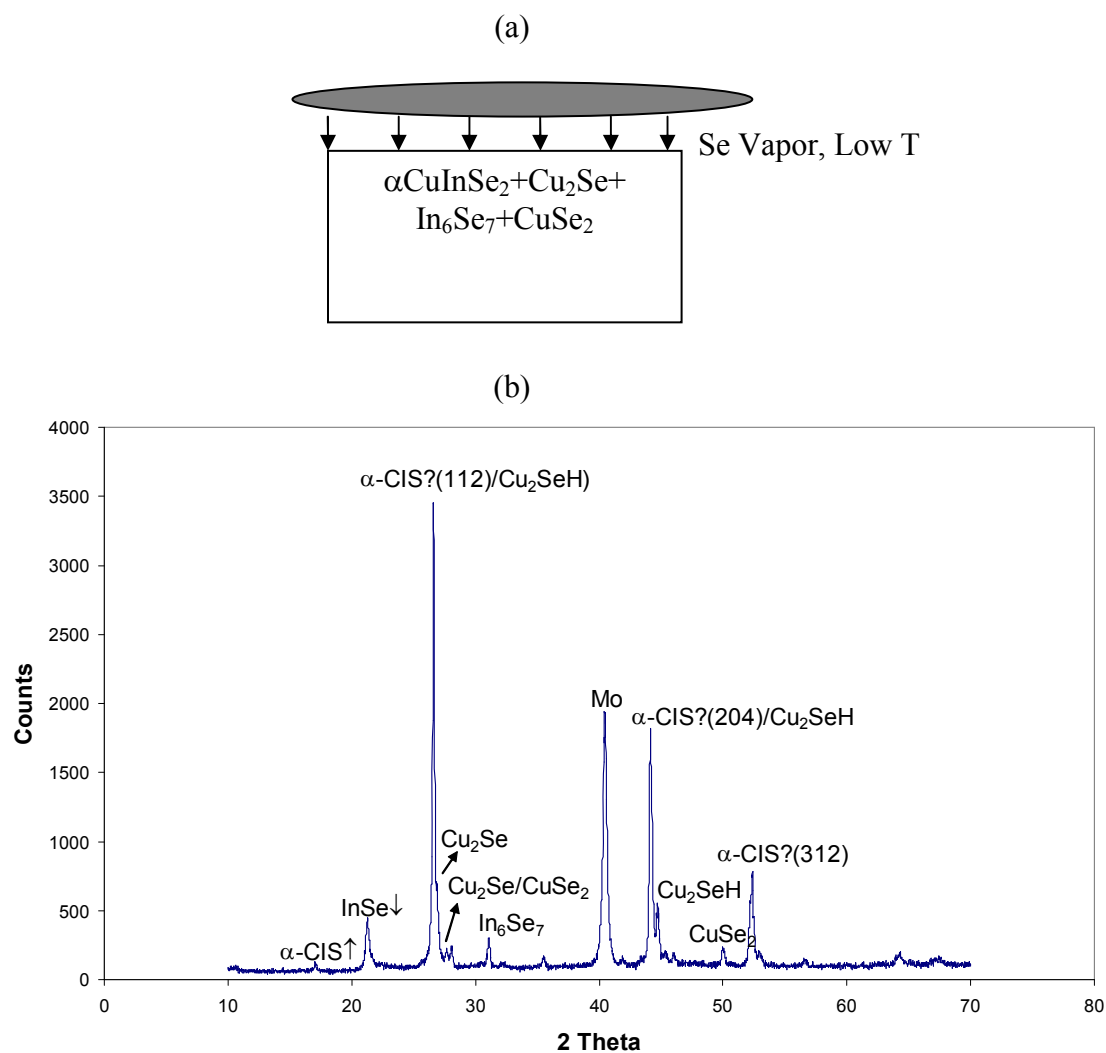
Figure 8-20. Film after step **III**: 480 ˚C, 60 s, 60 ˚C/s with Se lid (a) proposed structure (b) XRD pattern.

(a)

α-CuInSe$_2$ + very small amount InSe

(b)
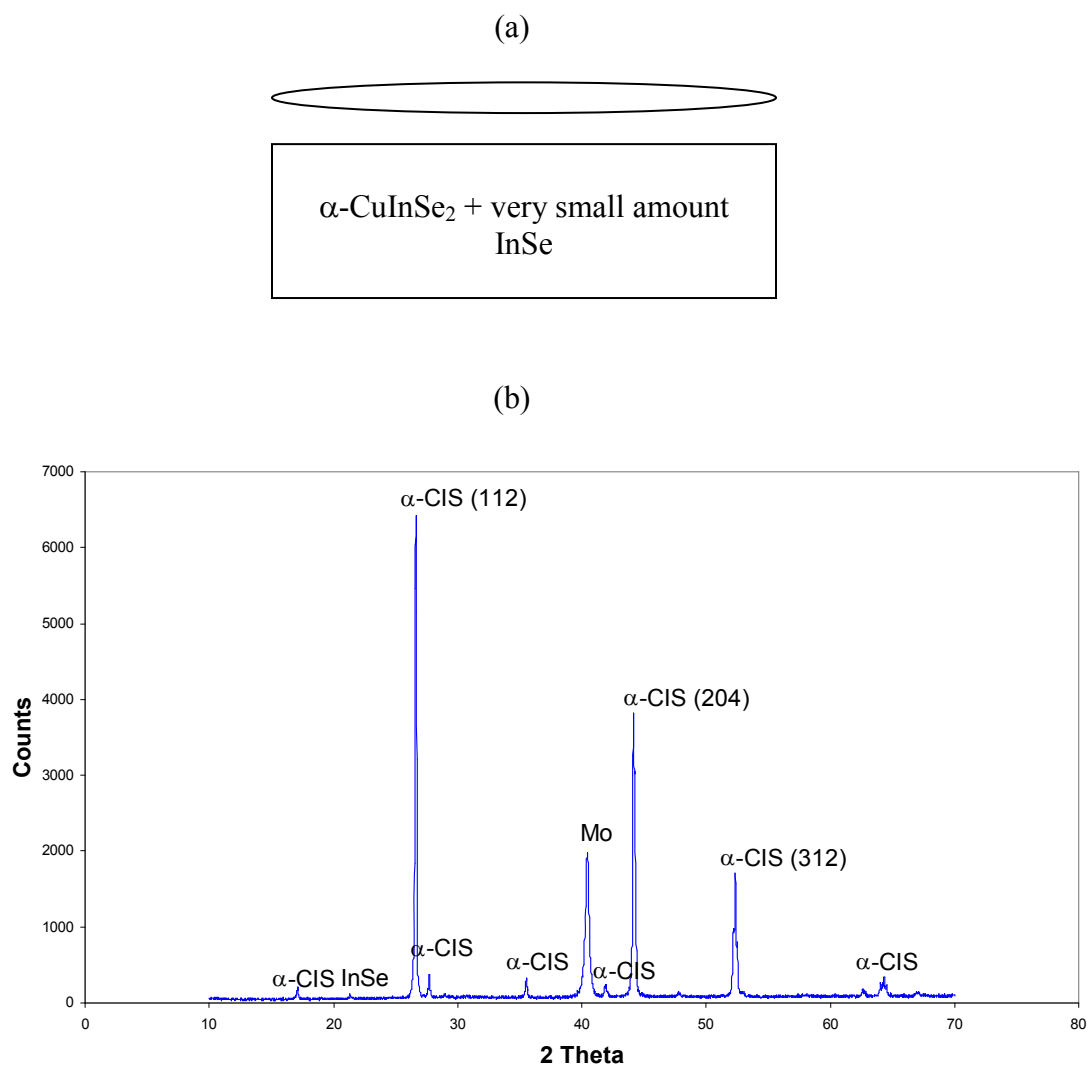
Figure 8-21. Film after step **IV**: 550 ˚C, 70 s, 60 ˚C/s with clear lid (a) structure (b) XRD pattern.

(a)

(b)

Figure 8-22. Precursor (a) structure (b) XRD pattern and composition data.
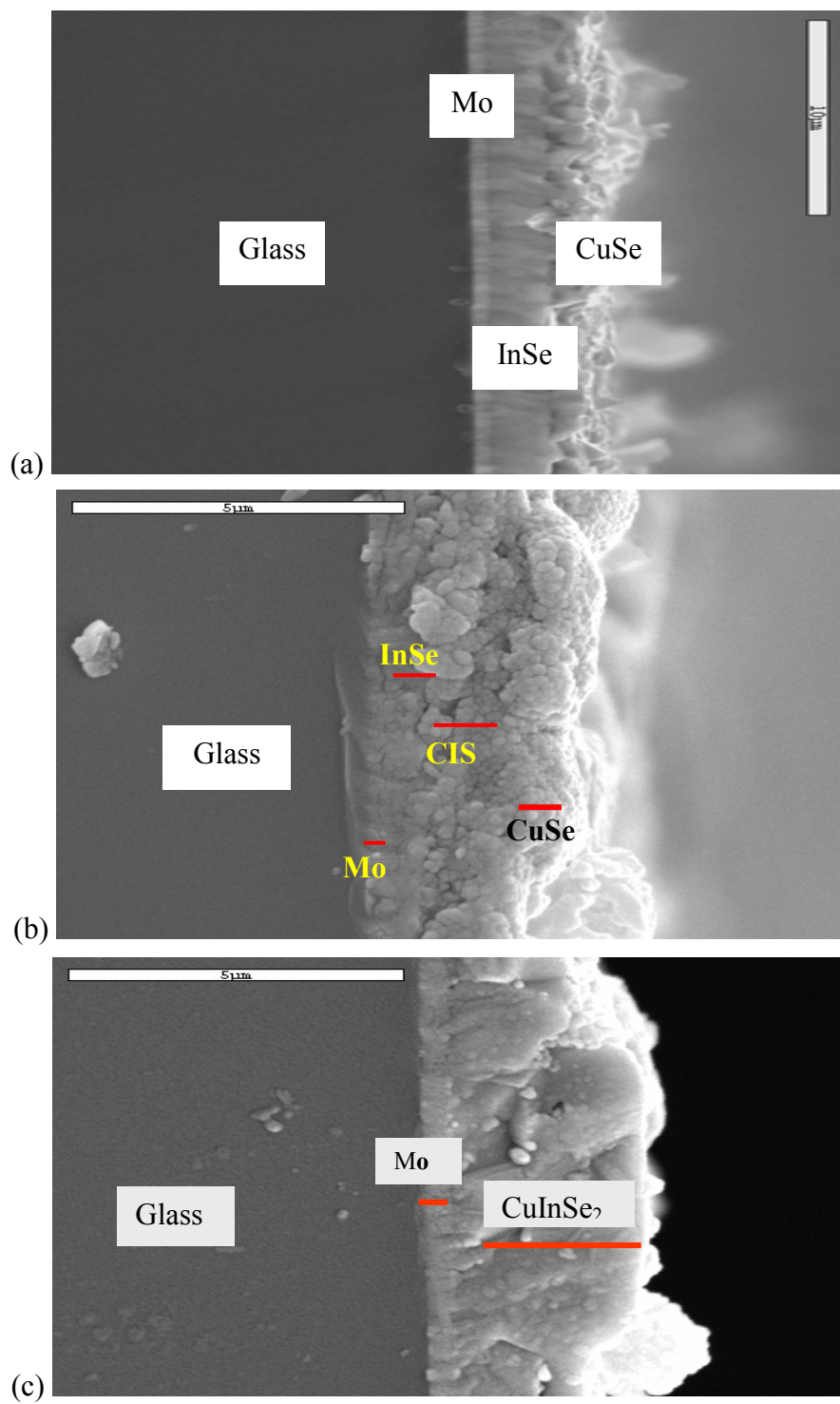
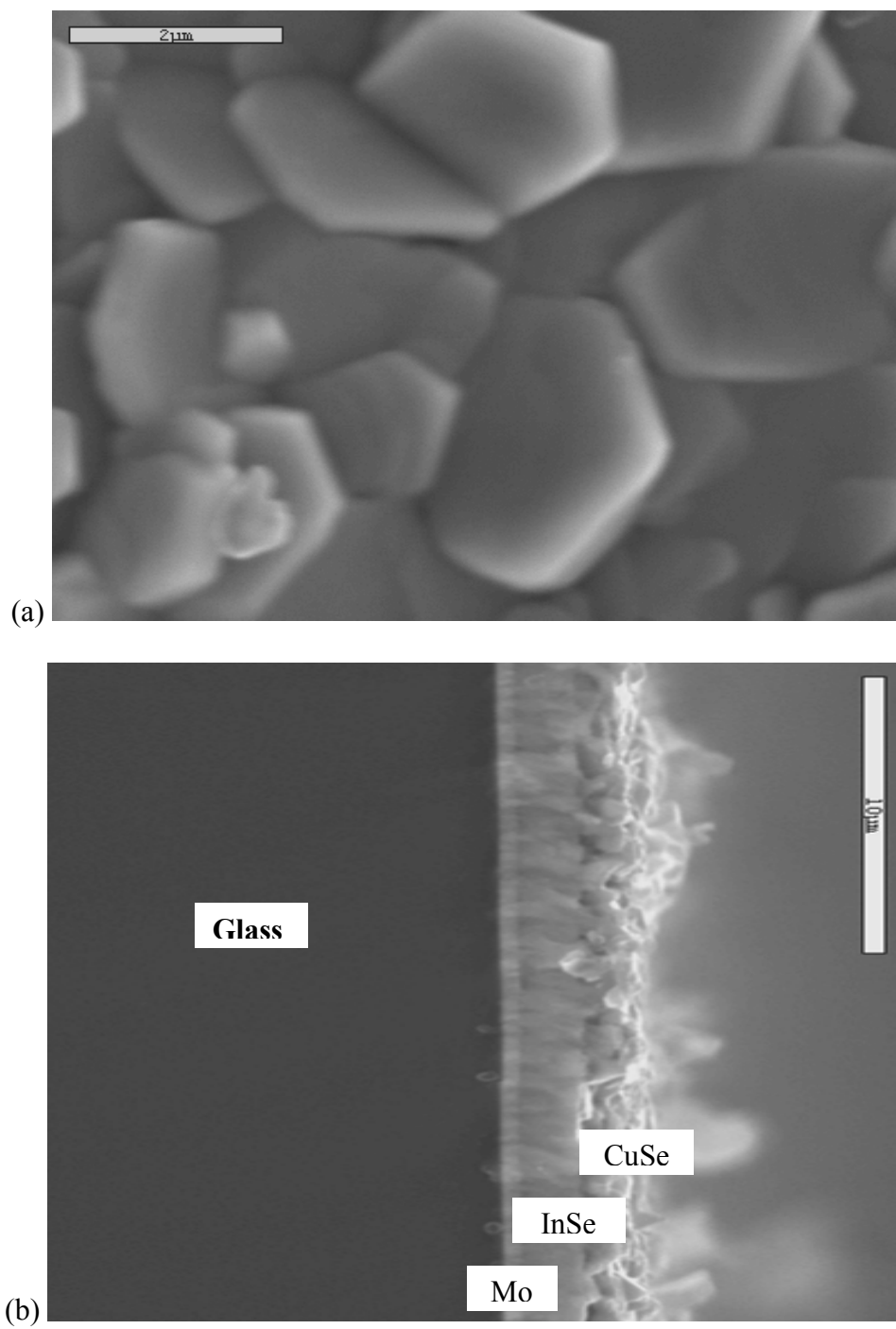Figure 8-23. SEM cross-sectional micrograph of (a) precursor, (b) after step I, and (c) after step **IV**.

(a)

(b)

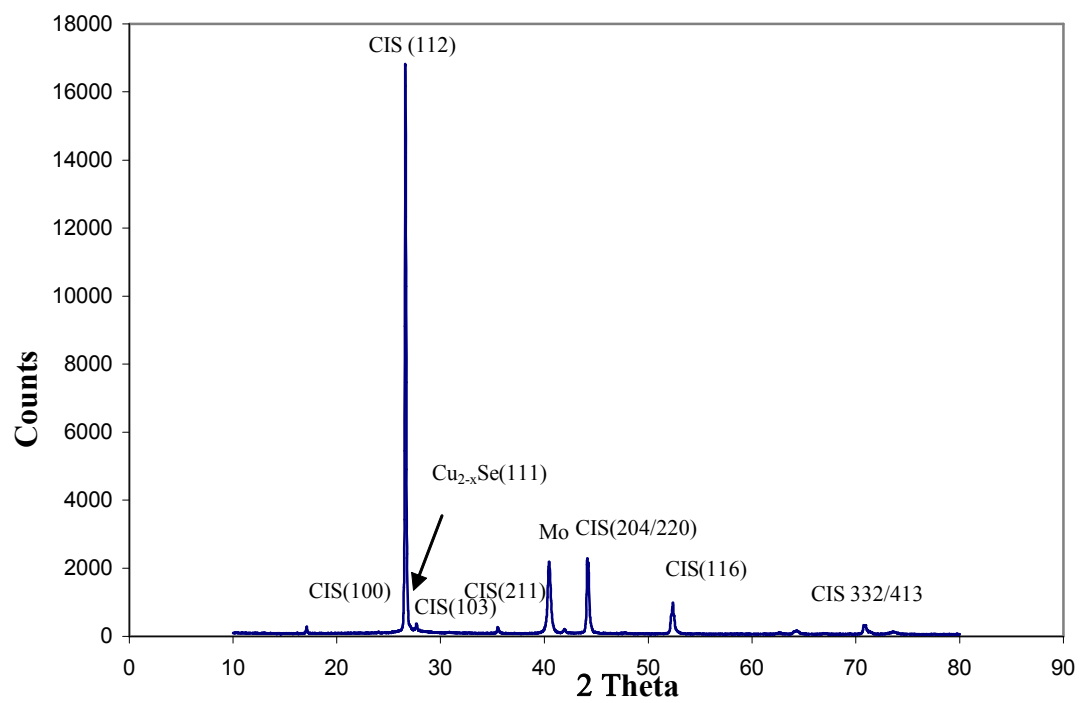Figure 8-24. SEM micrograph of the precursor (a) plane view (b) cross-section.

Figure 8-25. XRD pattern after RTP at 500 ºC for 2.5 min (Run 1).

500 C,2.5 mins

600nm 40000X
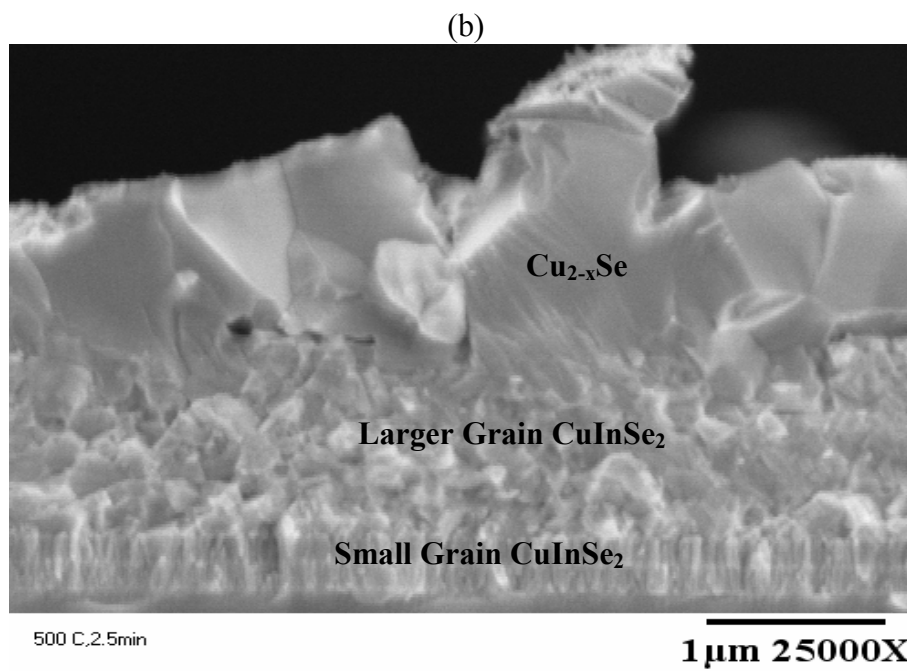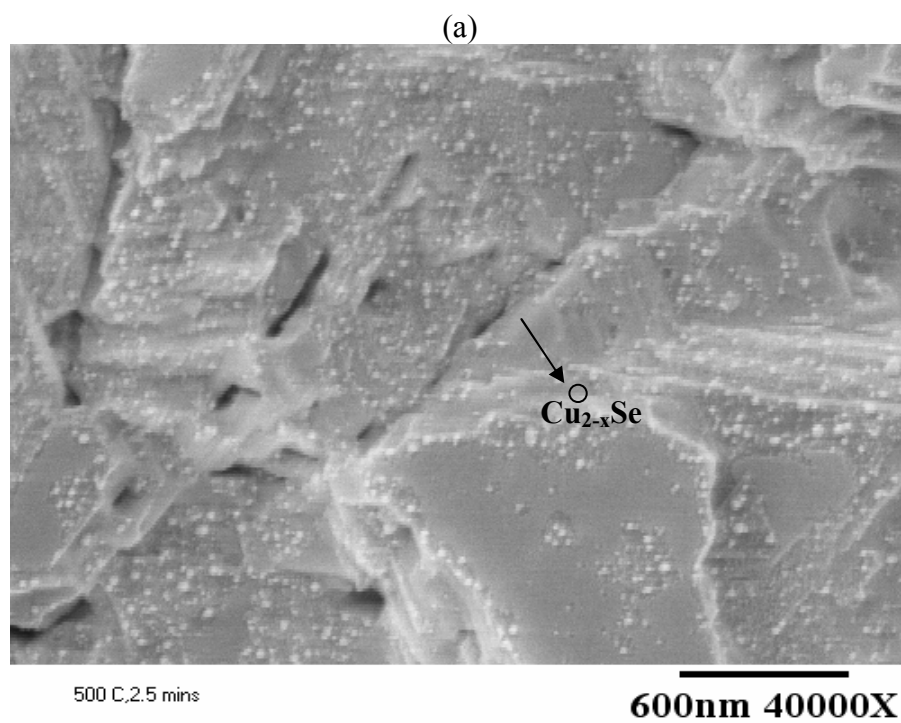
500 C,2.5min

1μm 25000X

Figure 8-26. SEM micrograph of film after RTP at 500 ºC for 2.5 min (Run 1)
(a) plane view (b) cross-section.
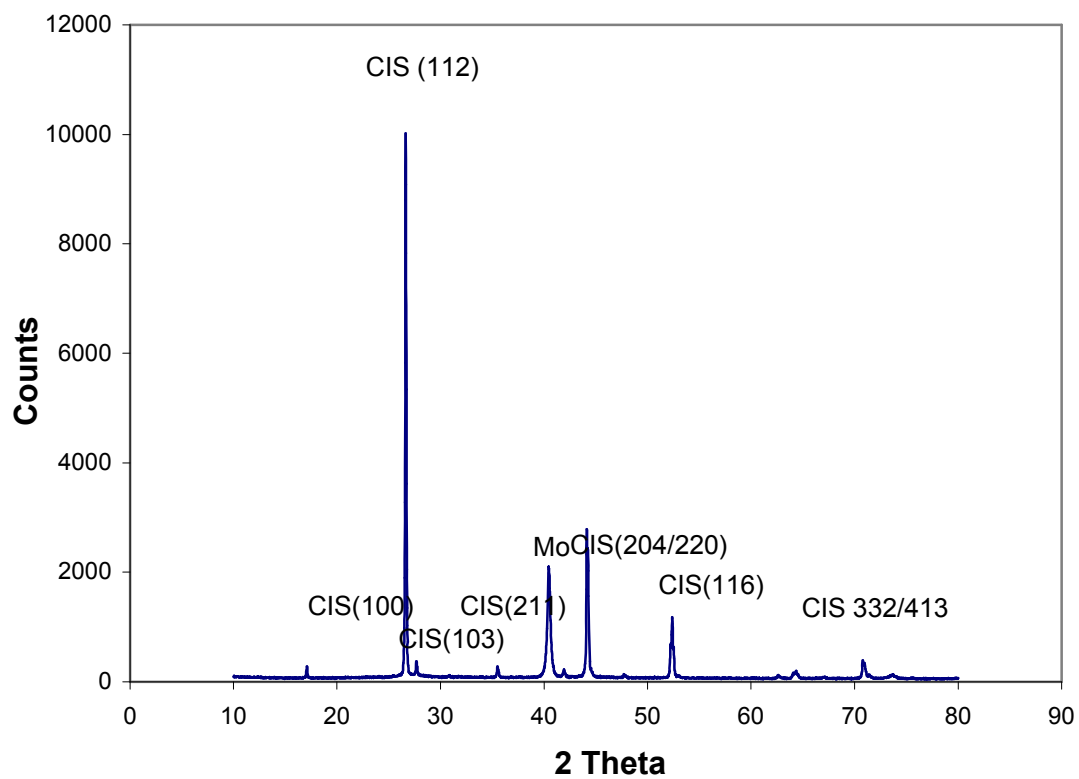
Figure 8-27. XRD pattern after RTP at 550 ºC for 4.5 min (Run 2)..

550 C, 4.5 min   1μm 30000X

550 C, 4.5 min   1μm 30000X

Figure 8-28. SEM micrograph of film after RTP at 550 ºC for 4.5 min (Run 2)
(a) plane view (b) cross-section.

(a)

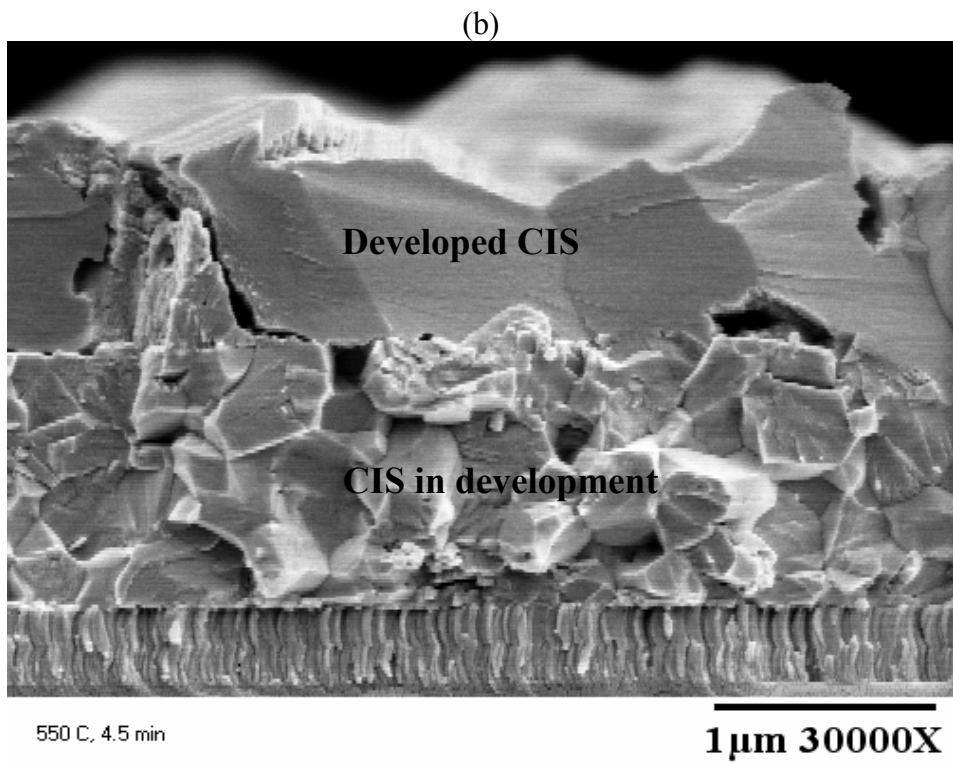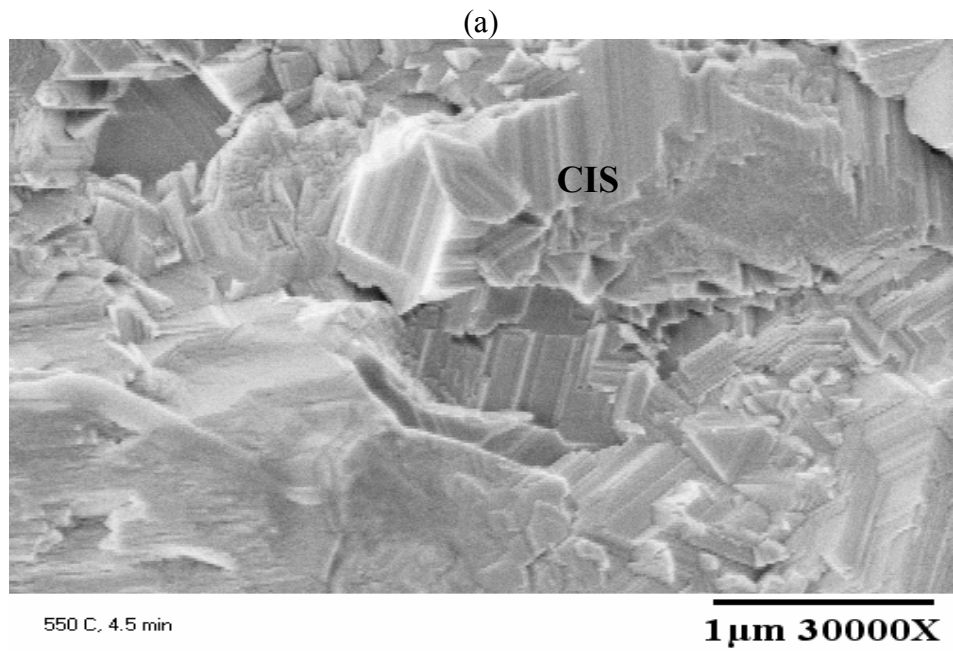

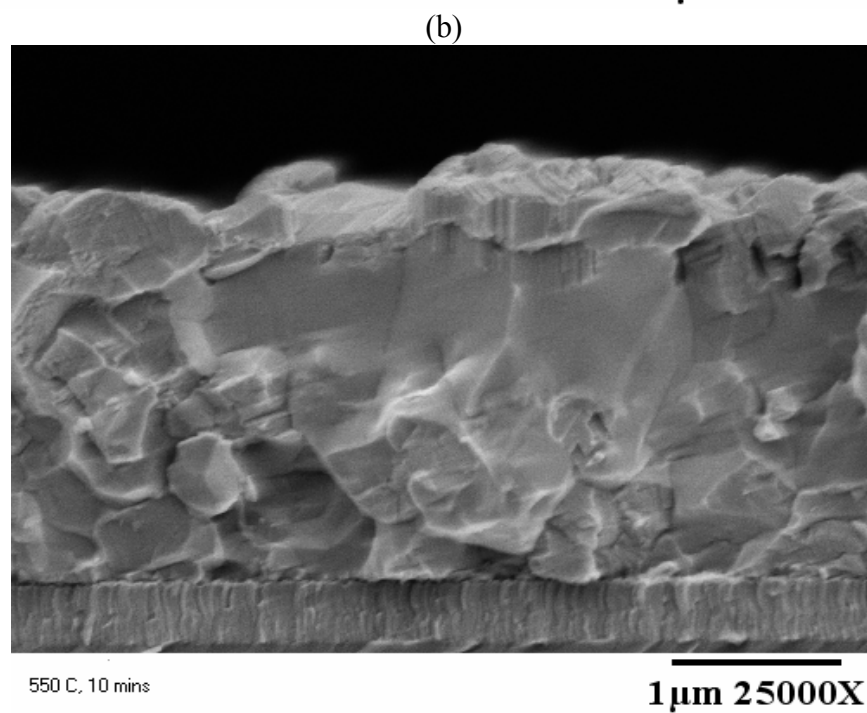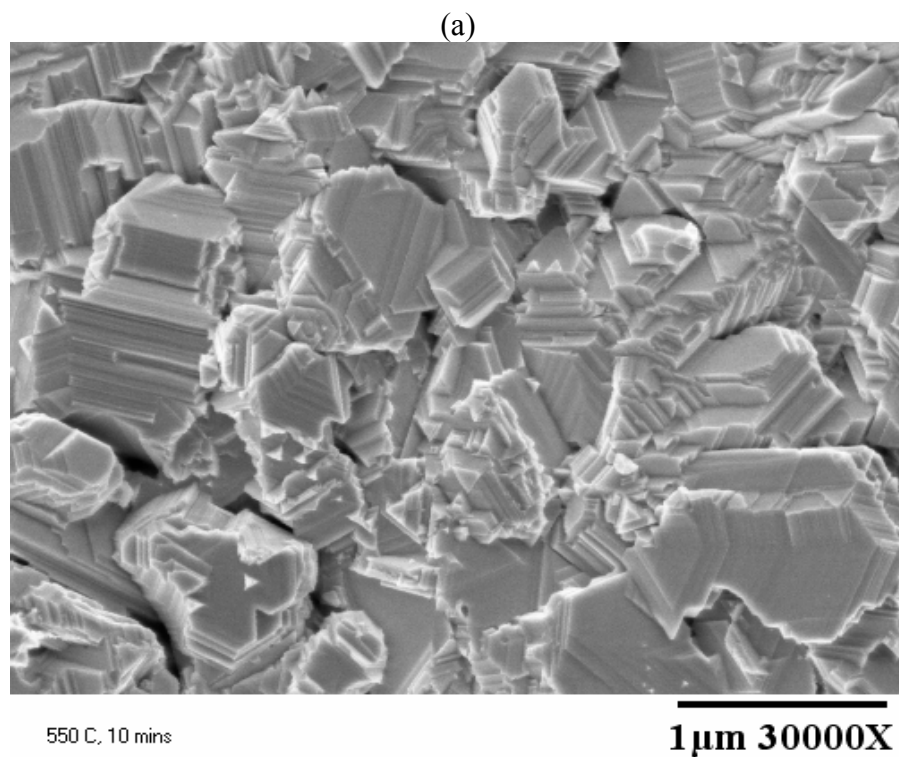550 C, 10 mins   1μm 30000X

(b)

550 C, 10 mins   1μm 25000X

Figure 8-29. SEM micrograph of film after RTP at 550 ºC for 10 min (Run 3)
(a) plane view (b) cross-section.
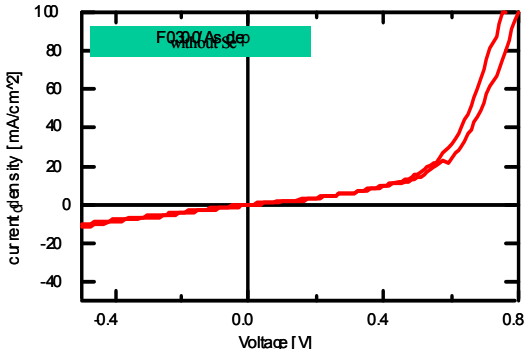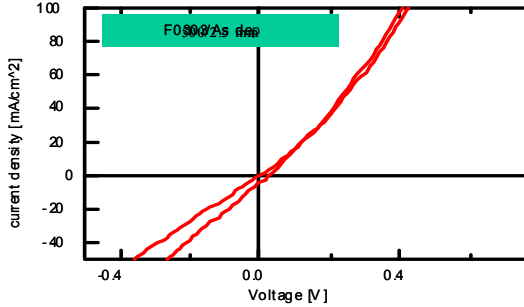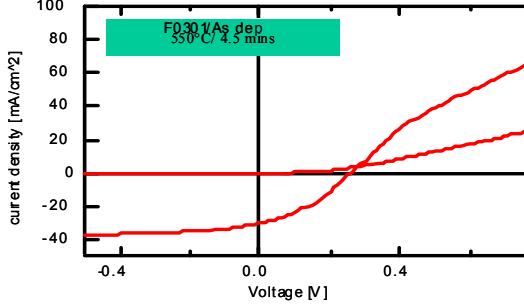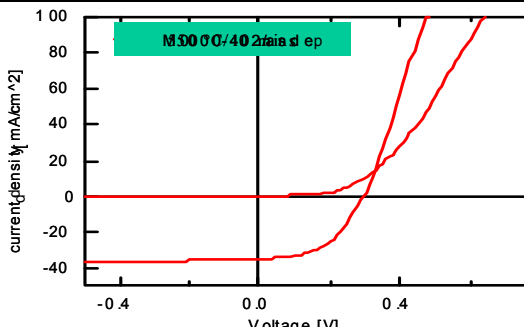
I-V Curve	V_{OC} (V)	J_{SC} (mA/cm^2)	I_{sc} (mA)	FF (%)	Eff (%)
	0.025	-0.48	-0.21	23.42	0.000
	0.024	-4.34	-1.86	24.25	0.025
	0.262	-30.36	-13.05	35.09	2.79
	0.296	-34.69	-14.9	49.54	5.08

Figure 8-30. Figure 3-30. I-V curves for the cells fabricated after without Se control and Runs 1-3 with Se control
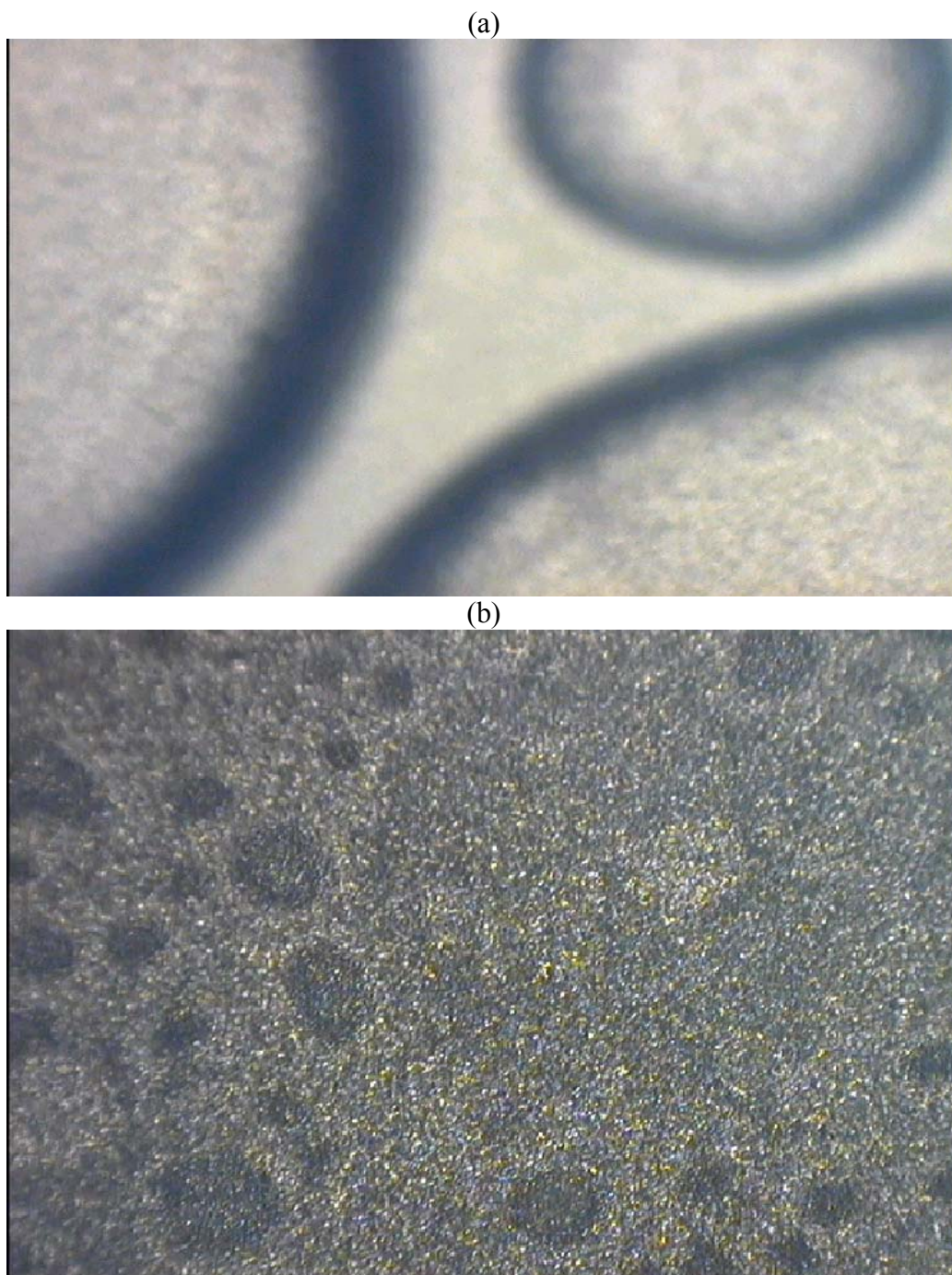
Figure 8-31. Optical plane view micrograph absorber film after RTP process on inverted structure precursor (a) InSe/CuSe/Mo/Glass (b) InSe/CuSe/InSe/Mo/Glass at magnification 10x structure (b) XRD pattern.

9 Investigation of Pulsed Non-Melt Laser Annealing on the Film Properties and Performance of Cu(In,Ga)Se2 Solar Cells.

9.1 Accomplishments

CIGS cells contain a thin (~ 50 nm) n+ CdS buffer layer deposited on a thick (~ 1 to 2 μm) p-type CIGS absorber. Although the exact location of the electrical junction relative to the metallurgical one is not known, it does lie near the surface of the absorber. Furthermore, analyses of CIGS film characterization results and cell performance data suggest that interfacial recombination near the CdS/CIGS metallurgical junction is a major limitation to the device performance. The possibility of repairing damage near this shallow junction, while preserving the composition gradients in the bulk CIGS films motivated exploration of NLA treatment. In this work CIGS absorber films were annealed using a 248 nm pulsed laser beam and the properties of the films and subsequent device performances were compared to untreated films.

The CIGS samples used in this study were provided by the National Renewable Energy Lab (NREL) and Shell Solar Inc. (SSI), and both sample sets were grown on the Mo- coated soda-lime glass substrates. For the Hall-effect measurements, however, the CIGS films were grown on the insulating soda-lime glass (SLG) substrates. A thin (50 nm) CdS buffer layer was deposited on the CIGS samples using Chemical Bath Deposition (CBD) at 75 $^{\circ}$C for 30 min. The NLA treatment was carried out using a pulsed 248 nm line derived from a KrF excimer laser system. In this study the laser pulse width was fixed at 25 ns and the energy density was varied in the range 20 to 60 mJ/cm^2 and the number of pulse cycles in the range 5 to 20. To study the effect of NLA on the CIGS film properties, NLA treatments were performed on the CIGS films with and without CdS buffer layers. After NLA treatments, a ZnO window layer was deposited on the CdS/CIGS/Mo/SLG sample by RF sputtering. Subsequent metallization (Ni-Al front contact grids) was carried out by e-beam evaporation through a shadow-mask. Finally, finished devices were produced by cutting the sample into separate cells with 0.429 cm^2 active area and attaching wires with In bumps on the Mo-coated glass substrates for back contacts. The performance of these cells was then tested.

The non-destructive Dual Beam Optical Modulation (DBOM) characterization method was used to measure the effective carrier lifetimes in the CIGS absorbers [9-4, 9-5], and to evaluate the effect of NLA treatment on the performance of CIGS cells. Within the sensitivity of the DBOM technique, the effective carrier lifetime was found to increase for CIGS films on Mo/SLG annealed using 5 cycles of laser pulse with an energy density in the range 30 to 60 mJ/cm^2. The results summarized in Table 9-1 show that a low energy NLA treatment can increase the effective carrier lifetime of the annealed samples and improve the performance of CIGS cells.

XRD patterns of CIGS and CdS/CIGS samples before and after NLA treatments show substantial narrowing of the diffraction peaks that belong to CIGS, as shown for two samples in Figure 9-1. These results can be interpreted as an improvement of the layer's crystallinity after

NLA treatment, which is consistent with the observed increase of the grain size (SEM) and the effective carrier lifetime in the CIGS films.

Table 9-1 Effective minority carrier lifetime (τ) of CIGS films deposited on Mo coated soda-lime glass substrates before and after NLA treatment as measured by DBOM [9-4,9-5].

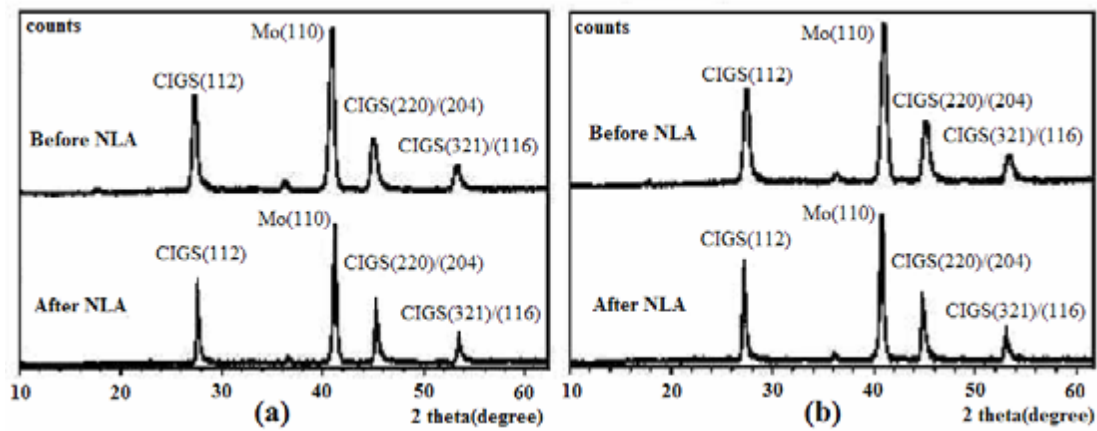| Sample #	τ before NLA (ns)	τ after NLA (ns)	NLA condition
CIGS-S1	1.77	4.87	30 mJ/cm^2, 5 pulses
CIGS-S2	2.82	3.39	40, 5
CIGS-S3	4.11	5.43	50, 5
CIGS-S4	4.51	6.31	60, 5

Figure 9-1. XRD spectra before and after NLA treatments for (a) a CIGS and (b) a CdS /CIGS sample.
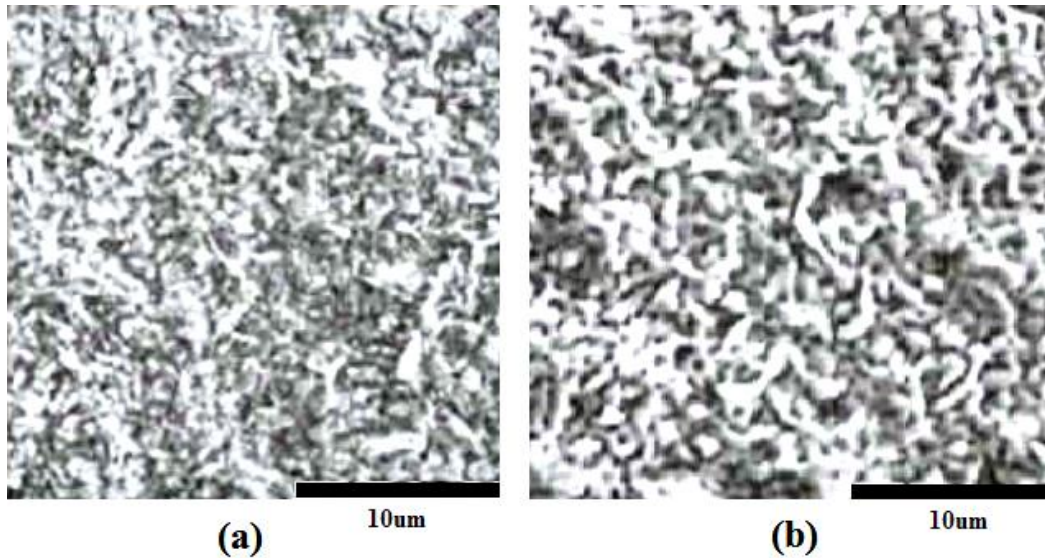
Figure 9-2. Surface morphology of CIGS films (a) without and (b) with NLA treatments at an energy density of 55 mJ/cm^2 (SEM images with magnification of 6000x).

As illustrated by SEM micrographs shown in Figure 9-2, the surface morphology and apparent grain size increased upon laser annealing. This result suggests that the energy density used was sufficient to cause atomic rearrangement in the near surface region, and thus the potential exists to modify the atomic defects in the near surface region.

Based on the encouraging DBOM results from the initial NLA treated CIGS samples, a second set of experiments were performed in which the energy density and number of the incident laser pulse were varied. Hall-effect measurements were made on the CIGS samples without a Mo layer prior and after annealing to determine the effects of NLA treatment on the carrier concentration, carrier mobility, and sheet resistivity of CIGS films.

Four CIGS films deposited on the glass substrate underwent pulsed NLA treatments at room temperature. The annealing conditions and the results of Hall-effect measurements (using an MMR Hall and Van Der Pauw measurement system) before and after the NLA treatments are summarized in Table 9-2. The results show a significant increase in the values of Hall mobility and a decrease in film resistivity following NLA treatment. The carrier mobility in the NLA treated CIGS films were 3 to 4 times greater than the values before annealing. Although the hole concentration decreased slightly after annealing, film resistivities decreased by 72 and 64% for CIGS films (samples H1 and H2) treated at an energy density of 20 mJ/cm^2 with 10 and 20 laser pulses, respectively. At an energy density of 40 mJ/cm^2, the film resistivity was reduced by more than 95% from that of the non-annealed samples (H3 and H4). Thus, both the energy density and the number of laser pulse play an important role in determining the resistivity of NLA treated CIGS absorber layers.

Table 9-2 Results of Hall-effect measurements for CIGS films deposited on the glass substrates before and after NLA treatments.

Sample #	Hole-concentration* (10^{16}/cm-3)	Hall-mobility* (cm^2/V-s)	Resistivity* (Ω-cm)	NLA condition
CIGS-H1	0.53/0.445	8.89/37.6	133/37.3	20 mJ/cm^2, 10 pulses
CIGS-H2	2.9/2.43	0.93/2.98	235/86.4	20, 20
CIGS-H3	4.3/1.8	1.54/6.1	94/2.67	40, 10
CIGS-H4	7.1/3.3	0.60/2.8	148/4.64	40, 20

* Data taken before/after NLA treatments.

Six CdS/CIGS samples treated by NLA with selected energy density and pulse number plus one control sample without NLA treatment were fabricated into finished devices. There were five cells on each device and each cell was tested using a photo- J-V system at room temperature. The NLA conditions and averaged photo- J-V results of these devices are summarized in Table 9-3. Note that the data in Table 9-3 were averaged from the measured values of five cells on each device and the standard deviation computed on the 5- cell measurements. In these experiments, improvements were found in the photo- J-V results of the annealed devices under 30mJ/cm^2, using 5 or 10 pulses (CIGS-D1 and CIGS-D2), as compared to results from the control sample (Ctrl-D). The data also show degradation in cell performance parameters such as open circuit voltage (V_{oc}), short-circuit current (J_{sc}), Fill Factor ($F.F.$), and cell efficiency (η_c) of the devices laser annealed with energy densities higher than 30 mJ/cm^2. It was also found that for devices annealed at the same energy density, the fill factor and conversion efficiency of the 5-cycle annealed devices are higher than those of 10-cycle annealed devices. These results suggest that an optimal NLA energy density and pulse number are approximately 30 mJ/cm^2 and 5 pulses, respectively.

Table 9-3 Cell performance parameters (V_{oc}, J_{sc}, $F.F.$ and η_c) from the measured photo-J-V characteristics of NLA-treated CIGS solar cells

Device #	V_{oc} (V)	J_{sc} (mA/cm^2)	F.F. (%)	η_c (%)	NLA conditions
CIGS-D1	0.576	31.60	66.50	12.07	30 mJ/cm^2, 5 pulses
CIGS-D2	0.568	31.25	63.11	11.12	30, 10
CIGS-D3	0.497	26.79	55.29	7.368	40, 5
CIGS-D4	0.493	26.71	53.08	7.040	40, 10
CIGS-D5	0.436	25.56	51.80	5.773	50, 5
CIGS-D6	0.433	25.23	47.77	5.201	50, 10
Ctrl-D	0.543	30.05	55.74	9.064	None

To better understand the specific differences between the control cell and the two 30 mJ/cm^2 NLA treated cells, dark J-V and quantum efficiency (Q-E) measurements as well as theoretical calculations of device parameters were made for selected cells from each of the three devices (Ctrl-D, CIGS-D1 and CIGS-D2).

The J-V characteristics for a p-n junction solar cell under uniform illumination condition can be expressed by [9-6, 9-7]

$$J(V) \cong J_0 (\exp \frac{q(V - R_s J)}{nkT} - 1) + \frac{V - R_s J}{R_{sh}} - J_{ph} \tag{1}$$

where J_{ph}, J_o, n, R_s and R_{sh} are the photocurrent density, saturation current density, diode ideality factor, series resistance, and shunt resistance, respectively.

To study the effect of pulsed NLA treatment on the diode characteristics, photo- and dark- J-V measurements were performed at room temperature for each the selected cell. The measured parameters and calculated values of J_o, n, and R_s [9-8, 9-9] are summarized in Table 9-4 (note that R_{sh} is quite high in all tested CIGS cells).

From the dark- J-V curves shown in Figure 9-3, both the dark current density and saturation current density, J_o, of the NLA treated cells are consistently smaller as compared to the control cell. These curves suggest that the recombination current through surface defects dominates the dark- J-V curve under forward bias condition before NLA treatment (with diode ideality factor n >4). After the NLA treatment, a significant reduction in the dark current density was observed apparently due to reduction of surface defect density, and the recombination current was dominated by bulk defects in the junction space charge region at higher bias (n ≈ 2). These results indicate that defects in the surface region and interface of absorber and buffer layers can be effectively reduced by NLA treatment, thus decreasing the recombination of minority carriers via interface states and defects in the junction space-charge region of CdS/CIGS cells. Although cells treated by the NLA exhibit higher series resistance (R_s), the negative effect of R_s increase on the diode characteristic remains relatively small due to the extremely low value of J_o.

Finally, the quantum efficiency (Q-E) was measured on the control and NLA treated cells. The results shown in Figure 4 indicate that for incident light with wavelengths greater than 480 nm, the Q-E of the NLA cells is higher than that of the control cell, indicating that the NLA treatment improves the effective carrier lifetime and diffusion length in the absorber layer and hence increases the short-circuit current density in comparison with the control cell. In the shorter wavelength regime (λ< 0.48 μm), no improvement of Q-E was observed between the control cell and the NLA treated cells. It is also noted that values of the Q-E for cell annealed with 10 cycles of laser pulse were found to be lower than that of the cell with 5 cycles of laser pulse at same energy density, again suggesting that the optimal laser pulse number is between 5 and 10 cycles.

Table 9-4 Device performance parameters determined from photo- J-V measurements and device parameters calculated from dark- J-V measurements for the control cell and selected NLA-treated CIGS cells

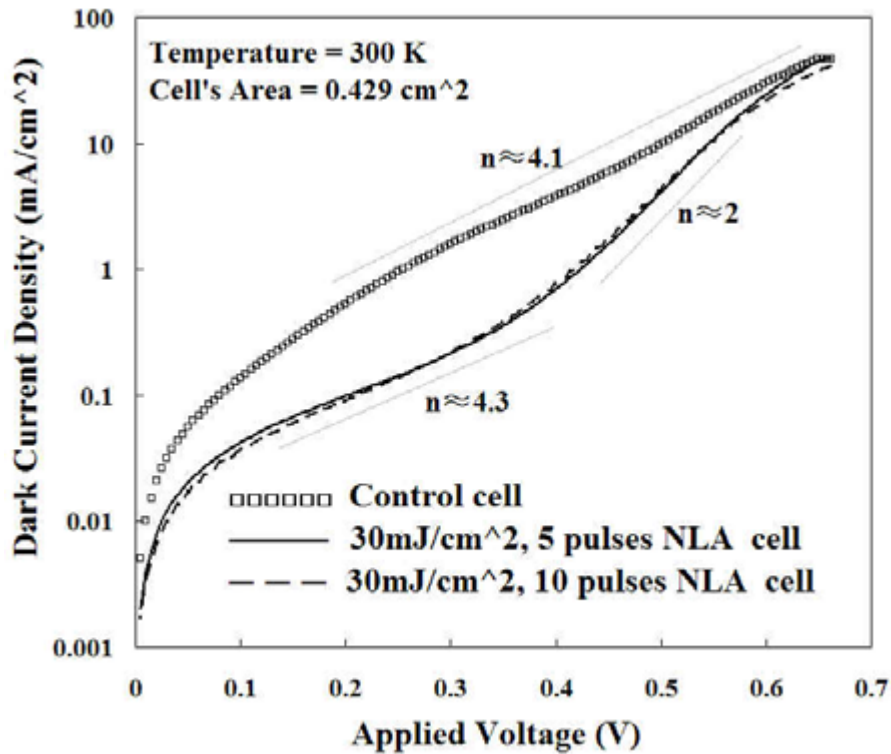| Cell #	Ctrl-D-C3	CIGS-D1-C3	CIGS-D2-C3
NLA condition	None	30 mJ/cm^2, 5 pulses	30 mJ/cm^2, 10 pulses
Cell area (cm^2)	0.429	0.429	0.429
V_{oc} (V)	0.528	0.577	0.572
J_{sc} (mA/cm^2)	29.78	34.24	32.00
F.F. (%)	48.86	67.88	66.78
Efficiency (%)	7.69	13.41	12.22
V_m (V)	0.365	0.458	0.453
J_m (mA/cm^2)	21.37	28.99	26.88
N	~4.13	~1.98	~1.96
J_0 (mA/cm^2)	~3.22x10^{-3}	~1.1x10^{-3}	~1.06x10^{-3}
R_s (Ω)	~10.17	~14.06	~15.94

Figure 9-3. Dark- J-V curve (semi-log plot) comparing the control cell to two NLA treated cells.
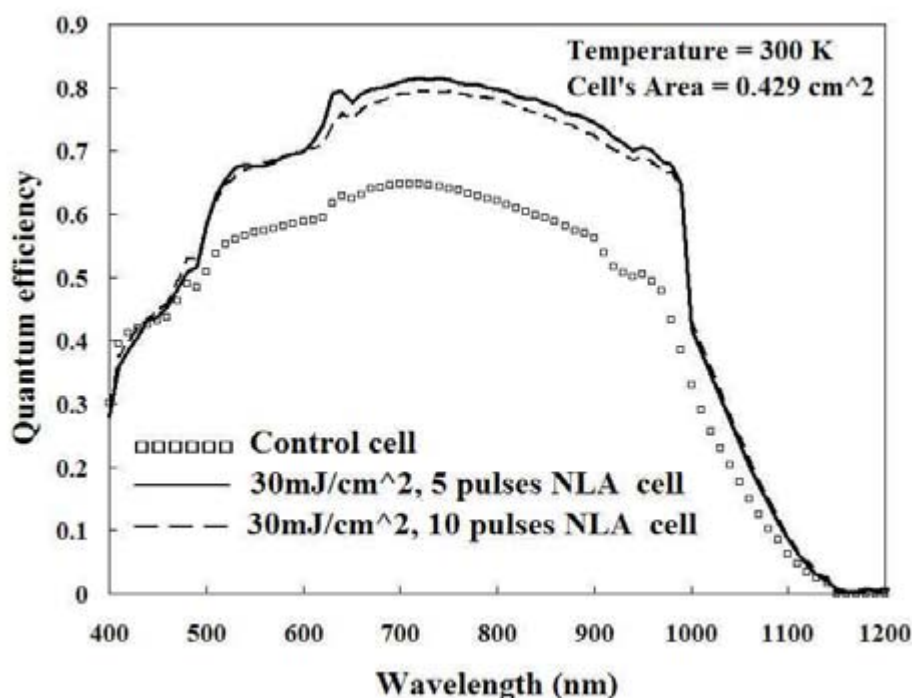
Figure 9-4. Quantum efficiency (Q-E) versus wavelength comparing the control cell to the two NLA-treated cells.

The results of pulsed NLA treatment on the film properties and the performance of CIGS solar cells are very encouraging. Examination of the structural and electrical properties of films from 2 different sources clearly showed the annealing step modified the near surface region. Increased surface feature size evidenced in SEM photos and CIGS diffraction peak narrowing is consistent with increased crystallinity. Furthermore, DBOM measurements of the effective carrier lifetime indicated the lifetime could be increased by as much as a factor of 2.75. Hall measurements of CIGS samples deposited on SLG revealed NLA treatment increased the mobility and resistivity and decreased the net free hole concentration of each sample, consistent with the hypothesis of annealing out electrically active defects in the near surface region. Based on a parametric study, the best NLA result was obtained with a pulsed laser energy density of 30 mJ/cm^2 and 5 pulse cycles. J-V and Q-E measurements were also made to study the effect of NLA treatment at the best condition on the performance of CIGS cells. The results show that pulsed NLA treatment has a beneficial effect on the cell performance with the cell efficiency increasing from 7.69 % to 13.41 and 12.22 % after annealing 2 different samples prior to device processing. The energy density of the laser beam and the number of pulse cycle were found to play a key role in changing the optical and electrical properties of the CIGS films and hence the cell performance.

9.2 References cited

[9-1]   J. S. Luo, W. T. Lin, C. Y. Chang, W. C. Tsai, *J. Appl. Phys.*, Vol. 82, p. 3621 (1997).

[9-2]   D. R. Chen, J. S. Luo, W. T. Lin, C. Y. Chang, P. S. Shih, *Appl. Phys. Lett.*, Vol. 73, p. 1355 (1998).

[9-3]   X. M. Lu, J. S. Zhu, W. S. Hu, Z. G. Liu, Y. N. Wang, *Appl. Phys. Lett.,* Vol. 66, p. 2481 (1995).

[9-4]   Sheng S. Li, B. J. Stanbery, C. H. Huang, C. H. Chang, Y. S. Chang, T. J. Anderson, "Effects of buffer layer processing on CIGS excess carrier lifetime: application of dual-beam optical modulation (DBOM) to process analysis [of solar cells]," 25th IEEE PVSC, Washington D.C., U.S.A., May 13-17, pp. 821-824 (1996).

[9-5]   C.H. Huang, Sheng S. Li, B.J. Stanbery, C.H. Chang, T.J. Anderson, "Investigation of buffer layer process on CIGS solar cells by dual beam optical modulation technique," 26th IEEE PVSC, Anaheim, U.S.A., Sep 29-Oct 3, pp. 407-410 (1997).

[9-6]   A. Fahrenbruch, R. Bube, Academic Press, New York, (1983).

[9-7]   S.M. Sze, Wiley, New York, (1985).

[9-8]   T. Yanagisawa, T. Kojima, T. Koyanagi, K. Takahisa, D. Nakamura, *Elect. Lett.*, Vol. 36, pp. 1659-1660 (2000).

[9-9]   M.K. El-Adawi, I.A. Al-Nuaim, *Vacuum*, Vol. 64, pp. 33-36 (2002).

10   Device Modeling and Simulation of CIGS Solar Cells

10.1 Accomplishments

Device modeling and simulation studies of a Cu(In$_{1-x}$,Ga$_x$)Se$_2$ (CIGS) thin film solar cell have been carried out. A variety of graded band-gap structures, including space charge region (SCR) grading, back surface region grading, and double grading of the CIGS absorber layer, are examined. The device physics and performance parameters for different band-gap profiles were analyzed. Based on the simulation results, an optimal graded band-gap structure for the CIGS solar cell is proposed. The performance of the optimally graded band-gap cell is superior to that of the uniform band-gap cell. The SCR grading of the CIGS absorber layer improves the open-circuit voltage (V$_{oc}$) without significantly sacrificing the short-circuit current (J$_{sc}$) compared to the uniform band-gap CIGS. The back surface grading enhances both V$_{oc}$ and J$_{sc}$. An optimal graded band-gap profile, such as a double grading consisting of the SCR grading and back surface grading, improves significantly the efficiency up to 19.83% AM1.5G compared to the uniform band-gap profile with 15.42% efficiency. A comparison of the simulation results with published data for the CIGS cells shows an excellent agreement of photo- current density-voltage and quantum efficiency characteristics.

10.2 Introduction

Much information is available in the literature regarding single-junction Cu(In$_{1-x}$,Ga$_x$)Se$_2$ (CIGS) solar cells. Increasing the open-circuit voltage (V$_{oc}$) to improve the overall performance of CIGS cells is highly desirable because it minimizes the interconnection losses in the manufacture of cell modules. When alloying the CuInSe$_2$ (CIS) with Ga to form CIGS thin films, the wider band-gap energy of the CIGS absorber layer can potentially better match the solar spectrum, as well as increase the V$_{oc}$ of the fabricated cells, at the expense of a reduction in the value of the short-circuit current density (J$_{sc}$). Introducing a spatial variation of the Ga content within the CIGS layer, the band-gap profile can be optimized to increase the photon absorption and carrier diffusion. Furthermore, the Ga profile can be adjusted to optimize the CIGS absorber band gap profile, and hence improve the V$_{oc}$ and J$_{sc}$ values. Thus, band-gap engineering geared to controlling the spatial distribution of the Ga content in the absorber layer can lead to enhancing the overall performance of CIGS cells.

In this report, device modeling and numerical simulations of CIGS cells are conducted to analyze the impacts of various band-gap profiles for the CIGS layers on the performance parameters of the cells. Such modeling works will provide insight into which structures may be desired. The investigation focuses on the study of the effect on performance caused by various band-gap profiles in the space charge region (SCR) and in the back surface region of the absorber layer. Seven band gap profiles are analyzed, including the baseline case of a uniform band-gap profile. Based on the simulation results, an optimal graded band-gap structure for the CIGS cell is proposed. The simulation results of the optimized cell are compared to the reported experimental data. Additionally, the performance parameters of simulated results for CIGS cells with comparable grading structures in the absorber layers were found in excellent agreement with the published data.

10.3 Cell Structure and Material Parameters

The schematic energy-band diagram under equilibrium condition for a typical ZnO/CdS/CIGS solar cell with a uniform band-gap profile is illustrated in Figure 10-1. An inverted surface layer, which is referred to as an ordered vacancy compound (OVC), is present between the CdS and CIGS layers in the diagram. Schmid *et al.* [10-1] have demonstrated the existence of such a thin OVC, In-rich *n*-type layer, on the surface of the as-deposited CIGS films, and assigned to it the stoichiometry of $CuIn_2Se_{3.5}$ or $CuIn_3Se_5$. However, some literatures [10-2] [10-3] revealed that the compound of In-rich surface layer might not be the OVC and used a more general term 'surface defect layer' for this thin *n*-type layer. The inverted surface layer is considered to be beneficial to the performance of CIGS cells because the electrical junction is shifted away from the high-recombination interface between the CdS and CIGS layer, and hence the recombination rate is reduced. However, the properties of the surface defect layer such as high defect densities and high resistivity might lead to deteriorating the cell performance.
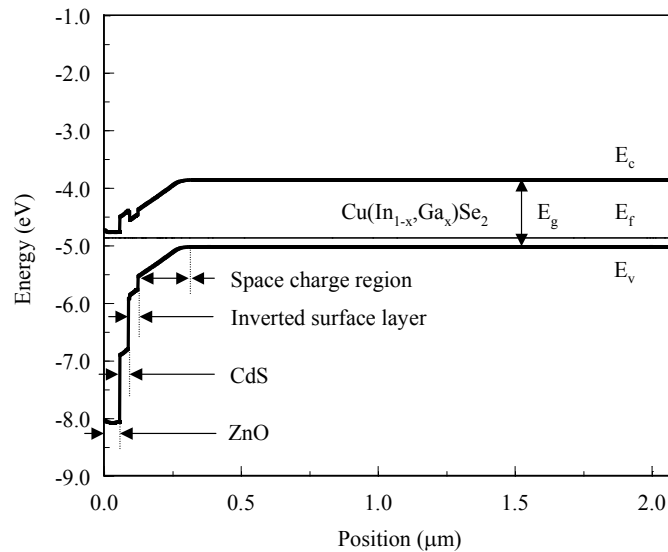

Figure 10-1. The schematic energy-band diagram of a typical ZnO/CdS/CIGS solar cell under equilibrium condition.

The CIGS cell structure considered in this study consists of the following material layers: *n*-ZnO, *n*-CdS, high-recombination interface, inverted surface, *p*-CIGS absorber, and a Mo on glass substrate. The computer simulation tool *AMPS-1D* (Analysis of Microelectronic and Photonic Structures) [10-4] was employed by specifying as input values the semiconductor parameters in each layer of the cell structure. The division of the layers for the cell structure is limited to the simplified device structure described above because of the limited knowledge available on the semiconductor parameters in each layer and uncertainties in the interface and junction properties arising from possible interdiffusion and reaction during the cell processing. The band gap of the CIGS absorber is engineered through the addition of a Ga profile. The anticipated changes in the physical properties of the CIS films with the addition of Ga include an increase in band gap, which mainly shifts the position of the conduction-band minimum [10-5],

as well as changes in the hole concentration [10-6], bulk defect densities [10-7], absorption coefficients, and electron affinities. The room temperature mobility was found to remain nearly constant while varying the Ga content over a wide range [10-6].

Except when otherwise mentioned, in the simulation studies an inverted surface layer with a thickness t = 30 nm, electron mobility μ_n = 10 cm^2/V-s, net carrier density n = 10^{12} cm^{-3}, and band gap E_g = 1.3 eV is inserted between the CdS and CIGS layers. Also, an interface layer with a high density of effective recombination centers is placed at the metallurgical junction between the inverted surface layer and the CdS layer. The total thickness of the absorber layer is maintained at 2 μm for all cases, including the various graded band-gap structures studied. In order to model an effective recombination center, a deep level defect is placed in the middle of the band gap of (*i*) the CdS layer, (*ii*) the high-recombination interface layer, (*iii*) the inverted surface layer, and (*iv*) the SCR of the CIGS absorber. To examine the effects of band-gap gradient on the device performance, most of the material parameters used in the simulations are maintained unchanged, except that the band gaps, electron affinities, and optical absorption coefficients are varied with the Ga mole fraction in the CIGS films.

10.4 Effect of Graded Band-gaps on Cell Performance

First, a simulation study of uniform band-gap CIS and CIGS cells is carried out to establish a baseline for comparison. Two representative band-gaps, namely 1.04 eV for CIS and 1.20 eV for CIGS, are considered. The simulation results are shown in Table 10-1. It is noted that the Cu(In$_{1-x}$,Ga$_x$)Se$_2$ cell with composition x ≈ 0.32 and E_g ≈ 1.20 eV [10-8] has a higher V_{oc} and a smaller J_{sc} than the CuInSe$_2$ cell corresponding to x ≈ 0 and E_g ≈ 1.04 eV, due to the smaller absorption coefficients and the reduction in the absorption of longer-wavelength photons. The effect of higher Ga-content of uniform band-gaps is not further analyzed because it has been reported in the literature that the device performance degraded when the Ga content in the Cu(In$_{1-x}$,Ga$_x$)Se$_2$ films exceeds 30 - 40%, *i.e.*, when x > 0.3 - 0.4 [10-9].

Table 10-1. Simulated performance parameters of the Cu(In$_{1-x}$,Ga$_x$)Se$_2$ for x = 0 (E_g = 1.04 eV), and Cu(In$_{1-x}$,Ga$_x$)Se$_2$ for x = 0.32 (E_g ≈ 1.20 eV) solar cells with a uniform absorber band-gap profile.

	x	E_g (eV)	η (%)	V_{oc} (mV)	J_{sc} (mA/cm^2)	F.F. (%)
CuInSe$_2$	0	1.04	13.00	500	38.01	68.4
Cu(In$_{1-x}$,Ga$_x$)Se$_2$	0.32	1.20	15.77	655	32.27	74.6

Second, a simulation study of the dependence of the cell performance on the band gap in the SCR of CIGS absorbers is carried out. The recombination rate in the SCR, which controls the V_{oc} of the CIGS cell, can be reduced by increasing the barrier height via the increase of the SCR band-gap. This improves the V_{oc}, but a small loss of J_{sc} might be expected if the wider

band-gap region is not sufficiently thin. The dependence of V_{oc} on the band gap in the SCR of CIGS cells has been reported [10-10]. In the simulation model, the SCR is composed of a series of layers of different band-gaps. The bottom-most layer in the SCR matches the band gap of 1.04 eV of the underlying CIGS bulk material, and the subsequent SCR layers located above linearly increase until reaching a wide band-gap end-point value (EPV) varying from 1.16 to 1.35 eV. More specifically, the EPV indicates the band gap of the SCR layer next to the inverted surface layer. The band-gaps of the inverted surface layer and of the remaining region of the CIGS bulk layer are maintained at $E_g = 1.30$ eV and 1.04 eV, respectively. The simulation results are shown in Figure 10-2, where the resulting performance parameters of V_{oc}, J_{sc}, fill factor (F.F.), and efficiency (η) are shown as a function of the EPV of the band gap in the SCR. The value of V_{oc} in Figure 10-2 (a) increases with increasing end-point band-gap in the SCR, improving from ~ 537 to ~ 551 mV, while the value of J_{sc} in Figure 10-2 (b) decreases slightly from ~ 37.9 to ~ 37.6 mA/cm^2. When comparing the performance of the graded band-gap cells reported in Figure 10-2 with the performance of the uniform band-gap CIS cell reported in Table 10-1, it is apparent that SCR grading improves the V_{oc} without significantly decreasing the J_{sc}. The F.F. values of the graded cells shown in Figure 10-2 (c) are also higher than that of the uniform band-gap CIS cell. The figure shows that different EPV values produce different F.F. values, but that the relationship is not monotonic. This is a consequence of the conduction-band offset between the inverted surface and CIGS layers. The value of η in Figure 10-2 (d) increases from ~ 15.3% to a maximum value of ~ 16.0% at an EPV value of ~ 1.30 eV. Comparing the efficiencies in Figure 10-2 (d) with the efficiency of the uniform-gap CIS cell in Table 10-1, it can be concluded that band-gap grading in SCR has a favorable effect on the final conversion efficiency.
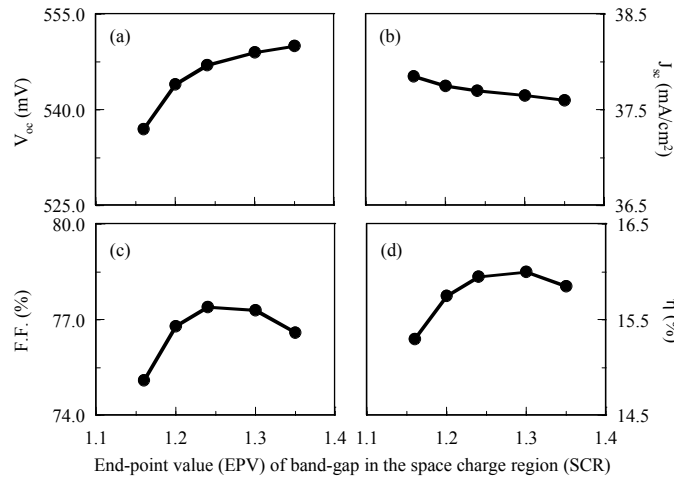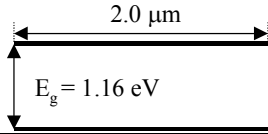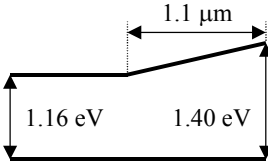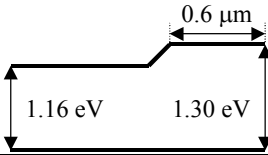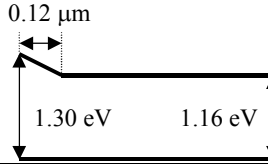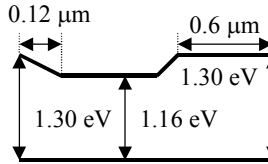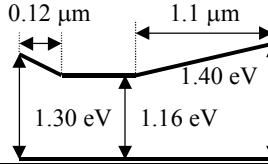

Figure 10-2. The dependence of cell performance parameters on the band-gap energy in the SCR of CIGS cells.

Third, a simulation study was conducted to evaluate the effect of graded band-gap profiles of the CIGS absorber on the performance of the cells. A total of seven band gap profile cases are considered, as shown in Table 10-2. The simulation results for each case yield the performance parameters η, V_{oc}, J_{sc}, and F.F reported in columns 3 to 6 of the table. The band-

gap profile of Case 1 is the baseline, featuring a uniform band-gap of 1.16 eV for the entire CIGS absorber layer. In Case 2, a back surface field (BSF) is formed by the normal grading, where the band gap is linearly increased towards the back, and in Case 3, a step grading is used, where a wider band-gap layer is placed in the back. In Case 4, a wider band-gap CIGS layer of 1.30 eV, decreasing linearly to 1.16 eV, is placed entirely in the SCR. In Case 5 and 6, a double graded band-gap structure using the wider band-gap layer in the SCR and in the back surface region of the absorber is introduced. Comparing the performance of the cell in Case 1, both the V_{oc} and J_{sc} with either a normal (Case 2) or step (Case 3) back surface grading are improved simultaneously, and hence the conversion efficiency is also increased, as shown in Table 10-2. The double graded band-gap structure of Case 6 realizes a high conversion efficiency of 18.39% AM1.5G. Figure 10-3 illustrates the schematic energy band diagram under equilibrium condition for Case 6 with a double band-gap grading. In this figure, a quasi-electrical field [10-11] can be established by the band-gap gradient with the incorporation of a high Ga content in the back region (near the Mo contact) of the CIGS absorber layers by reducing the back surface recombination and increasing the effective minority-carrier diffusion length. This results in an efficient carrier collection in the CIGS cells, and thus both the V_{oc} and J_{sc} are enhanced. The same trend was observed when comparing the performance of the cells in Cases 5 and 6 with that in Case 4. Case 7 is analogous to Case 6, except that the doping density in the CdS layer is increased to 6×10^{17} cm^{-3} and the deep- level defect densities are assumed to be equal to zero in the CIGS absorber. The result yields a maximum conversion efficiency of 19.83% for this cell.

Table 10-2. Simulated performance parameters of the CIGS solar cells with various absorber band-gap profiles.

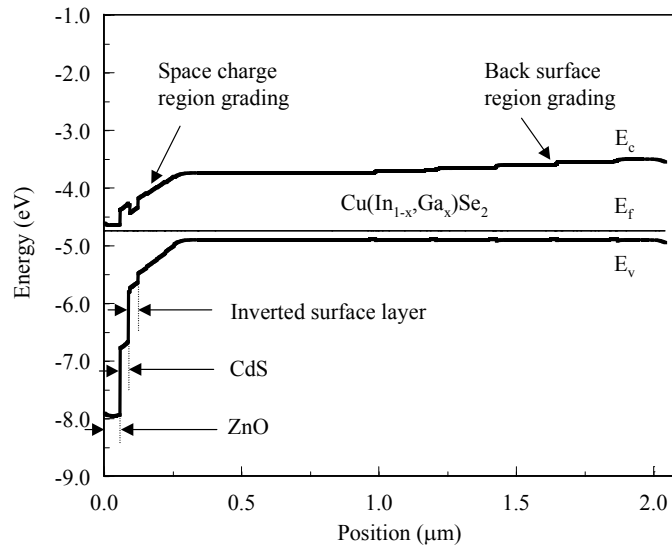| Band-gap profile		η (%)	V$_{oc}$ (mV)	J$_{sc}$ (mA/cm^2)	F.F. (%)
Case 1	2.0 μm; E$_g$ = 1.16 eV	15.42	617	34.05	73.4
Case 2	1.1 μm; 1.16 eV, 1.40 eV	15.72	622	34.61	73.1
Case 3	0.6 μm; 1.16 eV, 1.30 eV	15.81	620	34.77	73.3
Case 4	0.12 μm; 1.30 eV, 1.16 eV	17.57	658	33.55	79.6
Case 5	0.12 μm, 0.6 μm; 1.30 eV, 1.16 eV, 1.30 eV	18.34	669	34.46	79.6
Case 6	0.12 μm, 1.1 μm; 1.30 eV, 1.16 eV, 1.40 eV	18.39	675	34.31	79.4
Case 7	Same profile as Case 6	19.83	688	34.42	83.8

Figure 10-3. The schematic energy-band diagram of a CIGS cell with a double band-gap grading profile under equilibrium condition.

In summary, a proper band-gap grading consisting of a wider band-gap CIGS layer in the SCR and a back surface grading are capable of significantly improving the performance of the CIGS cells. In the simulation studies the band gaps in the SCR and in the back region and the thickness of the back surface grading layers are varied to achieve the optimal performance through reducing the carrier recombination and increasing the carrier collection for the given material parameters and device structure. Comparing the performance of a uniform band-gap cell (Case 1) with the graded band-gap cells (Case 5 and Case 6), the benefit of band-gap grading for the CIGS solar cells is clearly demonstrated.

10.5 Comparison with Experimental Data

Attempts are made to compare the simulation results with reported experimental data for the CIGS cells. The measured values are taken from the photo- current density- voltage (J-V) and normalized quantum efficiency (Q.E.) curves of an experimental CIGS cell with 18.8% efficiency under standard conditions produced at the National Renewable Energy Laboratory (NREL) [10-12] [10-13]. The performance of this experimental cell is compared with the simulated results of Cases 6 and 7 in Table 10-2, and the results are shown in Figures 10-4 and 10-5, where the solid line represents the simulated cell of Case 6, the dashed line represents the simulated cell of Case 7, and the solid circles denote the experimental values. Figure 10-4 shows that the photo- J-V curve for Case 6 closely matches the experimental curve for the NREL CIGS cell. The photo- J-V values obtained from the simulation of Case 7 suggest that a higher efficiency is possible. Figure 10-5 shows a comparison of the simulated Q.E. curve for Case 6 with the experimental curve. Good agreement was also observed in this case in the wavelength (λ) range of 0.5 μm $\leq \lambda \leq$ 1.2 μm.
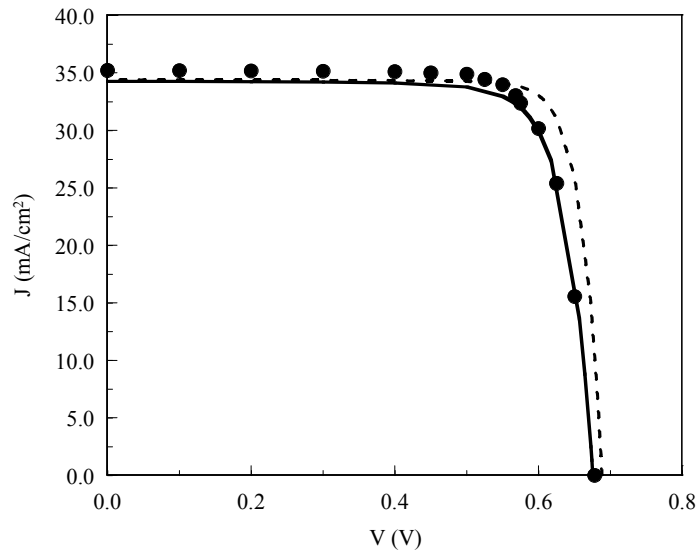
Figure 10-4. The photo-current density-voltage (J-V) curves for the simulated results (solid and dashed lines) and the reported experimental data (solid circles) [10-12] [10-13].
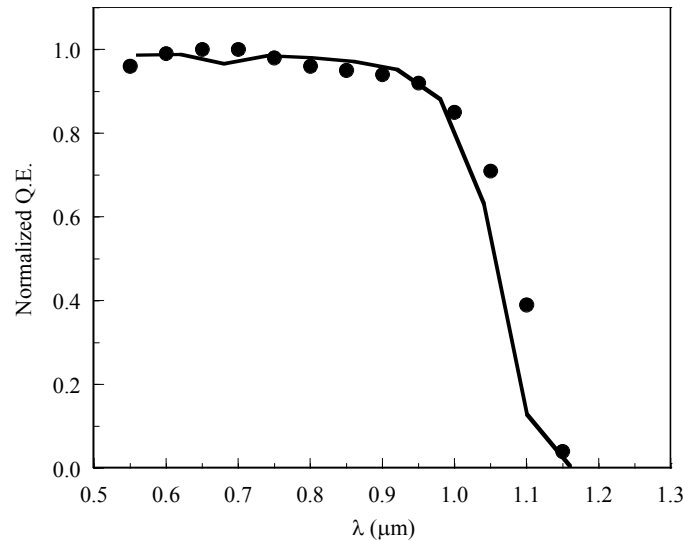

Figure 10-5. The normalized QE for the simulated results (solid line) and the reported experimental values (solid circles) [10-12].

A separate analysis is carried out to fit the performance of the simulated parameters with data available in the published literature for CIGS cells. Dullweber *et al*. have reported experimental results for band-gap grading in CIGS cells [10-10] [10-14]. The band-gap structure of the CIGS absorber layer in Table 10-3 is based on the Auger depth profile reported by Dullweber *et al*. [10-10], which allows defining the layer dimensions and compositions for the simulation model. For the simulation study, the depth profile is represented by an equivalent

band-gap profile in the CIGS absorber using the equation $E_g(y)$ [eV] $= 1.02 + 0.67\, y + 0.11\, y\,(y\text{-}1)$ proposed in [10-15], where the variable y denotes the ratio of Ga/(Ga+In). The resulting band-gap profile reveals a double-graded CIGS absorber layer with linearly graded band-gap structures in the SCR and in the CIGS bulk layers, as shown in Table 10-3, and is used as a set of input parameters for the simulation study. This notch structure is a particular case of double grading. Theoretical analysis and simulation studies of this structure have been reported [10-16]. The measured data are also taken from the J-V curve given in [10-10]. The key parameters used in fitting the simulation results to the experimental values are the defect density in the inverted surface layer, the defect densities of the mid-gap deep- level in the SCR, and the defect and hole densities in the CIGS absorber. The results are shown in Figure 10-6, where the simulated values are plotted using a solid line, and the experimental values are indicated by the solid circles. Although the simulated F.F. is slightly higher than the experiment, excellent agreement was observed in the J-V curve.

Table 10-3. The energy band-gap profile of the CIGS absorber layer used in simulation.
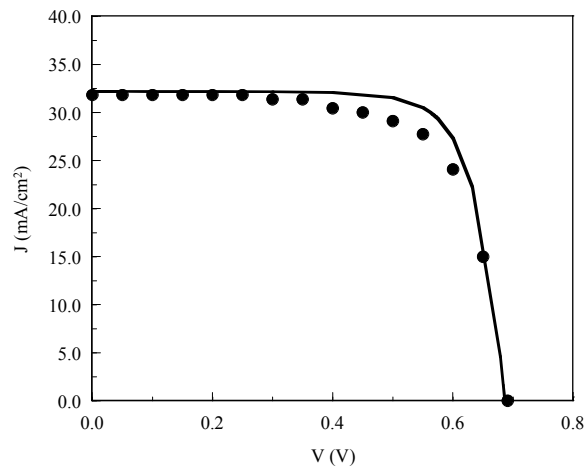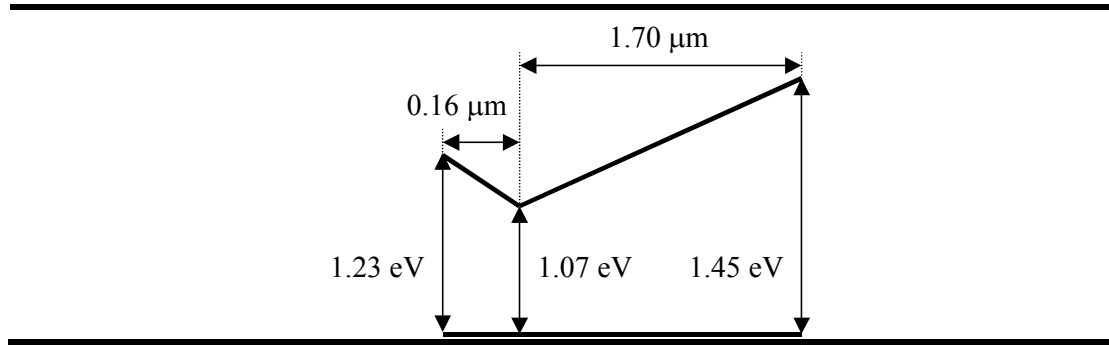

Figure 10-6. The photo-current density-voltage (J-V) curves for the simulated results (solid line) and the published data (solid circles) [10-10].

Finally, another work by Dullweber *et al*. [10-14] for CIGS cells with a normal or reverse graded absorber is considered for fitting the simulation results to experimental values. An absorber with normal grading profile is one where the band gap is increased linearly from the front to the backside in the entire absorber, while the absorber with reverse grading profile is one where the band gap is decreased linearly from the front to the back. To investigate these linearly graded structures via simulation, the composition depth profiles of the CIGS absorber given in [10-14] were used for the calculation of the band-gap profiles for the CIGS absorber. From the represented band-gap profiles, an absorber structure with normal grading is increased linearly from the front band-gap of 1.03 eV to the backside band-gap of 1.22 eV, while an absorber profile with reverse grading is decreased from 1.24 eV to 1.06 eV. Also, a uniform band-gap profile of 1.14 eV is considered. Experimental performance parameters are also extracted from [10-14] for the cases of normal, reverse, and uniform grading, and are compared with the simulated results. The major parameters used in fitting the simulated results to the experimental values are as described in the preceding paragraph. The results are shown in Figure 10-7, where the solid circle and triangle denote the simulated values and experimental data, respectively. The x-axis indicates CIGS absorber band-gap profiles consisting of the reverse grading, uniform, and normal grading from left to right. It is noted that from Figure 10-7 (a) V_{oc} is found to decrease from 565 to 509 mV (a change of 56 mV), from the reverse to the normal grading, while the value of J_{sc} increases from 32.5 to 37.5 mA/cm^2 (a change of 5 mA/cm^2) as shown in Figure 10-7 (b). These trends are also found in the experimental values. Excellent agreement was obtained on the performance parameters V_{oc}, J_{sc}, and F.F. Even though the values of η in the simulation are slightly higher than their experimental counterparts, a reasonable fit is nevertheless obtained.
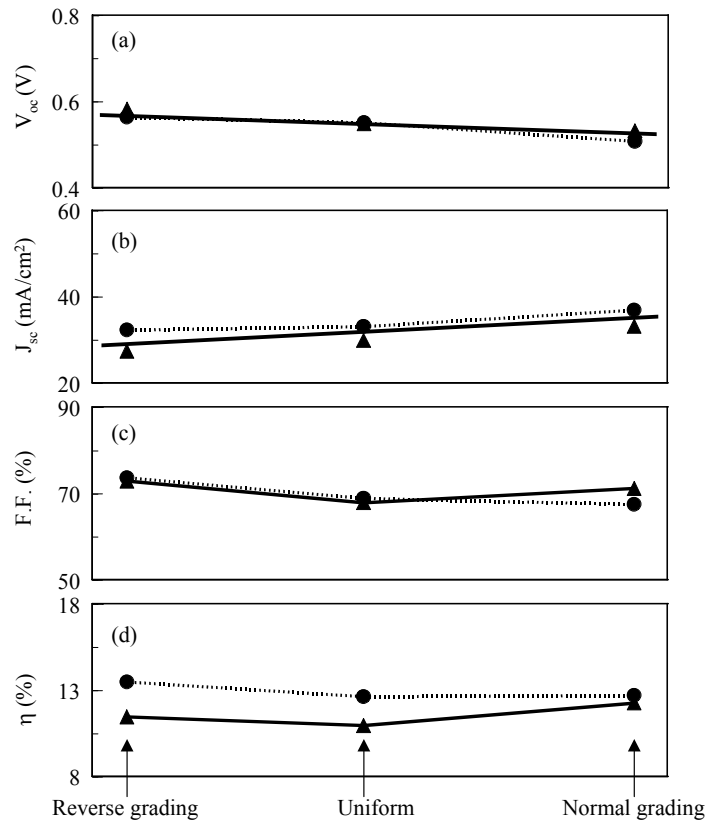
Figure 10-7. A comparison of the performance parameters for the simulated results (circles) and the published data (triangles) [10-14].

10.6 Conclusions

Comprehensive device modeling and numerical simulation studies for single-junction CIGS thin film solar cells have been carried out using the AMPS-1D device simulation program, including various absorber band-gap profiles. A detailed analysis of the graded band-gap structures for the CIGS cells has been presented. It is shown that band-gap grading using a wide band-gap layer in the SCR and/or back surface grading using the gradient of Ga content in the CIGS absorber layer greatly improve the performance of single-junction CIGS cells. Additionally, studies to fit the simulation results with the reported experimental data show reasonable agreement in the J-V and Q.E. curves between the modeling and the experimental data.

10.7 References Cited

[10-1] D. Schmid, M. Ruckh, F. Grunwald, and H.W. Schock, "Chalcopyrite/Defect Chalcopyrite Heterojunctions on the Basis of CuInSe$_2$", *Journal of Applied Physics*, Vol. 73, No. 6, pp. 2902-2909 (1993).

[10-2] R. Herberhoz, U. Rau, H.W. Schock, T. Haalboom, T. Gödecke, F. Ernst, C. Beilharz, K.W. Benz, and Cahen, "Phase Segregation, Cu Migration and Junction Formation in Cu(In,Ga)Se$_2$", *European Physical J. Appl. Phys*, Vol. 6, pp. 131-139 (1999).

[10-3] J. Guillemoles, T. Haalboom, T. Gödecke, F. Ernst, D. Cahen, "Phase and Interface Stability Issues in Chalcopyrite-based Thin Film Solar Cells", *Mat. Res. Soc. Symp. Proc.*, 485, pp. 127-132 (1998).

[10-4] H. Zhu, A.K. Kalkan, J. Hou, and S.J. Fonash, "Application of AMPS-1D for Solar Cell Simulation", *AIP Conference Proceedings*, No. 462, pp. 309-314 (1999).

[10-5] S.H. Wei and A. Zunger, "Band Offsets and Optical Bowings of Chalcopyrites and Zn-based II-VI Alloys", *J. Appl. Phys.*, Vol. 78, pp. 3846-3856 (1995).

[10-6] D.J. Schroeder, J.L. Herberholz, and A.A. Rockett, "Point Defects and Hole Transport in Epitaxial CuIn$_{1-x}$Ga$_x$Se$_2$", *11th Int. Conf. on Ternary and Multinary Compounds*, pp. 749-752 (1999).

[10-7] G. Henna, A. Jasenek, U. Rau, and H.W. Schock, "Influence of the Ga-content on the Bulk Defect Densities of Cu(In,Ga)Se$_2$", *Thin Solid Films*, Vol. 387, pp. 71-73 (2001).

[10-8] S.H. Wei, and S.B. Zhang, and A. Zunger, "Effects of Ga Addition to CuInSe$_2$ on Its Electronic, Structural, and Defect Properties", *Applied Physics Letters*, Vol. 72, pp. 3199-3201 (1998).

[10-9] T. Walter, R. Menner, M. Ruckh, L. Kaser, and H.W. Schock, "Parameter Studies and Analysis of High Efficiency Cu(In,Ga)Se$_2$ Based Solar Cells", *Conference Record of the 22nd IEEE Photovoltaic Specialists Conference*, pp. 924-929 (1991).

[10-10] T. Dullweber, G. Hanna, U. Rau, and H.W. Schock, "A New Approach to High-efficiency Solar Cells by Band Gap Grading in Cu(In,Ga)Se$_2$ Chalcopyrite Semiconductors", *Solar Energy Materials & Solar Cells*, Vol. 67, pp.145-150 (2001).

[10-11] H. Koremer, *RCA Review*, Vol. 18, pp. 332 (1957).

[10-12] M.A. Contreras, B. Egaas, K. Ramanathan, J. Hiltner, A. Swartzlander, F. Hasoon, and R. Noufi, "Progress Toward 20% Efficiency in Cu(In,Ga)Se$_2$ Polycrystalline Thin-film Solar Cells", *Progress in Photovoltaics: Research & Application*, Vol. 7, pp. 311-316 (1999).

[10-13] http://www.nrel.gov/measurements/voltage.html.

[10-14] T. Dullweber, G. Hanna, W. Shams-Kolahi, A. Schwartzlander, M.A. Contreras, R. Noufi, and H.W. Schock, "Study of the Effect of Gallium Grading in Cu(In,Ga)Se$_2$", *Thin Solid Films*, Vol. 361-362, pp. 478-481 (2000).

[10-15] T. Dullweber, U. Rau, M.A. Contreras, R. Noufi, and H.W. Schock, "Photogeneration and Carrier Recombination in Graded Gap Cu(In,Ga)Se$_2$ Solar Cells", *IEEE Transactions on Electron Devices*, Vol. 47, No. 12, pp. 2249-2254 (2000).

[10-16] A. Dhingra and A. Rothwarf, "Computer Simulation and Modeling of the Graded Bandgap CuInSe$_2$/CdS Solar Cell", *Conference Record of the 23rd IEEE Photovoltaic Specialist Conference*, pp. 475-480 (1993).

REPORT DOCUMENTATION PAGE

1. REPORT DATE *(DD-MM-YYYY)*	2. REPORT TYPE	3. DATES COVERED *(From - To)*
September 2006	Subcontract Report	2 October 2001–30 September 2005

4. TITLE AND SUBTITLE
Fundamental Materials Research and Advanced Process Development for Thin-Film CIS-Based Photovoltaics: Final Technical Report, 2 October 2001 – 30 September 2005

5a. CONTRACT NUMBER
DE-AC36-99-GO10337

5b. GRANT NUMBER

5c. PROGRAM ELEMENT NUMBER

6. AUTHOR(S)
T.J. Anderson, S.S. Li, O.D. Crisalle, and V. Craciun

5d. PROJECT NUMBER
NREL/SR-520-40568

5e. TASK NUMBER
PVB65101

5f. WORK UNIT NUMBER

7. PERFORMING ORGANIZATION NAME(S) AND ADDRESS(ES)
University of Florida
227 Chemical Engineering Bldg.
Gainesville, Florida 32611-6005

8. PERFORMING ORGANIZATION REPORT NUMBER
ADJ-2-30630-13

9. SPONSORING/MONITORING AGENCY NAME(S) AND ADDRESS(ES)
National Renewable Energy Laboratory
1617 Cole Blvd.
Golden, CO 80401-3393

10. SPONSOR/MONITOR'S ACRONYM(S)
NREL

11. SPONSORING/MONITORING AGENCY REPORT NUMBER
NREL/SR-520-40568

12. DISTRIBUTION AVAILABILITY STATEMENT
National Technical Information Service
U.S. Department of Commerce
5285 Port Royal Road
Springfield, VA 22161

13. SUPPLEMENTARY NOTES
NREL Technical Monitor: B. von Roedern

14. ABSTRACT *(Maximum 200 Words)*
The objectives for this thin-film copper-indium-diselenide (CIS) solar cell project cover the following areas: Develop and characterize buffer layers for CIS-based solar cell; grow and characterize chemical-bath deposition of $Zn_x Cd_{1-x}S$ buffer layers grown on CIGS absorbers; study effects of buffer-layer processing on CIGS thin films characterized by the dual-beam optical modulation technique; grow epitaxial $CuInSe_2$ at high temperature; study the defect structure of CGS by photoluminescence spectroscopy; investigate deep-level defects in $Cu(In,Ga)Se_2$ solar cells by deep-level transient spectroscopy; conduct thermodynamic modeling of the isothermal 500°C section of the Cu-In-Se system using a defect model; form α-$CuInSe_2$ by rapid thermal processing of a stacked binary compound bilayer; investigate pulsed non-melt laser annealing on the film properties and performance of $Cu(In,Ga)Se_2$ solar cells; and conduct device modeling and simulation of CIGS solar cells.

15. SUBJECT TERMS
PV; materials research; thin film; advanced process development; solar cell; copper indium diselenide; chemical-bath-deposition; epitaxial growth; optical modulation; photoluminescence spectroscopy; deep-level transient spectroscopy; thermodynamic modeling; simulation; CIGS.

16. SECURITY CLASSIFICATION OF:			17. LIMITATION OF ABSTRACT	18. NUMBER OF PAGES	19a. NAME OF RESPONSIBLE PERSON
a. REPORT	b. ABSTRACT	c. THIS PAGE	UL		
Unclassified	Unclassified	Unclassified			19b. TELEPHONE NUMBER *(Include area code)*